University of Southampton
Faculty of Engineering and Applied Science
School of Electronics and Computer Science

Iterative Decoding of Multilevel and Bit-Interleaved Coded Modulation

by

Ronald Yee Siong Tee
BEng., MSc.

A doctoral thesis submitted in partial fulfilment of the requirements for the award of Doctor of Philosophy at the University of Southampton

March 2008

SUPERVISOR: *Professor Lajos Hanzo*
M.Sc., Ph.D, FREng, DSc, FIEEE, FIET
Chair of Telecommunications
School of Electronics and Computer Science
University of Southampton
Southampton SO17 1BJ
United Kingdom

This thesis is dedicated to:

my mum
my dad

with all my love and respect...

UNIVERSITY OF SOUTHAMPTON

ABSTRACT

FACULTY OF ENGINEERING AND APPLIED SCIENCE
SCHOOL OF ELECTRONICS AND COMPUTER SCIENCE

Doctor of Philosophy

Iterative Decoding of Multilevel and Bit-Interleaved Coded Modulation

by
Ronald Yee Siong Tee

A comparative study of various coded modulation schemes is carried out in terms of their different block length, number of iterations and complexity, quantified by the number of trellis states as well as the EXtrinsic Information Transfer (EXIT) charts are used for analysing their decoding convergence and Bit Error Ratio (BER). A three-Dimensional (3-D) EXIT chart is introduced for MultiLevel Coding (MLC) invoking MultiStage Decoding (MSD). Based on this 3-D EXIT chart, we design a precoded-MLC scheme employing both MSD and Parallel Independent Decoding (PID).

In order to provide space diversity, we study the new arrangement of Bit-Interleaved Coded Modulation with Iterative Decoding (BICM-ID) and MLC combined with Space Time Block Codes (STBC) invoking a novel Sphere Packing (SP) modulation scheme. An equivalent-capacity-based design of MLCs based on this SP modulation is proposed. We use the Binary Switching Algorithm (BSA) to optimise our cost function for the sake of obtaining appropriate bit-to-SP-symbol mapping schemes. A hybrid mapping scheme is introduced for achieving unequal error protection. Furthermore, bit-to-SP-symbol mapping to 256 constellation points is designed for a serially concatenated BICM-ID aided twin-antenna STBC arrangement for creating a system, which is capable of outperforming an identical-throughput 16-level Quadrature Amplitude Modulation (16QAM) scheme.

Furthermore, the benefits of MLC PID designs employing Generalised Low Density Parity Check (GLDPC) codes are investigated, which results in a low-delay scheme useful for multimedia transmission. A stopping criterion is designed for this scheme for the sake of terminating the iterative decoding process, once the target BER is attained. We then contrive coding schemes for the wireless Internet by introducing a BICM-ID scheme combined with Luby Transform (LT) coding constructed for the

AWGN-contaminated Binary Erasure Channel (BEC). An improved robust LT packet-degree distribution is introduced for determining the specific number of LT source packets combined with modulo-2 additions in order to create an LT-encoded packet. Furthermore, a Log-Likelihood Ratio (LLR) based reliability estimation scheme is invoked in order to achieve a performance improvement based on this amalgamated design.

Finally, a near-capacity Irregular Bit-Interleaved Coded Modulation with Iterative Decoding (Ir-BICM-ID) scheme was designed with the aid of an EXIT chart. An Irregular Convolution Code (IrCC) is proposed for the sake of introducing a diverse range of outer code EXIT functions. By contrast, the inner code is based on the serially concatenated components constituted by an Irregular Unity-Rate Code (IrURC) and an Irregular Mapper (IrMapper). An EXIT chart matching algorithm is invoked for constructing an Ir-BICM-ID scheme, which exhibits a narrow but still open EXIT tunnel and hence approaches the theoretical capacity limit.

Acknowledgements

I would like to express my heartfelt gratitude to Professor Lajos Hanzo for his continuous support and invaluable advice throughout the journey of my research. His enthusiasm in research work and his generous and sincere character have truly inspired me, not only in terms of research activities, but also as a mould to my character. I would never forget his constant support during my predicament in Southampton General Hospital and his encouragement when my work was destroyed in the fire.

Many grateful thanks to my colleagues and the staff of Communication group for their support, help and fruitful discussion. Special thanks to Dr. Soon Xin Ng who is a good friend and a mentor of mine. Many appreciations also to Prof. Sheng Chen, Dr. Lie-Liang Yang, Dr. Robert Maunder, Dr. Jos Akhtman, Dr. Andreas Wolfgang, Dr. Osamah Alamri, Mohammed El-Hajjar, Seung Hwan Won, Noor Othman, Thanh Nguyen Dang, Chong Xu, Chun-Yi Wei, Anh Pham Quang, Vicky Kuo, Dr. Xiang Liu, Dr. Wei Liu, Augustine Koh, Dr. Jiang Ming, Dr. Bee Leong Yeap, Nan Wu, Shuang Tan, Wei Fang, Rong Zhang, Nicholas Bonello, Lei Xu, Lingkun Kong and other colleagues and staff, too many to mention here. My gratitude to Denise Harvey for her help in administrative matters.

The financial support of Overseas Research Student (ORS) scheme as well as of the School of Electronics and Computer Science (ECS) are gratefully acknowledged.

My appreciation also to my faithful friends in Portswood church especially to Andy Piper and Karen Tan as well as my housemates who helped me throughout my stay in Southampton. Last but not least, I want to thank my beloved family, dad, mum and my sister. For me, family is the warmest place to find a shelter in a storm.

List of Publications

Journal Papers

1. **R. Y. S. Tee**, F. C. Kuo and L. Hanzo,"Multilevel Generalised Low-Density Parity-Check Codes," IEE Electronics Letters, vol. 42, Issue 3, pp. 167-168, 2 February 2006.

2. **R. Y. S. Tee**, O. Alamri, S. X. Ng and L. Hanzo, "Equivalent Capacity Based Joint Multilevel Coding And Space Time Transmit-Diversity Design," to appear in IEEE Transactions on Vehicular Technology.

3. **R. Y. S. Tee**, O. Alamri, S. X. Ng and L. Hanzo, "Bit-Interleaved Sphere-Packing-Aided Space-Time Coded Modulation," to appear in IEEE Transactions on Vehicular Technology.

4. **R. Y. S. Tee**, R. G. Maunder and L. Hanzo, "EXIT-Chart Aided Near-Capacity Irregular Bit-Interleaved Coded Modulation Design," to appear in IEEE Transactions on Wireless Communications.

5. T. D. Nguyen, **R. Y. S. Tee**, L. L. Yang and L. Hanzo, "H-ARQ-Aided Systematic Luby Transform Codes," submitted to IEEE Transactions on Vehicular Technology, April 2008.

Conference Papers

6. **R. Y. S. Tee**, S. X. Ng and L. Hanzo, "Three-Dimensional EXIT Chart Analysis of Iterative Detecltion Aided Coded Modulation Schemes," in IEEE Vehicular Technology Conference-Spring (VTC), vol. 5, (Melbourne, Austrialia), pp. 2494-2498, May 2006.

7. **R. Y. S. Tee**, F. C. Kuo and L. Hanzo, "Generalized Low-Density Parity-Check Coding Aided Multilevel Codes," in IEEE Vehicular Technology Conference-Spring (VTC), vol. 5, (Melbourne, Australia), pp. 2398-2402, May 2006.

8. **R. Y. S. Tee**, T. D. Nguyen, L. L. Yang and L. Hanzo, "Serially Concatenated Luby Transform Coding and Bit-Interleaved Coded Modulation Using Iteratlive

Decoding for the Wireless Internet," in IEEE Vehicular Technology Conference-Spring (VTC), vol. 1, (Melbourne, Australia), pp. 22-26, May 2006.

9. **R. Y. S. Tee**, S. X. Ng and L. Hanzo, "Precoder-aided iterative detection assisted multilevel coding and three-dimensional EXIT-chart analysis," in IEEE Wireless Communications and Networking Conference (WCNC), vol. 3, (Las Vegas, USA), pp. 1322-1326, 3-6 April 2006.

10. **R. Y. S. Tee**, O. Alamri and L. Hanzo, "Joint Design of Twin-Antenna Assisted Space-Time Multilevel Sphere Packing Aided Coded Modulation," in IEEE Vehicular Technology Conference-Fall (VTC), (Montreal, Canada), pp. 1-5, September 2006.

11. **R. Y. S. Tee**, O. Alamri, S. X. Ng and L. Hanzo, "Equivalent-Capacity-Based Design of Space-Time Block-Coded Sphere-Packing-Aided Multilevel Coding," in IEEE Proceedings of International Conference on Communications (ICC), (Glasgow, UK), pp. 24-27, 24-28 June 2007.

12. **R. Y. S. Tee**, T. D. Nguyen, S. X. Ng, L-L. Yang and L. Hanzo, "Luby Transform Coding Aided Bit-Interleaved Coded Modulation for the Wireless Internet," in IEEE Vehicular Technology Conference-Fall (VTC), (Baltimore, USA), pp. 2025 - 2029, October 2007.

13. M. El-Hajjar, **R. Y. S. Tee**, H. Bin, L-L. Yang and L. Hanzo, "Downlink Steered Space-Time Spreading Assisted Generalised Multicarrier DS-CDMA Using Sphere-Packing-Aided Multilevel Coding," in IEEE Vehicular Technology Conference-Fall (VTC), (Baltimore, USA), pp. 472 - 476, October 2007.

14. **R. Y. S. Tee**, R. G. Maunder, J. Wang and L. Hanzo, "Near-Capacity Irregular Bit-Interleaved Coded Modulation," in IEEE Vehicular Technology Conference-Fall (VTC), (Singapore), May 2008.

15. T. D. Nguyen, **R. Y. S. Tee**, L. L. Yang and L. Hanzo, "Hybrid ARQ Aided Systematic Luby Transform Coded Modulation," submitted to IEEE Global Communications Conference (Globecom), (New Orleans, USA), 2008.

Contents

Chapter 1

Introduction

Forward Error Correction (FEC) codes protect the transmission of the source data with the aid of parity bits for the sake of detecting and correcting transmission errors, which has different pros and cons in comparison to the error detection and retransmission schemes using Automatic Repeat reQuest (ARQ) mechanisms. The history of FEC evolved from Shannon's [1] mile-stone paper in which he demonstrated that reliable communications with an infinitesimally low probability of error is achievable, when the rate of transmission is lower than the capacity of the channel. This may be achieved with the aid of incorporating redundant parity bits by employing FEC codes to protect the original information bits.

The Hamming code was one of the first FEC codes [2] designed in 1950. Convolutional codes, which constitute important FECs have been widely used since their introduction by Elias in 1955 [3]. Convolutional codes may be decoded using the Viterbi Algorithm (VA) invented in 1967 [4] and, by the Maximum A-Posteriori (MAP) algorithm discovered in 1974 [5].

By contrast, Bose-Chaudhuri-Hocquenghem (BCH) codes constitute block codes, which were named after their inventors in 1959 [6] and 1960 [7]. Reed-Solomon (RS) codes represent a specific class of non-binary BCH codes, which were invented in 1960 [8]. Gallager devised the attractive family of Low-Density Parity Check (LDPC) codes in 1963 [9]. However, rather surprisingly, LDPCs did not attract substantial attention until the discovery of turbo codes in 1993 [10]. The invention of Turbo codes also triggered extensive research in the field of iterative decoding of both parallel [11] and serial concatenated codes [12,13].

1.1 A Historical Perspective on Coded Modulation

When using separate coding and modulation, achieving a close-to-Shannon-limit performance often requires a low coding rate, hence resulting in a high bandwidth expansion. Therefore, a bandwidth efficient MultiLevel Coding (MLC) scheme, which was based on the joint design of coding and modulation, was proposed by Imai and Hirawaki [14] in 1977. This scheme employed several component codes and invoked a MultiStage Decoding (MSD) method, where the redundant FEC bits may be absorbed without bandwidth expansion by expanding the modulated phasor constellation. This multistage decoding procedure was further investigated by Calderbank in [15].

Ungerböck's concept of Trellis Coded Modulation (TCM) was independently proposed in 1982, which amalgamated the design of coding and modulation into a single entity with the aid of Ungerböck's constellation partitioning [16]. MLC based on Ungerböck's partitioning of the modulated signal sets were also studied by Pottie *et al.* [19]. The performance of MLCs and TCM in Gaussian channels was further investigated by Kofman *et al.* in [21], when using interleavers and limited soft-output based MSD. The MLC aided TCM design constructed with the aid of convolutional codes having maximum Hamming distance for transmission over Rayleigh fading channel was presented in [20]. The specific rate of the individual component codes of MLCs designed for approaching the capacity was determined by Huber *et al.* [22]. The provision of Unequal Error Protection (UEP) is important in multimedia transmissions, hence Lin *et al.* [26,27] designed UEP aided MLCs for both symmetric and asymmetric constellations.

In order to exploit the powerful error correction capability of LDPCs, Hou *et al.* employed them as MLC component codes and designed power- and bandwidth-efficient MLC schemes for Code Division Multiple Access (CDMA) [30]. In order to obtain a further diversity gain with the aid of multiple transmit and receive antennas, Lampe *et al.* proposed a multiple-antenna assisted transmission scheme for MLCs [31]. The employment of Multi-Dimensional (M-D) space-time MLCs involving M-D partitioning was carried out in the work of Martin *et al.* [32] in order to obtain substantial coding gains.

In 1982, the TCM concept was adopted by Zehavi to improve the achievable time-diversity order while maintaining a minimum Hamming distance, which led to the con-

Year	**Author(s)**	**Contribution**
1977	Imai and Hirawaki [14]	Proposed MLC invoking multistage decoding.
1982	Ungerböck [16]	Invented TCM employing Ungerböck partitioning (UP).
1982	Zehavi [17]	Invented BICM for transmission over Rayleigh fading channels.
1987	Wei [18]	Pioneered rotationally invariant differentially encoded multidimensional constellation for the design of TCM.
1989	Calderbank [15]	Investigated MSD aided MLC.
1989	Pottie and Taylor [19]	Designed MLC based on UP strategies.
1993	Seshadri and Sundberg [20]	Studied the performance of Multilevel TCM in Rayleigh fading channel.
1994	Kofman [21]	Studied the performance of MLC in AWGN channels.
1994	Huber and Wachsmann [22]	Calculated the equivalent capacity of MLC schemes.
1997	Li and Ritcey [23]	Designed BICM-ID using UP strategy.
1998	Caire *et al.* [24]	Analysed the theoretical error bound of BICM.
1998	Robertson *et al.* [25]	Designed iterative turbo-detection aided TTCM.
2000	Shu Lin *et al.* [26, 27]	Designed UEP for MLC based on symmetrical and asymmetrical phasor constellations.
2001	Ritcey *et al.* [28]	Introduced improved bit-to-symbol mapping for BICM-ID.
2004	Huang *et al.* [29]	Designed improved mapping schemes for space-time BICM-ID.
2004	Hou *et al.* [30]	Employed LDPC as MLC component codes and introduced a novel semi-BICM structure.
2004	Lampe *et al.* [31]	Proposed MLC-aided multiple-antenna assisted transmission schemes.
2006	Martin *et al.* [32]	Devised an MLC based multidimensional mapping scheme for space-time codes.
2007	Mohammed *et al.* [33, 34]	Introduced multidimensional mapping for space-time BICM-ID employing the Reactive Tabu Search technique.
2007	Matsumoto *et al.* [35]	Introduced an adaptive coding technique for multilevel BICM aided broadband single carrier signaling.
2008	Simoens *et al.* [36]	Investigated the effects of linear precoding on BICM-ID for transmission over AWGN channels.

Table 1.1: History of coded modulation contributions.

cept of Bit-Interleaved Coded Modulation (BICM) [17]. This improved the achievable coded modulation performance, when communicating over Rayleigh fading channels. The theory underlying BICM was extensively analysed by Caire *et al.* in terms of its channel capacity, error bound and design guidelines in [24]. For the sake of introducing the iterative decoding of BICM and hence achieving an improved performance in Additive White Gaussian Channels (AWGN), the Bit-Interleaved Coded Modulation based Iterative Decoding (BICM-ID) philosophy was proposed by Li *et al.* [23] using the Ungerböck's TCM partitioning strategy.

The multidimensional TCM concept was pioneered by Wei [18] for the sake of achieving rotational invariance which has the potential of dispensing with the false locking problems of carrier recovery as well as the concomitant avalanche-like error propagation. To introduce iterative decoding, two parallel TCM schemes were invoked by Robertson *et al.* in [25]. This parallel concatenated design was later termed as Turbo TCM (TTCM).

Since the optimisation of the bit-to-symbol mapping for BICM-ID was found to be crucial in assisting the scheme's iterative decoding convergence, Ritcey *et al.* further improved the mapping [28] schemes. BICM-ID was combined with space time codes to achieve a spatial diversity gain and the corresponding mapping schemes were further improved by Huang *et al.*. Mohammed *et al.* [33] later extended the findings of [29] to multidimensional constellation labelling by employing the Reactive Tabu Search (RTS) technique [37].

A MultiLevel BICM scheme (ML-BICM) was combined with ARQ and adaptive coding in the work of Matsumoto [35] *et al.*. This flexible design could be viewed as layer-by-layer link adaptation combined with an effective retransmission scheme. The multidimensional mapping used could be interpreted as a combined mapping function, a serially concatenated rate-one precoder and a Gray mapper. Simoens *et al.* [36] investigated the optimised linear block precoder aided design of BICM-ID communicating over AWGN channels for the sake of achieving an infinitesimally low BER.

The major contributions of the past three decades in the field of coded modulation, particularly in multilevel and bit-interleaved coded modulation are summarised in Table 1.1.

1.2 Outline of Thesis and Novel Contributions

1.2.1 Outline of Thesis

The outline of the thesis is presented below.

- **Chapter 2: Multilevel Coding Theory**

  This chapter introduces the background of MLCs. Section 2.2 highlights the design of signal labelling, rate design criteria as well as the encoding and decoding structures. BICM and BICM-ID are also characterised in terms of the philosophy of using bit interleavers, their decoding methods as well as bit-to-symbol mapping schemes in Section 2.3 and 2.4, respectively.

- **Chapter 3: MLC Design Using EXIT Chart Analysis**

  The iterative detection of BICM-ID and MLC schemes is analysed with respect to their convergence behaviour using EXIT chart analysis in this chapter. Section 3.2 presents the comparative study of different coded modulation schemes, namely that of MLC, BICM, BICM-ID, TCM and TTCM as a function of their trellis complexity expressed in terms of the number of trellis states and interleaver length. The simulation results showing these comparisons are presented in Section 3.2.3. EXIT charts employed as a design tool for iterative decoding are described in Section 3.3, characterising the iterative detection aided performance of BICM-ID schemes. Three-dimensional EXIT charts are used for studying the convergence behaviour of MLC schemes in Section 3.3.3. A precoder-aided MLC design is introduced in Section 3.4, which employs the above-mentioned 3-D EXIT analysis. The performance improvements achieved by this system are presented in Section 3.4.3.

- **Chapter 4: Sphere Packing Aided MLC/BICM Space-Time Design**

  This chapter studies the new arrangement of MLC combined with Space Time Block Codes (STBC) invoking a new type of M-D Sphere Packing (SP) modulation scheme termed as a STBC-SP-MLC arrangement. A similar arrangement using BICM to replace the MLC coding block is also used, which is referred to as an STBC-SP-BICM arrangement. Section 4.2 describes Alamouti's twin-antenna based STBC scheme. The SP modulation and its soft demodulation technique are outlined in Sections 4.3 and 4.4. The STBC-SP-MLC arrangement is presented in Section 4.5, where we further highlight the features of the system, as well as its equivalent capacity based design employed for determining the rates of our MLC component codes and the appropriate bit-to-SP-symbol mapping schemes. In Section 4.5.4, the UEP scheme created by this system is investigated by introducing a *hybrid* bit-stream partitioning strategy. Section 4.6 considers this STBC-SP-BICM arrangement, presenting the general system structure as well as a range of various mapping schemes. EXIT charts are invoked for further analysis both with and without precoder enhancements, and the corresponding simulation results are discussed in Section 4.6.5.

- **Chapter 5: MLC/BICM Schemes for Multimedia Communications and the Wireless Internet**

  This chapter provides MLC designs for low-latency multimedia applications employing Parallel Independent Decoding (PID) aided Generalised Low-Density Parity Check (GLDPC) component codes. Furthermore, BICM schemes invoking Luby-Transform (LT) coding constructed for hostile AWGN-contaminated BEC propagation conditions are investigated in a wireless Internet scenario. The Multilevel GLDPC (MLC-GLDPC) schemes are detailed in Section 5.2. We outline the associated GLDPC structure, together with the MLC-GLDPC encoding and decoding methods, when using BCH and Hamming codes as constituent codes. Section 5.3 describes the design objectives of invoking both inner and outer iterations. The GLDPC code's syndrome checking method used and the associated simulation results are provided in Sections 5.3.1 and 5.3.2. The design philosophy of Fountain codes and LT codes contrived for the wireless Internet are detailed in Sections 5.4.1 and 5.4.2. Sections 5.4.2.1 and 5.4.2.2 describe the LT code's degree distribution leading to the concept of the *improved Robust* distribution. A novel serially concatenated LT and BICM-ID (LT-BICM-ID) arrangement is presented in Section 5.4.3, outlining the system's construction. In Section 5.5, we enhance the LT-BICM-ID system with the aid of an LLR reliability estimation scheme employed for declaring packet erasure in the amalgamated LT-BICM-ID structure. Section 5.5.4 details the bit-by-bit LT decoding procedures, while our simulation results are discussed in Section 5.5.5.

- **Chapter 6: Near Capacity Irregular BICM-ID Design**

This chapter outlines the concept of irregular component codes employed in the amalgamated BICM-ID scheme. The resultant scheme is termed as Irregular Bit-Interleaved Coded Modulation using Iterative Decoding (Ir-BICM-ID), which employs three different irregular components, namely Irregular Convolutional Codes (IrCC), Irregular Unity-Rate Codes (IrURC) and Irregular Mappers (IrMapper), for the sake of approaching the theoretical capacity limit. The proposed Ir-BICM-ID scheme is detailed in Section 6.2, where the detailed schematic showing the separate subcodes is shown in Figure 6.3. We characterise the resultant near-capacity scheme using EXIT chart analysis in Section 6.3, demonstrating that it exhibits a narrow but still open tunnel between the outer and inner codes' EXIT functions. Section 6.4.1 introduces an IrCC combined with both different-rate convolutional codes and memoryless repetition codes, in order to create a diverse range of EXIT functions, as illustrated in Figure 6.6. The inner EXIT functions, which are generated using the combination of an IrURC and an IrMapper are illustrated in Section 6.4.2. An appropriate EXIT chart matching algorithm is detailed in Section 6.4.3, while our simulation results characterising the proposed Ir-BICM-ID scheme are discussed in Section 6.5. Finally, we conclude this chapter in Section 6.6.

- **Chapter 7: Conclusions and Future Work**

  This chapter summarises the main findings of our research along with our suggestions for future work.

1.2.2 Novel Contributions

This thesis is based on the publications and manuscript submissions [38–50], while the novel contributions of the research include the following:

- Different coded modulation schemes, namely the MLC, BICM, BICM-ID, TCM and TTCM, were studied comparatively in terms of their performance versus trellis-complexity, their ability to support unequal error protection classes as well as in terms of the effects of the interleaver length, when fixing the number of iterations. The general structure of a novel 3-D EXIT chart was devised, when using 8-level Phase Shift Keying (8PSK) and three en(de)coders. The 3-D EXIT characteristics are useful for analysing the iterative decoding convergence of three-component MLC schemes using MSD [39].

- Based on the 3-D EXIT charts, a novel precoded-MLC scheme was proposed [42], where the EXIT chart based convergence analysis was facilitated. The precoded-MLC scheme provided substantial BER improvements when transmitting over uncorrelated Rayleigh fading channels.
- In order to introduce transmit diversity, we developed the novel STBC-SP-MLC scheme of Chapter 4 which utilised the M-D SP in Alamouti's twin-antenna based transmitter design. Explicitly, we introduced a novel equivalent capacity based code-rate design for determining the MLC component rates, various bit-to-SP-symbol mapping schemes, a novel Cost Function (CF) for attaining the most appropriate mapping using the Binary Switching Algorithm (BSA) and a *hybrid* UEP bit-to-SP-symbol mapping design [43,44,48].
- A novel STBC-SP-BICM arrangement was proposed [47]. The schemes having $M = 16$ and $M = 256$ SP constellation points were investigated, where the minimum of the CF was found with the aid of the BSA. When designing the bit-to-SP-symbol mapping, various layers of the SP constellation space were used and diverse precoded systems were designed.
- Multilevel schemes invoking GLDPCs as their component codes were proposed [38] using implementationally attractive short BCH and Hamming constituent codes. A novel stopping criterion was also designed for both the inner and outer iterations of the MLC-GLDPC scheme.
- A serially concatenated LT-BICM-ID scheme was proposed for the wireless Internet [41]. To further develop the system, an LLR based packet reliability estimation scheme was presented [45] for the amalgamated LT-BICM-ID design.
- An EXIT-chart aided Ir-BICM-ID design was proposed [49, 50] for the sake of achieving a near-capacity performance. The outer IrCC scheme generates a diverse range of outer EXIT functions, which were closely matched by those of the combination of an IrURC and IrMapper. A novel EXIT function matching algorithm was used for creating a narrow, but still open EXIT tunnel, which led to a near-capacity Ir-BICM-ID scheme.

Chapter 2

Multilevel Coding Theory

2.1 Introduction

In wireless communications, bandwidth has always been a precious resource. However, the entire suite of high-definition multimedia services increasingly requires real-time or low-latency, high-rate transmissions. The aforementioned demanding multimedia applications require reliable, high-integrity transmissions as well as the error-free transmission of certain important data, which leads to the requirement of creating FEC scheme exhibiting an Unequal Error Protection (UEP) capability.

An attractive technique of increasing the achievable data rate without increasing the associated bandwidth or symbol rate is constituted by the employment of coded modulation. The concept of MultiLevel Coding (MLC) was proposed by Imai and Hirakawa [14] as a powerful bandwidth efficient coded modulation technique using several component codes in conjunction with employing appropriate bit-to-symbol mapping strategies.. The component codes employed are typically binary codes, which have different rates and error correcting capabilities.. The rationale of this coding technique is that of increasing the achievable Euclidean distance between the legitimate encoded sequences. This enables code designers to adjust the associated distance properties in order to meet the target performance. Due to the employment of different-rate component codes, MLC facilitates the flexible adjustment of the effective coding rate for meeting the specifications of diverse applications. The appropriate design of specific code rates assigned to each component code was investigated for example in [21, 51].

For the decoding of MLCs, both MultiStage Decoding (MSD) [51] and Parallel

Independent Decoding (PID) [51] can be employed. Imai suggested [14] that MSD can be readily used for reducing the associated complexity of maximum likelihood decoding, which may require an excessive computational cost, while providing modest further performance benefits. MSD may be viewed as a *serial* decoding technique [15,52]. Each decoder of the MSD scheme may be considered as an independent scheme receiving its input information from a binary channel constituted by one of the bits of a non-binary signal constellation which exploits the *a priori* information provided by the other binary channels of the MLC scheme. This *a priori* information is then used as the *extrinsic* information provided by other MLC protection levels for the separate decoding stages. Naturally, this MSD philosophy introduces a decoding delay and the aforementioned PID technique may be able to reduce the associated decoding delay in certain applications.

A close relative of MLCs is constituted by Bit-Interleaved Coded Modulation (BICM) proposed by Zehavi in [17], which may be interpreted as a coded modulation scheme employing bit-based interleaving combined with a single convolutional component code and Gray mapping. Each output bit of the convolutional encoder is independently bit-interleaved to increase the achievable time-diversity order, which is typically associated with an increased Hamming distance. In order to further improve the attainable performance of BICM, Bit-Interleaved Coded Modulation using Iterative Decoding (BICM-ID) [23, 53, 54] was proposed, which employed turbo-style iterations between the decoder and demodulator in conjunction with different partitioning strategies.

Another representative of the MLC family is Trellis Coded Modulation (TCM) [16]. TCM constitutes another joint coding and modulation scheme, which was originally proposed for transmission over Gaussian channels. TCM uses the technique of signal set expansion in order to accommodate the redundant coding bits without bandwidth expansion. TCM will be reviewed as a special case of MLC, where each bit protection level corresponds to a specific bit of the TCM constellation. .The most common TCM scheme transmits non-binary symbols, where the most significant bit of the TCM symbol typically remains uncoded, because the two corresponding phasor points are the farthest from each other. The corresponding two bit-values will result in parallel transitions in the trellis. TCM employs the technique of Ungerböck Partitioning (UP) [16] in order to maximise the Euclidean distance between the unprotected bits of the symbol constellation. More sophisticated mapping schemes have also been proposed, which also may involve mapping to multidimensional signal points [18].

2.2 Multilevel Coding

The fundamental idea of MLC is that of protecting each bit of the modulated constellation points with the aid of a different-rate binary code $\mathbb{C}_i$, creating a different protection level i. These binary component codes may be selected from the family of convolutional codes or block codes. Consider for example an $M = 2^l$-ary Phase Shift Keying (PSK) signal constellation, which is partitioned into l protection levels using UP, where l is the number of bits per 2^l-ary PSK symbol. Here, the Minimum Squared Euclidean Distance (MSED) between the phasor points of each of the separate protection classes is maximised.

Figure 2.1 shows the encoder of a typical MLC scheme. The input source bit stream $\mathbf{u}$ is serial-to-parallel converted into individual bit u_i, which is the bit being assigned to level i. The encoded bit of the encoder $\mathbb{C}^i$ is denoted as v_i. The modulated constellation points of the signal x_j, $0 \leq j \leq 2^l - 1$ are represented by the binary labels $v_0, v_1, ..., v_{l-1}$, where $v_i \in \{0, 1\}$ represents the binary label at the i^{th} protection level, assuming that the notation of v_i is retained after the bit-interleaver π. The coded bits $v_0, v_1, ..., v_{l-1}$ are mapped to the 2^l-ary PSK symbol sequence with the aid of the mapping function $\kappa(.)$. This bit-to-symbol mapping $\kappa(v_{l-1}...v_1v_0)$ results in a signal x.

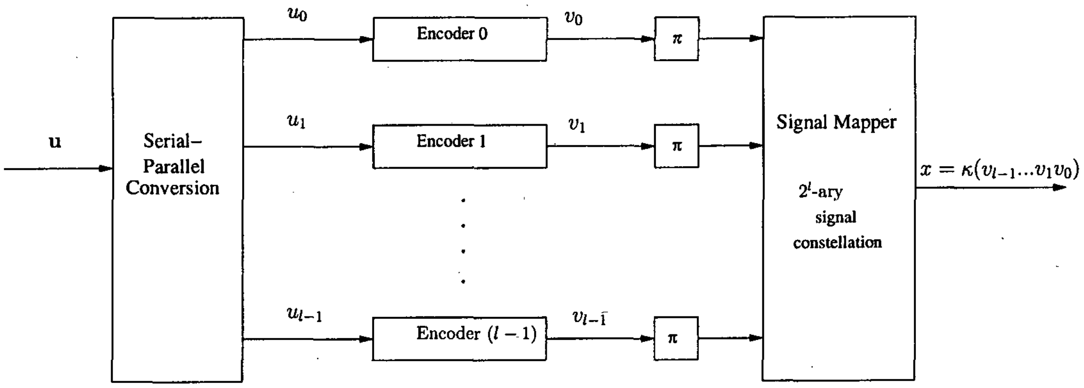

Figure 2.1: MLC encoder.

Given the 2^l-ary PSK constellation, where the number of information bits at each of the l-level is K_0,K_1...K_{l-1}, while the number of the corresponding encoded bits is

N_0,N_1,...,N_{l-1}, respectively, the resultant effective throughput becomes

$$\eta = \frac{K_0}{N_0} + \frac{K_1}{N_1} + ... + \frac{K_{l-1}}{N_{l-1}} \text{ bits/symbol.} \tag{2.1}$$

Given a total of K number of source bits, each binary component code $i = 0...l-1$ independently encodes K_i bits, yielding $\sum_{i=0}^{l-1} K_i = K$. The corresponding encoded bit sequence length is represented by N_i, where the total number of encoded bits becomes $\sum_{i=0}^{l-1} N_i = N$. Therefore the combined coding rate of the MLC scheme is given by

$$R = \frac{1}{N}\sum_{i=0}^{l-1} K_i = \frac{K}{N}. \tag{2.2}$$

2.2.1 Signal Labelling

Each of the MLC bits is mapped to a constellation symbol x by partitioning of the signal x into subsequent smaller subsets as seen in Figure 2.2. There are many types of bit-to-symbol mapping or labelling strategies, which can influence the properties of the MLC scheme. The historically first and most common partitioning used in coded modulation schemes, such as TCM and MLC arrangements is constituted by Ungerböck's set Partition (UP) [16]. UP is used to maximise the minimum Euclidean distance amongst different constellation points of the same partition or protection class, which is increased at every further partitioning step. Again, Figure 2.2 shows the classic 8PSK UP partitioning proposed by Ungerböck. The modulated symbol denoted in Figure 2.3 as x_j, $j \in [0, M-1]$ for the M-ary PSK scheme is considered, where $M = 2^l$. Moreover, x_i consists of the 3 bits $\{v_2v_1v_0\}$, where the intra-set distances are $d_0 = 2\sin(\pi/8)$, $d_1 = \sqrt{2}$ and $d_2 = 2$.

Observe from Figure 2.2 that at partitioning level 1, when the apriori knowledge of bit v_0 is know, the signal x is subsequently divided into two subsets of $x(v_0 = 0)$ and $x(v_0 = 1)$. Explicitly, at partitioning level $i = 1$, the signal subset of $x(v_{l-1}...v_1v_0)$ would be further divided into $x(v_{l-1}...v_10)$ and $x(v_{l-1}...v_11)$. The partitioning operation continues, until a pair of signal points is left at the partitioning level $l-1$.

Again, different partitioning strategies have been proposed, some of which have been used for achieving unequal error protection [26,55]. Block Partitioning (BP) was proposed in [56] where the signal points are partitioned as seen in Figure 2.4. Observe

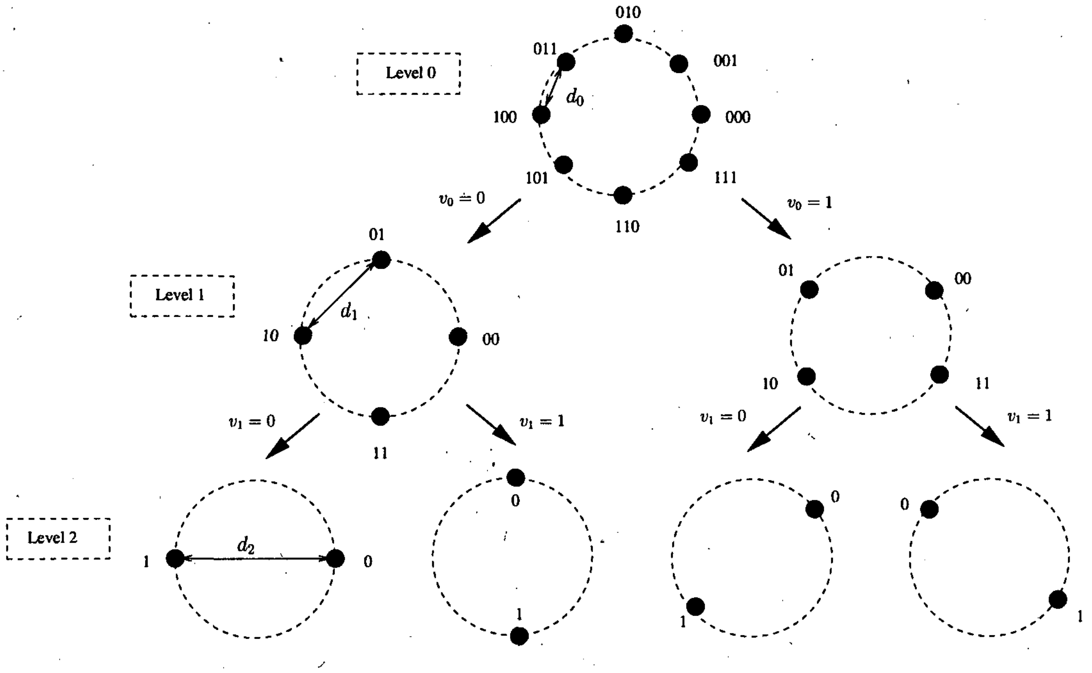

Figure 2.2: Ungerböck Partitioning (UP) of the 8PSK signal.

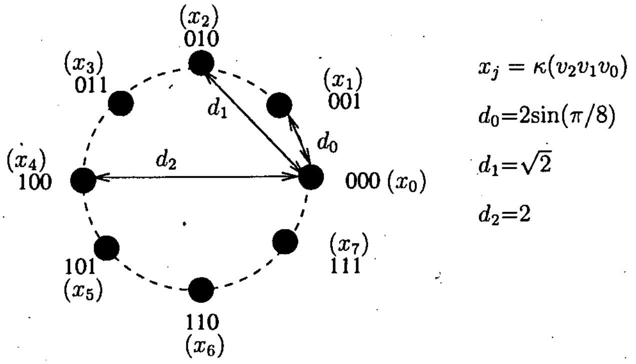

Figure 2.3: 8PSK Ungerböck Set Partitioning portraying the gradually increasing minimum subset distances.

that the minimum Euclidean distance remains the same at all partitioning level. The design objective of BP aims for having the minimum number of nearest neighbours rather than for maximising the intra-set distance, as illustrated in Figure 2.4.

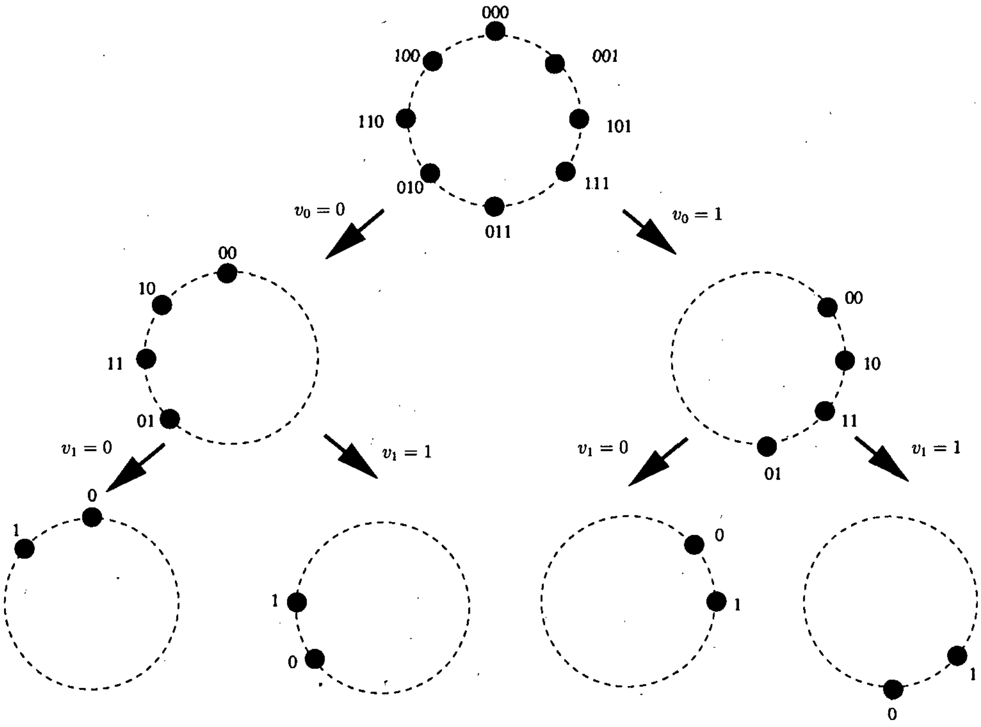

Figure 2.4: Block Partitioning (BP) of the 8PSK constellation.

There are other types of unconventional partitioning strategies. For example, the *mixed* partitioning or *hybrid* partitioning was proposed in [26,27] based on a hybrid of UP and BP. *Hybrid*-I partitioning [26] applies BP to the first i number of partitioning levels, while UP to the rest of the $(l - i - 1)$ levels. An alternative partitioning scheme referred to as *hybrid*-II was proposed in [26] in order to strike a trade-off between the less powerful error protection of the higher partitioning levels and the increased error protection of the most significant bit. Again, the corresponding *hybrid* partitioning schemes are shown in Figure 2.5.

2.2.2 Equivalent Channel

The set of random variables representing the transmitted and received signals as well as the l-bit codewords are denoted by X, Y and V, where the mutual information between the transmitted signal set and received signal set are denoted as

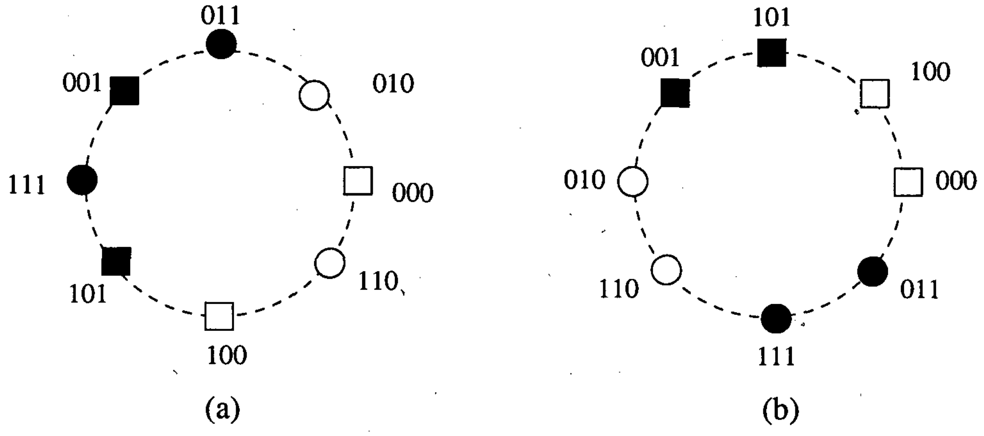

Figure 2.5: *Hybrid*-I (a) and *hybrid*-II (b) partitioning of the 8PSK constellation [57] ©IEEE, 1999. At partitioning level 1, the hollow symbols indicate 0, while the black filled symbol indicate 1. At partitioning level 2, the square indicates 0, while the circle indicates 1.

$I(Y;X)=I(Y;V_0V_1...V_{l-1})$. When employing the chain rule of mutual information [51,58], we arrive at

$$\begin{aligned} I(Y;X) &= I(Y;V_0V_1...V_{l-1}) \\ &= I(Y;V_0)+I(Y;V_1|V_0)+...+I(Y;V_{l-1}|V_0V_1...V_{l-2}). \end{aligned} \tag{2.3}$$

The chain rule of mutual information from Equation (2.3) can be further expressed as follows

$$I(Y;V_i...V_{l-1}|V_0...V_{i-1}) = I(Y;V_i|V_0...V_{i-1})+I(Y;V_{i+1}...V_{l-1}|V_0...V_i). \tag{2.4}$$

The concept of a so-called equivalent channel i was introduced in [51] in order to model the provision of information by the different protection classes for each other with the aid of the chain rule. Rearranging Equation (2.4), the equivalent channel i can be represented as

$$I(Y;V_i|V_0...V_{i-1}) = I(Y;V_i...V_{l-1}|V_0...V_{i-1})-I(Y;V_{i+1}...V_{l-1}|V_0...V_i). \tag{2.5}$$

Equation (2.3) suggests that when having a total of l partitioning levels, the bits $v_0...v_{l-1}$ can be divided into l equivalent channels, which consist of binary digit v_i, where $v_0,...,v_{i-1}$ are known because they have already been decoded. When the signal set x_j, $j=0,...,M-1$, is transmitted over a time-variant wireless channel, the binary digits of v_k, for $k<i$ as well as the wireless channel have to be known for successful decoding.

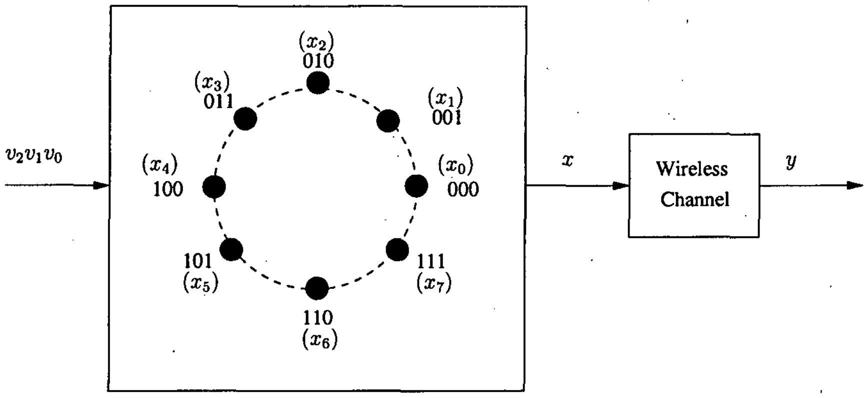

Figure 2.6: Actual channel for 8PSK modulation over wireless transmission.

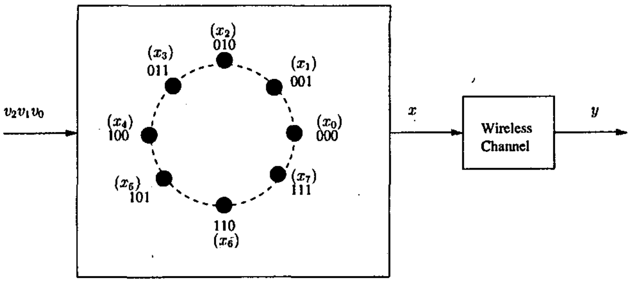

(a) *Equivalent channel* 0 with no *a priori* lower level bit information.

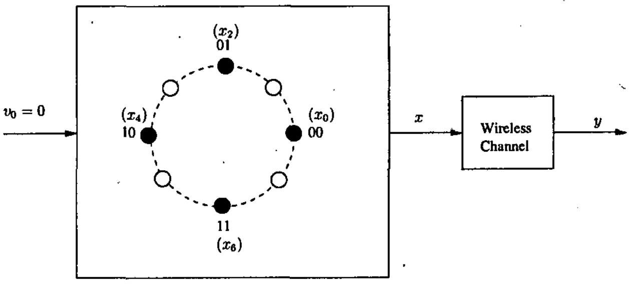

(b) *Equivalent channel* 1 with information given by level-0 signal bits $v_0 = 0$.

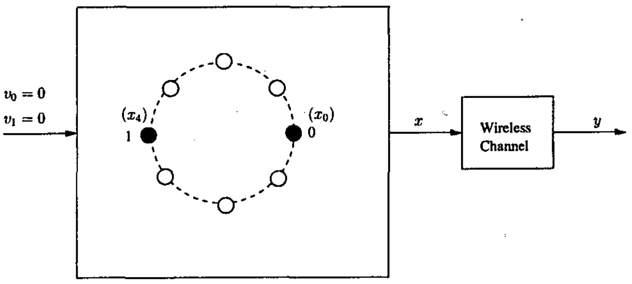

(c) *Equivalent channel* 2 with information given by level-0 and level-1 signal bits $v_0 = 0, v_1 = 0$.

Figure 2.7: Equivalent channels for 8PSK modulation.

Figure 2.6 shows an 8PSK symbol transmitted over a wireless communication channel. The channel-encoded bits $v_0 ... v_{l-1}$ are mapped using the mapping function $\kappa(.)$ to the symbol x before being transmitted over a wireless communication channel. We refer to this as the actual channel conveying the 8PSK modulated signal. However, according to Equation (2.3) this actual channel can be represented by three separate equivalent channels, as illustrated in Figure 2.7. Figure 2.7 (a) shows the equivalent channel at level 0, which resembles the complete signal set without any useful *a priori* information. When provided by *a priori* information from the previous or lower MLC level $v_0 = 0$, the equivalent channel for level 1 can be represented according to Figure 2.7 (b). The equivalent channel providing *a priori* information for level 2 can further be reduced to a smaller signal set, given the *a priori* information from the previous two MLC levels, as portrayed in Figure 2.7 (c).

Observe from Equation (2.5) and Figure 2.7 that the mutual information between the received signals and the hypothesized transmitted symbol might not be the same for different subsets at a particular partition level i due to the non-congruent [1] partitioning scheme. Hence, the average mutual information can be obtained by averaging all possible combinations of the subsets $v_0 v_1 ... v_{i-1}$ by calculating the corresponding expectation values as follows [51]

$$I(Y; V_i ... V_{l-1} | V_0 ... V_{i-1}) = \mathrm{E}_{v_0 ... v_{i-1} \in \{0,1\}} \{ I(Y; V_i ... V_{l-1} | v_0 ... v_{i-1}) \}. \tag{2.6}$$

2.2.3 Decoding of MLCs

The iterative decoding of MLCs adopts the turbo-detection-like iterations [59], where the outer decoder components constituted by the MLC decoder and the inner component constituted by the symbol-to-bit demapper. There are two different MLC decoding methods, namely MultiStage Decoding (MSD) and Parallel Independent Decoding (PID) [15, 52, 60–63], which will be outlined in Sections 2.2.3.2 and 2.2.3.1.

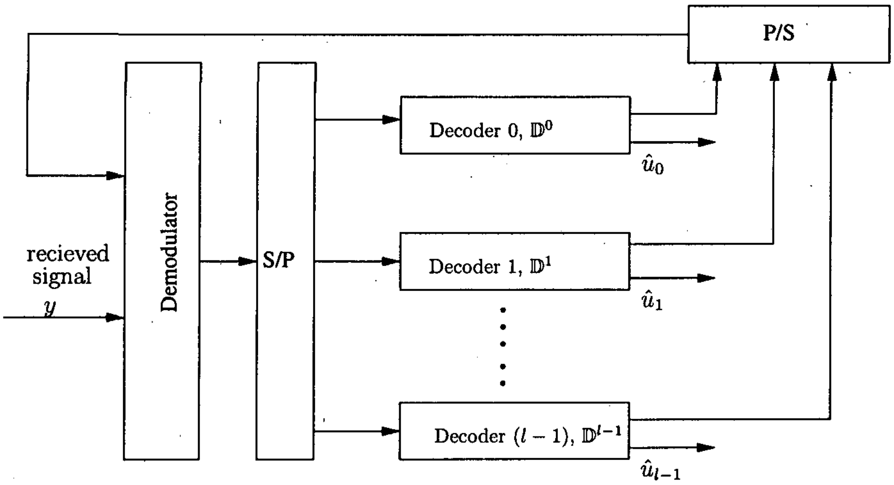

Figure 2.8: The PID's structure.

2.2.3.1 Parallel Independent Decoding

The PID's structure is shown in Figure 2.8, where $\mathbb{D}^i$ represents the decoder of component-i. The Parallel to Serial (P/S) convertor arranges the serial bit-based Log Likelihood Ratios (LLR) representing the soft information $\mathbb{D}^i$ output in the form of the parallel stream of Figure 2.8, which quantifies the match between the i^{th} bit of the k modulated symbol and the corresponding channel output. The LLR of a coded bit v_i is represented as $L(v_i)$, which is defined as the logarithm of the ratio of the probabilities for that bit between its two possible values as follows

$$L(v_i) = \ln\left(\frac{p(v_i = 1)}{p(v_i = 0)}\right). \tag{2.7}$$

Given the transmitted bit v_i and the corresponding received signal of y_k, the conditional LLR $L(y_k|v_i)$ is formulated at the demodulator as:

$$L(y_k|v_i) = \ln\left(\frac{P(y_k|v_i = 1)}{P(y_k|v_i = 0)}\right). \tag{2.8}$$

Assuming that an 8PSK modulation scheme is employed, as exemplified in Figure 2.8, three component decoders are used, namely $\mathbb{D}^0$, $\mathbb{D}^1$ and $\mathbb{D}^2$. The PID structure of Figure 2.8 invokes these three decoders and initially each of these has independent signal label. These signal labels group them into the constellation sets shown in Figure 2.9. In Figure 2.9 (a) decoder $\mathbb{D}^0$ has the alternate signal labels of '0' and '1'. The

---

[1] At a particular partitioning level i, the signal points generated after obtaining perfect *a priori* information of $v_0 \ldots v_{i-1}$, result in different constellation points having unidentical mutual information.

decoders $\mathbb{D}^1$ and $\mathbb{D}^2$ operate on the basis that the signal labels are grouped without any *a priori* knowledge during the first decoding of the PID scheme. The PID scheme typically exhibits a worse performance than the higher-delay MSD, where the different protection classes provide extrinsic information for each other.

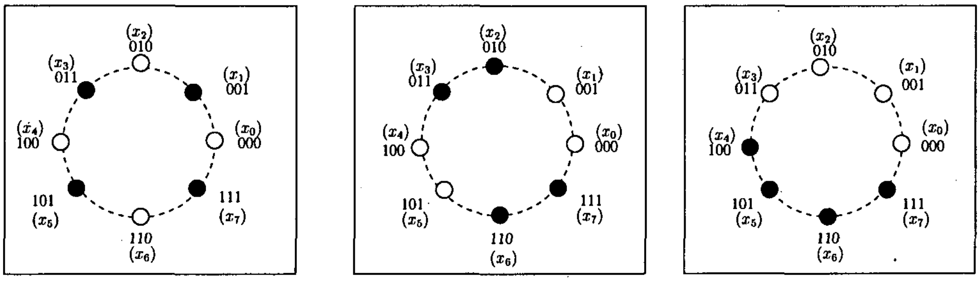

(a) $\mathbb{D}^0$ with $v_0 \in \{0,1\}$.

(b) $\mathbb{D}^1$ with $v_1 \in \{0,1\}$.

(c) $\mathbb{D}^2$ with $v_2 \in \{0,1\}$.

Figure 2.9: 8PSK constellation depicted at each decoder $\mathbb{D}^i$, where a filled black label refers to $v_i = 1$ and a hollow label refers to $v_i = 0$.

We obtain the conditional LLR of the transmitted bit v_i from Equation (2.8), and the decoder $\mathbb{D}^i$ generates the bit-based LLR soft information of Figure 2.8, which is also known as the *a posteriori* LLR given as follows

$$L(v_i|y_k) = \ln\left(\frac{P(v_i = 1|y_k)}{P(v_i = 0|y_k)}\right), \tag{2.9}$$

where v_i refers to the encoded bit transmitted by the level-i encoder and y_k represents the corresponding received symbol at the output of the demodulator. The constellation points associated with bit i having the value of '0' and '1' are represented as white and black circles in Figure 2.9, respectively.

Hence, each decoder $\mathbb{D}^i$ generates the *extrinsic* LLRs as follows

$$L_e(v_i) = \ln\left(\frac{p(v_i = 1|\mathbf{y}_{k\neq i})}{p(v_i = 0|\mathbf{y}_{k\neq i})}\right), \tag{2.10}$$

where $\mathbf{y}_{k\neq i}$ is a sequence of y values, excluding the one corresponding to the label i of that particular bit.

The *a priori* LLRs provided after further iterations between the symbol-to-bit demapper and the MLC decoder furnish additional information to indicate the likelihood of the subsets of signal points labelled by the black and white symbols, as seen in Figure 2.9. The digits of all the modulated symbols are updated with the LLRs generated at level i by utilising the corresponding *extrinsic* information of Equation (2.10).

2.2.3.2 Multistage Decoding

Decoding of the MLC would result in a high complexity, if we were to use the Maximum Likelihood Decoding (MLD) [14]. However, as suggested in [14], the MultiStage Decoding (MSD) method has the potential of significantly reducing the complexity, while maintaining a similar decoding performance to that of the MLD.

In MSD, the component codes are decoded stage by stage with only one decoder activated at a time. Each component code is decoded with the aid of soft decision assisted MSD. The decoding process starts with the first component and then continues to subsequent components, where the soft information representing the bits is passed from one stage to the next. Therefore, instead of having to consider the full combined trellis of all decoders jointly, the number of trellis branches considered by a single stage of the MSD imposes a significantly lower complexity [15].

Owing to this fact MSD is suboptimum. There is a potential degradation of achievable BER performance, when decision was propagated from a lower level to a higher level. Hence, MSED is arranged to be higher at the lower levels for avoiding error propagation. The decoding performance of the MSD is typically higher than that of the PID, because it uses the *a priori* information from the other single decoder stages and the demodulator is invoked l times per iteration compared to only one time per iteration in the PID scheme. However, for l number of decoders, the MSD is expected to exhibit a decoding delay which is l times higher than that of the PID.

Figure 2.10 shows the structure of a MSD. The received signal sequence at the input of the demodulator is $\mathbf{y} = (y_0, y_1, ..., y_{l-1})$, where we denote the received symbol at each constituent decoder $\mathbb{D}^i$ as y_i. The encoded symbols of the component code $\mathbb{C}^i$ are successively decoded by the corresponding $\mathbb{D}^i$. At detection level i, decoder $\mathbb{D}^i$ has the information of the received block $\mathbf{y} = (y_0, y_1, ...y_{i-1})$, with $0...i-1$ being the indices of the previous decoding stages.

Since we introduced an iterative scheme in Figure 2.10, the *a priori* information about the transmitted signal points can be obtained from the extrinsic information derived in each decoder. Each iteration will include feeding the next decoder stage with new *a priori* information, until the $(l-1)^{st}$ level MLC decoder is reached. The next iteration will continue with decoder $\mathbb{D}^0$ up to $\mathbb{D}^{l-1}$, but this time level $\mathbb{D}^0$ will have new *a priori* information from the previous iteration.

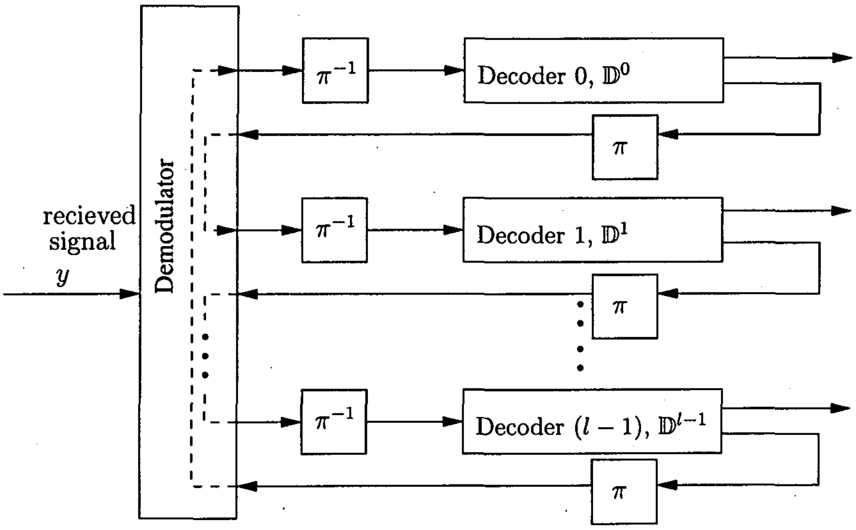

Figure 2.10: MSD structure.

2.2.4 MAP Decoding

MLC has the ability to employ different codes as its component codes, including block, convolutional or concatenated codes. Different codes such as BCH [6,64], LDPC [9], systematic or non-systematic convolutional codes [55] have been employed in the literature. A subset of specific MLC schemes, for example, BICM-ID and TCM use trellis-based convolutional codes. The classic Maximum A Posteriori (MAP) algorithm may be employed for their trellis-based decoding. In order to make a fair comparison between different coded modulation schemes, we will employ convolutional component codes in our MLC scheme to be designed in Chapter 3 and each component code will invoke the MAP decoding algorithm, as we will show in the comparative study of Section 3.2.

The MAP decoder provides an APosteriori Probability (APP) or *a posteriori* LLR y, $L(u_k|\mathrm{y})$ for the decoded bit u, given the received symbol, Bayes' rule is used for calculating the APP, which provides the joint probability of a and b as follows

$$P(a,b) = P(a|b) \cdot P(b). \tag{2.11}$$

With the aid of Bayes' rule formulated in Equation (2.11), the *a posteriori* LLR of the information bit u_k can be expressed as

$$\begin{aligned} L(u_k|\mathbf{y}) &= \ln\left(\frac{P(u_k=1|\mathbf{y})}{P(u_k=0|\mathbf{y})}\right) \\ &= \ln\left(\frac{P(u_k=1,\mathbf{y})}{P(u_k=0,\mathbf{y})}\right). \end{aligned} \tag{2.12}$$

Let us consider the numerator or denominator of Equation (2.12) for the transmitted bit $u_k = i$. Then we can rewrite the individual bit-probabilities of Equation (2.12) as

$$\begin{aligned} P(u_k=i,\mathbf{y}) &= P(\overline{S}_{k-1}=m',\overline{S}_k=m,\mathbf{y}) \\ &= P(\overline{S}_{k-1}=m',\overline{S}_k=m,\mathbf{y}_1^{k-1},\mathbf{y}_k,\mathbf{y}_k^N). \end{aligned} \tag{2.13}$$

Provided that the previous decoder state was $\overline{S}_{k-1} = m'$ and the current state is $\overline{S}_k = m$, there are no parallel trellis transitions and hence m' and m uniquely identify the value of u_k. Furthermore, as seen in Figure 5.6 of [65] the received sequence $\mathbf{y}$ may be divided into three sections, namely the received sequence $\mathbf{y}_1^{k-1}$ associated with the previously received sequence up to the present transition, the received symbol $\mathbf{y}_k$ at the current transition and the received sequence $\mathbf{y}_{k+1}^N$ after the present transition.

Assuming that the channel is memoryless and using Bayes' rule, Equation (2.13) may be expressed as

$$\begin{aligned} & P(\overline{S}_{k-1}=m',\overline{S}_k=m,\mathbf{y}) \\ = {} & P(\mathbf{y}_{k+1}^N|\overline{S}_{k-1}=m',\overline{S}_k=m,\mathbf{y}_1^{k-1},\mathbf{y}_k)\cdot P(\overline{S}_{k-1}=m',\overline{S}_k=m,\mathbf{y}_1^{k-1},\mathbf{y}_k) \\ = {} & P(\mathbf{y}_{k+1}^N|\overline{S}_k=m)\cdot P(\overline{S}_{k-1}=m',\overline{S}_k=m,\mathbf{y}_1^{k-1},\mathbf{y}_k) \\ = {} & P(\mathbf{y}_{k+1}^N|\overline{S}_k=m)\cdot P(\mathbf{y}_k,\overline{S}_k=m|\overline{S}_{k-1}=m',\mathbf{y}_1^{k-1})\cdot P(\overline{S}_{k-1}=m',\mathbf{y}_1^{k-1}) \\ = {} & P(\mathbf{y}_{k+1}^N|\overline{S}_k=m)\cdot P(\mathbf{y}_k,\overline{S}_k=m|\overline{S}_{k-1}=m')\cdot P(\overline{S}_{k-1}=m',\mathbf{y}_1^{k-1}) \\ = {} & \overline{\beta}_k(m)\cdot\overline{\gamma}_k(m',m)\cdot\overline{\alpha}_{k-1}(m'). \end{aligned} \tag{2.14}$$

The forward recursive operations of the MAP decoder can be formulated as follows

[5]

$$\begin{aligned}
\overline{\alpha}_k(m) &= P(\overline{S}_k = m, \mathbf{y}_1^k) \\
&= \sum_{\text{all } m'} P(\overline{S}_k = m, \overline{S}_{k-1} = m', \mathbf{y}_1^{k-1}, \mathbf{y}_k) \\
&= \sum_{\text{all } m'} P(\overline{S}_k = m, \mathbf{y}_k | \overline{S}_{k-1} = m', \mathbf{y}_1^{k-1}) \cdot P(\overline{S}_{k-1} = m', \mathbf{y}_1^{k-1}) \\
&= \sum_{\text{all } m'} P(\overline{S}_k = m, \mathbf{y}_k | \overline{S}_{k-1} = m') \cdot P(\overline{S}_{k-1} = m', \mathbf{y}_1^{k-1}) \\
&= \sum_{\text{all } m'} \overline{\gamma}_k(\overline{S}_{k-1} = m', \overline{S}_k = m) \cdot \overline{\alpha}_{k-1}(\overline{S}_{k-1} = m'). \qquad (2.15)
\end{aligned}$$

Similarly, the backward recursive operations can be expressed as [5]

$$\begin{aligned}
\overline{\beta}_{k-1}(\overline{S}_{k-1} = m') &= P(\mathbf{y}_k^N | \overline{S}_{k-1} = m') \\
&= \sum_{\text{all } m} P(\mathbf{y}_k, \mathbf{y}_{k+1}^N, \overline{S}_k = m | \overline{S}_{k-1} = m') \\
&= \sum_{\text{all } m} P(\mathbf{y}_{k+1}^N | \overline{S}_{k-1} = m', \overline{S}_k = m, \mathbf{y}_k) \cdot P(\mathbf{y}_k, \overline{S}_k = m | \overline{S}_{k-1} = m') \\
&= \sum_{\text{all } m} P(\mathbf{y}_{k+1}^N | \overline{S}_k = m) \cdot P(\mathbf{y}_k, \overline{S}_k = m | \overline{S}_{k-1} = m') \\
&= \sum_{\text{all } m} \overline{\beta}_k(\overline{S}_k = m) \cdot \overline{\gamma}_k(\overline{S}_{k-1} = m', \overline{S}_k = m). \qquad (2.16)
\end{aligned}$$

To carry out the recursions formulated in Equations (2.15) and (2.16), the $\overline{\gamma}_k(\overline{S}_{k-1} = m', \overline{S}_k = m)$ values can be calculated as follows [5]

$$\begin{aligned}
\overline{\gamma}_k(\overline{S}_{k-1} = m', \overline{S}_k = m) &= P(\mathbf{y}_k, \overline{S}_k = m | \overline{S}_{k-1} = m') \\
&= P(\mathbf{y}_k | \overline{S}_{k-1} = m', \overline{S}_k = m) \cdot P(\overline{S}_k = m | \overline{S}_{k-1} = m') \\
&= P(\mathbf{y}_k | \overline{S}_{k-1} = m', \overline{S}_k = m) \cdot P(u_k) \\
&= P(\mathbf{y}_k | u_k = i) \cdot P(u_k). \qquad (2.17)
\end{aligned}$$

Here, the probability of the input information bit, which triggers a trellis-transition from $\overline{S}_{k-1} = m'$ to $\overline{S}_k = m$ is denoted as $P(u_k)$. This is also the *a priori* soft information of the u_k bit.

Equation (2.17) consists of two parts, namely the *a priori* source information of $P(u_k)$ and the channel characteristics expressed in terms of the channel-induced transition probability $(\mathbf{y}_k | \overline{S}_{k-1} = m', \overline{S}_k = m)$.

For BPSK transmission over an AWGN channel, the channel-induced transition probability can be expressed as

$$P(\mathbf{y}_k|u_k = i) = \frac{1}{\sqrt{\pi N_0}}\exp\left(-\frac{(y-\sqrt{E_s}u_k)^2}{N_0}\right), \tag{2.18}$$

where N_0 is the single-sided power spectral density of the AWGN and E_s is the transmitted energy per channel symbol.

Finally, the *a posteriori* LLRs provided by the MAP decoder are given as [5]

$$L(u_k|\mathbf{y}) = \ln\left(\frac{\sum_{(m',m)\Rightarrow u_k=1}\overline{\alpha}_{k-1}(m')\cdot\overline{\gamma}_k(m',m)\cdot\overline{\beta}_k(m)}{\sum_{(m',m)\Rightarrow u_k=0}\overline{\alpha}_{k-1}(m')\cdot\overline{\gamma}_k(m',m)\cdot\overline{\beta}_k(m)}\right). \tag{2.19}$$

2.2.5 Code-Rate Design Rules

One of the important issues in designing a powerful MLC is to assign the appropriate coding rate for each individual protection level. In this section we focus our attention on two existing design rules.

2.2.5.1 Capacity Based Code-Rate Design Rule

The capacity based rules of assigning the appropriate channel coding rate were proposed in [22,51]. We can maximise the mutual information over the selectable parameters for the entire set of constellation points. For the random variables X and Y, the mutual information $I(X;Y)$ is a measure of the dependence between X and Y. More explicitly, $I(X;Y)$ quantifies the information about X, given the occurrence of Y. The channel capacity C is defined as the highest possible average mutual information $I(X;Y)$ [66]

$$C = \max_{p(x)} I(X;Y), \tag{2.20}$$

where $I(X;Y) = \sum_{x,y} p(x,y)\log_2\frac{p(x|y)}{p(x)}$.

Let us denote the modulated symbols of $\log_2 M$-bit at the input and output of the channel as x as well as y and assume that the channel is a discrete-time memoryless channel. The channel capacity derived from Equation (2.20) becomes

$$\begin{aligned} C(y) &= \max_{p(x)} E[I(X;Y)], \\ &= \max \sum_{m=0}^{M-1} \int p(y|x_m)p(x_m)\log_2\frac{p(y|x_m)}{p(y)}dy. \end{aligned} \tag{2.21}$$

For traditional M-PSK and M-QAM having equiprobable symbols we have $p(x_m)=1/M$. Therefore, according to the capacity rule, it is stated that the individual coding rate R^i of protection level i of an M-ary MLC scheme should be chosen to be the same as the capacity C^i of the equivalent channel i, which is formulated as

$$R^i = C^i, \tag{2.22}$$

where $i=0,1,...,l-1$.

Let the l-bit signal set be $\mathbf{x}$, where we have $\mathbf{X} = \{x_m | m \in 0,1,...M-1\}$. The subsets of signal points at protection level i - given that the lower bit-protection level is denoted as $\mathbf{X}_{v_0 \ldots v_{i-1}}$. Furthermore, the conditional Probability Density Function (PDF) of the received signal y, given x_m is denoted as $f_y(y|x_m)$. The capacity of a memoryless channel for such a signal set $\mathbf{X}$ having a channel output variable y within the space $\mathfrak{R}$ is given as [67]

$$C(\mathbf{X}) = \int_{\mathfrak{R}} \frac{1}{|\mathbf{X}|} \sum_{x_m \in \mathbf{X}} f_y(y|x_m) \log_2 \frac{f_y(y|x_m)}{\frac{1}{|\mathbf{X}|}\sum_{x_k \in \mathbf{X}} f_y(y|x_k)} dy, \tag{2.23}$$

where $p(x_m) = \frac{1}{|\mathbf{X}|}$.

The equivalent capacity C^0 of level 0, given the transmitted bits are $v_0 \in \{0,1\}$ may be expressed as [67]:

$$C^0 = \frac{1}{2} \sum_{v_0=0}^{1} \int_{\mathfrak{R}} f_y(y|v_0) \log_2 \frac{f_y(y|v_0)}{f_y(y)} dy. \tag{2.24}$$

The term $f_y(y|v_0)$ represents the conditional PDF of the received signal y, given the information v_0 of bit protection level 0. Provided that v_0 is already given, the signal set $\mathbf{X}$ reduces to $\mathbf{X}_{v_0}$, where the PDF is given as

$$f_y(y|v_0) = \frac{1}{|\mathbf{X}_{v_0}|} \sum_{x_m \in \mathbf{X}_{v_0}} f_y(y|x_m). \tag{2.25}$$

Upon substituting Equation (2.25) into Equation (2.24), we arrive at [67]:

$$\begin{aligned}
C^0 &= \frac{1}{2}\int_{\Re}\sum_{v_0=0}^{1}\sum_{x_m\in\mathbf{X}_{v_0}}\frac{1}{|\mathbf{X}_{v_0}|}f_y(y|x_m)\left[\log_2\frac{\frac{1}{\mathbf{X}_{v_0}}\sum_{x_k\in\mathbf{X}_{v_0}}f_y(y|x_k)}{f_y(y)}-\log_2\frac{f_y(y|x_m)}{f_y(y|x_m)}\right]dr \\
&= \frac{1}{2}\int_{\Re}\sum_{v_0=0}^{1}\sum_{x_m\in\mathbf{X}_{v_0}}\frac{1}{|\mathbf{X}_{v_0}|}f_y(y|x_m)\left[\log_2\frac{f_y(y|x_m)}{f_y(y)}-\log_2\frac{f_y(y|x_m)}{\frac{1}{\mathbf{X}_{v_0}}\sum_{x_k\in\mathbf{X}_{v_0}}f_y(y|x_k)}\right]dr \\
&= \int_{\Re}\sum_{x_m\in\mathbf{X}}\frac{1}{|\mathbf{X}|}f_y(y|x_m)\log_2\frac{f_y(y|x_m)}{f_y(y)}dr \\
&\quad -\frac{1}{2}\sum_{v_0=0}^{1}\int_{\Re}\sum_{x_m\in\mathbf{X}_{v_0}}f_y(y|x_m)\log_2\frac{f_y(y|x_m)}{\frac{1}{\mathbf{X}_{v_0}}\sum_{x_k\in\mathbf{X}_{v_0}}f_y(y|x_k)}dr \\
&= C(\mathbf{X})-C(\mathbf{X}_{v_0}), \qquad (2.26)
\end{aligned}$$

which physically suggests that the capacity of subchannel '0' is given by the MLC scheme's capacity minus the capacity of the scheme, given the perfect knowledge of v_0.

Equation (2.26) shows that at level 0, the equivalent capacity is the difference of the sum capacities of the entire set of subchannels in the signal constellation and that recorded for one of the signal subsets identified by the signal label of level 0. This equation can be extended to level 1 as follows

$$C^1 = C(\mathbf{X}_{v_0}) - C(\mathbf{X}_{v_0v_1}). \qquad (2.27)$$

The generalisation of Equation (2.27) can be shown to be [67]

$$C^i = C(\mathbf{X}_{v_0\ldots v_{i-1}}) - C(\mathbf{X}_{v_0\ldots v_i}), \qquad (2.28)$$

which is similar to the chain rule of Equation (2.5).

Figures 2.11 and 2.12 show the equivalent capacity obtained from Equation (2.5) by the capacity rule. Both modulation schemes employ the same UP strategy and are transmitted over an AWGN channel. Note that the dashed vertical curve indicates the capacity of $C(\mathbf{X})$=2.5 bits/symbol. The equivalent capacities of 8-level Amplitude Shift Keying (8ASK) and 8PSK correspond to the optimum individual coding rates (R_0, R_1, R_2) of (0.52,0.98,1) and (0.51,0.96,1), respectively.

2.2.5.2 Balanced Distance Based Code-Rate Rule

Another popular rule used in addition to the capacity-based rule of Section 2.2.2 is the Balanced Distance Rule [51] (BDR), which considers the minimum Euclidean distance

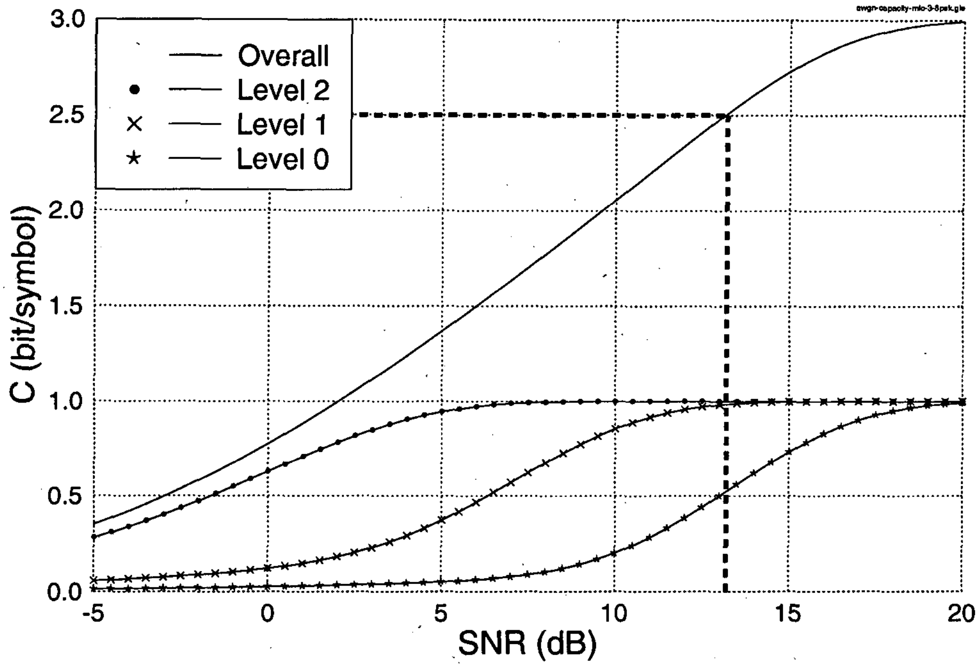

Figure 2.11: Equivalent capacity for 8ASK transmitted over an AWGN channel employing Ungerböck's set partitioning.

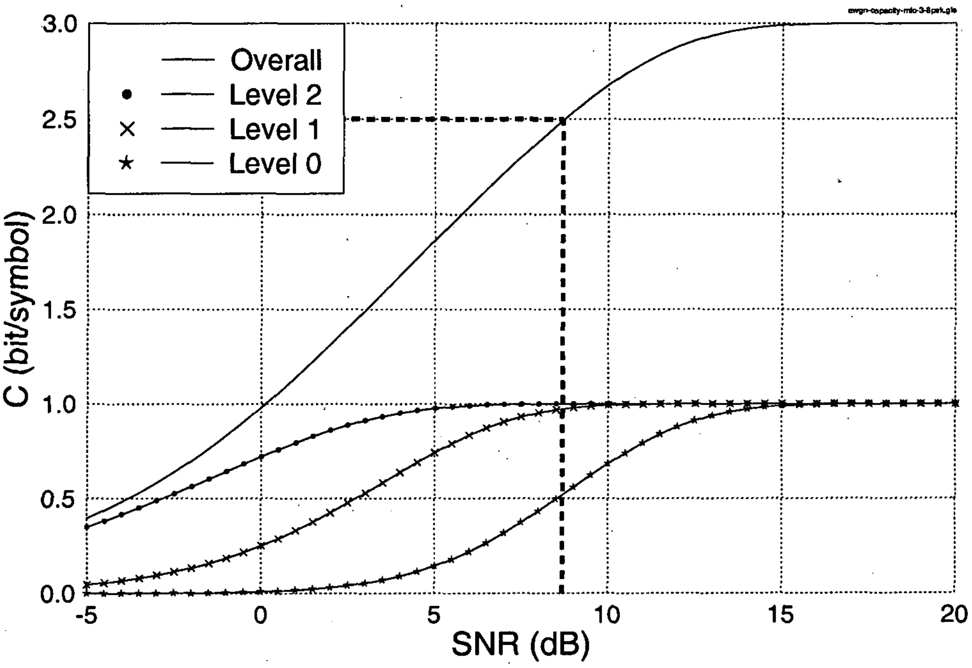

Figure 2.12: Equivalent capacity for 8PSK transmitted over an AWGN channel employing Ungerböck's set partitioning.

within the signal constellations. The MSED of the MLC codeword d^2 is lower bounded by [19]:

$$d^2 \geq \min_{i=0,\ldots,l-1} (d_i^2 \delta_i), \tag{2.29}$$

where δ_i represents the Hamming distance of the code C^i at level i, while d_i^2 denotes the MSED of signal points subsets $\mathbf{X}_{v_0 v_1 \ldots v_{i-1}}$ at partitioning level i. This so-called Product Distance (PD) given by $d_i^2\delta_i$ reflects the delicate balance between the Euclidean distance of the constellation points, suggesting that a lower Euclidean distance may be counter-balanced by using a stronger code having a larger Hamming distance and vice versa. Hence, according to the BDR [51], the rate of the individual code components at protection level i of an MLC scheme can be chosen by satisfying the following condition:

$$d_i^2\delta_i = \mathbb{K}, \tag{2.30}$$

where $i = 0, 1, ..., l-1$ and $\mathbb{K}$ is a constant.

The work reported in [15, 19, 68] was carried out based on the BDR [51] to achieve a high asymptotic gain by maximising the value of d^2 in Equation (2.29). This method might introduce a high coding rate for the lowest protection level of decoder $\mathbb{D}^0$ which may exceed the capacity C^0 of the equivalent channel. Transmission over this high-rate equivalent channel might not be possible at a high reliability, which may result in subsequent error propagation from the lower to the higher MLC levels, where the higher MLC levels [2] typically provide a lower error correction capability.

2.2.6 Unequal Error Protection

The provision of Unequal Error Protection (UEP) is important in wireless communication in order to best protect the perceptually most important speech, audio and video information bits and hence to ensure better multimedia source decoding results. In MLC, the coding rate, the bit-to-symbol mapping scheme and the distance of the modulated constellation points can be adjusted to achieve UEP. The bit-to-symbol mapping strategy determines the MSED of the MLC scheme, which was defined as d^2_{min}. The design of using binary linear block codes for supporting UEP in the context of MLC schemes requires that we satisfy the following inequalities [55]

$$d^2_{min,0} \geq d^2_{min,1} \geq \ldots \geq d^2_{min,(l-1)}, \tag{2.31}$$

---

[2] In order to avoid any potential confusion, in our forthcoming discourse we will always refer either to MLC levels or protection levels.

where $d^2_{min,i}$ denotes the MSED of code $\mathbb{C}^i$ at MLC level i in the context of an $(M = 2^l)$-ary modulated MLC scheme.

Again, for transmission over AWGN channels, satisfying this inequality typically results in decreasing the error protection capability of the higher MLC coding levels. As shown in [26, 57], at low-to-medium Signal-to-Noise Ratios (SNR) the UEP capability may be destroyed by the high BER of the lower-level MLC decoding stages owing to error propagation.

The Block Partitioning (BP) scheme of Section 2.2.1 may be invoked as a mapping strategy to reduce the number of nearest neighbours at each partitioning level, as shown in Figure 2.4. This scheme typically has a constant minimum intra-set distance at each partitioning level and the coding rate of each MLC's level may vary according to Equation (2.31), where the employment of a stronger code offers a better protection for the more important source-coded bits and a lower protection for the less significant source-encoded bits. The number of nearest neighbour constellation points is minimised, since at each block partitioning level only those constellation points that are located near the constellation partition boundary have neighbours at the minimum distance, which corresponds to a significant reduction of the constellation points at the minimum distance compared to Ungerböck's set partitioning. Nonetheless, this pair of low-distance constellation points typically degrades the average BER of equi-distant partitioning schemes, such as Ungerböck's partitioning. Hence it is only recommended for UEP applications, noting again, that this may be expected to degrade the average BER of the system.

In order to improve overall BER performance, it was shown in [26] that for 8PSK modulation the zero and first level can be independently decoded, which results in avoiding error propagation from the MLC level-0 to level-1. The *Hybrid*-I partitioning scheme of Figure 2.5 may be used for the partitioning level-0 of block partitioning, while the rest of the MLC levels may invoke the UP scheme shown in Figure 2.5. The *hybrid*-I partitioning compromises the achievable BER performance on the first MLC level but exhibits an improved coding gain at the second MLC level. In other words, the associated tradeoff is that we tolerate a BER performance loss at the first MLC level, while increasing the intra-set distance at the second MLC level, which allows us to reduce the second level's BER.

The specific example of UEP that was proposed in [26] was highlighted in this section. This design was contrived, in order to reduce the error propagation from level-0 to level-1 and from level-1 to level-2 of the decoding process. Observe from Figure 2.13 (a) that the MLC scheme employs block partitioning as its bit-to-symbol mapping scheme, where at partition level 0, the bit '0' and '1' are labelled with the hollow and black filled shapes, respectively. At partitioning level 1, the bit '0' and '1' are associated with the square and circle. The partitioning can be considered in two dimensions, having the x-axis and y-axis as their divider. Note that at level-0 the partitioning divides the plane into the left and right plane partitioned by the y-axis, while at level-1 the partitioning divides the plane into the upper and lower half-planes, dissected by the x-axis. Since the partitioning can be carried out independently in the x- and y-directions, the decoding of the first two levels can be carried out with the aid of a parallel scheme. The decision is then passed to the level-2 decoder of Figure 2.13 for the final decoding step, yielding the third decoded bit. Note that the independently decoded level-0 and level-1 decoders result in no error propagation from the lower two MLC levels to the third level (level-2).

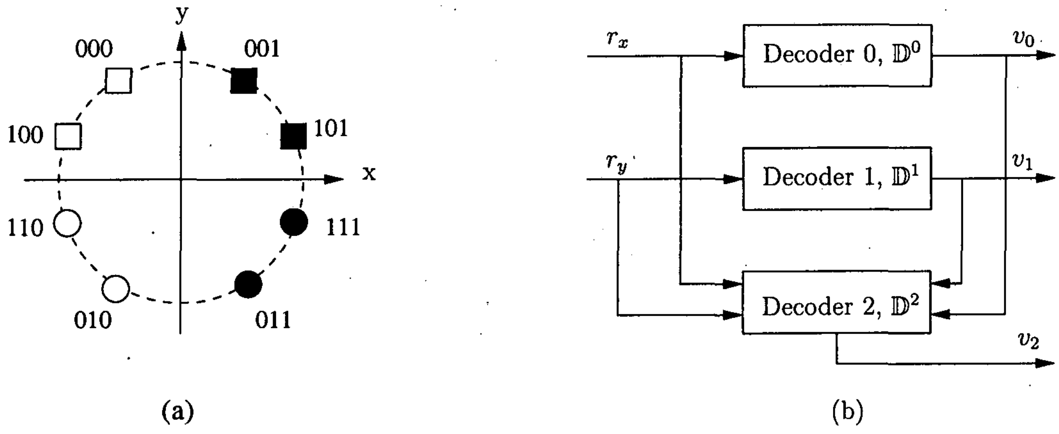

Figure 2.13: UEP decoding for 8PSK block partitioning: (a) block partitioning labelling and (b) decoder scheme [26] ©IEEE, 2000.

As a design alternative, non-uniformly spaced constellations were used in [27, 56] in order to achieve UEP in the context of MLC schemes. One of the possible non-uniformly spaced constellations can be generated from the conventional 8PSK constellation by adjusting the angle θ between two signal constellation points in a quadrant. This changes the intra-set distance between each signal points at each partitioning level-i. Observe in the example provided in Figure 2.14 that upon adjusting the angle

θ, the lower two MLC decoding levels can achieve an improved BER performance due to their enhanced intraset distances [27], when using block partitioning. The family of unconventional constellations is further exemplified by a design proposed in [56], where a simple one-dimensional 8ASK scheme having unequal distances between the constellation points. The main concept is to adjust the intra-set distances according to the significance of the information bits.

We would like to emphasise nonetheless that any deviation from the classic equidistant modulated signal constellation is expected to degrade the average BER, because the BER improvement of the highest-protection class is typically achieved at the cost of more dramatically degrading the BER of the reduced-protection class.

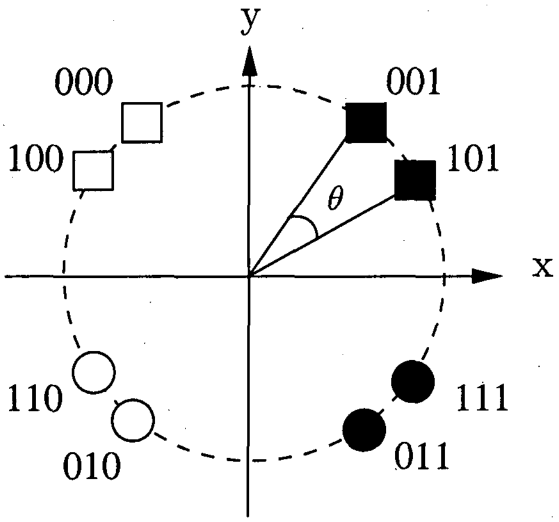

Figure 2.14: Non-uniformly spaced 8PSK constellation using block partitioning based labelling [27] ©IEEE, 2000.

2.3 Bit-Interleaved Coded Modulation

The MLC scheme of Figure 2.8 in Section 2.2.3.1 using PID invokes l parallel equivalent channels. The transmission of the encoded symbol v_i over equivalent channel i takes place after mapping to the modulated symbol x. The decoding operations obey the parallel independent structure portrayed in Figure 2.8. The BICM scheme of Figure 2.15 can be viewed as a specific MLC-PID scheme, where instead of using l encoders, a single encoder is employed and the l encoded bits are mapped to the modulated symbol x of an extended BICM constellation. Separate pseudo-random bit interleavers are used for each encoded bit to generate independent parallel bits, which are then then mapped to the BICM constellation. BICM was proposed by Zehavi [17] to improve the diversity order of Ungerböck's TCM scheme for transmission over Rayleigh fading channel.

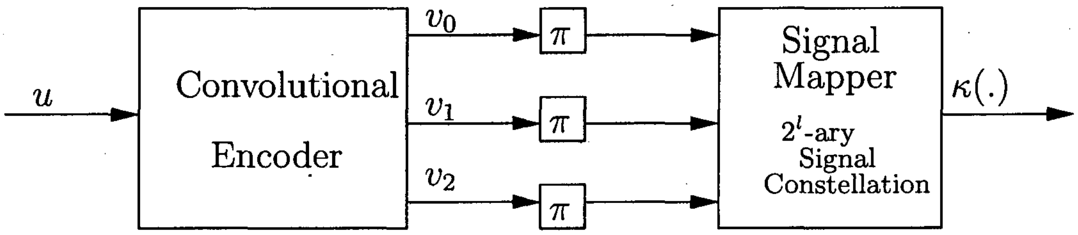

Figure 2.15: BICM encoder.

BICM employs a non-systematic convolutional code combined with a bit-interleaver for each of its encoded bit. Figure 2.15 shows the BICM encoder proposed by Zehavi [17], which has the three basic blocks, namely the convolutional encoder, the bit interleavers π and the bit-to-BICM symbol mapper κ. A binary information sequence $\mathbf{u}$ is input to the BICM encoder (n, k) having a rate of R. Before the convolutional encoder, the serial message stream $\mathbf{u}$ is arranged into parallel bits $u_0, u_1..., u_{k-1}$ and fed into the respective bit position of the convolutional encoder. At the encoder's output, there are n number of bits per u input bits, which results in the encoded bits of $v_0, v_1, ..., v_{n-1}$.

Each of these encoded bits is bit-interleaved before being mapped according to Gray labelling using the mapping function of $\kappa(v_{n-1}...v_1v_0)$. The signalling constellation set of modulated symbols has $M = 2^l$ points. This mapping scheme represents a one-to-one correspondence, where the mapping of bits to symbols is denoted as $\kappa : \{0, 1\} \rightarrow \chi$. The design objective of BICM is to achieve a maximum minimum Hamming distance amongst the encoded codewords, rather than maximising free Euclidean distance amongst the constellation points, as would be the case for Ungerböck's set partitioning TCM. The Euclidean distance is the appropriate design criterion, when the most likely error event is corrupted by AWGN to an adjacent set-partitioned constellation point. By contrast, the Hamming distance of the l-bit BICM symbols has to be maximised, when the most likely error event may be corruption by fading channels to another l-bit BICM symbol.

To achieve a higher coding rate and a reduced decoding complexity, punctured

Code Rate	Puncturing Pattern	Hamming Distance
1/2	1111 1111	7
2/3	1111 1x1x	4
4/5	1111 1xxx	3

Table 2.1: Punturing pattern proposed by Hagenauer [69] for a memory-4 RCPC. The mother code of $k = 4$ and $n = 8$ is employed.

convolutional codes can be used for the BICM encoder, which is based on a low-rate mother code, where some of the encoded bits can be removed according to the optimum puncturing patterns, for the sake of increasing the corresponding coding rates. This allows us to use the same encoder and decoder for different-rate BICM schemes. Rate-Compatible Puncture Convolutional codes (RCPC) were proposed by Hagenauer in [69], where sets of different-rate codes were generated from a single mother code. RCPCs also constitute an attractive design alternative for Hybrid Automatic Repeat reQuest type-II (HARQ-II) schemes [70–72], where only redundant punctured bits are transmitted as and when needed in order to improve the overall throughput of the system. Furthermore, RCPCs may be used for creating irregular convolutional codes [73] for the sake of adjusting the coding rate in order to provide UEP. An example of using a rate $R = 1/2$ mother code is shown in Table 2.1. The symbol 'x' in the puncturing pattern of Table 2.1 denotes bits which are removed for the sake of obtaining an increased coding rate.

In case of Gray labelling, each modulated symbol differs from the other neighbouring symbol by a single bit. In other words, $\kappa : \{0, 1\} \rightarrow \chi$ represents Gray labelling, when χ_b^i differs from $\chi_{\bar{b}}^i$ in a single-bit position at the minimum-distance neighbours, where b is the value of the bit and $\bar{b}$ is the complement value of b, which is either 0 or 1 and i is the position of the bit. The notation χ_b^i represents the mapping function $\kappa(.)$ having b value at i^{th} bit position. Figure 2.16 shows the Gray labelling for the standard 8PSK constellation associated with the mapping $\kappa \rightarrow \chi_b^i$, where $i = 0, 1, 2$.

Figure 2.16 illustrates each signal constellation point, when a certain bit position having a value of 1 or 0 is considered. The black circle denotes the bit value of 1, while the shaded circle represents the bit value of 0. We now associate bit i with level i of a typical MLC. It may be observed in Figure 2.16 for χ_1^0 of level 0 that we

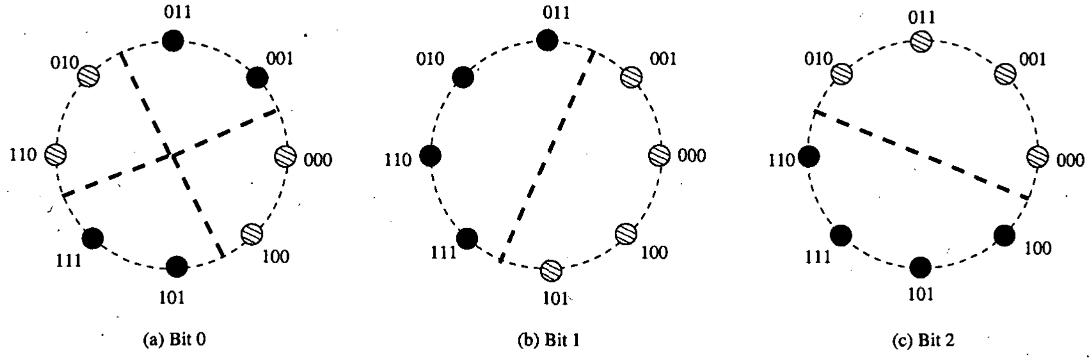

(a) Bit 0 (b) Bit 1 (c) Bit 2

Figure 2.16: Gray labelling of 8PSK.

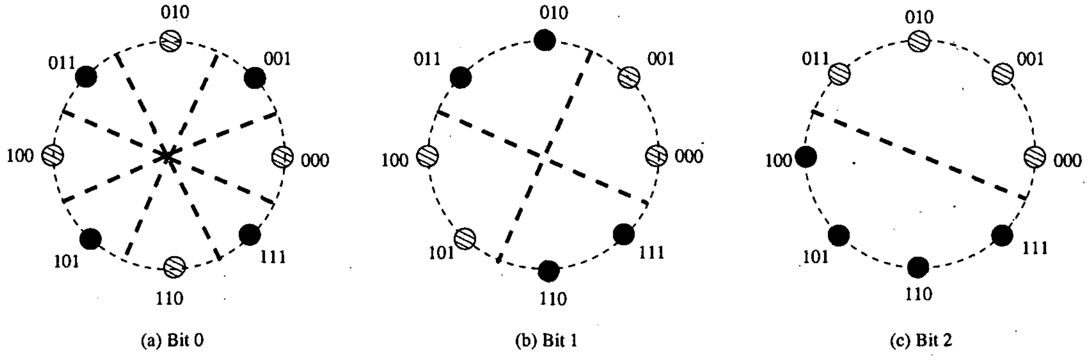

(a) Bit 0 (b) Bit 1 (c) Bit 2

Figure 2.17: UP labelling of 8PSK.

can partition the constellation into two regions, which are the two groups of black circles separated by the thick broken lines. Observe in Figure 2.16 that for both level 1 and level 2 associated with bit 1 and bit 2 we only have a single region of black filled phasors, which is separated from the shaded phasors by a single separating line. Therefore, when the number of regions is reduced from two to one, the number of nearest neighbours is also reduced from four to two.

Given a low number of nearest neighbours, the probability for a bit to be wrongly decoded to a different region becomes lower. Hence, when decoding without iterations, Gray mapping is employed for BICM, because there is no *a priori* information provided by the previous iteration and hence the decoding of the level-i bit does not depend on the other bits of the different levels. Compared to the UP scheme of TCM as proposed by Ungerböck [16], the separate regions in Figure 2.17 are partitioned by the broken lines and the number of resultant nearest neighbours is increased from two to four at bit-1 for example, as shown in Figure 2.17. Note that there are eight, four and two separate regions at bit level 0, 1 and 2 respectively.

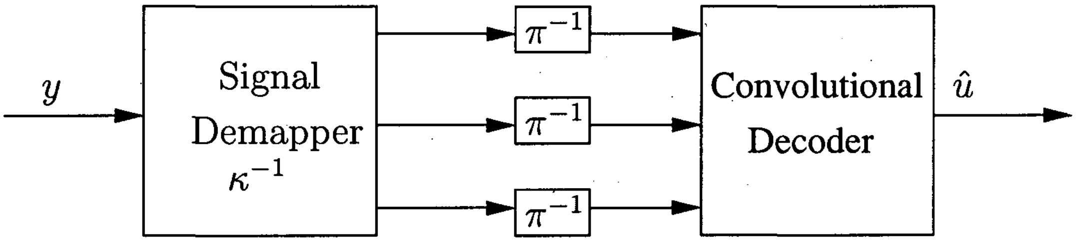

Figure 2.18: BICM decoder.

Figure 2.18 shows the decoder of BICM, which also consist of three separate parts, namely the demapper κ^{-1}, the deinterleaver π^{-1} and the channel decoder. The demodulator receives the signal y from the channel and produces three estimated bit-LLRs as its soft information. These LLRs are then fed as *a priori* information to the convolutional decoder, before the resultant decoded information bit sequence is decided upon. Note that both the Viterbi Algorithm (VA) and the MAP algorithm [65] may be used by the convolutional decoder. The 8PSK constellation can be characterised as $\chi = \sqrt{E_s}e^{2n\pi j/8}$, where $j = 0, 1, ..., 7$ and E_s is the transmitted symbol energy. The energy E_b per information bit is given by $E_b = E_s/k$ for a rate $R = (n, k)$ code. For transmission over a Rayleigh channel using perfectly coherent detection, the discrete-time received signal is

$$y_t = h_t x_t + n_t, \tag{2.32}$$

where h_t is the Rayleigh-distributed fading coefficient, while n_t is the AWGN having a variance of $\sigma_I^2 = \sigma_Q^2 = N_0/2$, where N_0 is the noise Power Spectral Density (PSD). Zehavi [17] suggested that BICM decoding may be carried out by computing the soft-bit metric and then invoking the classic VA-based convolutional decoder. For each received signal y, $2l$ bit-metrics λ, with l bit position each having binary values of '0' and '1', are computed based on the Maximum Likelihood (ML) decision rule as

$$\begin{aligned} \lambda(v_t^i) &= \log \sum_{x \in \chi_b^i} P(y_t|x, h_t) \\ &\approx \max_{x \in \chi_b^i} \log P(y_t|x, h_t). \end{aligned} \tag{2.33}$$

The term $P(y_t|x_t, h_t)$ is the PDF of the received signal y_t, given the transmitted symbol x and the fading coefficient h_t at time t instant, where the in-phase and quadrature-phase of fading component is given as $h_{t,1}$ and $h_{t,2}$. This PDF can be expressed using the in-phase and quadrature-phase components ($y_{t,1}$,$y_{t,2}$) and ($x_{t,1}, x_{t,2}$) as follows

$$P(y_t|x_t, h_t) = \frac{1}{2\pi\sigma^2}e^{-\frac{(y_{t,1}-h_{t,1}x_{t,1})^2+(y_{t,2}-h_{t,2}x_{t,2})^2}{2\sigma^2}}. \tag{2.34}$$

Using the max-log-based approximation of the soft-bit metrics, we have [54]

$$\begin{aligned} \lambda(v_t^i) &\approx \max_{x_t \in \chi_b^i} \log P(y_t|x_t, h_t) \\ &\sim \min_{x_t \in \chi_b^i} ||y_t - h_t x_t||^2. \end{aligned} \tag{2.35}$$

The $2l$ bit metric calculations generated for each received signal are shown in Figure 2.19. The first bit having a value of zero and one as in the symbols (χ_0^0, χ_1^0) respectively, can be expressed as follows [54]

$$\lambda(v_t^0 = 0) = \min(d_{110}^2, d_{010}^2, d_{000}^2, d_{100}^2) \tag{2.36}$$

$$\lambda(v_t^0 = 1) = \min(d_{011}^2, d_{001}^2, d_{101}^2, d_{111}^2), \tag{2.37}$$

where the term d_i^2 is the squared Euclidean distance between the received signal y_t and the faded version of the transmitted signal x_t^i.

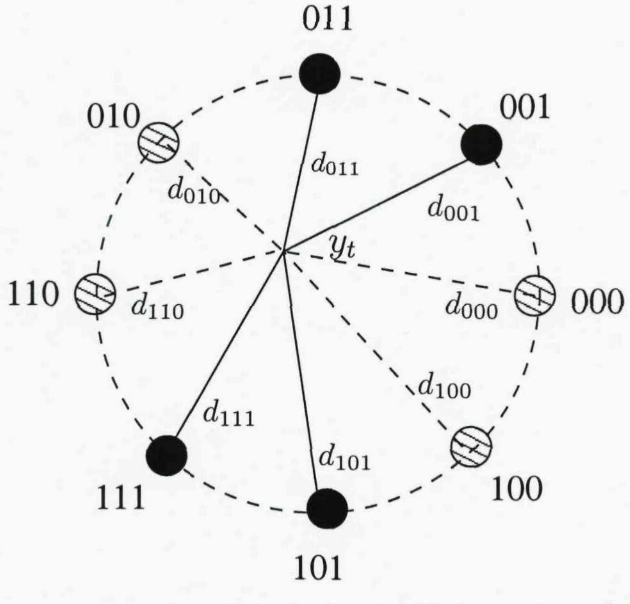

Figure 2.19: Bit metric calculation for the first bit position χ_b^0 of BICM.

2.4 Bit-Interleaved Coded Modulation Using Iterative Decoding

BICM was originally proposed for transmission over non-Gaussian environments, such as Rayleigh fading channels and hence the Hamming distance of the adjacent BICM symbols was maximised. By contrast, the Free Euclidean Distance (FED) of the constellation points was optimised, when designing TCM for transmission over AWGN channels. Li and Ritcey [23, 53, 54] proposed a turbo-like iterative detection approach for employment in BICM, which was termed as Bit-Interleaved Coded Modulation using Iterative Decoding (BICM-ID). In this new BICM-ID scheme, a different bit-to-symbol mapping strategy was employed and the soft-information gleaned from the decoder was fed back as *a priori* information to the symbol-to-bit demapper for further iterations. The encoder of BICM-ID is identical to that shown in Figure 2.15, while the decoder is detailed in Figure 2.20.

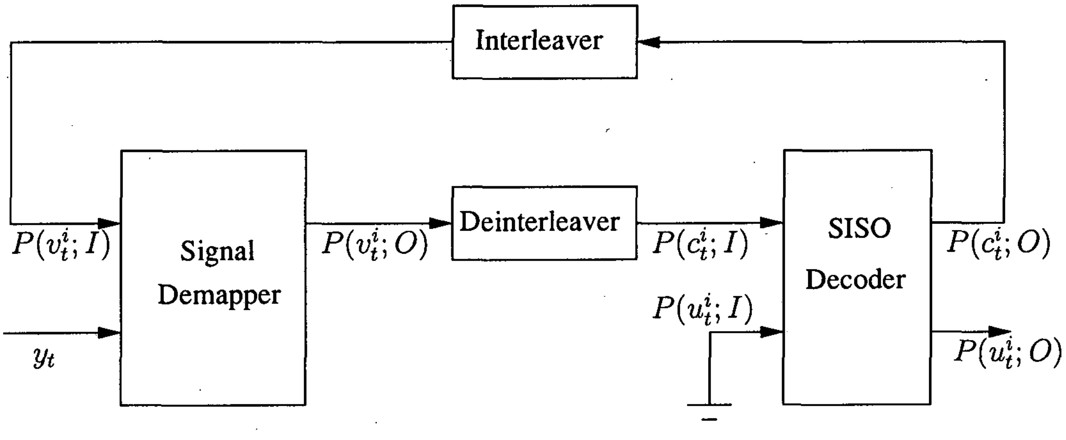

Figure 2.20: BICM-ID decoder [53] ©IEEE, 1998.

In Figure 2.20 the convolutional decoder represents a SISO decoder, which may be viewed as a 'four-port' device having two inputs and two outputs [74]. The signal demapper obtains the received signal y from the channel's output. Observe in Figure 2.20 that the *a priori* probability of the coded bit v_t^i after interleaving is denoted by $P(v_t^i; I)$ while the notations c_t^i and v_t^i represent the coded bits before and after the interleaver at time index t and bit-position i within the l-bit symbol. The output of the demapper is the *a posteriori* probability of $P(v_t^i; O)$, which would be rearranged after the deinterleaver in order to present the soft-information in the required order to the SISO decoder. The *a priori* probability of the information bit u_t^i is represented by $P(u_t^i; I)$, while the *a priori* probability of the coded bits c_t^i is denoted by $P(c_t^i; I)$ in Figure 2.20. The SISO decoder outputs the two corresponding *a posteriori* probabilities, namely $P(u_t^i; O)$ and $P(c_t^i; O)$. The computation of $P(u_t^i; O)$ and $P(c_t^i; O)$ is based on the *extrinsic* information. Note also that the term $P(u_t^i; I)$ is not utilised during the BICM-ID decoding process seen in Figure 2.20.

When considering an AWGN channel, the fading coefficient is $h_t = 1$ in Equation (2.32). The conditional PDF of the received signal can be expressed as

$$P(y_t|x_t) = \frac{1}{2\pi\sigma^2} e^{-\frac{|y_t - x_t|^2}{2\sigma^2}}. \tag{2.38}$$

The *a posteriori* probability criterion can be used as our soft-metric, which is expressed as [53]:

$$\begin{aligned} P(v_t^i = b|y_t) &= \sum_{x_t \in \chi_b^i} P(x_t|y_t) \\ &= \frac{\sum_{x_t \in \chi_b^i} P(y_t|x)P(x)}{P(y_t)} \\ &\sim \sum_{x \in \chi_b^i} P(y_t|x)P(x), \end{aligned} \tag{2.39}$$

where $i \in \{0, 1, 2\}$ and $b \in \{0, 1\}$. The probability $P(x)$ here is the *a priori* information, which can be used for soft-feedback. This term is not used by the non-iterative BICM decoder and all symbols are assumed to be equiprobable, since there is no readily available *a priori* information during the first-pass decoding process. Hence, we have $P(v_t^i = b; O) = P(v_t^i = b|y_t)$. Since in iterative BICM-ID we are considering *extrinsic a posteriori* probability, the subset $\chi_b^i = \{\kappa(v_2 v_1 v_0)|v_i = b; v_j \in \{0, 1\}, j \neq i\}$ contains the modulated signal points corresponding to $v_i = b$.

During the second iteration, the *a priori* probability $P(v_t^i)$ is fed back to the demodulator and it is no more an identical probability, which was assumed previously during the first iteration in the absence of *a priori* information. For each symbol $x_t \in \chi$ we have

$$\begin{aligned} P(x_t) &= p(\kappa([v_2(x_t) v_1(x_t) v_0(x_t)])) \\ &= \prod_{j=0}^{2} P(v_t^j = v_j(x_t); I), \end{aligned} \tag{2.40}$$

where $v_i(x_t) \in \{0,1\}$ represents the i^{th} bit of the signal x_t. Here we assume having three perfectly random and independent bit-interleavers, rendering $P(v_t^0)$,$P(v_t^1)$ and $P(v_t^2)$ independent of each other.

In the possession of $P(v_t^i)$, during the second and all further iterations, we define the new *extrinsic a posteriori* probability at the demapper's output as [53]

$$\begin{aligned} P(v_t^i = b; O) &= \frac{P(v_t^i = b|y_t)}{P(v_t^i = b; I)} \\ &= \sum_{x_t \in \chi_b^i} \left(P(y_t|x_t) \prod_{j \neq i} P(v_t^j = v^j(x_t); I) \right), \end{aligned} \tag{2.41}$$

where $i \in \{0,1,2\}$ and $b \in \{0,1\}$. Given this *extrinsic* probability, a turbo-like *extrinsic* information exchange between the demapper and decoder becomes possible, with the demapper acting as the inner code and the convolutional decoder as the outer one. In order to compute $P(v_t^i = b; O)$ from Equation (2.41), we only require the *a priori* probability of the *other* bits in the same received symbol.

2.4.1 Mapping Schemes

As mentioned earlier, a non-Gray mapping strategy is used for the iterative BICM-ID scheme. Li [54] proposed UP to be employed. Observe in Figure 2.17 that, as opposed to merely identifying the minimum number of nearest neighbours, taking level-2 for example, the *a priori* information gleaned from bit 0 and bit 1 during the second iteration will provide bit 2 with a limited set of possible pairs to choose from.

Hence, to optimise the first or later iterative decoding steps, the intra-set Euclidean distance of all points is increased. Clearly, as shown in Figures 2.21 (a) and 2.21 (b), the UP scheme constitutes a better choice than Gray mapping since it has an increased Euclidean distance for bit-2. This scheme however will result in a worse performance during the first-pass decoding than Gray mapping, which will be improved after the successive iterations beyond that of the Gray mapper's performance. The presence of feedback errors will also lead to erroneous decisions in selecting signal pairs, which would in turn cause error propagation affecting the overall decoding performance. Therefore, the choice of a more appropriate labelling, such as UP, results in an increased Euclidean distance at the higher bit protection levels.

Tran *et al.* [75] proposed the Modified Set Partitioning (MSP) scheme shown in Figure 2.21 (c), which may be considered as an enhancement of the original UP scheme

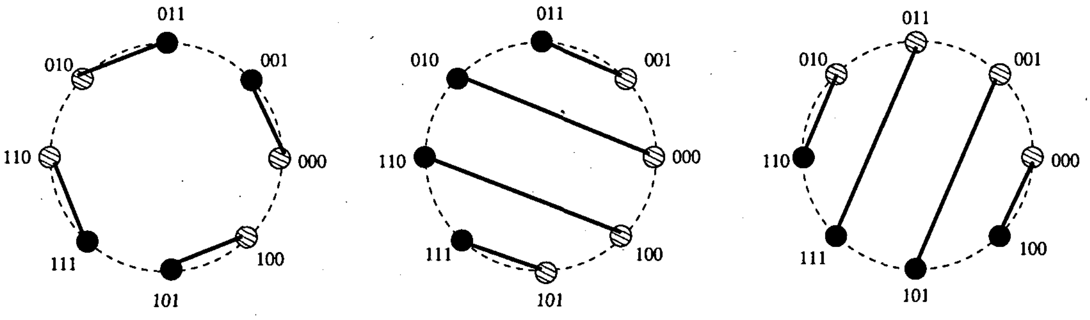

(a) Bit 0 (b) Bit 1 (c) Bit 2

(a) Gray mapping

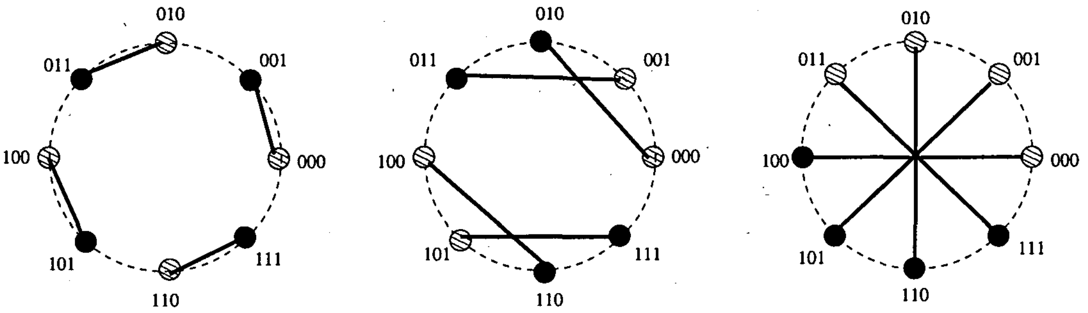

(a) Bit 0 (b) Bit 1 (c) Bit 2

(b) Ungerboeck set partitioning

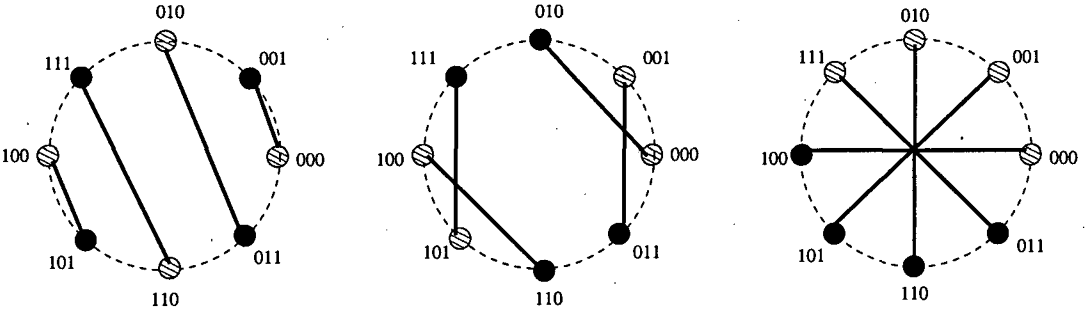

(a) Bit 0 (b) Bit 1 (c) Bit 2

(c) Modified set partitioning

Figure 2.21: Mapping schemes of BICM-ID 8PSK constellation [53], [75] ©IEEE.

seen in Figure 2.21 (a). The labels of 011 and 111 are interchanged with respect to that of the original UP scheme. The protection distance of bit-1 and bit-2 is the same for both UP and MSP, but the Euclidean distance of bit-0 is larger in the MSP scheme of Figure 2.21 (c) compared to the UP arrangement of Figure 2.21 (b). This means that MSP would show an improved iterative detection aided performance, as verified in [75] for a rate-2/3, 16-state outer convolutional code using the generator polynomials of $G_1 = (7,1,4)_8$, $G_2 = (2,5,7)_8$ and having a Hamming distance of 5.

Another approach of designing a mapping scheme is based on capacity or mutual information [75]. Let us consider again the mutual information $I(x;y)$ as given in Equation (2.21), which is repeated here for the sake of convenience

$$\begin{aligned} I(x;y) &= 1/M \sum_{m=0}^{M-1} I(x_m;y) \\ &= \max \sum_{m=0}^{M-1} \int p(y|x_m)p(x_m)\log_2\frac{p(y|x_m)}{p(y)}dy, \end{aligned} \tag{2.42}$$

where x and y represent the transmitted and received signals, and $I(x;y)$ denotes the mutual information between the transmitted symbol x and the received symbol y.

We can observe from Equation (2.42) that the symbol-wise mutual information would be independent of the specific choice of the mapping scheme for a particular constellation. However, the bit-wise mutual information conditioned on the other *a priori* bits can be expressed as [76]:

$$I(x;y) = \sum_{i=0}^{l-1} I_i, \tag{2.43}$$

where $l = \log_2 M$ and I_i denotes the bit-wise mutual information, given that the i number of other bits in the symbol are perfectly known.

Since the symbol-wise mutual information $I(x;y)$ is a constant, for example, we can sacrifice some mutual information at MLC level 0, noted as I_0, in order to obtain higher values for the other bit-wise mutual information $I_1, I_2, ..., I_{l-1}$. The conditional bit-wise mutual information is given as [75]

$$I_i = \overline{I(v_i;y|v_0...v_{i-1})}, \tag{2.44}$$

where v_i denotes the coded bits in a symbol having a total of l bits. The bar in $\overline{I(.)}$ represents the average mutual information evaluated over all possible combinations of the "other i bits that are known".

2.5 Conclusion

In this chapter, we presented an overview of MLC concepts as well as the basics of BICM-ID schemes. In Section 2.2, we outlined the philosophy of MLC schemes using different signal labelling, encoder and decoder structures, rate designs, UEP and a variety of other design rules. The decoding structures of MLC arrangements, namely the MSD and PID schemes were discussed in Sections 2.2.3.2 and 2.2.3.1, respectively. The equivalent capacity based code-rate design rule was detailed in Section 2.2.5.1 with the aid of the corresponding mutual information calculations.

We continued by detailing the structure of BICM in Section 2.3. Various constellation set partitioning as well as demodulation schemes were also discussed. Since BICM was originally designed for transmission over Rayleigh fading channels using non-iterative decoding, the introduction of BICM-ID was outlined in Section 2.4. Both BICM and BICM-ID decoding schematics were detailed in Figures 2.18 and 2.20. The choice of effective bit-to-symbol mapping schemes was discussed in Section 2.4.1.

Chapter 3

MLC Design Using EXIT Analysis

3.1 Introduction

In this chapter, the attainable performance of iteratively detected coded modulation schemes having different block lengths, decoding complexity and an unequal error protection capability is studied, when communicating over AWGN channels using 8PSK modulation. More specifically, the coded modulation schemes investigated include MLC [14], TCM [16], TTCM [25], BICM [17] as well as BICM-ID [23].

With the objective of studying the iterative detection aided performance of MSD assisted MLCs, we propose a novel three-Dimensional (3-D) EXIT [77] chart for investigating the effects of different symbol-to-bit demapper characteristics. In the recent past, different constellation labelling strategies have been employed in the context of MLC for the sake of increasing either the Euclidean distance or the Hamming distance associated with the different modulation phasor points in order to achieve a better iterative detection performance with the aid of optimised bit-to-symbol mappers/demappers [51,60,78]. Instead of optimising the modem constellation labelling, in this chapter we introduce a serially concatenated unity-rate code [79] having a recursive structure as a precoder in the context of MLC schemes for the sake of enhancing the demapper's convergence characteristics. Furthermore, we benchmark our MLC MSD scheme against the PID scheme of [51], which exhibits a significantly reduced decoding delay.

The proposed 3-D EXIT chart is then invoked for studying the precoder-aided multilevel coding scheme employing both MSD and PID for communicating over both

AWGN and uncorrelated Rayleigh fading channels with the aid of 8PSK modulation. At BER=10^{-5}, the precoder is capable of enhancing the achievable E_b/N_0 performance by 0.5dB to 2.5dB over the aforementioned AWGN and Rayleigh channels, respectively.

3.2 Comparative Study of Coded Modulation Schemes

The MLC and the related BICM-ID schemes were discussed in Sections 2.2 and 2.4. Now we proceed by investigating their BER performance as a function of their parameters versus their associated complexity.

3.2.1 System Overview

Figure 3.1 provides an overview of various coded modulation schemes, noting that the MLC and BICM-ID schemes were detailed in Sections 2.2 and 2.4. The interleaver and deinterleaver are denoted as π and π^{-1} in Figure 3.1. At the transmitter, random information bits are generated as the source data bits $\mathbf{u}$, before being fed into the encoders. All the encoders used are trellis-based convolutional codes in order to ensure their fair comparison in terms of the associated decoding complexity. Hence the component codes employed in the MLC are also convolutional codes. The encoded sequence is then appropriately interleaved, yielding the bit stream $\mathbf{v}$, and then mapped to the modulation constellation points. Here we consider 8PSK modulation and the bit-to-symbol mapper is designed according to a suitable mapping strategy employing the mapping function of $\kappa(\mathbf{v})$ to be detailed in Table 3.1. The channel imposes the AWGN n and hence the received signal becomes $y = x + n$. The complex AWGN variables are represented as $n = n_I + jn_Q$. Their variance is given by the power of the double sided noise power spectral density of $\sigma^2 = \sigma_I^2 = \sigma_Q^2 = N_0/2$.

At the receiver, the demapper converts the received signals into logarithmic domain probabilities. These probabilities are then deinterleaved and fed into the log-MAP decoders. The log-domain branch-metrics of the MAP symbol decoder are given by the Gaussian PDF

$$p(y_k|x_k) = \frac{1}{2\pi\sigma_n^2} e^{-\frac{|y_k - x_k|^2}{2\sigma_n^2}}, \tag{3.1}$$

when the modulated signal is transmitted over non-fading, AWGN-contaminated channel.

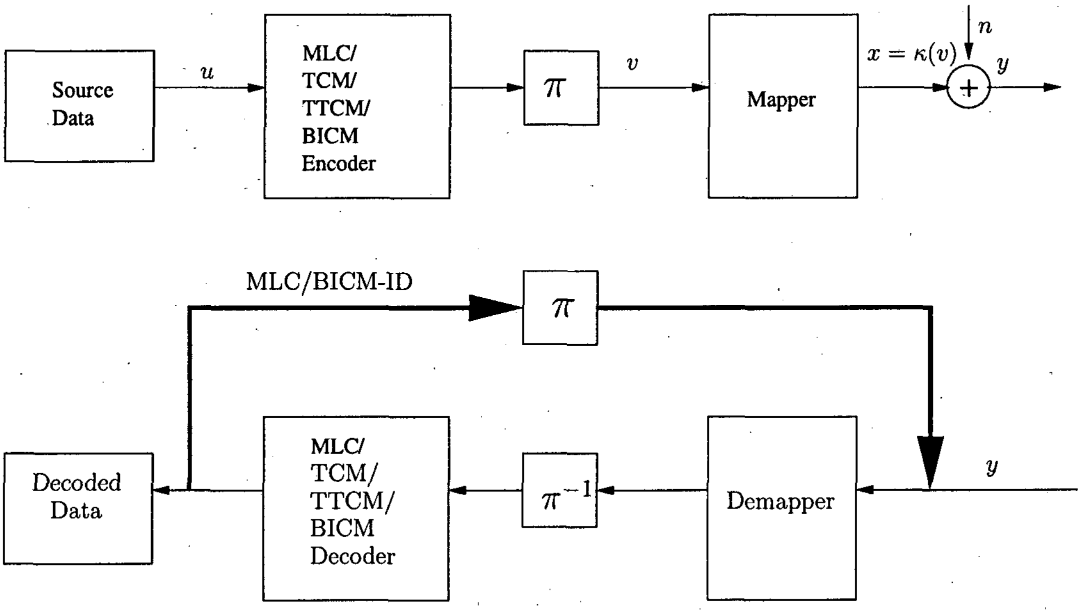

Figure 3.1: System model of the coded modulation schemes considered. Naturally, the BICM and TCM schemes are non-iterative. The iterative decoding of TTCM is carried out by exchanging extrinsic information between two inner component codes, namely the upper and lower codes, which is simplified as the TTCM decoder block [25]. For the MLC and BICM-ID schemes, the iterative decoding is invoked between the inner demapper and the outer MLC as well as BICM-ID decoders, as indicated by the thick black line of the diagram.

We continue by noting that naturally, the TCM and BICM schemes of Section 2.3 are decoded non-iteratively. By contrast, both the MLC and BICM-ID schemes perform turbo-detection invoking iterations between the demapper and decoder, as exemplified in Sections 2.2 and 2.4. The TTCM [25, 65] scheme employs the well-established structure of Turbo Codes (TC) [59, 65, 80], using TCM as its component codes. With the parallel concatenated turbo encoding structure in mind, the upper TCM component encoder processes the original information bits, while the lower TCM component encoder encodes an interleaved version of the upper one. TTCM uses two parallel MAP decoders, with the *extrinsic* information fed back from output of one decoder to the other.

When encoding k number of data bits per information symbol, the coding rate of TCM, BICM and BICM-ID becomes $R = \frac{k}{k+1}$ for a 2^{k+1}-ary modulated signal constellation. When the number of uncoded bits in TCM is $\bar{k} < k$, we have $2^{\bar{k}}$ parallel transition branches in the trellis [16]. In the context of MLC, the coding rate of the

Mapping Type	Mapping Indices to Corresponding Signal Points ($\cos 2\pi i/M$, $\sin 2\pi i/M$) for $i \in$ 0 1 2 3 4 5 6 7
Gray	0 1 3 2 6 7 5 4
UP	0 1 2 3 4 5 6 7
BP	7 3 6 2 4 0 5 1
MP	0 2 1 7 4 6 5 3

Table 3.1: Different bit to symbol Mapping Strategies : Gray, Ungerböck's set Partitioning (UP), Block Partitioning (BP) and Mixed Partitioning (MP) [51], where M is the number of constellation points.

amalgamated scheme would be $R = (R_0 + R_1 + ... + R_{l-1})/l$, when assuming l levels of potentially different-rate encoding. The coding rate of each component code of the MLC scheme may be determined with the aid of the capacity-based design rules of [51] for the sake of approaching the channel capacity, as outlined in Section 2.2.2. For example, for protection level-0, we may aim for an effective throughput of 2 bits/symbol and at this throughput the Shannonian capacity is asymptotically reached at an E_b/N_0 value of around 5.85dB in conjunction with 8PSK modulation employing Ungerböck's Partitioning [16]. Therefore, this specific code rate assigned to this protection level can be chosen from the set of available codes, which performs as close to the Shannonian capacity as possible.

As mentioned earlier, convolutional codes are used as component codes in all of the TCM, TTCM, BICM, BICM-ID and MLC schemes. These convolutional codes [81] are punctured, when requiring high coding rates. For the sake of achieving the best possible performance, a range of different bit-to-symbol mapping strategies are employed in our coded modulation schemes. Some examples of signal mapping arrangements are constituted by Gray Mapping, Ungerböck Partitioning (UP), Block Partitioning (BP) and Mixed/Hybrid Partitioning (MP) [51], which map the natural binary encoded bits to the different modulated constellation points, as discussed in Section 2.2.1. These signal mapping strategies can also be represented in a simple mathematical form, as shown at the top of Table 3.1.

3.2.2 System Parameters

The generator polynomials uniquely and unambiguously describe the different-rate, different-memory encoders and the associated encoder structures. The description of the generator polynomials is typically given in an octal form. A specific example of a generator polynomial is given in Figure 3.2 for Paaske's rate-2/3 non-systematic convolutional code having a memory length of $\varphi = 4$ [82].

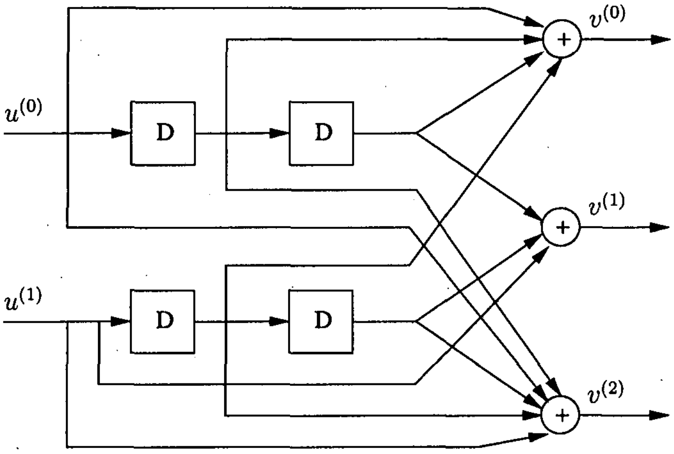

Figure 3.2: An example of Paaske's non-systematic convolutional encoder for $\varphi = 4$ [83].

Since the encoder of Figure 3.2 is a k/n-rate encoder, the information bits at time instant N can be represented as two input sequences formulated as $\mathbf{u}^{(0)}=(u_0^{(0)}, u_1^{(0)}, ..., u_N^{(0)})$ and $\mathbf{u}^{(1)}=(u_0^{(1)}, u_1^{(1)}, ..., u_N^{(1)})$. The resultant output bit sequences are denoted as $\mathbf{v}^{(0)}$, $\mathbf{v}^{(1)}$ and $\mathbf{v}^{(2)}$, respectively. Hence the generator polynomials $\mathbf{g}_i^{(j)}$ associated with input i and output j can be represented as

$$\begin{aligned} \mathbf{g}_0^0 &= [111], \mathbf{g}_0^1 = [001], \mathbf{g}_0^2 = [110]; \\ \mathbf{g}_1^0 &= [010], \mathbf{g}_1^1 = [101], \mathbf{g}_1^2 = [111]. \end{aligned} \tag{3.2}$$

The generator polynomials expressed in octal form are given by [83]

$$\begin{aligned} \mathbf{g}_0^0 &= [7], \mathbf{g}_0^1 = [1], \mathbf{g}_0^2 = [6] \\ \mathbf{g}_1^0 &= [2], \mathbf{g}_1^1 = [5], \mathbf{g}_1^2 = [7] \end{aligned} \tag{3.3}$$

The corresponding generator matrix is formulated as follows

$$\mathbf{G(D)} = \begin{bmatrix} 1+D+D^2 & D^2 & 1+D \\ D & 1+D^2 & 1+D+D^2 \end{bmatrix}. \tag{3.4}$$

Based on this generator polynomial notation, our BICM encoders and MLC convolutional component codes are parameterised in Table 3.2. The puncturing pattern used for generating high-rate codes from a mother code may be obtained using Rate-Compatible Punctured Convolutional (RCPC) codes [69] and the puncturing pattern designed in [84], which are summarised in Table 3.3.

Rate	State(ν), memory(φ)	$g^{(1)}$	$g^{(2)}$	$g^{(3)}$	$g^{(4)}$	d_{free}
1/3	8, 3	13	15	17	-	10
	16, 4	25	33	37	-	12
	32, 5	47	53	75	-	13
	64, 6	133	145	175	15	
1/2	8, 3	15	17	-	-	5
	16, 4	23	35	-	-	7
	64, 6	133	171	-	-	10
2/3	8, 3	4	2	6	-	4
		1	4	7	-	
	16, 4	7	1	4	-	5
		2	5	7	-	
	64, 6	64	30	64	-	7
		30	64	74	-	
3/4	8, 3	4	4	4	4	4
		0	6	2	4	
		0	2	5	5	
	32, 5	6	2	2	6	5
		1	6	0	7	
		0	2	5	5	
	64, 6	6	1	0	7	6
		3	4	1	6	
		2	3	7	4	

Table 3.2: Generator polynomial coefficients in octal format for the non-systematic convolutional codes of Odenwalder, Larsen and Paaske [82,83]. The notation φ and ν represent the code's memory and its corresponding number of states, while d_{free} indicates the free Hamming distance.

For the TCM encoder we adopt the notations from Ungerböck's classic paper [85], representing the polynomial coefficients as follows

$$\mathcal{H}^j(D) = \Lambda^j_\varphi \cdot D^\varphi + \Lambda^j_{\varphi-1} \cdot D^{\varphi-1} + \ldots + \Lambda^j_1 \cdot D + \Lambda^j_0, \tag{3.5}$$

where φ denotes the encoder's memory and D represents the unit delay associated with a single register stage. The coefficient Λ^j_i is a binary value, which indicates the presence

Rate	State(ν), memory(φ)	$g^{(1)}$	$g^{(2)}$	puncturing matrix	d_{free}
5/6	8, 3	15	17	1 0 0 1 0 0 1 1 1 1	3
	64, 6	133	171	1 1 1 1 1 1 0 0 0 0	3
11/12	8 , 3	15	17	1 0 0 0 0 0 0 0 0 1 0 1 1 1 1 1 1 1 1 1 0 1	2

Table 3.3: Generator polynomial coefficients in octal format and puncturing pattern based on Hagenauer's Rate-Compatible Punctured Convolutional (RCPC) codes [69] and on near-unity-rate punctured convolutional codes [84]. The notation φ and ν represent the number of memory and its corresponding states, while d_{free} indicates the free Hamming distance.

of a connection with the aid of a binary value of '1' and the absence of the connection with a value of '0'. Each polynomial $\mathcal{H}^j(D)$ corresponds to the jth information bit, while $\mathcal{H}^0(D)$ is associated with the parity bit of the encoder's feedback polynomial.

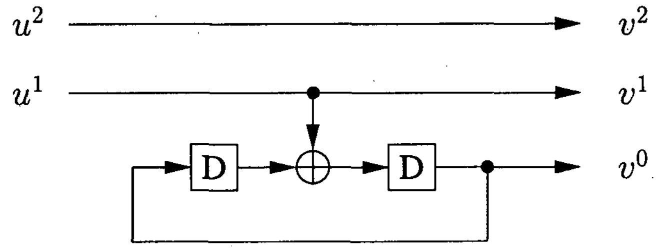

Figure 3.3: An example of Ungerböck's four-state TCM convolutional encoder for 8PSK [16].

Figure 3.3 shows an example of Ungerböck's [16] four-state TCM convolutional encoder for 8PSK. The generator polynomial of Equation (3.5) is given in its octal format in Equation (3.7). The generator polynomials used in our simulations are parameterised in Table 3.4 [85], which obey the format of [85]:

$$\begin{aligned} \mathcal{H}(\mathbf{D}) &= \begin{bmatrix} \mathcal{H}^0(D) & \mathcal{H}^1(D) & \mathcal{H}^2(D) \end{bmatrix} \\ &= \begin{bmatrix} 1+D^2 & D & 0 \end{bmatrix} \\ &= \begin{bmatrix} 101 & 010 & 000 \end{bmatrix} && (3.6) \\ &= \begin{bmatrix} 5 & 2 & 0 \end{bmatrix}. && (3.7) \end{aligned}$$

Code	State(ν), memory(φ)	$\tilde{k}$	$\mathcal{H}^0(D)$	$\mathcal{H}^1(D)$	$\mathcal{H}^2(D)$
8PSK	4, 2	1	5	2	-
8PSK	8, 3	2	11	02	04
8PSK	32, 5	2	45	16	34
8PSK	64, 6	2	103	30	66
8PSK	128, 7	2	277	54	122
8PSK	256, 8	2	435	72	130

Table 3.4: Generator polynomial coefficients in octal format for Ungerböck's TCM codes [85]. The notations φ and ν represent the code memory its corresponding states, respectively. The value $\tilde{k}$ shows that $\tilde{k}$ out of k information bits are convolutionally encoded.

3.2.3 Simulation Results

In this section we present simulation results for the previously mentioned range of different coded modulation schemes. The effective throughput of the system is $R \cdot \log_2 M$, when using an M-ary modulation constellation and an overall coding rate of R. The effective throughput was fixed to 2 Bits Per Symbol (BPS) in conjunction with 8PSK modulation. In Figure 3.4, the BER performance of MLC is shown, when employing both the MSD and PID decoding methods highlighted in Sections 2.2.3.2 and 2.2.3.1.

The component codes are punctured convolutional codes having a coding rate of $R_0 = 1/3, R_1 = 3/4, R_2 = 11/12$ [52]. For the sake of simplicity here we do not follow the exact capacity rules proposed in [51] for adjusting the MLC scheme's coding rate and employ readily available convolutional codes. The PID scheme of Figure 2.8 has a potentially tripled decoding speed compared to the corresponding MSD MLC scheme, although the PID requires three separate parallel decoders for 8PSK. However, at the relatively low E_b/N_0 of 4dB, the PID using three iterations exhibited a high BER of around 4×10^{-2} compared to the MSD's low BER of 7×10^{-4}. This significant BER advantage of the MSD is mainly due to the fact that extra *a priori* information is provided to decoder of the lower-integrity subchannels by those of the higher-integrity subchannels which is not the case for the PID. Hence, in this section we will only use the MSD.

Coded modulation schemes exhibit an implementational complexity, which is exponentially proportional to the number of trellis decoding states, which linearly proportional to the number of iterations. Since the number of trellis states is 2^{φ}, where φ is the memory of the codes, both TCM and BICM have a complexity, which is pro-

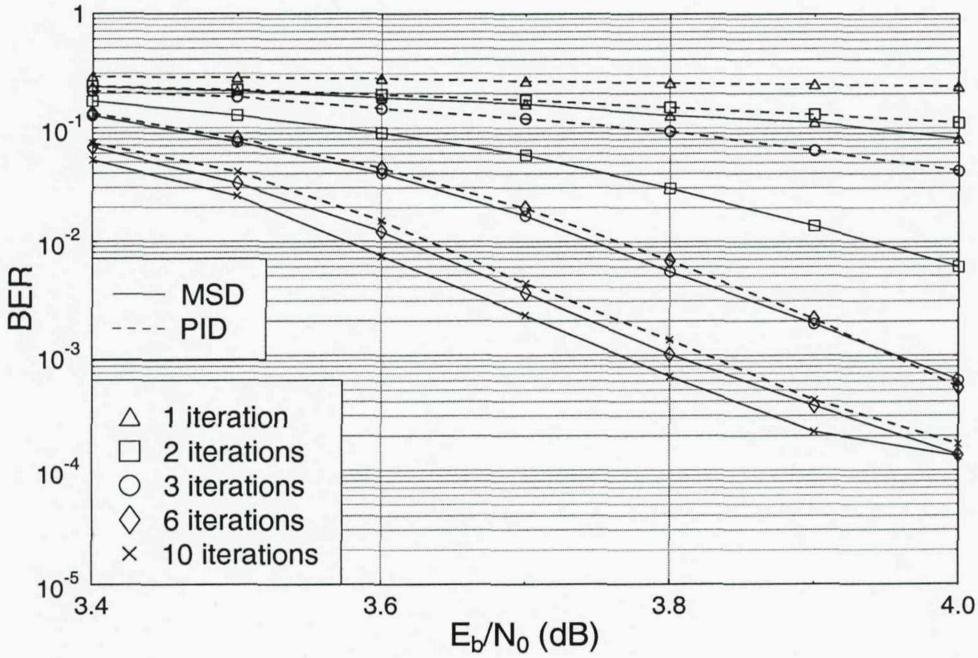

Figure 3.4: BER versus E_b/N_0 performance of both the MSD and PID decoders of Figures 2.10 and 2.8 for the MLC scheme of 3.1 having an effective throughput of 2BPS and using 8PSK modulation for transmission over an AWGN channel. All other code parameters are summarised in Table 3.5.

portional to $\nu = 2^{\varphi}$. The TTCM scheme invokes two TCM component codes and n decoding iterations, hence its complexity is proportional to $\nu = 2 \cdot n \cdot 2^{\varphi}$. The BICM-ID arrangement of Figure 2.20 feeds its *extrinsic* information from the decoder to the demodulator during each decoding iteration. The complexity of the demapper may be assumed to be insignificant. Hence BICM-ID exhibits a complexity, which is proportional to $\nu = n \cdot 2^{\varphi}$. By contrast, MLC employs l number of component codes, with each of the component codes having a memory of φ_i at i^{th} component code. Hence

Coded Modulations	Rate
MLC	$R_0 = 1/3, R_1 = 3/4, R_2 = 11/12$
TCM, TTCM	2/3
BICM, BICM-ID	2/3
Channel	Uncorrelated Rayleigh fading
Decoder type	Log-MAP

Table 3.5: Code parameters employed for simulations. The polynomial generator for the coded modulations are given in Tables 3.2, 3.3 and 3.4.

when using MSD and n iterations its complexity is commensurate with the sum of the individual decoder's complexity, which is expressed as $\nu = n \cdot \sum_{i=0}^{i=l-1} 2^{\varphi_i}$.

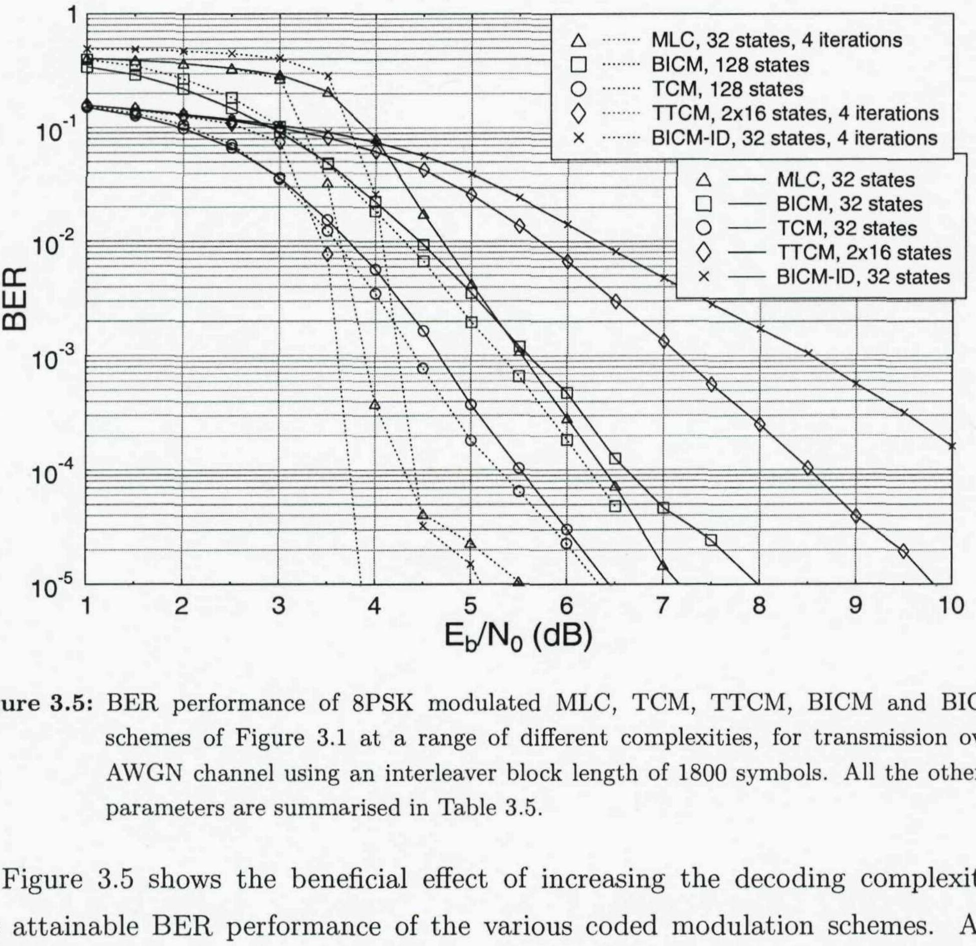

Figure 3.5: BER performance of 8PSK modulated MLC, TCM, TTCM, BICM and BICM-ID schemes of Figure 3.1 at a range of different complexities, for transmission over an AWGN channel using an interleaver block length of 1800 symbols. All the other code parameters are summarised in Table 3.5.

Figure 3.5 shows the beneficial effect of increasing the decoding complexity on the attainable BER performance of the various coded modulation schemes. Again, all schemes have the same effective throughput of 2 BPS. Explicitly, 32-state MLC, 32-state BICM, 32-state TCM, 2 × 16-state TTCM and 32-state BICM-ID exhibit a similar complexity. Observe in Figure 3.5 that non-iterative TCM outperforms all the other schemes, which require several iterations to perform well. More explicitly, at BER $= 10^{-4}$ TCM has an approximately 1dB coding advantage over both MLC as well as BICM, and a gain in excess of 3dB and 4dB, when compared to the identical-complexity TTCM and BICM-ID schemes, respectively. Without iterations, TTCM using punctured component codes does not benefit from sufficient *extrinsic* information exchange. Similarly, BICM-ID which was designed for fading channels using UP, but when using no iterations in the context of AWGN channels, it exhibits a poor performance.

Still referring to Figure 3.5, we then increased the complexity of the various coded modulation schemes either by invoking a higher memory length or by increasing the number of iterations, as appropriate. Observe that TTCM outperforms the other coded modulation arrangements, closely followed by MLC and BICM-ID, which have quite similar performances, requiring an E_b/N_0 around 4.4dB for achieving a BER of 10^{-4}. Increasing the memory length of TCM and BICM, the required E_b/N_0 becomes 5.3dB and 6.2dB, respectively. Therefore, increasing the memory length of TCM and BICM from $\varphi = 5$ to $\varphi = 7$ and hence quadrupling their complexity improves their performance in their context of AWGN channel by less than 0.5dB, while the iterative TTCM, MLC and BICM-ID schemes exhibit a significant E_b/N_0 improvement of up to 5dB upon quadrupling their complexity, which renders the latter iterative schemes more attractive. Note that the formation of an error floor is observed for the BICM-ID and MLC schemes, when the target BER is around 10^{-5}. This is due to the fact that the curves of the inner and outer component codes do not exhibit an open EXIT tunnel, as would be outlined in Section 3.3.

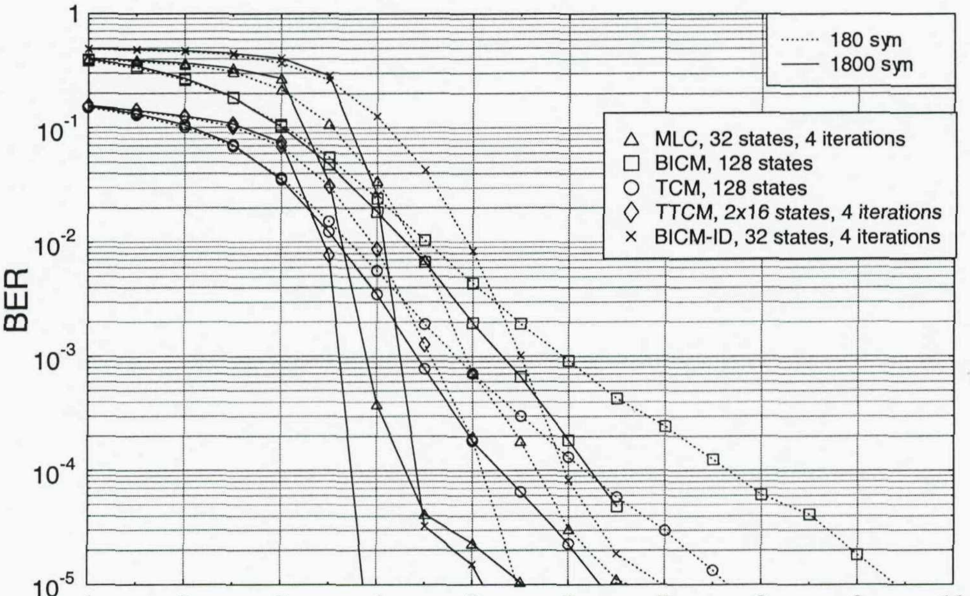

Figure 3.6: BER performance of 8PSK modulated MLC, TCM, TTCM, BICM and BICM-ID schemes of Figure 3.1 using different interleaver block lengths for transmission over AWGN channels at a given fixed complexity associated with a total of 128 trellis states. All the other code parameters are summarised in Table 3.5.

Figure 3.6 illustrates the effect of employing different turbo interleaver block lengths by the various coded modulation schemes while still communicating over an AWGN channel. More specifically, the block lengths of 180 and 1800 symbols are compared. As expected, increasing the turbo interleaver block length improves the attainable performance of the iterative schemes of MLC, BICM-ID and TTCM for transmission over AWGN channels. Observe in Figure 3.6 that BICM-ID has a high sensitivity to the interleaver's block length and at BER = 10^{-4} it exhibits an approximately 1.5dB gain over the similar-complexity non-iterative BICM scheme having 128 trellis states. As seen in Figure 3.6, MLC shows a 1.35dB increase in its coding gain at BER = 10^{-4}, as a benefit of using l encoders, where each encoder requires a commensurately longer interleaver, when the input data is divided into a number of different-protection parallel streams. TCM and BICM obtain an E_b/N_0 improvement of less than 1.5dB at BER = 10^{-4} and hence they are outperformed by the iterative schemes, especially by TTCM, as evidenced by Figure 3.6.

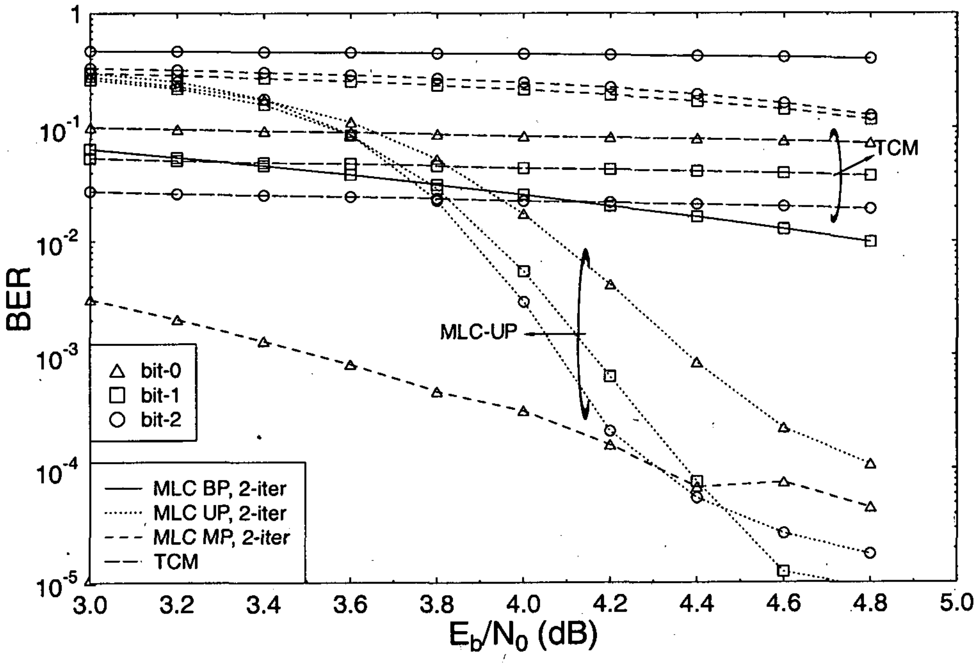

Figure 3.7: BER versus E_b/N_0 for the three different-integrity subchannels in MLC using UP, BP, MP mapping, as well as TCM assisted by two turbo iterations. The schematic diagram is shown in Figure 3.1 and all the other code parameters are summarised in Table 3.5.

Providing UEP is important in the context of speech [86] and video transmission [87]. Figure 3.7 illustrates the fact that MLC is the most flexible scheme in terms of providing UEP among the coded modulation schemes studied, when combined with an appropriate choice of mapping the encoded bits to modulated symbol constellation. To elaborate a little further, all schemes in this figure have three input data bits that have to be protected. The individual decoded bits of TCM exhibit a similar BER performance, i.e. they have no UEP capability, as stated above. Similarly, the UP based mapping of MLCs exhibits almost identical BER performance for all its bits, which shows the lack of UEP capability. This is a consequence of the fact that the stronger code is applied to the specific phasor constellation points labelled by the bits, which are separated by a small Euclidean distance, while the weaker codes at the higher protection levels of the MLC scheme are supported by a large Euclidean distance. The MLC scheme using BP has an equal Euclidean distance for all of its three different bits. Note that bit 0 of the BP-based MLC scheme exhibits a BER below 10^{-5} and thus its BER curve is not shown in Figure 3.7, while bit 2 has a clearly inadequate BER. The MP scheme has its bit 0 strongly protected, while both bit 1 and bit 2 exhibit a similarly inadequate BER performance.

3.3 EXIT Chart Analysis

EXIT charts [76,77,88] constitute a useful tool in the design of iterative schemes, since the characteristics of the constituent components can be visualised based on their exchange of mutual information. The EXIT chart is based on visualising the flow of *extrinsic* information either between the inner and outer decoders of a serial concatenated scheme or between the upper and lower decoders in a parallel concatenated system. The formulation of a 'turbo-cliff' after a certain number of iterations enables us to predict an infinitesimally low BER for E_b/N_0 in excess of the 'turbo-cliff', which we also often referred to as attaining 'convergence' to the $[I_A, I_E] = [1, 1]$ point in the EXIT chart.

3.3.1 Mutual Information

BICM-ID constitutes a serially concatenated arrangement, where the inner and outer codes are constituted by the demapper and SISO decoder of Figure 2.20 respectively. Figure 3.8 shows the iterative decoder of a serially concatenated arrangement, such as the BICM-ID scheme. The inner demapper receives the noise-contaminated signal y at the output of the AWGN channel. The corresponding Gaussian PDF is given by Equation (3.1). The information exchanged between the inner and outer codes is represented in the form of soft LLR values.

The inputs of the demapper of Figure 3.8 are the channel output observations y and the *a priori* LLRs L_A^M are passed from the outer decoder to the demapper of Figure 3.8. The demapper outputs the *a posteriori* LLRs L_P^M, which are then extracted from the *a priori* LLRs L_A^M to obtain the *extrinsic* LLR L_E^M of Figure 3.8. The SISO decoder then processes this information as its *a priori* LLR L_A^D. This outer decoder generates the hard-decoded bit $\hat{u}$ and the soft *a posteriori* LLR L_P^D of Figure 3.8. The *extrinsic* LLR L_E^D gleaned from the decoder is then obtained by subtracting L_P^D from L_A^D. All the LLR values are clearly illustrated in Figure 3.8.

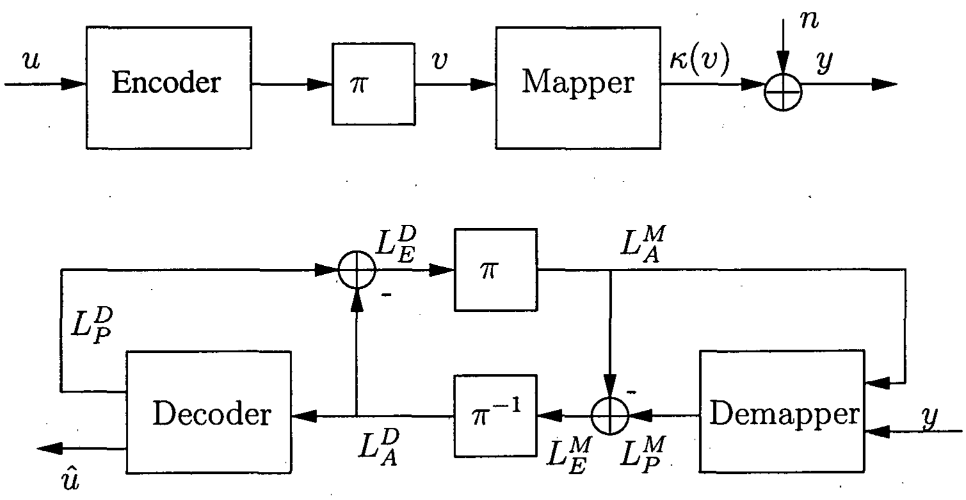

Figure 3.8: Serial concatenated system with iterative decoding.

By considering an idealised infinite-length interleaver, the EXIT chart analysis is based on two assumptions [77]

- the *a priori* LLRs remain fairly uncorrelated,
- the PDF of the *a priori* LLRs may be modelled by the Gaussian distribution.

3.3.1.1 Inner Demapper

First we investigate the transfer characteristic of the inner demapper. Since we model the *a priori* LLRs L_A^M by an independent Gaussian random variable n_a in conjunction with the information bits $x \in \{+1, -1\}$, we have [77]

$$L_A^M = \varrho_a \cdot x + n_a, \tag{3.8}$$

where $\varrho_a = \sigma_a^2/2$ and σ_a^2 is the variance of the noise while the corresponding mean is zero. The probability density function of the *a priori* LLRs can be expressed as

$$p_a(\xi|X=x) = \frac{e^{\frac{-(\xi-\sigma^2/2\cdot x)^2}{2\sigma_a^2}}}{\sqrt{2\pi}\sigma_a}. \tag{3.9}$$

The mutual information between the transmitted encoded bit sequence X and the *a priori* LLR L_A^M is denoted as $I_A^M = I(X; L_A^M)$ where we have $0 \leq I_A^M \leq 1$. This mutual information is given by [77]

$$I_A^M = \frac{1}{2}\sum_{x=-1,+1}\int_{-\infty}^{\infty} p_a(\xi|X=x)\log_2\frac{2p_a(\xi|X=x)}{p_a(\xi|X=-1)+p_a(\xi|X=1)}d\xi. \tag{3.10}$$

The detailed derivation of equations above can be referred to Appendix A. Consequently, using Equation (3.9), I_A^M can be further expressed as

$$I_A^M(\sigma_a) = 1 - \int_{-\infty}^{\infty}\frac{e^{\frac{-(\xi-\sigma_a^2/2)^2}{2\sigma_a^2}}}{\sqrt{2\pi}\sigma_a}\log_2[1+e^{-\xi}]d\xi. \tag{3.11}$$

In order to simplify Equation (3.11) and highlight the inter-dependency of I_A^M on σ, the notation $J(.)$ is introduced as follows

$$J(\sigma) \triangleq I_A^M(\sigma_a = \sigma), \tag{3.12}$$

where $\sigma > 0$, $\lim_{\sigma\to 0} J(\sigma) = 0$ and $\lim_{\sigma\to\infty} J(\sigma) = 1$.

It is infeasible to express $J(\sigma)$ in closed form. However it was noted in [77] that the function $J(\sigma)$ is monotonically increasing and therefore its unique inverse exists, yielding:

$$\sigma_a = J^{-1}(I_A^M). \tag{3.13}$$

Its approximate value is given by [89]

$$J(\sigma_a) \approx (1-2^{-H_1\sigma_a^{2H_2}})^{H_3}, \tag{3.14}$$

$$J^{-1}(I_A^M) \approx (-\frac{1}{H_1}\log_2(1-(I_A^M)^{1/H_3}))^{1/(2H_2)}, \tag{3.15}$$

where H_1=0.3073, H_2=0.8935 and H_3=1.1064.

Figure 3.9 shows the plot of the function $J(\sigma)$ against the value of σ according to (3.12), which is indeed, a monotonically increasing function.

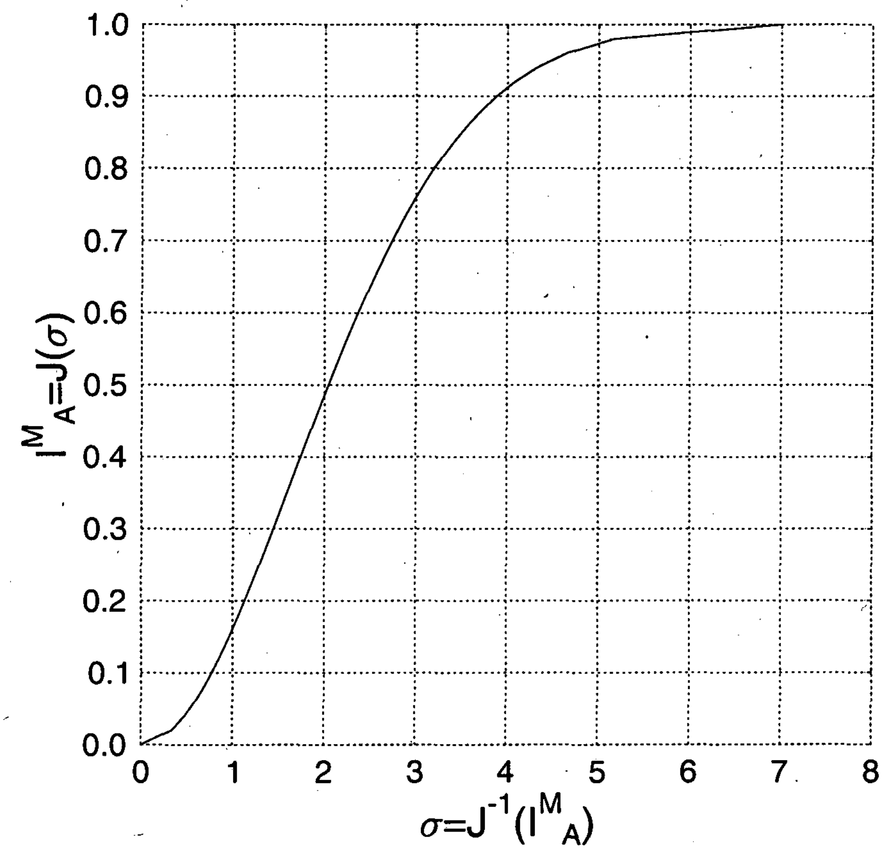

Figure 3.9: The $J(.)$ function, also denoted as the mutual information I_A^M as a function of σ.

The mutual information between the encoded information bits X and the *extrinsic* LLR L_E^M is denoted as $I_E^M = I(X; L_E^M)$. With reference to Equation (3.10), I_E^M can be expressed as [77]

$$I_E^M = \frac{1}{2}\sum_{x=-1,+1}\int_{-\infty}^{\infty} p_e(\xi|X=x)\log_2\frac{2p_e(\xi|X=x)}{p_e(\xi|X=-1)+p_e(\xi|X=1)}d\xi. \tag{3.16}$$

The *extrinsic* LLR L_E^M of Figure 3.8 depends on the *a priori* LLR L_A^M and on the channel's output observation y. The mutual information of I_E^M clearly depends on I_A^M and E_b/N_0, hence the resultant extrinsic transfer characteristic can be represented as

$$I_E^M = T_M(I_A^M, E_b/N_0). \tag{3.17}$$

In order to generate the extrinsic transfer function (I_A^M, I_E^M), the following step by step procedures have to be followed

- Firstly, the noise variance σ_n^2 is set according to the E_b/N_0 value considered.

- We then consider a specific I_A^M range and the corresponding value of σ_a can be obtained from $\sigma_a = J^{-1}(I_A^M)$, as observed in Equation (3.13).

- Given ϱ_a and $\sigma_a = J^{-1}(I_A^M)$, we now have $\varrho_a = \sigma^2/2$ and hence according to Equation (3.8), the *a priori* LLR L_A^M can be expressed as $L_A^M = \varrho_a \cdot x + n_a$, which is assumed to be Gaussian distributed.

- Given the *a priori* LLR L_A^M just calculated at the input of the demapper of Figure 3.8, we can calculate $I_E^M = I(X; L_E^M)$. More explicitly, I_E^M can be obtained from Equation (3.16). Although the assumption of having a Gaussian distributed *a priori* LLR is fairly accurate at the commencement of iterations, provided that a sufficiently long interleaver is used, during the later iterations this may not be the case. A more accurate, although more laborious technique is to estimate this PDF with the aid of Monte Carlo simulations, where we generate a more accurate estimate of the PDF using an experimentally generated histogram.

To expound a little further, it was suggested in [90] that Equation (3.16) can be replaced by invoking the ergodicity theorem, namely by replacing the expectation value by the corresponding time average. This measurement of the mutual information's PDF can be applied for non-Gaussian or unknown distributions with the aid of a sufficiently large number of samples N as [90]

$$\begin{aligned} I_E^M(X; L_E^M) &= 1 - \int_{-\infty}^{\infty} p_e(L_E^M | X = x) \log_2(1 + e^{-L_E^M}) dL_E^M \\ &= 1 - \mathrm{E}[\log_2(1 + e^{-L_E^M})] \\ &\approx 1 - \frac{1}{N} \sum_{n=1}^{N} \log_2(1 + e^{-x(n) \cdot L_E^M(n)}). \end{aligned} \tag{3.18}$$

3.3.1.2 Outer Decoder

The extrinsic transfer characteristic of the outer decoder of Figure 3.8 bears similarity to that of the inner demapper. The outer decoder is a SISO scheme, which is a four-terminal device as seen in Figure 3.10. The mutual information quantifies the relationship of the *extrinsic* output (I_E^u, I_E^v) and the *a priori* input (I_A^u, I_A^v) for both the original uncoded information data bits u and for the coded bits v, respectively. Hence the mutual information can be represented with the aid of the functions $I_E^u = T_u(I_A^u, I_A^v)$ as well as $I_E^v = T_v(I_A^u, I_A^v)$ of Figure 3.10.

Our serially concatenated system shown in Figure 3.8 obtains only a single *a priori*

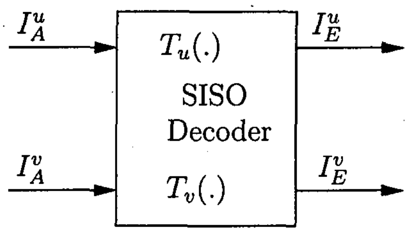

Figure 3.10: The SISO decoder of an EXIT module, corresponding to the EXIT function of mutual information of between input and output of data and coded bits.

L_A^D input namely from the inner demapper, which can also be observed in Figure 2.20. The extrinsic transfer characteristic describes the relationship between the *a priori* input L_A^D and the *extrinsic* output L_E^D. The mutual infomation $I_E^D = I(V; L_E^D)$ between the channel encoded bits v and output *extrinsic* LLR L_E^D is independent of the effect of E_b/N_0 experienced by the system. Hence the EXIT function can be expressed as

$$I_E^D = T_D(I_A^D), \tag{3.19}$$

where $I_A^D = I(V; L_A^D)$ is the mutual information between the channel coded bits v and the *a priori* LLRs L_A^D. The calculation of I_A^D and I_E^D is similar to that of the inner demapper highlighted in Section 3.3.1.1.

3.3.2 Performance of BICM-ID

The performance of the BICM-ID scheme can be characterised with the aid of EXIT chart analysis, as described in Section 3.3.1. Figure 3.11 shows the EXIT characteristics of the BICM-ID scheme. Note that the EXIT curve of the inner demapper starts at a lower I_E^M value and increases steadily as the E_b/N_0 value increases from 0dB to 10dB in steps of 1dB. The EXIT curve of the outer decoder is shown as the dashed curve. It is observed from Figure 3.11 that an open EXIT tunnel can exist between the inner and outer EXIT curves, for $E_b/N_0 = 4$dB and above, producing an iterative gain.

The simulation based decoding trajectory is illustrated in Figures 3.12 and 3.13. The extrinsic mutual information are calculated for I_E^M and I_E^D with the aid of the *extrinsic* LLR output of the inner demapper and of the outer decoder, respectively using Equation (3.18). This simulated decoding trajectory of the real system demonstrates in Figures 3.12 and 3.13, how close the trajectory matches the EXIT curves. Based on Figure 3.12 we infer that at $E_b/N_0 = 4$dB we need five iterations in order to approach the $I_E = 1$ point and hence achieve a low BER. By contrast, a good

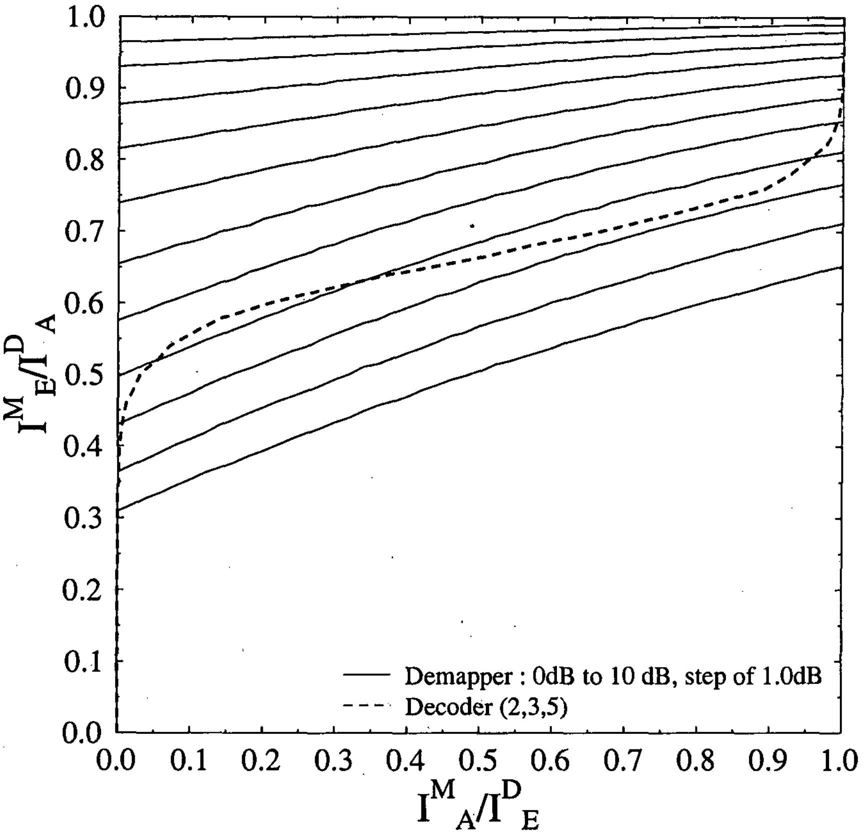

Figure 3.11: EXIT characteristic curves for the inner demapper and the outer decoder of the BICM-ID scheme of Figure 3.1, when communicating over an AWGN channel.

performance is predicted with the aid of three iterations at $E_b/N_0 = 5$dB. Since the EXIT curve assumes having a high interleaver length, the simulations presented here correspond to an interleaver depth of 10^4 bits, as opposed to the 1800-bit interleaver used in the comparative study of Figure 3.6.

The invention of EXIT charts enables us to design a code based on achieving iterative convergence to the (1,1) point of the EXIT tunnel in order to attain a good BER performance. Let us briefly consider the shape of each individual component code, namely that of the inner and outer code. If the inner and outer EXIT curves intersect before reaching the point of convergence at (1,1), the scheme will be unable to achieve an infinitesimally low BER. The narrower the EXIT tunnel, the more iterations are required to reach the point of convergence. Figure 3.14 illustrates the EXIT curves of a 1/2, 2/3 and 3/4-rate BICM-ID decoder having different memory lengths.

In the case of the inner demapper, the EXIT characteristic clearly illustrates how

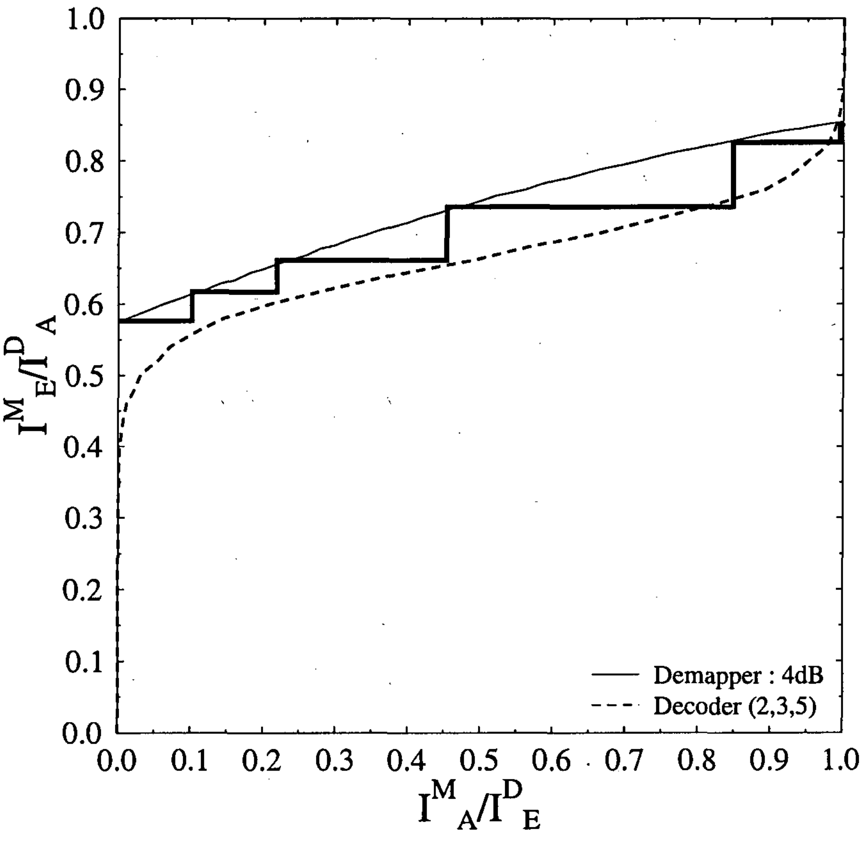

Figure 3.12: Decoding trajectory of the BICM-ID scheme of Figure 3.8 employing set partitioning at $E_b/N_0 = 4$dB in conjunction with an interleaver depth of 10^4 bits, when communicating over an AWGN channel.

the design of an efficient demapper closely matching the shape of the outer code, can support the code design in terms of achieving a good BER performance. Figure 3.15 shows the EXIT curve of the inner demapper employing different mapping schemes, as outlined in Table 3.1. Note that the EXIT curve corresponding to employing Gray mapping has a relatively high starting point, at the abscissa value of zero but results in a horizontal line associated with no iteration gain.

3.3.3 Performance of MLC

The performance of the MLC scheme employing iterative decoding cannot be readily portrayed with the aid of the classic two-Dimensional (2-D) EXIT chart analysis employed in Section 3.3.2. Let us now consider a MLC using MSD and employing 8PSK modulation. The decoder of the MSD-aided MLC of Figure 2.10 is again investigated

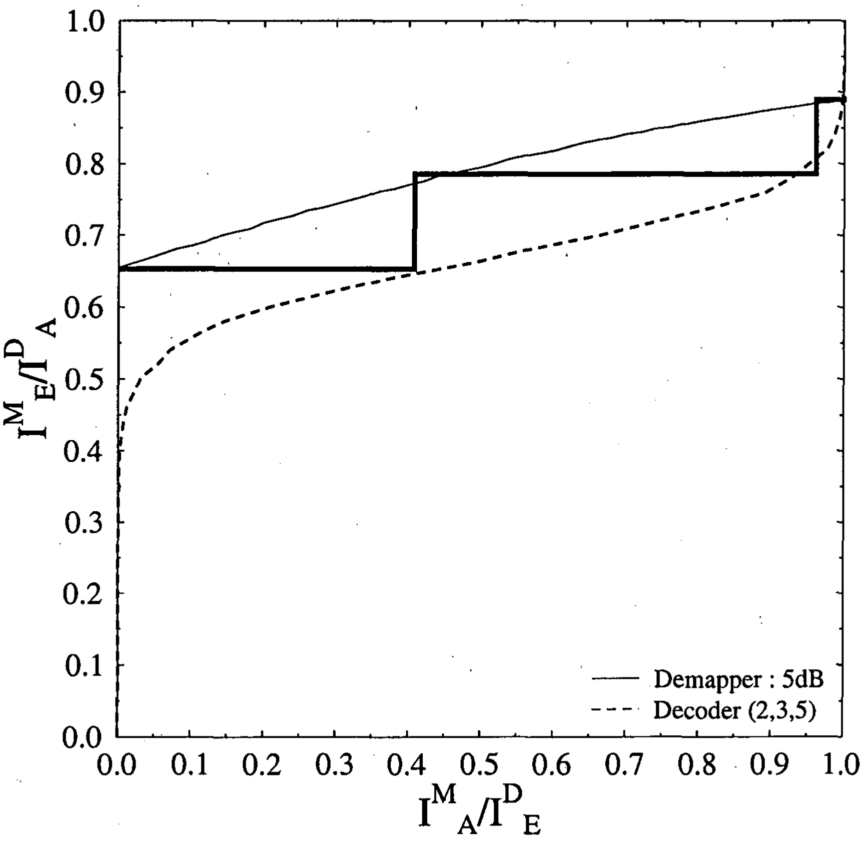

Figure 3.13: Decoding trajectory of the BICM-ID scheme of Figure 3.8 employing set partitioning at $E_b/N_0 = 5$dB with the aid of an interleaver depth of 10^4 bits, when communicating over an AWGN channel.

in Figure 3.16, which illustrates a three-level UEP MSD-aided MLC design using 8PSK modulation and three decoders, namely $\mathbb{D}^0$, $\mathbb{D}^1$ and $\mathbb{D}^2$ for bit 0 ($b0$), bit 1 ($b1$) and bit 2 ($b2$), respectively.

In Figure 3.17, we show the general structure of EXIT chart generation for the MSD of Figure 3.16. Note that L_A represents the LLRs of the information bits of the relevant decoder, while $L^i_{A(o)}$ denotes the LLRs of the *other* decoders' information bits. Considering the decoder at protection *level* 0 and referring to the schematic of Figure 3.17, the associated information bit is $b0$, while the corresponding information bits of the other decoders are $b1$ and $b2$, respectively. Hence L^i_A, which is the LLR associated with the black box in the figure, is generated from L_{b0}. The *a priori* LLRs generated by the *other* decoders are L_{b1} and L_{b2}, as indicated by the hollow boxes in Figure 3.17, are then computed along with their individual average values for the sake of obtaining the combined *a priori* LLR of $L^i_{A(o)}$ as the input soft bit value for the

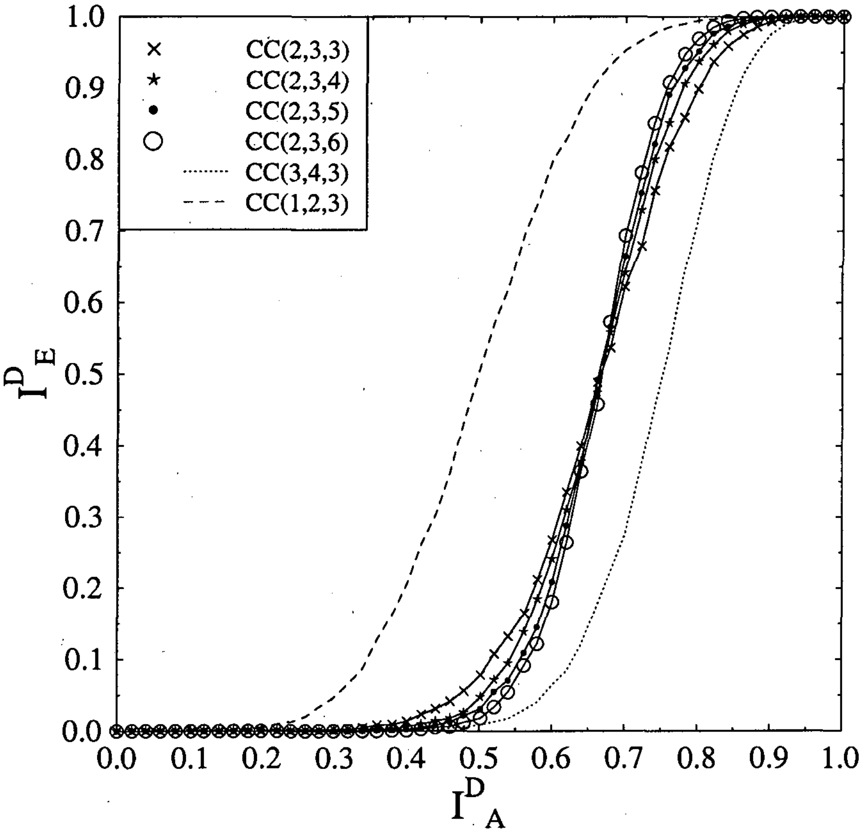

Figure 3.14: Extrinsic transfer characteristic of several convolutional encoders with different rate and constraint lengths.

iterative demapper. Similar operations are carried out at the *level* 1 and 2 decoders, each having the corresponding information bit represented by the black box at different positions in Figure 3.17. The demapper of the MLC decoder is treated similarly to the demodulator of the iterative BICM-ID [53] scheme. When the *a priori* probability P_a is different from 0.5, the extrinsic probability of the MLC demapper is given by [53] and Equation (2.41) is repeated here for convenience

$$P_e(v_t^i = b) = \sum_{x_t \in \chi_b^i} \left(P(y_t|x_t) \prod_{j \neq i} P_a(v_t^j = v^j(x_t)) \right). \tag{3.20}$$

For 8PSK modulation, the bit index is $i = 0, 1, 2$, where we have $v_i = b$, $b \in \{0, 1\}$, and following the notation of [53], the subset of modulated signals is denoted by $\chi_b^i = \{\kappa(v_2 v_1 v_0) | v_i = b; v_j \in 0, 1, j \neq i\}$. The mapping function $\kappa(.)$ of the different mapping schemes used in our design study was illustrated in Table 3.1. For an AWGN channel, $P(y_t|x_t)$ is given by Equation (3.1). Since we have $j \neq i$, which excludes the own

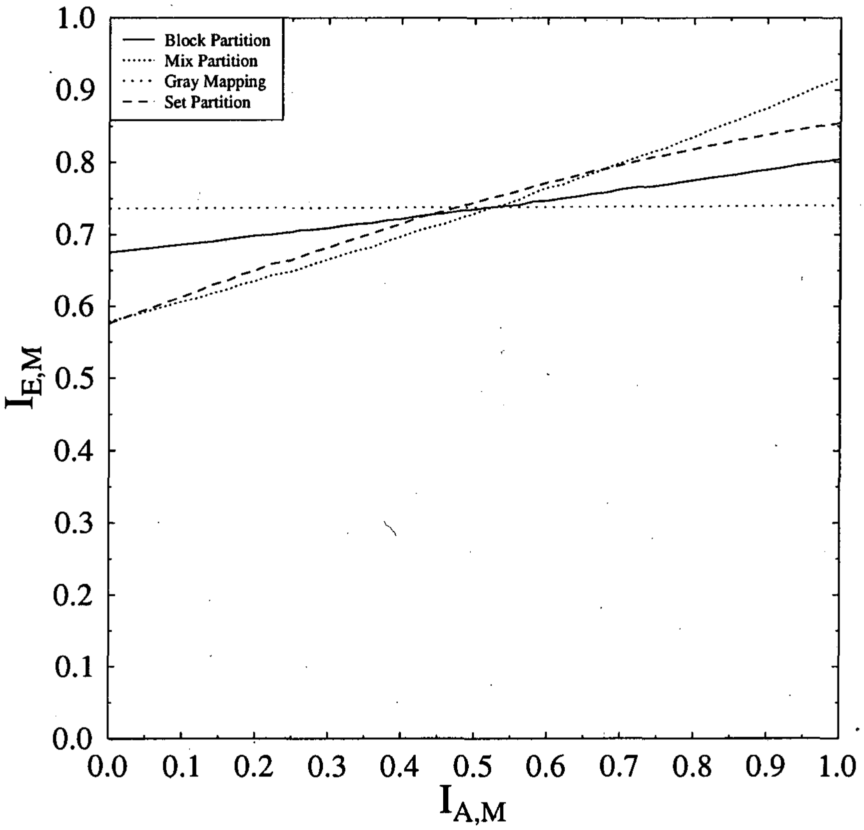

Figure 3.15: Extrinsic transfer characteristic of the inner demapper which employs different mapping strategies as outlined in Table 3.1, when communicating over an AWGN channel at $E_b/N_0 = 4$dB.

intrinsic information of each bit, the output LLR is only affected by the *extrinsic* information of the *other* decoders.

Let us now investigate the decoding convergence of the schemes studied using a 3-D EXIT chart with reference to Figure 3.17 in the context of three different en(de)coders employing UP based labelling. To expound a little further, the reason for requiring a 3-D EXIT chart in the context of our 8PSK based MLC scheme is, because when employing MSD there is an iterative information exchange amongst the three separate MLC decoders of the different protection levels, rather than between only two constituent decoders, as in the case of conventional EXIT charts. The results of our 3-D EXIT chart analysis are shown in Figures 3.18, 3.19 and 3.20. At each level of the MLC decoding scheme, the demapper constitutes the inner decoder, while the outer decoders are the corresponding MAP decoders. The concept of 3-D EXIT charts was first proposed in the context of the three-stage serially concatenated system of [91]. Further

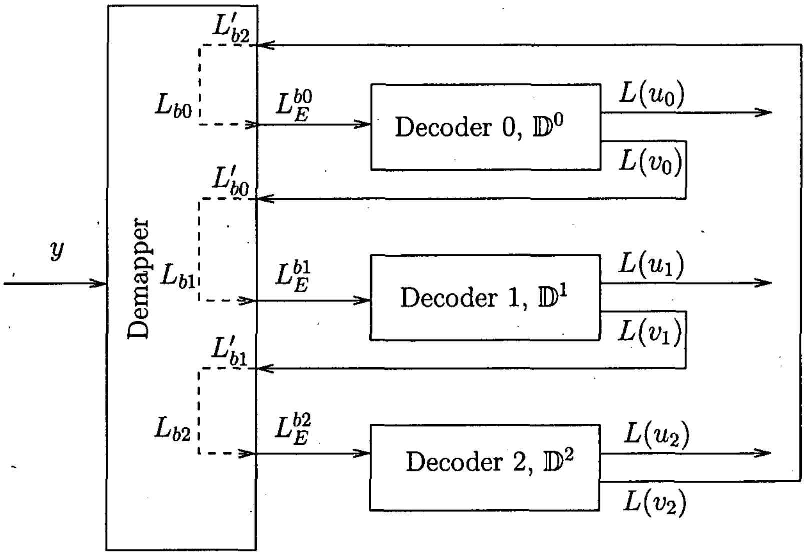

Figure 3.16: MSD decoder of the 8PSK modulated MLC scheme with channel information y. The notations $L(u_i)$ and $L(v_i)$ represent the output LLRs of the three decoders for both the information bits and the encoded bits. The subscript i represents the bit index in $b0$, $b1$ and $b2$. Furthermore, L_{bi} denotes the associated information bits' LLRs for the corresponding decoder $\mathbb{D}^i$, which is further augmented in Figure 3.17, while L'_{bi} denotes the *a priori* LLRs forwarded by the *other* decoders $\mathbb{D}^i$ to the input of the inner demapper. L_E^{bi} denotes the *extrinsic* LLRs provided by the demapper. Figures 3.18, 3.19 and 3.20 constitute the 3-D EXIT chart visualisation of the MLC MSD decoders $\mathbb{D}^0$, $\mathbb{D}^1$ and $\mathbb{D}^2$, respectively.

research on transforming multi-dimensional EXIT charts into a single two-dimensional EXIT chart in the context of either parallel or serial concatenated codes was reported in [92]. Our research further developed the 3-D EXIT chart to suit the MLC MSD scheme investigated.

In Figure 3.18, I_A^i/I_E^i and I_A^o/I_E^o denote the mutual information of the inner and outer codes, respectively. Furthermore, $I_{A(o)}^i$ in Figure 3.18 represents the mutual information at the demapper's input generated from the *a priori* knowledge provided by the *other* decoders, where the superscript i represents the *inner* code, while the subscript $A(o)$ represents the *a priori* knowledge gleaned from the *other* decoders. As seen in Equation (3.20), the *extrinsic* probability information exploited by the MLC demapper is only affected by the information bits provided by the *other* decoders, hence I_E^i of the demapper changes only as a function of $I_{A(o)}^i$.

As observed in Figure 3.17, the mutual information is exchanged between the inner demapper by passing I_E^i to the outer MAP decoder, which iteratively exchanges I_E^o

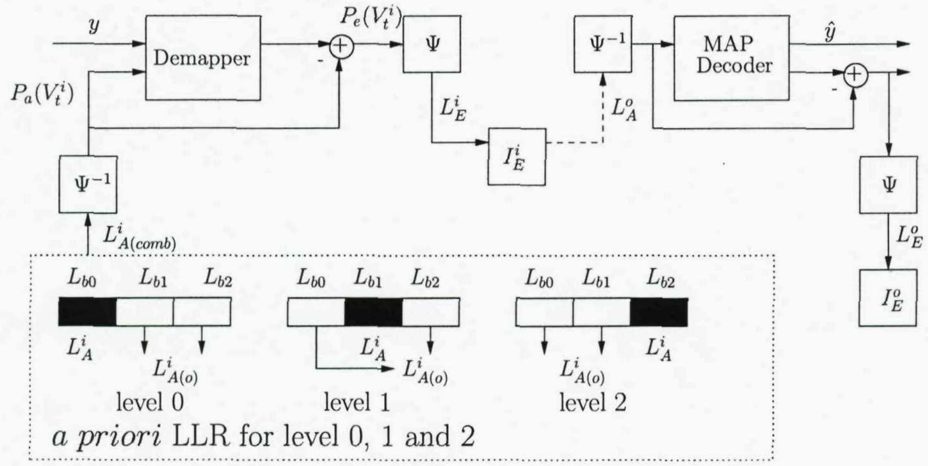

Figure 3.17: General structure of EXIT chart generation for the MSD of 3-level MLC when using 8PSK and three en(de)coders. L_b^a represents the LLR values, where the superscript a denotes the inner (i) or outer (o) codes, while the subscript b denotes the input *a priori* (A) or output *extrinsic* (E) information. L_{b0}, L_{b1} and L_{b2} are independent Gaussian distributed LLR generated for bits 0, 1 and 2 respectively. Furthermore, Ψ and Ψ^{-1} denote the LLR-to-symbol probability and symbol probability-to-LLR conversion. The arrow drawn in dash line represents the *extrinsic* LLR demapper output, which becomes the LLR input of the decoder after demapping. The filled black box represents the *a priori* LLR of the associated information bit, while the hollow box denotes the *a priori* LLR of the bits of the *other* decoders. Finally, I_E^i and I_E^o denote the mutual information used for plotting the EXIT chart.

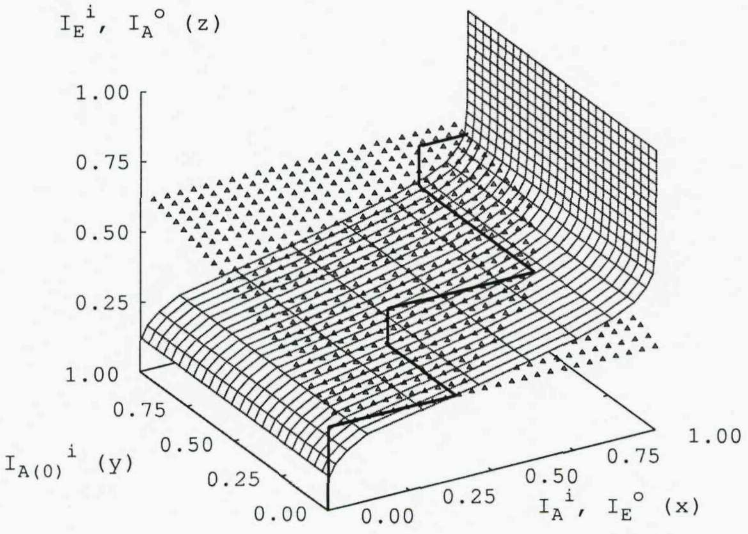

Figure 3.18: 3-D EXIT Chart for Level 0 of the MLC scheme at E_b/N_0 = 4dB.

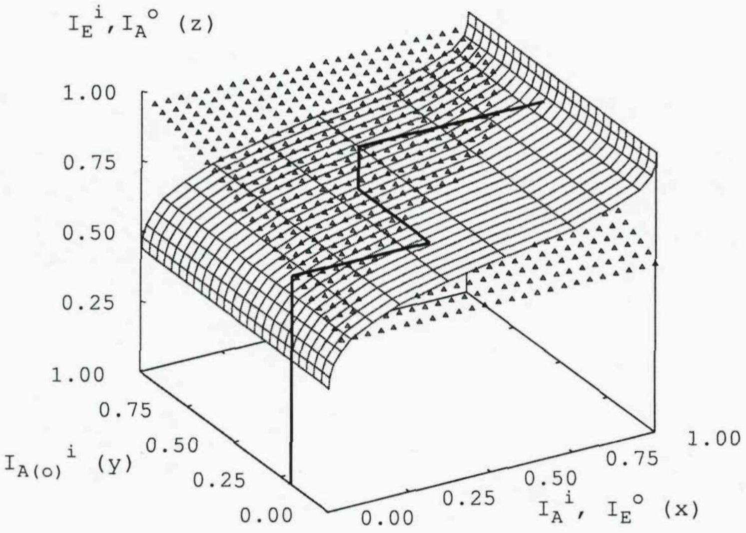

Figure 3.19: 3-D EXIT Chart for Level 1 of the MLC scheme at E_b/N_0 = 4dB.

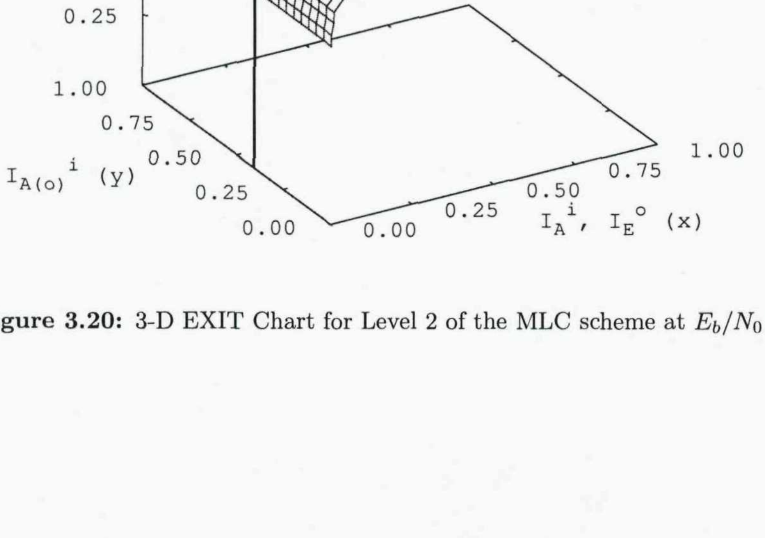

Figure 3.20: 3-D EXIT Chart for Level 2 of the MLC scheme at E_b/N_0 = 4dB.

with the inner demapper. In the 8PSK based MLC scheme, we have three different-integrity decoding levels ($b0$, $b1$, $b2$) and each level is represented in one of the three 3-D EXIT charts shown in Figures 3.18, 3.19 and 3.20, respectively. In all three figures, the EXIT plane marked with triangles is computed based on the inner demapper's output *extrinsic* information I_E^i at a given *a priori* input I_A^i and $I_{A(o)}^i$, characterising its *extrinsic* probability P_e forwarded to the outer MAP decoders. By contrast, the EXIT plane of these figures, which is represented by the mesh of rectangles was obtained based on the MAP decoder's *extrinsic* output I_E^o at a given demapper extrinsic information I_E^i.

Commencing from decoder 0 having only the channel's output information, but no *a priori* LLR from the *other* decoders, the I_E^i trajectory curve emanates from the central corner of the graph in Figure 3.18, with the x, y coordinate values equal to 0. When the *extrinsic* LLR L_E^{b0} provided by the demapper output seen in Figure 3.16 is passed to $\mathbb{D}^0$, the decoding trajectory moves in a direction parallel to the x axis at a certain I_E^o value, quantifying the *extrinsic* information contribution of the outer decoder $\mathbb{D}^0$. The output *extrinsic* LLR $L(v_0)$ is then passed to the second-level demapper, where it becomes the *a priori* information L'_{b0}, as seen in Figure 3.16. Hence, at the second decoding level, the demapper benefits from both the channel LLRs and the *a priori* LLRs L'_{b0} provided by the first decoded level. We can therefore observe that $I_{A(o)}^i$ of level 1 in Figure 3.19 emerges from a positive value of the y axis. The iterative process evolves further then to the third decoder output at protection level 2, as shown in Figure 3.20.

At the third decoder $\mathbb{D}^2$ of Figure 3.16, the *extrinsic* LLRs $L(v_2)$ are fed back as the *a priori* information L'_{b2} to the decoder $\mathbb{D}^0$ of the first level. At this stage, namely during the first iteration, we can observe from Figure 3.18 that the trajectory of $I_{A(o)}^i$ moves in parallel to the y axis as a benefit of the *a priori* knowledge L'_{b1} and L'_{b2} provided by the *other* decoders from protection level 1 and level 2 of the MLC scheme, and the output of the demapper 0 benefits from an iteration gain, where the decoding trajectory moves vertically along the z axis, between the two EXIT planes denoted by the mesh of triangles and rectangles, respectively, reaching a specific value of I_E^i. This is the *extrinsic* information gleaned during the second iteration in decoder 0. The same process continues, as the *a priori* information is forwarded from the first protection level towards the third protection level of the MLC scheme.

The zig-zag shaped trajectory evolves within the 3-D tunnel constituted by the inner demapper's and outer decoder's EXIT curves. The highest possible iteration gain would be reached, if the trajectory converged to the point (1,1,1). However, due to the deficient demapper characteristic, the decoding trajectory of Figure 3.18 fails to reach this point at protection level 0, since it is trapped between the EXIT planes. By contrast, the demapper characteristics reach better convergence both at protection level 1 and 2, as seen in Figure 3.19 and 3.20 respectively, approaching the point (1,1,1) more closely. Hence, the iterative MLC scheme's performance is limited. Furthermore, note that the decoding trajectory fits closely, but not exactly into the EXIT chart's tunnel due to the fact that the MLC scheme's three encoded bits become slightly dependent on each other after the first iteration and therefore the corresponding LLRs do not obey a perfect Gaussian distribution. Nonetheless, the 3-D EXIT chart provides an adequate prediction of the MLC scheme's iterative behaviour. Observe from the 3-D EXIT chart analysis of Figure 3.18 that the performance of the level-0 decoder $\mathbb{D}^0$ may potentially be improved by enhancing the convergence behaviour of the inner demapper, which will be investigated in Section 3.4.

3.4 Precoder-Aided MLC

In this section, the novel 3-D EXIT chart of previous Section 3.3.3 is developed further for investigating the iterative behaviour of MLCs invoking MSD. The extrinsic information transfer characteristics of both the symbol-to-bit demapper used and those of the different-protection constituent decoders suggest that potential improvements can be achieved by appropriately designing the demapper. To further extend our investigations, the proposed 3-D EXIT chart is then invoked for studying the precoder-aided multilevel coding scheme employing both MSD and PID for communicating over both AWGN and uncorrelated Rayleigh fading channels with the aid of 8PSK modulation.

As shown in Figure 3.15, the demapper is capable of shaping the EXIT tunnel to allow a possible convergence to occur. In the recent past, different constellation labelling strategies have been employed in the context of MLC for the sake of increasing either the Euclidean distance or the Hamming distance associated with the different modulation phasor points in order to achieve a better iterative detection performance with the aid of optimised bit-to-symbol mappers/demappers [51] [60] [78]. Alternatively, instead of optimising the modem constellation labelling, a serially concatenated unity-rate code [79] having a recursive structure as a precoder in the context of MLC can be used for the sake of enhancing the demapper's convergence characteristics. The concept of precoding effect was first presented for magnetic recording channels [93] and further expended to other channels [94, 95]. The precoder has a recursive structure which can be described in terms of shift registers having feedback connections determined by feedback polynomials.

3.4.1 System Overview

Figures 3.21 and 3.22 outline our MSD and PID schemes designed for operating in conjunction with 8PSK modulation, respectively. The notations $L(u_i)$ and $L(v_i)$ represent the output LLRs of the decoders for the original information bits and for the MLC-encoded bits, respectively. The subscript i represents the index of the different-protection bits $b0$, $b1$ and $b2$, while L_E^{bi} denotes the *extrinsic* LLR generated at the output of the *inner* demapper. The rectangle drawn in dashed lines in both Figures 3.21 and 3.22 represents the Unity-Rate Code (URC) decoder schemes constituted by unity-rate recursive decoders inserted after the demapper. In Figure 3.21, L_{bi} denotes the associated information bits' LLRs for the corresponding decoder $\mathbb{D}^i$, while L'_{bj} denotes the *a priori* LLRs forwarded by the *other* decoder $\mathbb{D}^j$ to the input of the inner demapper.

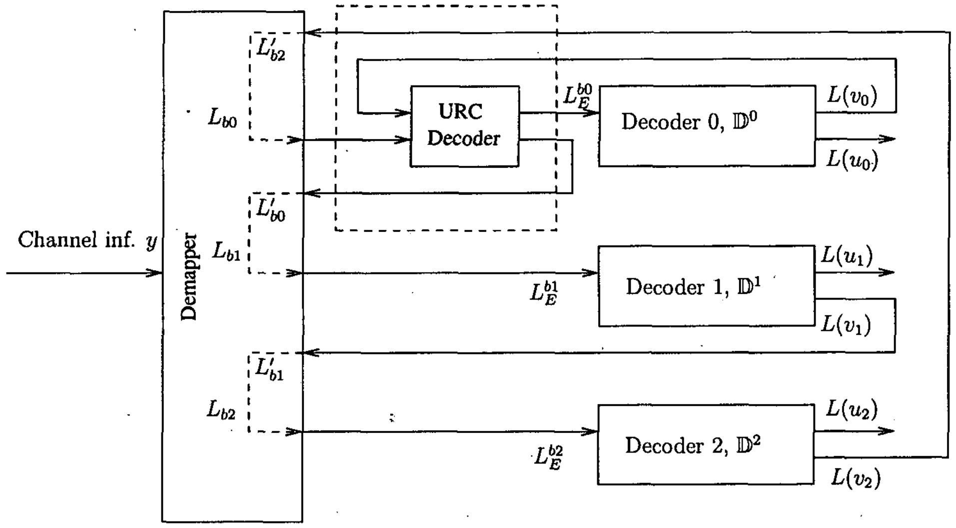

Figure 3.21: MSD decoder of the 8PSK modulation based precoder-aided MLC scheme. The URC decoder represents the unity-rate code's decoder.

To elaborate a little further, in the MSD decoder of Figure 3.21 the *a priori* infor-

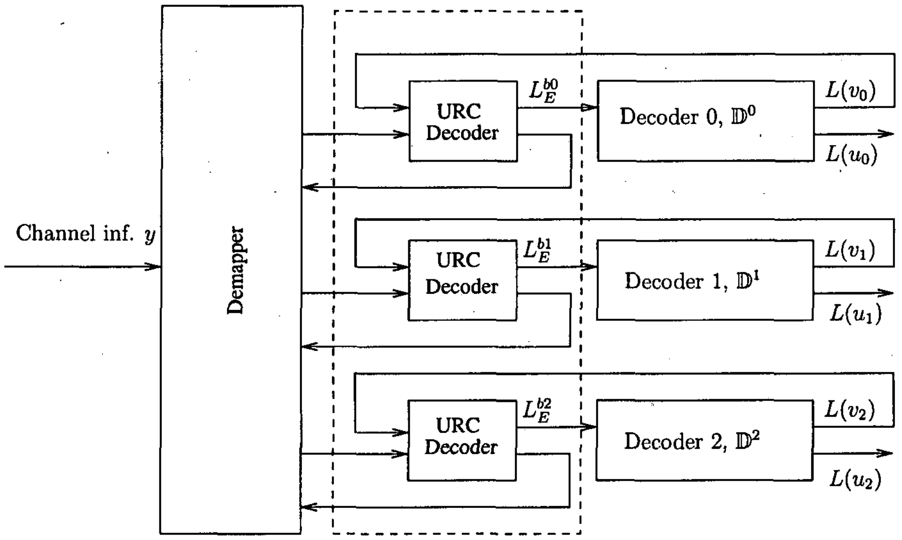

Figure 3.22: PID decoder of the 8PSK modulation based precoder-aided MLC scheme. The URC decoder represents the unity-rate code's decoder.

mation is fed by the lower-protection decoder to the higher-protection scheme. Each of the bits $b0$, $b1$ and $b2$ is decoded by the corresponding decoder, namely by $\mathbb{D}^0$, $\mathbb{D}^1$ and $\mathbb{D}^2$. The decoder $\mathbb{D}^i$ processes both the received information bits of L_{bi} as well as the *a priori* information provided by the *other* decoders and conveyed by the inner demapper seen in Figure 3.21. By contrast, the PID structure shown in Figure 3.22 does not make use of the decisions carried out at other protection levels. Instead, each decoder $\mathbb{D}^i$ processes the *a priori* knowledge in a parallel and independent manner. Hence, this potentially results in a reduction of the associated processing delay.

We employ a unity-rate precoder since the rate-one precoder introduces no coding overhead and hence retains the original coding rate. Its simple structure also means that we would have a low complexity at the receiver. Figure 3.23(a) portrays the unity-rate code employed in our precoder-aided MLC scheme, where D is a shift register stage and $\oplus$ represents the modulo-2 operation. Figure 3.23(b) shows the trellis diagram of the precoder. The trellis transitions are denoted by a_i/b_i, where a_i denotes the input of the precoder at time i, while b_i indicates the corresponding precoder output.

In the system advocated, we employ convolutional codes as our component code, where the individual coding rates of the MLC MSD and MLC PID schemes are 1/3, 3/4, 11/12 [52] and 1/2, 3/4 and 3/4 [51], respectively. This is the same MLC scheme as the one used in the comparative study of Section 3.2. Since the specific coding rates

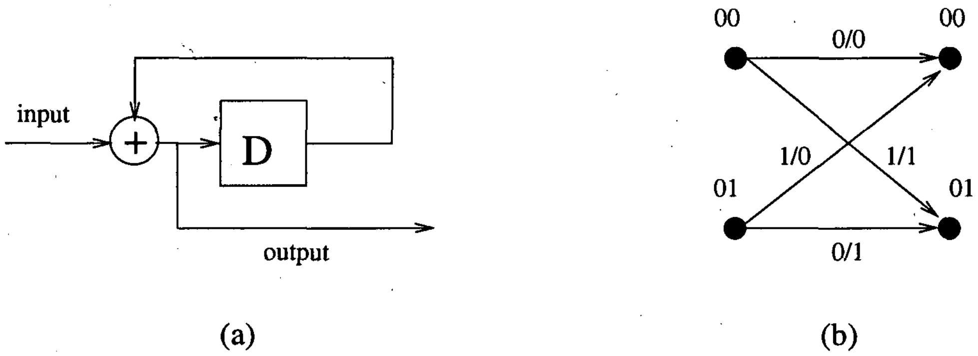

Figure 3.23: Unity rate memory-1 precoder.

that are readily available for convolutional codes are constrained, we do not follow the exact capacity rules proposed in [51] for adjusting the MLC scheme's coding rate. The resultant effective throughput of the 8PSK system considered becomes 2 bits per symbol. All system parameters are summarised in Table 3.6.

Coding rate MSD (R_0, R_1, R_2)	(1/3, 3/4, 11/12)
Coding rate PID (R_0, R_1, R_2)	(1/2, 3/4, 3/4)
Precoders' trellis states	00 and 01
Modulation	8PSK
Mapping type	Ungerböck Partitioning (UP)
Interleaver length	1800 symbols

Table 3.6: System parameters.

3.4.2 EXIT Chart Based Convergence Analysis

The thick zig-zag shaped lines of Figures 3.18, 3.19 and 3.20 seen in the 3-D EXIT of the non-precoded MLC scheme of Section 3.3.3 represent the decoding trajectory evolving within the 3-D tunnel, constituted by the inner demapper's and the outer decoder's EXIT planes. If the trajectory succeeds in converging to the point $(1, 1, 1)$, the highest possible iteration gain is reached. We observe that the decoding trajectory of protection *level* 0 fails to reach this point owing to its deficient demapper characteristics. Hence, in order to improve the iterative decoding convergence of the overall MLC system, we have to improve the demapper characteristic at protection *level* 0. This can be achieved by introducing the precoders [79] shown in the dash-line boxes of Figure 3.21 and 3.22.

The beneficial effect of precoding on the attainable decoding convergence has been demonstrated by Narayanan in [93], where the recursive precoder of $G(D) = 1 + D^a$ was shown to attain a substantial gain. In the precoder's generator polynomial, a represents an integer, which corresponds to the number of shift register stages employed in the precoder structure. Here, we employ a low-complexity rate-1 precoder having the generator polynomial $G(D) = 1 + D$ without adding further redundancy to the inner code's demapper, which allows us to maintain the inner code's original coding rate. Figure 3.23 demonstrates the implementational simplicity of the precoder, which has a 2-state trellis.

The schematic of generating the 3-D EXIT plane for protection *level* 0 of the precoder-aided MSD is shown in Figure 3.24. The 3-D EXIT plane of Figure 3.18 shows that the inner demapper characteristics are only affected by the information bits provided by the LLRs of the *other* $L^i_{A(o)}$ decoders, regardless of its own intrinsic LLR L^i_A. Hence in Figure 3.24, $L^i_{A(info)}$ would only be regarded as dummy information and would not be exploited in the 3-D EXIT chart for the sake of reducing its dimensions. In other words, the *inner* code's EXIT plane will not be affected by varying the values of $L^i_{A(info)}$. The LLR $L^i_{A(data)}$ is generated by the *outer* MAP decoder and input to the precoder. Therefore, the LLRs $L^i_{A(o)}$, $L^i_{A(data)}$ and L^i_E corresponding to the mutual information $I^i_{A(o)}$, I^i_A and I^i_E are used for plotting the inner demapper's EXIT characteristic. The *inner* EXIT characteristic plane is a function of $I^i_E = f(I^i_A, I^i_{A(o)})$.

Figure 3.25 portrays the 3-D EXIT chart employing the precoder. The EXIT planes marked with the mesh of triangles and dashed lines characterise the precoded demapper at $E_b/N_0 = 6$dB and $E_b/N_0 = 4$dB, respectively, while the mesh of rectangles represents the outer MAP decoder's EXIT characteristics. Observe in Figure 3.25 that there is no iteration gain at $E_b/N_0 = 4$dB, since the EXIT plane is trapped below the MAP decoder's plane. By contrast, at $E_b/N_0 = 6$dB we are able to obtain an open tunnel between the two EXIT planes, which eventually reaches the point of decoding convergence at $(1, 1, 1)$. Note that the trajectory evolves between the two planes and the *a priori* knowledge extracted from the associated information bits affects the *extrinsic* information as opposed to the MLC scheme characterised in Figure 3.18 to 3.20. More explicitly, with the aid of the precoder's *a priori* information, the trajectory no longer evolves in parallel to the y axis, as seen in Figures 3.18, 3.19 and 3.20, but instead it evolves in an angle as a function of both I^i_A (x axis) and $I^i_{A(o)}$ (y axis), as shown in the

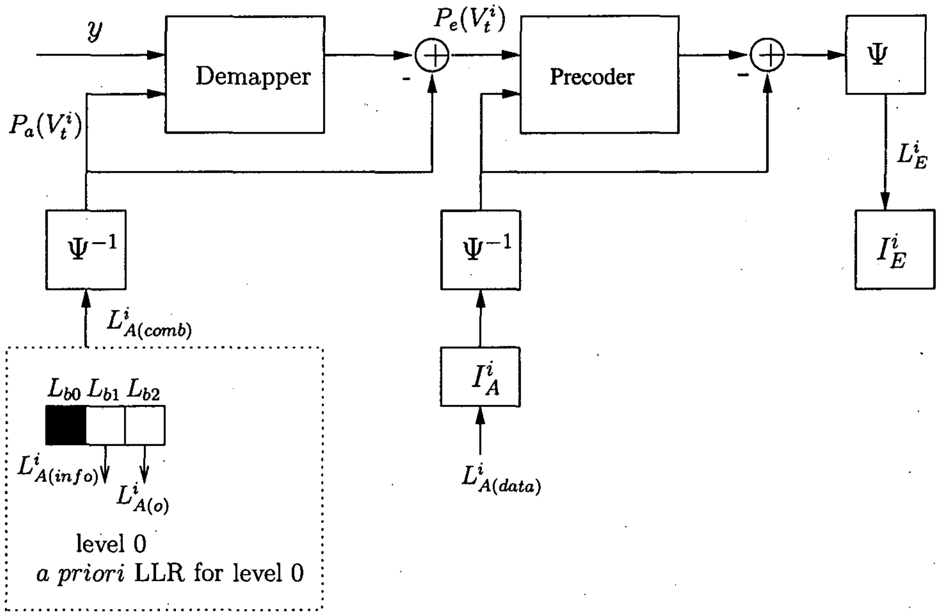

Figure 3.24: EXIT chart generation for the MSD MLC scheme of Figure 3.21, when using 8PSK and three en(de)coders.

dotted section of the trajectory seen in Figure 3.25. We now continue our discourse by introducing the precoder in the PID aided MLC scheme shown in Figure 2.8.

3.4.3 Simulation Results

In this section we characterise the BER performance of the precoder-aided iterative MLC scheme of Figure 3.21 and 3.22 using 8PSK as well as Ungerböck Partition (UP) [51] based mapping. Figure 3.26 shows the attainable BER versus E_b/N_0 performance, when communicating over an AWGN channel. The precoder-aided MLC scheme of Figure 3.21 is outperformed by the MLC scheme at an E_b/N_0 below 5dB. This is, because the precoded scheme does not exhibit any iteration gain for E_b/N_0 below 4dB, as shown in the 3-D EXIT plane of Figure 3.25 with the aid of the plane indicated by the dotted dashed lines. Once the EXIT plane has an open tunnel at the higher E_b/N_0 of 6dB, the associated BER performance is substantially improved, with the advent of introducing precoder as observed in Figure 3.26. Note that the precoder-aided scheme exhibits a 'turbo-like' behaviour in Figure 3.26 and exhibits no error floor, as opposed to the conventional MLC scheme. A more significant BER performance improvement can be observed in Figure 3.27, when communicating over an uncorrelated Rayleigh fading channel.

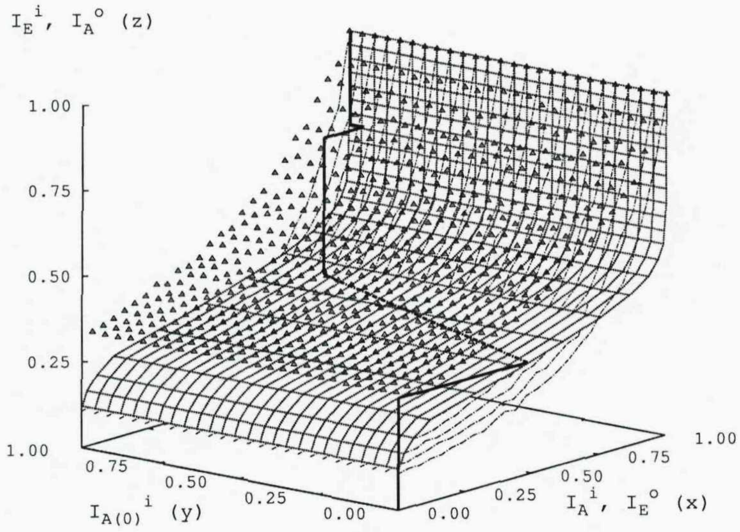

Figure 3.25: 3-D EXIT chart for protection level 0 of the precoder-aided MLC scheme of Figure 3.21 at $E_b/N_0 = 4$dB (dotted dashed lines) and $E_b/N_0 = 6$dB (mesh of triangles).

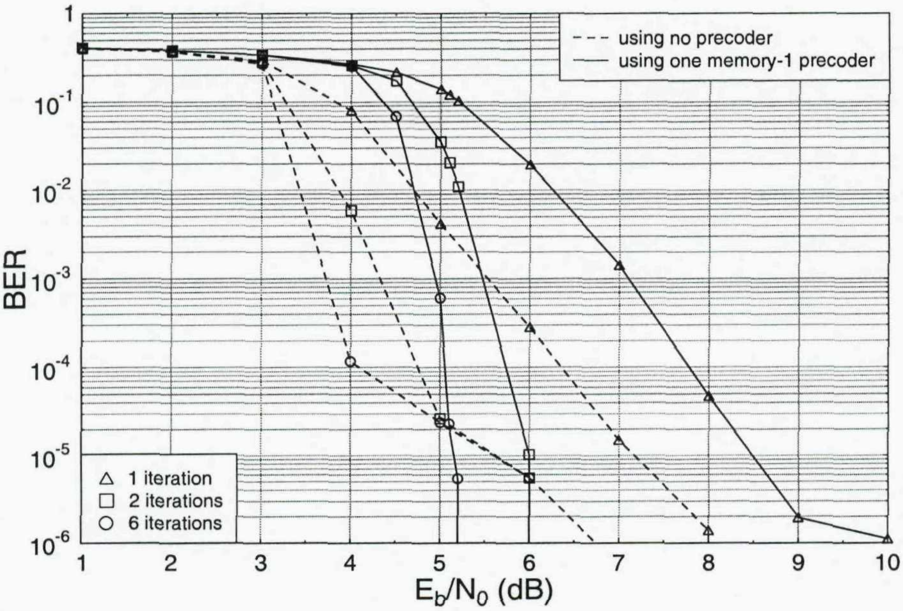

Figure 3.26: BER versus E_b/N_0 performance of the conventional and precoder-aided 8PSK modulated MLC MSD scheme of Figure 3.21, communicating over an AWGN channel.

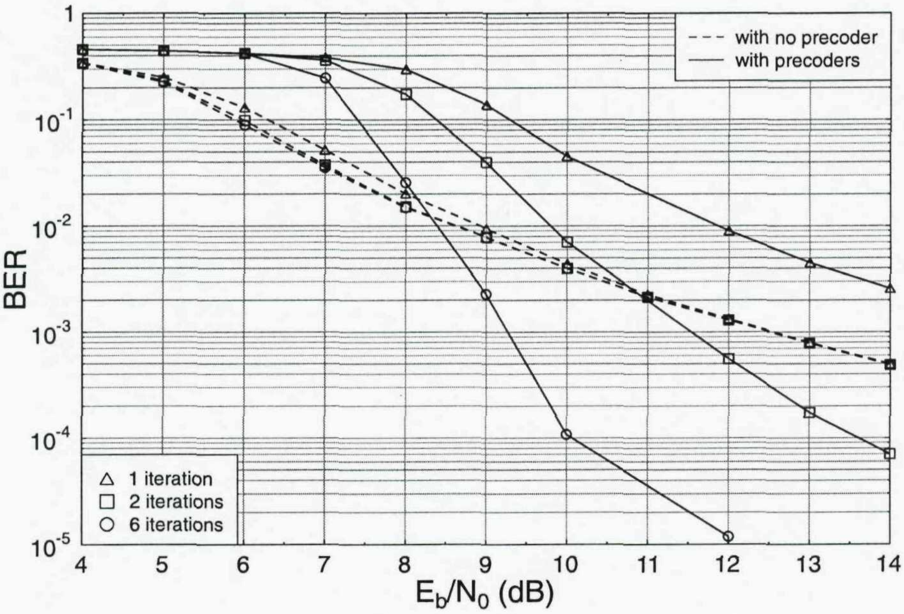

Figure 3.27: BER versus E_b/N_0 performance of both conventional and precoder-aided 8PSK modulated MLC MSD scheme of Figure 3.21, communicating over uncorrelated Rayleigh channel.

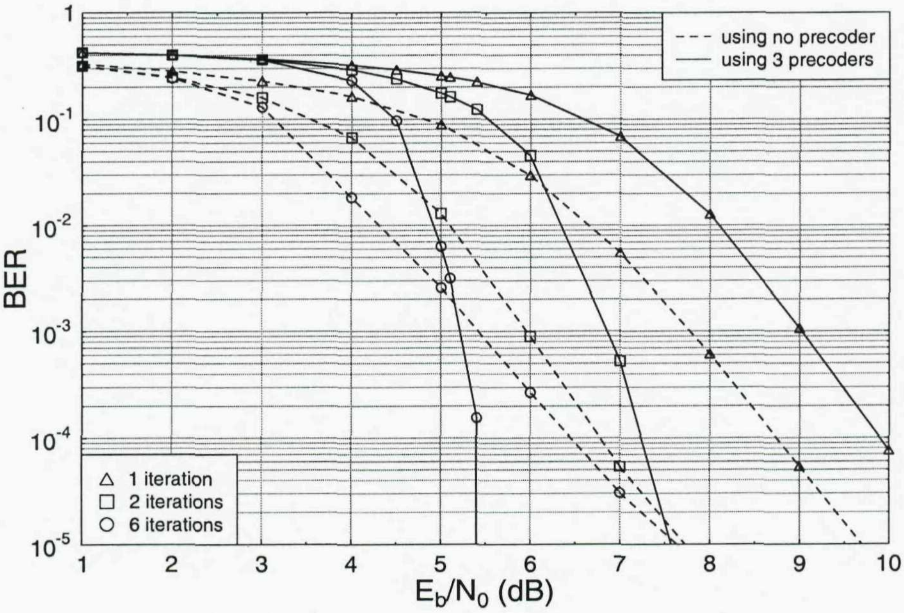

Figure 3.28: BER versus E_b/N_0 performance of both conventional and precoder-aided 8PSK modulated MLC PID scheme of Figure 3.22, communicating over AWGN channel.

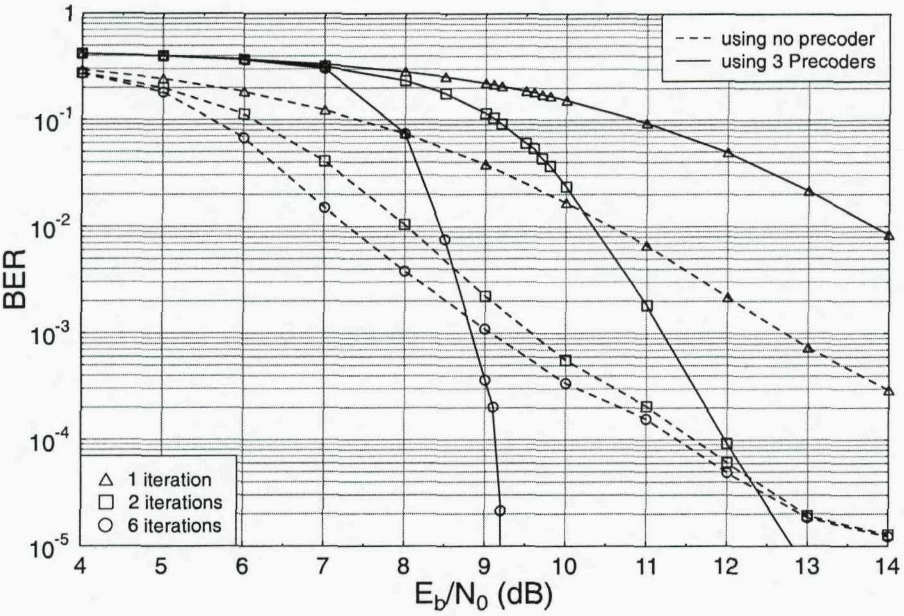

Figure 3.29: BER versus E_b/N_0 performance of both conventional and precoder-aided 8PSK modulated MLC PID schemes of Figure 3.22, communicating over uncorrelated Rayleigh channels.

Figures 3.28 and 3.29 illustrate the attainable BER performance of the precoder-aided MLC PID scheme communicating over both AWGN and uncorrelated Rayleigh fading channels. At BER $= 10^{-5}$, the precoder-aided MLC scheme exhibits a significant coding advantage of about 2dB in AWGN channels and about 5dB in uncorrelated Rayleigh channels. Note that PID becomes capable of outperforming MSD in the precoder-aided MLC scheme, as the benefit of its higher iteration gain. This is due to the fact that the decision errors of the lower protection levels may spread to the higher levels in MSD. Furthermore, UP-based mapping, which maximises the Euclidean distance of phasor constellation points for the sake of obtaining an iteration gain, performs better in AWGN channels. In Figure 3.30, we further compare the precoder-aided MLC PID scheme to other coded modulation schemes having the same expressed complexity in terms of the number of trellis states and communicating over uncorrelated Rayleigh fading channels. Our precoder-aided MLC scheme exhibits a better BER performance associated with a coding advantage of 2.5dB at BER$=10^{-5}$ compared to the best-performing BICM-ID coded modulation scheme, although it is outperformed by TTCM, both of which were detailed in [65].

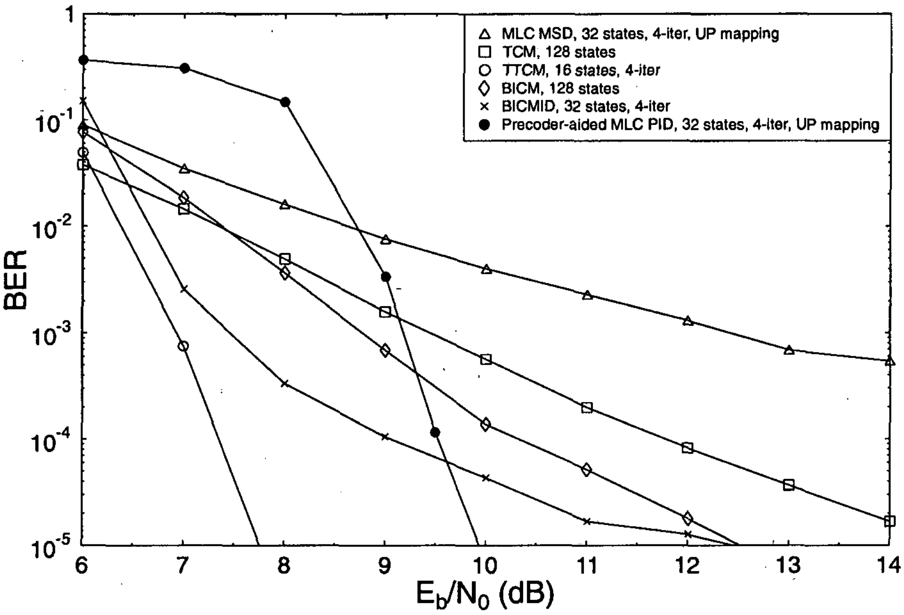

Figure 3.30: BER versus E_b/N_0 performance of various coded modulation schemes of Figures 3.1 and 3.22 having MAP decoding complexity associated with 128-trellis states, when communicating over uncorrelated Rayleigh channels using 8PSK modulation. The system parameters are summarised in Tables 3.5 and 3.6.

3.5 Chapter Conclusions

In conclusion, this chapter presented a comparative study of a diverse coded modulation schemes, namely of MLC, BICM, BICM-ID, TCM and TTCM. The TTCM scheme was shown to outperform the other schemes at a given implementational complexity associated with a total of 128 trellis states. Even though the performance of TCM may become better than that of BICM in conjunction with an increased complexity of 128 trellis states, it is outperformed by the iterative schemes of MLC and BICM-ID, both of which have a coding advantage close to 1dB. Of all classic coded modulation schemes, only MLC has the strength of added benefit of UEP capability and its average performance is similar to that of the BICM-ID scheme.

Our 3-D EXIT chart designed for MSD provides an efficient prediction of the joint iterative decoding performance of the inner demapper and outer decoder. This novel 3-D EXIT analysis provides an insight into the iterative decoding convergence behaviour of MLC MSD schemes. The decoding trajectory traverses between the 3-D EXIT planes, enabling us to improve the characteristics of both the MLC component codes as well as the demapper without carrying out bit-by-bit simulations.

Based on the 3-D EXIT charts, we proposed a recursive precoder for the sake of improving the demapper's EXIT characteristics. We employed 3-D EXIT charts for the sake of investigating the iterative convergence of precoder-aided MLC schemes. Our simulation results outlined in Figures 3.26, 3.27, 3.28 and 3.29 illustrate that the precoder-aided iterative MLC scheme achieves a significant BER performance improvement both in AWGN and uncorrelated Rayleigh channels. This was achieved without reducing the overall coding rate and without significantly increasing the complexity of the conventional MLC scheme. At BER $= 10^{-5}$ the precoder was capable of enhancing the achievable E_b/N_0 performance by 0.5dB and 5dB, when communicating over AWGN and Rayleigh channels, respectively.

Chapter 4

Sphere Packing Aided Space Time MLC/BICM Design*

4.1 Introduction

In Chapter 3 we introduced the concept of EXIT chart analysis and applied it to both MLC and BICM-ID schemes in Section 3.3.2. A precoder was also invoked by the modulator in order to achieve a better convergence behaviour for the system. It was shown in [96–98] that the bit-to-symbol mapping plays an integral part in enhancing the attainable coded modulation performance. Signal mapping entails the design process of assigning the bits to the signal constellation set. Various carefully designed 2-Dimensional (2-D) and Multi-Dimensional (M-D) bit-to-symbol mapping schemes have been proposed in the literature in order to improve the achievable BER performance [31, 32, 99].

In order to further improve the performance of this MLC scheme, a useful transmit diversity gain can be obtained by introducing Alamouti's Space Time Block Codes (STBC) [100]. Alamouti's concept of STBC was further generalised to an arbitrary number of transmitters by Tarokh *et al.* [101], but no attempt was made in [100] and [101] to jointly optimise the space-time signal design of the two consecutive time-slots and two transmit antennas. In order to jointly design the space-time signals of the transmit antennas, here we employ a novel Sphere Packing (SP) modulation scheme combined with orthogonal transmit diversity design, which was introduced by

---

*Part of this chapter is based on the collaborative research outlined in [43, 44, 47, 48].

Su *et al.* [102].

Alamri *el al.* developed a soft-bit turbo-detection sphere packing [102] aided concatenated STBC design [103, 104] for the sake of obtaining an iterative gain by exchanging extrinsic information with an outer decoder. Motivated by the substantial performance improvement reported [103,104], we combine the SP concept with a MLC scheme in order to create an improved orthogonal transmit diversity design. The minimum Euclidean Distance (ED) of symbols defined in an M-D space may be maximised by finding the most meritorious mapping of the bits to the signalling constellation.

Due to the complex nature of the bit-to-SP symbol mapping in M-D SP modulation, we adopt a Cost Function (CF) in term of Euclidean distances between different constellation points to be minimised by the Binary Switching Algorithm (BSA) [97]. The SP multilayer constellation points are further designed with a combination of different layers with maximum minimum Euclidean distance. The mapping can again be optimised by applying BSA for obtaining the minimum CF. The M-D modulated symbols are then fed into the STBC encoder. We term this scheme as a Space-Time Block Code Sphere Packed MultiLevel Coded modulation (STBC-SP-MLC) arrangement.

The equivalent capacity rules [51] have been proposed for conventional 1-D and 2-D modulated signal constellations for transmission over AWGN as well as Rayleigh fading channels as described in Section 2.2.2. In this chapter, we further extend these concepts for the sake of improving the design of our STBC-SP-MLC scheme, invoking a 4-Dimensional (4-D) SP constellation. More explicitly, the equivalent capacity design [51] will be further developed for determining the optimum LDPC constituent code rates of the STBC-SP-MLC scheme in conjunction with various bit-to-SP-symbol mapping strategies in the 4-D SP space. To deepen our discourse on Unequal Error Protection (UEP), we propose a new *hybrid* partitioning for our novel STBC-SP-MLC scheme in conjunction with a particular CF. The BSA is utilised for obtaining the optimum arrangement of the various mapping schemes. The BER performance of the individual MLC protection classes of the amalgamated MLC scheme as well as of the UEP *hybrid* scheme will be evaluated by computer simulations, when invoking the optimum LDPC coding rates.

Bit-Interleaved Space-Time Coded Modulation using Iterative Decoding (BI-STCM-ID) has also been proposed for obtaining both space and time diversity [29,33]. In this chapter, we propose a novel Space-Time Block Coded Sphere Packed Bit-Interleaved

Coded Modulation (STBC-SP-BICM) arrangement which is a new multidimensional BI-STCM-ID scheme invoking SP modulation. We investigate the new SP constellation and mapping scheme in comparison to the identical-throughput conventional QPSK and 16QAM schemes. Finally, a unity-rate precoder [79] is amalgamated with the SP mapper for the sake of improving the attainable iterative gain.

4.2 Space Time Block Code

An efficient twin antenna transmitter design was proposed by Alamouti [100], which is referred to as an STBC. The STBC encoder is preceded by a modulator, which groups B information bits into an M-ary modulated symbol, giving $B = \log_2 M$. At the encoder, the block of two consecutive symbols x_1, x_2 is mapped to the STBC symbols according to the generator matrix of

$$\mathbf{G}_2(x_1, x_2) = \begin{bmatrix} x_1 & x_2 \\ -x_2^* & x_1^* \end{bmatrix}, \tag{4.1}$$

where the rows and columns represent the temporal and spatial dimensions associated with two consecutive time slots and two transmit antennas. In other words, the rows of the generator matrix represent time slots, while the columns represent transmit antennas. The symbol x_i^* is the conjugate of x_i. During the first time slot, the symbols x_1 and x_2 are simultaneously transmitted by the first and second antenna, respectively. During the second time slot, the symbol $-x_2^*$ and x_1^* are transmitted by the first and second antenna, simultaneously. Encoding is carried out both in the spatial and time domains, as seen in Table 4.1.

	antenna 1	antenna 2
time slot t	x_1	x_2
time slot $t+1$	$-x_2^*$	x_1^*

Table 4.1: Encoding and transmission sequence for the twin-antenna STBC.

Figure 4.1 shows a two-transmit-antenna, one-receive-antenna STBC scheme [100], where Tx represents the transmit antenna and Rx the receive antenna. Let $h_1(t)$ and $h_2(t)$ represent the complex-valued fading channel coefficients of the first transmitter and second transmitter at time instant t. Alamouti's model assumes that the channel coefficients remain constant over two consecutive time slots and can be expressed as

$$h_1(t) = h_1(t+1) = h_1 = |h_1|e^{j\theta_1}, \tag{4.2}$$

$$h_2(t) = h_2(t+1) = h_2 = |h_2|e^{j\theta_2}, \tag{4.3}$$

where h_i and θ_i, $i = 1, 2$, are the amplitude and phase shift of the complex-valued channel coefficient for the path spanning from transmit antenna i to the receiver antenna.

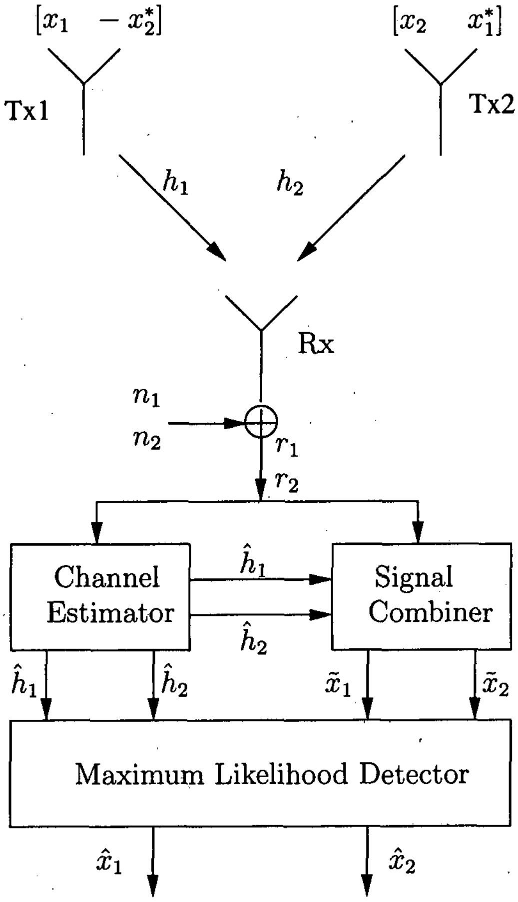

Figure 4.1: Two-transmit-antenna, one-receive-antenna STBC.

The signal received at the receive antenna over the two consecutive time slots t and $t+1$ can be represented by r_1 and r_2. These can be further expressed as

$$r_1 = h_1x_1 + h_2x_2 + n_1, \tag{4.4}$$

$$r_2 = -h_1x_2^* + h_2x_1^* + n_2, \tag{4.5}$$

where n_1 and n_2 are independent complex-valued AWGN having a zero mean and a power spectral density of $N_0/2$ per dimension at time t and $t+1$, respectively.

The channel estimator gives the estimated channel's fading coefficient $\hat{h}_1$ and $\hat{h}_2$ at the receiver. The Channel State Information (CSI) enables the receiver to enhance its performance, with the aid of its knowledge of both $\hat{h}_1$ and $\hat{h}_2$. Referring to Alamouti's model, we assume having a perfect CSI, which provides the correct values of h_1 as well as h_2. Hence associated decision statistics constructed by combining the received signals r_1 and r_2 with the aid of the perfectly estimated CSI is given by [100]

$$\tilde{x}_1 = h_1^* r_1 + h_2 r_2^*, \tag{4.6}$$

$$\tilde{x}_2 = h_2^* r_1 - h_1 r_2^*. \tag{4.7}$$

To further expand these two equations, the expression of r_1 and r_2 in Equations (4.4) and (4.5) can be substituted into Equations (4.6) and (4.7) as follows

$$\tilde{x}_1 = (|h_1|^2 + |h_2|^2)x_1 + h_1^* n_1 + h_2 n_2^*, \tag{4.8}$$

$$\tilde{x}_2 = (|h_1|^2 + |h_2|^2)x_2 - h_1 n_2^* + h_2^* n_1. \tag{4.9}$$

The combined received signals $\tilde{x}_1$ and $\tilde{x}_2$ are then passed to the maximum likelihood detector, which decides on the specific pair of signals $(\hat{x}_1, \hat{x}_2)$ that minimises the distance metric of

$$d^2(r_1, h_1\hat{x}_1 + h_2\hat{x}_2) + d^2(r_2, -h_1\hat{x}_2^* + h_2\hat{x}_1^*), \tag{4.10}$$

over the legitimate values of $\hat{x}_1$ and $\hat{x}_2$. More explicitly, the term $d^2(x, y)$ denotes the squared Euclidean distance between two complex-valued signals x and y, which can be calculated as

$$d^2(x, y) = (x - y)(x^* - y^*). \tag{4.11}$$

Using Equation (4.11), the decision criterion of Equation (4.10) can be expanded as follows

$$\begin{aligned}
&d^2(r_1, h_1\hat{x}_1 + h_2\hat{x}_2) + d^2(r_2, -h_1\hat{x}_2^* + h_2\hat{x}_1^*) \\
&\qquad = (r_1 - h_1\hat{x}_1 - h_2\hat{x}_2)(r_1^* - h_1^*\hat{x}_1^* - h_2^*\hat{x}_2^*) \\
&\qquad + (r_2 + h_1\hat{x}_2^* - h_2\hat{x}_1^*)(r_2^* + h_1^*\hat{x}_2 - h_2^*\hat{x}_1) \\
&\qquad = (|h_1|^2 + |h_2|^2)(|\hat{x}_1|^2 + |\hat{x}_2|^2) \\
&\qquad - h_1^* r_1 \hat{x}_1^* - h_2 r_2^* \hat{x}_1^* - h_1 r_1^* \hat{x}_1 - h_2^* r_2 \hat{x}_1 \\
&\qquad - h_2^* r_1 \hat{x}_2^* + h_1 r_2^* \hat{x}_2^* - h_2 r_1^* \hat{x}_2 + h_1^* r_2 \hat{x}_2 \\
&\qquad + |r_1|^2 + |r_2|^2.
\end{aligned} \tag{4.12}$$

Let us further introduce the squared distance $d^2(\tilde{x}_1, \hat{x}_1)$ and $d^2(\tilde{x}_2, \hat{x}_2)$ using Equations (4.6) and (4.7), resulting in the following expressions

$$\begin{aligned}
d^2(\tilde{x}_1, \hat{x}_1) &= (\tilde{x}_1 - \hat{x}_1)(\tilde{x}_1^* - \hat{x}_1^*) \\
&= |\hat{x}_1|^2 + |\tilde{x}_1|^2 - h_1^* r_1 \hat{x}_1^* - h_2 r_2^* \hat{x}_1^* - h_1 r_1^* \hat{x}_1 - h_2^* r_2 \hat{x}_1,
\end{aligned} \tag{4.13}$$

and

$$\begin{aligned}
d^2(\tilde{x}_2, \hat{x}_2) &= (\tilde{x}_2 - \hat{x}_2)(\tilde{x}_2^* - \hat{x}_2^*) \\
&= |\hat{x}_2|^2 + |\tilde{x}_2|^2 - h_2^* r_1 \hat{x}_2^* + h_1 r_2^* \hat{x}_2^* - h_2 r_1^* \hat{x}_2 + h_1^* r_2 \hat{x}_2.
\end{aligned} \tag{4.14}$$

We then substitute Equations (4.13) and (4.14) into Equation (4.12). All the terms that are not functions of $\hat{x}_1$ and $\hat{x}_2$ are omitted. Finally, the decision criterion at the output of maximum likelihood decoder can be expressed as

$$(\hat{x}_1, \hat{x}_2) = \arg \min_{(\hat{x}_1, \hat{x}_2) \in \mathbb{X}} (|h_1|^2 + |h_2|^2 - 1)(|\hat{x}_1|^2 + |\hat{x}_2|^2) + d^2(\tilde{x}_1, \hat{x}_1) + d^2(\tilde{x}_2, \hat{x}_2), \tag{4.15}$$

where $\mathbb{X}$ is the set of all possible modulated symbol pairs $(\hat{x}_1, \hat{x}_2)$.

Since the decision rule concerning $\tilde{x}_i$ depends only on $x_i = 1, 2$, we can separate the maximum likelihood decoding rule of Equation (4.15) into two independent decoding criteria for x_1 and x_2 as follows

$$\hat{x}_1 = \arg \min_{\hat{x}_1 \in \mathbb{Z}} \left[(|h_1|^2 + |h_2|^2 - 1)|\hat{x}_1|^2 + d^2(\tilde{x}_1, \hat{x}_1) \right] \tag{4.16}$$

$$\hat{x}_2 = \arg \min_{\hat{x}_2 \in \mathbb{Z}} \left[(|h_1|^2 + |h_2|^2 - 1)|\hat{x}_2|^2 + d^2(\tilde{x}_2, \hat{x}_2) \right], \tag{4.17}$$

where $\mathbb{Z}$ represents the legitimate constellation set. If we consider the specific case of M-PSK modulated signal constellations, the amplitude of all legitimate modulated signals, $\hat{x}_i$, $i = 1, 2$ is constant. This leads to the following simplification

$$\begin{aligned} \hat{x}_1 &= \arg\min_{\hat{x}_1 \in \mathbb{Z}} d^2(\tilde{x}_1, \hat{x}_1), && (4.18) \\ \hat{x}_2 &= \arg\min_{\hat{x}_2 \in \mathbb{Z}} d^2(\tilde{x}_2, \hat{x}_2). && (4.19) \end{aligned}$$

Equations (4.8) and (4.9) also shows mathematically that if the fading coefficient is small for one of the two taps h_i owing to a deep magnitude fade, it is possible that the other coefficient is high, as a benefit of their independent fading characteristics. Hence, a twin-antenna design is capable of providing spatial or transmit diversity, in order to obtain a better decoding performance.

4.3 Orthogonal G$_2$ Design Using Sphere Packing

Let us now provide a rudimentary introduction to SP [105], which is a powerful modulation scheme that jointly designs the SP symbols of the two time-slots and two antennas of an STBC scheme. The concept of introducing sphere packing in the context of orthogonal transmit-diversity designs was introduced by Su *et al.* [102]. Alamri *et al.* further extended the design to a turbo detection aided iterative scheme [104,106].

The G$_2$ generator matrix was outlined in Equation (4.1). Referring to the original G$_2$ design [100], x_1 and x_2 denotes the conventional Binary Phase Shift Keying (BPSK) modulated symbols mapped to the first and second transmit antennas of the STBC transmitter during the first time slot while the conjugates $-x_2^*$ and x_1^* are transmitted during the second time slot. The original contribution [100] made no effort to jointly design the signal constellation for x_1 and x_2 at the two transmit antennas across the two time-slots.

For M number of SP modulated symbols, there are M legitimate space-time signals $\mathrm{G}_2(x_{q,1}, x_{q,2})$, where we have $q = 0, 1, ..., M-1$. The transmitter will select the modulated signal from these M legitimate symbols to be transmitted over the two antennas across two consecutive time slots. This implies that the throughput of the system is given by $\log_2 M/2$ bits per channel use. Since the SP symbol is designed for the joint space-time symbol using both $x_{q,1}$ and $x_{q,2}$ on the basis of maximising the minimum Euclidean distance from all other $(M-1)$ legitimate symbols, this system results in the minimum SP symbol error probability [102].

Let us now consider a 4-D SP scheme having phasor points of $(a_{q,1}, a_{q,2}, a_{q,3}, a_{q,4})$, $q = 0, 1, ..., M-1$. These phasor points belong to the real-valued Euclidean space $\mathbb{R}^4$, where each $a_{q,d}$, $d = 1, 2, 3, 4$, provides a coordinate point for the two time-slot's complex-valued phasor points. The complex-valued symbol $x_{q,1}$ and $x_{q,2}$ can be further expressed as

$$\begin{aligned} \{x_{q,1}, x_{q,2}\} &= T_{sp}(a_{q,1}, a_{q,2}, a_{q,3}, a_{q,4}), \\ &= \{a_{q,1} + ja_{q,2}, a_{q,3} + ja_{q,4}\}, \end{aligned} \tag{4.20}$$

where the SP mapping function T_{sp} maps the SP symbols $(a_{q,1}, a_{q,2}, a_{q,3}, a_{q,4})$ to the original complex-valued QPSK symbols $x_{q,1}$ and $x_{q,2}$, for $q = 0, 1, ..., (M-1)$. Figures 4.2 and 4.3 illustrate the M legitimate 2-D complex vectors and 4-D real-valued vectors for $\mathbf{G}_2$ space-time signals, respectively.

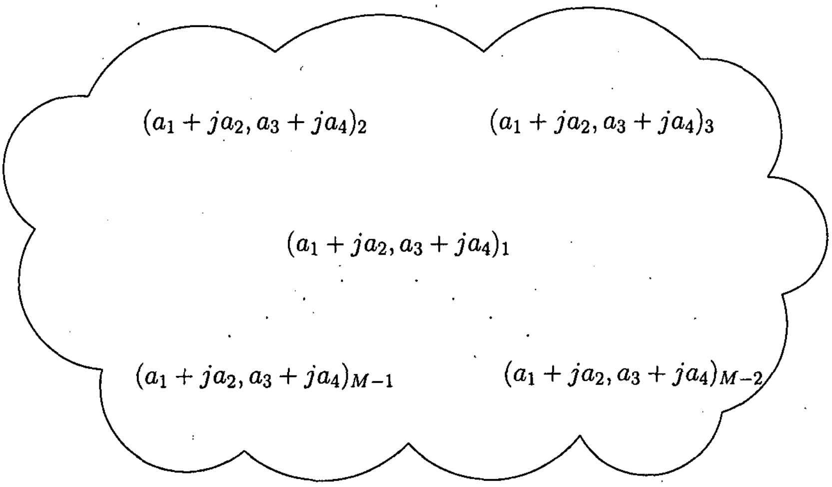

Figure 4.2: The M legitimate 2-dimensional complex vectors for $\mathbf{G}_2$ space-time signals [107].

A 4-D SP symbol is based on the lattice D_4, which is defined in [105] as a lattice having the best Euclidean distance from all other $(M-1)$ legitimate constellation points in the real-valued Euclidean space $\mathbb{R}^4$. In other words, D_4 is defined as a lattice that consists of all legitimate SP constellation points having integer coordinates of $(a_{q,1}, a_{q,2}, a_{q,3}, a_{q,4})$, $q = 0, 1, ..., M-1$, uniquely describing the M legitimate combinations of the two time-slot's complex-valued QPSK symbols in Alamouti's design. However, these unique points are subject to the SP constraint of [105]

$$a_{q,1} + a_{q,2} + a_{q,3} + a_{q,4} = k_q, \qquad q = 0, \dots, M-1, \tag{4.21}$$

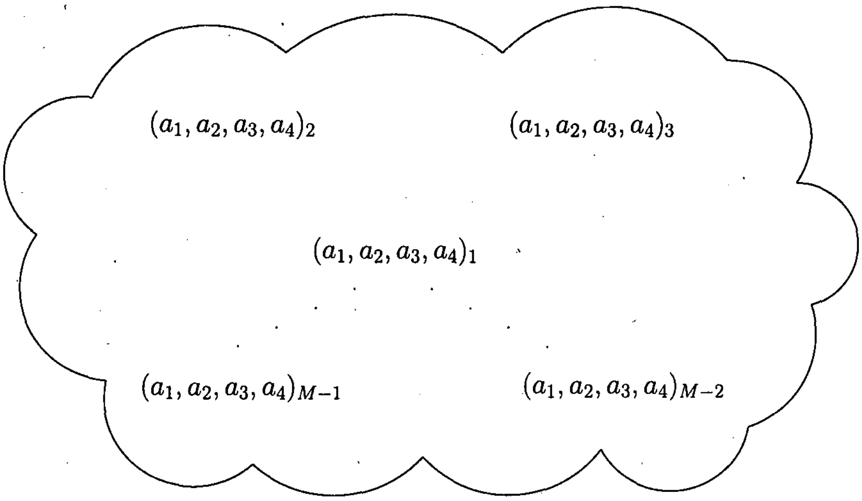

Figure 4.3: The M legitimate 4-dimensional real-valued vectors for $\mathbf{G}_2$ space-time signals [107].

where k_q is an even integer value.

Let us assume that the SP symbol set $\mathbb{Z} = \{\mathbf{s}^q = [a_{q,1}\ a_{q,2}\ a_{q,3}\ a_{q,4}] \in \mathbb{R}^4 : 0 \leq q \leq M-1\}$ selected from the lattice D_4, which is constituted by a set of M legitimate constellation points having a total energy of

$$E_{\text{total}} \triangleq \sum_{q=0}^{M-1} (|a_{q,1}|^2 + |a_{q,2}|^2 + |a_{q,3}|^2 + |a_{q,4}|^2). \tag{4.22}$$

Furthermore, we introduce the space-time signals

$$\begin{aligned} \mathbf{C}_q &= \sqrt{\frac{2M}{E_{\text{total}}}} \mathbf{G}_2(x_{q,1}, x_{q,2}), \\ &= \sqrt{\frac{2M}{E_{\text{total}}}} \mathbf{G}_2(a_{q,1} + ja_{q,2}, a_{q,3} + ja_{q,4}), \qquad q = 0, \ldots, M-1, \end{aligned} \tag{4.23}$$

which constitute a set of $\{\mathbf{C}_q{:}0 \leq q \leq M-1\}$ whose diversity products depends on the minimum Euclidean distance of the M legitimate modulated symbols in $\mathbb{Z}$.

The normalisation factor $\sqrt{2M/E_{\text{total}}}$ used in Equation (4.23) is introduced to ensure that the space-time signal of Equation (4.23) satisfies the energy constraint of Equation (4.22). To elaborate a little further, let us consider the general space time signal, expressed in the following $(T \times N_t)$-dimensional matrix [108]

$$\mathbf{C} = \begin{bmatrix} c_1^1 & c_1^2 & \cdots & c_1^{N_t} \\ c_2^1 & c_2^2 & \cdots & c_2^{N_t} \\ \vdots & \vdots & \ddots & \vdots \\ c_T^1 & c_T^2 & \cdots & c_T^{N_t} \end{bmatrix}_{T \times N_t}, \tag{4.24}$$

where the space-time signal is transmitted over N_t transmit antennas mapped to T time slots. The notation c_t^i represents the symbols transmitted by transmit antenna i, for $i = 1, 2, ..., N$ in time slot t, for $t = 1, 2, ..., T$. The energy constraint for the corresponding space time signals is given by

$$E\big[||\mathbf{C}||_F^2\big] = N_t T, \tag{4.25}$$

where $E[\cdot]$ refers to the expected value and $||\mathbf{C}||_F$ is the Frobenius norm of $\mathbf{C}$ [109], which can be written as

$$||\mathbf{C}||_F^2 = \mathrm{tr}(\mathbf{C}^{\mathcal{H}}\mathbf{C}) = \mathrm{tr}(\mathbf{C}\mathbf{C}^{\mathcal{H}}) = \sum_{t=1}^{T}\sum_{i=1}^{N_t} |c_t^i|^2, \tag{4.26}$$

where $(.)^{\mathcal{H}}$ denotes the complex conjugate transpose of a matrix and tr(.) denotes the trace of a matrix. Having outlined the general form of the space-time signal matrix, we now consider the specific space-time signal of Equation (4.23), which can be written in the following form

$$\mathbf{C}_q = n_f \begin{bmatrix} x_{q,1} & x_{q,2} \\ -x_{q,2}^* & x_{q,1}^* \end{bmatrix}. \tag{4.27}$$

The notation n_f represents a normalisation factor to be used in Equation (4.23). By referring to Equation (4.26), the energy of the space-time signal in Equation (4.27) can be expressed as

$$\begin{aligned} E\big[||\mathbf{C}_q||_F^2\big] &= E\big[\, n_f^2 \cdot \big(|x_{q,1}|^2 + |x_{q,2}|^2 + |x_{q,2}^*|^2 + |x_{q,1}^*|^2\big) \,\big] \\ &= 2 \cdot n_f^2 \cdot E\big[|x_{q,1}|^2 + |x_{q,2}|^2\big] \\ &= 2 \cdot n_f^2 \cdot E\big[|a_{q,1}|^2 + |a_{q,2}|^2 + |a_{q,3}|^2 + |a_{q,4}|^2\big]. \end{aligned} \tag{4.28}$$

Equation (4.22) shows that the average energy of a single SP symbol can be expressed as

$$E\big[|a_{q,1}|^2 + |a_{q,2}|^2 + |a_{q,3}|^2 + |a_{q,4}|^2\big] = \frac{E_{\text{total}}}{M}. \tag{4.29}$$

Upon substituting Equation (4.29) into Equation (4.28), we arrive at

$$\begin{aligned} E[\|\mathbf{C}_q\|_F^2] &= 2 \cdot n_f^2 \cdot \frac{E_{\text{total}}}{M} \\ &= T \cdot N_t \qquad \text{(from Equation(4.25))} \\ &= 2 \cdot 2 = 4. \end{aligned} \tag{4.30}$$

Hence, we finally obtain the normalisation factor n_f in Equation (4.23) as follows

$$n_f = \sqrt{\frac{2M}{E_{\text{total}}}}. \tag{4.31}$$

To further illustrate the SP concept, we now consider an $M = 16$ scheme in comparison to a conventional QPSK modulation scheme. Firstly, for $M = 16$ signal points, the G$_2$ encoder matrix can be represented as $\mathbf{G}_2(x_{q,1}, x_{q,2})$, $q = 0, \ldots, 15$. Let $S0$, $S1$, $S2$ and $S3$ represent four legitimate two-bit QPSK symbols each having $x_{q,1}$ and $x_{q,2}$ where $q = 0, 1, ..., 15$. The transmitter of this QPSK system is outlined in Figure 4.4. Secondly, we consider SP modulation using $M = 16$ points selected from the lattice D_4 having $(a_{q,1}, a_{q,2}, a_{q,3}, a_{q,4})$, where $q = 0, 1, ..., 15$. This is a real-valued SP representation of $x_{q,1}$ and $x_{q,2}$, which is further illustrated in Figure 4.5. The effective throughput and the associated transmission block sizes for different values of M are summarised in Table 4.2.

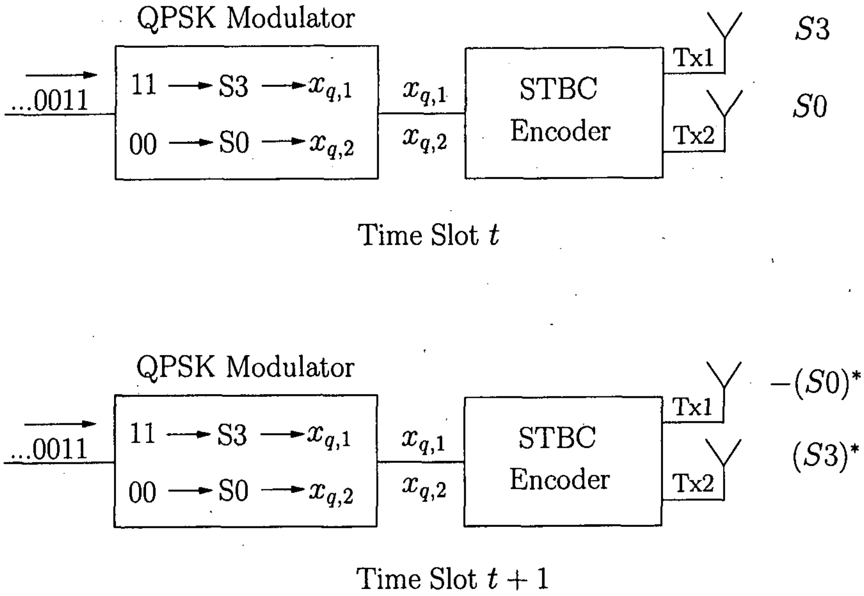

Figure 4.4: Transmission of two QPSK symbols over two consecutive time slots [107].

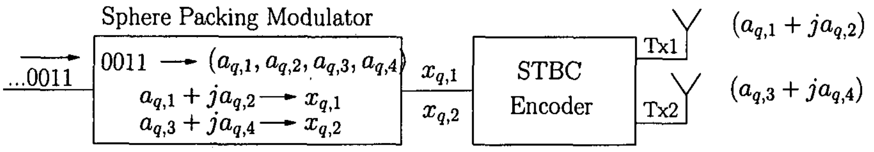

Time Slot t

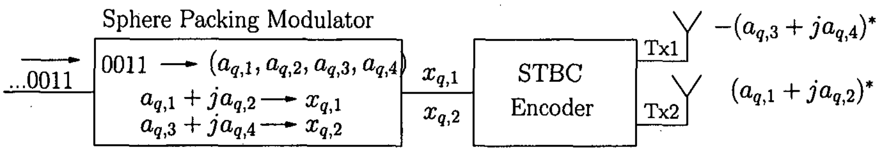

Time Slot $t + 1$

Figure 4.5: Transmission of a single SP symbol over two consecutive time slots [107].

M	Block Size (bits)	Throughput (b/s/Hz)
4	2	1
8	3	1.5
16	4	2
32	5	2.5
64	6	3
128	7	3.5
256	8	4
512	9	4.5
1024	10	5
2048	11	5.5
4096	12	6

Table 4.2: Throughput of SP aided $\mathbf{G}_2$ systems for different SP signal set sizes M.

4.3.1 SP Constellation Points

The normalisation factor n_f given in Equation (4.23) is $\sqrt{2M/E_{\text{total}}}$. This also implies that the orthogonal $\mathbf{G}_2$ space-time signal is multiplied by a factor, which is inversely proportional to $\sqrt{E_{\text{total}}}$. It is therefore desirable to choose a specific subset of M points from the entire signal set of legitimate points hosted by D_4, which gives the minimum total energy E_{total}, while maintaining a certain minimum distance amongst the SP points.

In the context of the lattice D_4, the legitimate constellation points are categorised into different layers based on their norms or energy, which is also the distance from the origin. Table 4.3 shows the first 10 layers of constellation points hosted by D_4, in which the origin of SP is located at layer-0 at the coordinate value of (0, 0, 0, 0). Taking Layer-1 as an example, there are a total of 24 legitimate constellation points having an identical minimum energy of $E = 2$. In other words, the SP symbol centred at the origin (0, 0, 0, 0), would have 24 minimum-distance or nearest-neighbour SP symbols around it. These layer-1 neighbours can each be represented by the coordinates of (+/-1, +/-1, 0, 0), where any choice of signs and any ordering of the coordinates is legitimate, as listed in Table 4.10. The resultant 24 legitimate symbols may be readily listed on the basis of these combinations. Figure 4.6 shows these 24 legitimate first-layer symbols hosted by the lattice D_4.

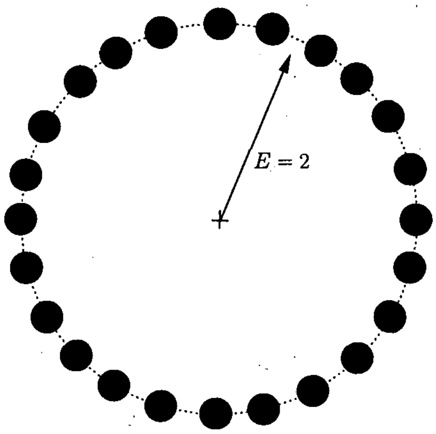

Figure 4.6: The 24 first-layer SP constellation points hosted by D_4 having the minimum energy of $E = 2$ [107].

Hence, for $M = 16$ SP scheme, a specific selection of 16 SP points is carried out from a total of 24 legitimate layer-1 SP symbols. An exhaustive computer search has to

Layer	Constellation Points				Norm	Number of Combinations
0	0	0	0	0	0	1
1	+/-1	+/-1	0	0	2	24
2	+/-2	0	0	0	4	8
	+/-1	+/-1	+/-1	+/-1	4	16
3	+/-2	+/-1	+/-1	0	6	96
4	+/-2	+/-2	0	0	8	24
5	+/-2	+/-2	+/-1	+/-1	10	96
	+/-3	+/-1	0	0	10	48
6	+/-3	+/-1	+/-1	+/-1	12	64
	+/-2	+/-2	+/-2	0	12	32
7	+/-3	+/-2	+/-1	0	14	192
8	+/-2	+/-2	+/-2	+/2	16	16
	+/-4	0	0	0	16	8
9	+/-4	+/-1	+/-1	0	18	96
	+/-3	+/-2	+/-2	+/-1	18	192
	+/-3	+/-3	0	0	18	24
10	+/-4	+/-2	0	0	20	48
	+/-3	+/-3	+/-1	+/-1	20	96

Table 4.3: The first 10 layers of D_4.

be implemented for determining the optimum choice of M, which possess the highest minimum Euclidean distance, hence minimising the SP-symbol error probability. The search for other layers can be extended to obtain different SP constellation points and will be further discussed later in Sections 4.5.3 and 4.6.2.

4.4 Iterative Demapping for Sphere Packing

An iterative demapping of the SP symbols has to be employed in order to exchange the soft-bit values with the soft input outer decoder for iterative decoding in the schematic of Figure 4.7. Referring to Figure 4.1 and assuming perfect CSI, the complex-valued channel output symbols generated after combining the signals of time-slots $\tilde{x}_1$ and $\tilde{x}_2$

are obtained, as shown in Equations (4.8) and (4.9). Here we denote the most likely transmitted symbols as $x_{q,1}$ as well as $x_{q,2}$ and hence we arrive at

$$\begin{aligned} \tilde{x}_1 &= (|h_1|^2 + |h_2|^2) \cdot x_{q,1} + \acute{n}_1, && (4.32) \\ \tilde{x}_2 &= (|h_1|^2 + |h_2|^2) \cdot x_{q,2} + \acute{n}_2, && (4.33) \end{aligned}$$

where h_1 and h_2 represent the complex-valued non-dispersive channel coefficients associated with the first and second transmit antennas, respectively. The notation $\acute{n}_1$ and $\acute{n}_2$ represents the zero-mean complex Gaussian random variables having a variance of $\sigma_{\acute{n}}^2 = (|h_1|^2 + |h_2|^2) \cdot \sigma_n^2$. From the SP-function T_{sp} of Equation (4.20), the received SP symbol $\mathbf{r}$ can be written as

$$\mathbf{r} = T_{sp}^{-1}(\tilde{x}_1, \tilde{x}_2), \tag{4.34}$$

where we have $\mathbf{r} = \{[\tilde{a}_1\ \tilde{a}_2\ \tilde{a}_3\ \tilde{a}_4] \in \mathbb{R}^4\}$. The received SP symbol $\mathbf{r}$ can be further expressed as

$$\mathbf{r} = h \cdot \sqrt{\frac{2M}{E_{\text{total}}}} \cdot \mathbf{s}^q + \mathbf{w}, \tag{4.35}$$

where $h = (|h_1|^2 + |h_2|^2)$, $\mathbf{s}^q \in \mathbb{Z}$, $0 \leq q \leq M-1$, and $\mathbf{w}$ is a 4-D real-valued Gaussian random variable having a covariance matrix of $\sigma_w^2 \cdot \mathbf{I}_{N_D} = \sigma_{\acute{n}}^2 \cdot \mathbf{I}_{N_D} = h \cdot \sigma_n^2 \cdot \mathbf{I}_{N_D}$. Since the symbol constellation set $\mathbb{Z}$ is four-dimensional, we have $N_D = 4$. Hence, we now compute the conditional PDF $p(\mathbf{r}|\mathbf{s}^q)$, which is given by

$$\begin{aligned} p(\mathbf{r}|\mathbf{s}^q) &= \frac{1}{(2\pi\sigma_w^2)^{\frac{N_D}{2}}} \exp\Big(-\frac{1}{2\sigma_w^2}(\mathbf{r} - \alpha \cdot \mathbf{s}^q)(\mathbf{r} - \alpha \cdot \mathbf{s}^q)^T\Big), \\ &= \frac{1}{(2\pi\sigma_w^2)^{\frac{N_D}{2}}} \exp\left(-\frac{1}{2\sigma_w^2}\left(\sum_{i=1}^{N_D}(\tilde{a}_i - \alpha \cdot a_{q,i})^2\right)\right), && (4.36) \end{aligned}$$

where $\alpha = h \cdot \sqrt{\frac{2M}{E_{\text{total}}}}$.

For an SP symbol $\mathbf{r}$ which carries B number of encoded binary bits $\mathbf{b} = (b_0, \ldots, b_{B-1})$, the LLR for bit b_k, $k = 0, 1, ..., B-1$ can be expressed as [76]

$$L(b_k|\mathbf{r}) = L_a(b_k) + \ln \frac{\sum_{\mathbf{s}^q \in Z_1^k} p(\mathbf{r}|\mathbf{s}^q) \cdot \exp\left(\sum_{j=0, j\neq k}^{B-1} b_j L_a(b_j)\right)}{\sum_{\mathbf{s}^q \in Z_0^k} p(\mathbf{r}|\mathbf{s}^q) \cdot \exp\left(\sum_{j=0, j\neq k}^{B-1} b_j L_a(b_j)\right)}, \tag{4.37}$$

where Z_1^k and Z_0^k are subsets of the symbol constellation $\mathbb{Z}$, so that $Z_1^k \triangleq \{\mathbf{s}^q \in \mathbb{Z} : b_k = 1\}$ and likewise, $Z_0^k \triangleq \{\mathbf{s}^q \in \mathbb{Z} : b_k = 0\}$. In other words, Z_i^k represents all SP symbols of the set $\mathbb{Z}$, where we have $b_k = i \in \{0, 1\}$, $k = 0, \ldots, B-1$. Equation (4.37) can be further expanded to

$$\begin{aligned} L(b_k|\mathbf{r}) &= L_a(b_k) + \ln \frac{\sum_{\mathbf{s}^q \in Z_1^k} \exp\left(-\frac{1}{2\sigma_w^2}(\mathbf{r} - \alpha \cdot \mathbf{s}^q)(\mathbf{r} - \alpha \cdot \mathbf{s}^q)^T + \sum_{j=0, j\neq k}^{B-1} b_j L_a(b_j) \right)}{\sum_{\mathbf{s}^q \in Z_0^k} \exp\left(-\frac{1}{2\sigma_w^2}(\mathbf{r} - \alpha \cdot \mathbf{s}^q)(\mathbf{r} - \alpha \cdot \mathbf{s}^q)^T + \sum_{j=0, j\neq k}^{B-1} b_j L_a(b_j) \right)} \\ &= L_A^M + L_E^M. \end{aligned} \tag{4.38}$$

We can use the max-log approximation [65] to simplify the computation of Equation (4.38) as follows

$$\begin{aligned} L(b_k|\mathbf{r}) = L_a(b_k) &+ \max_{\mathbf{s}^q \in Z_1^k} \left[-\frac{1}{2\sigma_w^2}(\mathbf{r} - \alpha \cdot \mathbf{s}^q)(\mathbf{r} - \alpha \cdot \mathbf{s}^q)^T + \sum_{j=0, j\neq k}^{B-1} b_j L_a(b_j) \right] \\ &- \max_{\mathbf{s}^q \in Z_0^k} \left[-\frac{1}{2\sigma_w^2}(\mathbf{r} - \alpha \cdot \mathbf{s}^q)(\mathbf{r} - \alpha \cdot \mathbf{s}^q)^T + \sum_{j=0, j\neq k}^{B-1} b_j L_a(b_j) \right]. \end{aligned} \tag{4.39}$$

4.4.1 Example of Iterative Decoding for $M = 4$

Let us now consider an example of the SP demapping scheme for $M = 4$ as an easy illustration of Equation (4.37). For four SP symbols, we obtain $\mathbf{s}^q$, where $q \in \{0, 1, 2, 3\}$. This corresponds to the bits b_k, $k = 0, 1$. The LLR-value of b_0 can be written as [107]

$$\begin{aligned} L(b_0|\mathbf{r}) &= \ln \frac{p(b_0 = 1|\mathbf{r})}{p(b_0 = 0|\mathbf{r})} \\ &= \ln \frac{p(b_0 = 1, b_1 = 0|\mathbf{r}) + p(b_0 = 1, b_1 = 1|\mathbf{r})}{p(b_0 = 0, b_1 = 0|\mathbf{r}) + p(b_0 = 0, b_1 = 1|\mathbf{r})}. \end{aligned} \tag{4.40}$$

To further extend Equation (4.40), we use Bayes' rule formulated as

$$p(X|Y) = \frac{p(Y|X) \cdot p(X)}{p(Y)}, \tag{4.41}$$

where X and Y are two random variables.

Hence, Equation (4.40) can be expressed with the aid of Equation (4.41) as

$$L(b_0|\mathbf{r}) = \ln \frac{p(\mathbf{r}|b_0 = 1, b_1 = 0) \cdot p(b_0 = 1, b_1 = 0) + p(\mathbf{r}|b_0 = 1, b_1 = 1) \cdot p(b_0 = 1, b_1 = 1)}{p(\mathbf{r}|b_0 = 0, b_1 = 0) \cdot p(b_0 = 0, b_1 = 0) + p(\mathbf{r}|b_0 = 0, b_1 = 1) \cdot p(b_0 = 0, b_1 = 1)}. \tag{4.42}$$

For ideal bit interleavers, b_0 and b_1 are independent of each other. Therefore, Equation (4.42) may be written as

$$\begin{aligned}
L(b_0|\mathbf{r}) &= \ln\frac{p(\mathbf{r}|b_0=1,b_1=0)\cdot p(b_0=1)\cdot p(b_1=0)\ +\ p(\mathbf{r}|b_0=1,b_1=1)\cdot p(b_0=1)\cdot p(b_1=1)}{p(\mathbf{r}|b_0=0,b_1=0)\cdot p(b_0=0)\cdot p(b_1=0)\ +\ p(\mathbf{r}|b_0=0,b_1=1)\cdot p(b_0=0)\cdot p(b_1=1)} \\
&= \ln\frac{p(b_0=1)}{p(b_0=0)}\ +\ \ln\frac{p(\mathbf{r}|b_0=1,b_1=0)\cdot p(b_1=0)\ +\ p(\mathbf{r}|b_0=1,b_1=1)\cdot p(b_1=1)}{p(\mathbf{r}|b_0=0,b_1=0)\cdot p(b_1=0)\ +\ p(\mathbf{r}|b_0=0,b_1=1)\cdot p(b_1=1)} \\
&= L_a(b_0)\ +\ \ln\frac{p(\mathbf{r}|b_0=1,b_1=0)\ +\ p(\mathbf{r}|b_0=1,b_1=1)\cdot\big(p(b_1=1)/p(b_1=0)\big)}{p(\mathbf{r}|b_0=0,b_1=0)\ +\ p(\mathbf{r}|b_0=0,b_1=1)\cdot\big(p(b_1=1)/p(b_1=0)\big)} \\
&= L_a(b_0)\ +\ \ln\frac{p(\mathbf{r}|b_0=1,b_1=0)\ +\ p(\mathbf{r}|b_0=1,b_1=1)\cdot\exp\big(\ln\big(p(b_1=1)/p(b_1=0)\big)\big)}{p(\mathbf{r}|b_0=0,b_1=0)\ +\ p(\mathbf{r}|b_0=0,b_1=1)\cdot\exp\big(\ln\big(p(b_1=1)/p(b_1=0)\big)\big)} \\
&= L_a(b_0)\ +\ \ln\frac{p(\mathbf{r}|b_0=1,b_1=0)\ +\ p(\mathbf{r}|b_0=1,b_1=1)\cdot\exp\big(L_a(b_1)\big)}{p(\mathbf{r}|b_0=0,b_1=0)\ +\ p(\mathbf{r}|b_0=0,b_1=1)\cdot\exp\big(L_a(b_1)\big)} \\
&= L_a(b_0)\ +\ \ln\frac{p(\mathbf{r}|\mathbf{s}^1)\ +\ p(\mathbf{r}|\mathbf{s}^3)\cdot\exp\big(L_a(b_1)\big)}{p(\mathbf{r}|\mathbf{s}^0)\ +\ p(\mathbf{r}|\mathbf{s}^2)\cdot\exp\big(L_a(b_1)\big)}. \qquad (4.43)
\end{aligned}$$

4.5 STBC-SP-MLC

Having outlined the concept of STBC and SP modulation, let us now consider the STBC-SP-MLC arrangement of Figure 4.7 described in Section 4.1 in more depth. The STBC in our design will consist of two transmit antennas and a single receive antenna.

4.5.1 System Overview

The schematic of the proposed STBC-SP-MLC system is shown in Figure 4.7. The binary source bit stream $\mathbf{u}$ is serial-to-parallel (S/P) converted at the transmitter. The four individual source bits, namely u_0, u_1, u_2, u_3, are protected by four different-rate MLC encoders, as seen in Figure 4.7. The output bits of encoder $\mathbb{C}^i$, are denoted as b_i, where $i = 0, 1, 2, 3$. We employ LDPC component codes owing to their powerful error correcting capability, low complexity and flexible coding rates. The random nature of the parity check matrix construction of LDPC codes allows us to dispense with the employment of additional channel interleavers. Each LDPC codeword is decoded

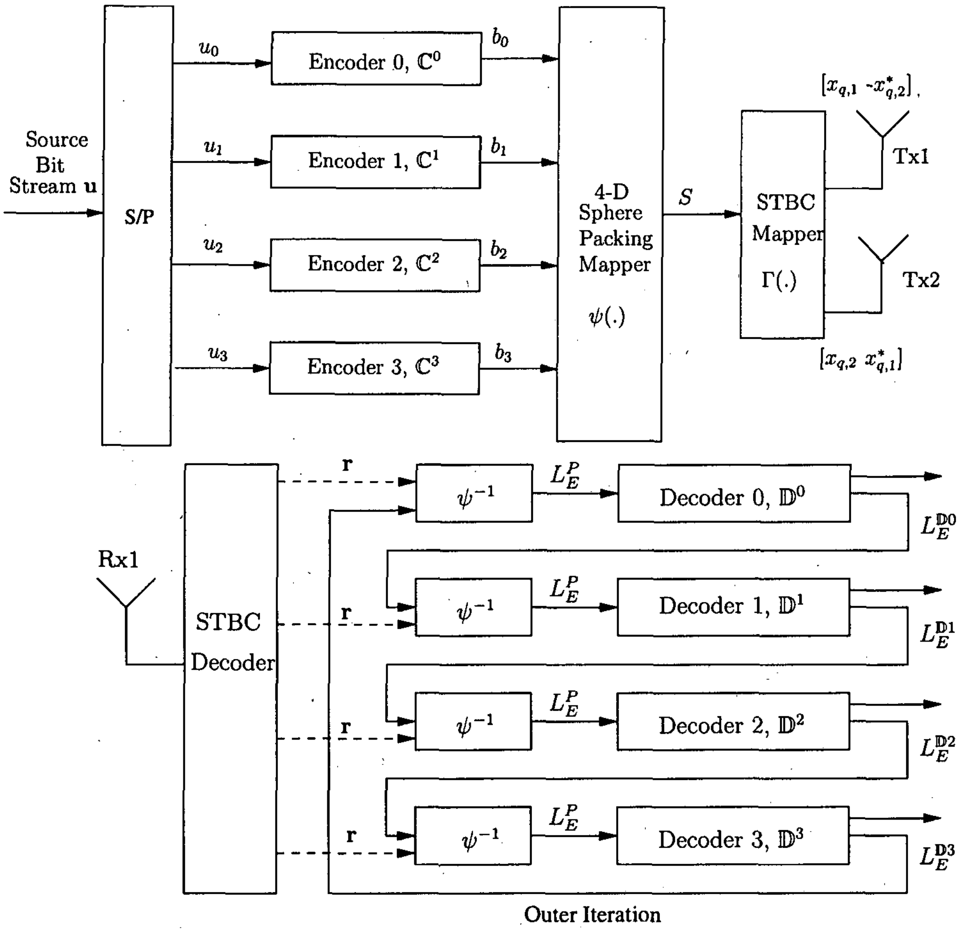

Figure 4.7: The Space-Time Block-Coded Sphere Packing aided Multilevel coding (STBC-SP-MLC) scheme.

using the belief propagation algorithm [9]. The MLC encoded bit substreams are then forwarded to the sphere packing modulator ψ of Figure 4.7.

The 4-D SP phasor point is denoted as $S = (a_{q,1}, a_{q,2}, a_{q,3}, a_{q,4})$, where we have $q = 0, 1, 2, ..., M-1$ and M is the number of SP constellation points as shown in Equation (4.20). Here we would like to represent the four individual coordinates of S in the 4-D SP-space using real values, while satisfying the D_4 constraint of $(a_1 + a_2 + a_3 + a_4) = k$, where k is an even integer, again detailed in Equation (4.21).

After SP-modulation, the 4-D SP symbol is mapped to two complex-valued 2-bit symbols of a two-antenna STBC scheme. Refer to Equation (4.20), the bit-to-symbol mapping function of the system is denoted as $\Gamma(\psi(b_1, b_2, b_3, b_4)) = \Gamma(a_{q,1} + ja_{q,2}, a_{q,3} + ja_{q,4}) = \{x_{q,1}, x_{q,2}\}$. Here, $\psi(.)$ is the SP function used for mapping the original input bits to the SP symbols and $\Gamma(.)$ represents the mapping of the 4-D SP symbols to the complex-valued 2-bit symbols $x_{q,1}$ and $x_{q,2}$ after STBC encoding.

Figure 4.7 also shows the single-antenna aided STBC receiver. The STBC decoder forwards its complex-valued symbols $\mathbf{r}$ to the SP-demodulator ψ^{-1} of Figure 4.7 and the resultant bits are then decoded at the different-protection LDPC decoders in an iterative MSD manner. At the initial iteration, the SP-demodulator ψ^{-1} of Figure 4.7 only receives the SP input symbol $\mathbf{r}$ from the STBC decoder. The *extrinsic* LLRs L_E^P produced by the SP-demodulator are fed into the level-0 decoder of $\mathbb{D}^0$, which then outputs a set of corresponding *extrinsic* LLRs $L_E^{\mathbb{D}^0}$ to the demodulator.

This LLR provides useful *a priori* information for the SP demodulator, where the LLRs gleaned from the previous MLC protection level are updated. As the decoding process continues, each MSD level receives useful *a priori* LLRs from the previous MSD level, which can be exploited in the LDPC decoder. The next outer iteration seen in Figure 4.7 commences, when the LLR information of the SP-demodulator has been updated with the *extrinsic* information received from all MSD levels. The SP symbol $\mathbf{r}$ received by the STBC decoder can be obtained from Equation (4.35) and the *extrinsic* LLR of a single bit b_k output by the demodulator is expressed in Equation (4.38).

4.5.2 Equivalent Capacity Design

The classic technique of applying an equivalent capacity [51] based code-design has been detailed in Section 2.2.2. Generally, the calculation of the channel capacity is based on the maximisation of the mutual information I over all the relevant parameters, where the capacity of a particular channel can be formulated as $C = \max_{p(S_i)} I(r;S)$ where r denotes the legitimate received signal, with S representing the legitimate transmitted symbol. Similar to Equation (2.3), we then apply the so-called chain-rule of mutual information [51] as follows

$$I(r;S) = I(r;b_0) + I(r;b_1|b_0) + ... + I(r;b_{l-1}|b_0,b_1,...,b_{l-2}), \qquad (4.44)$$

where b_i, $i = 0...l-1$, denotes the individual bits of the different MLC protection levels. The so-called equivalent channel concept of [51] is based on the chain-rule in Equation (4.44), where each protection level provides *extrinsic* information for the other bits and hence may be viewed as an independent equivalent 'channel'. This concept of having l equivalent channels for bit i will be exploited in conjunction with the *a priori* information gleaned from the previous $(i-1)$ protection levels, where the bits $b_0, ..., b_{i-1}$ have already been decoded and hence are assumed to be known [1].

In the proposed STBC-SP-MLC scheme invoking 4-D SP modulation, each 4-D SP symbol is mapped to the complex-valued symbols $x_{q,1}$ and $x_{q,2}$, before being mapped to the two consecutive timeslots associated with the two STBC transmit antennas, as shown in Figure 4.7. The resultant signal is then transmitted over a correlated Rayleigh fading channel. Therefore each of the four STBC symbols is encoded by two bits and hence becomes two-dimensional. These STBC symbols have an unequal probability of occurrence within the resultant 4-bit SP signal constellation points, as it will be shown in the context of Table 4.10. The partitioning of the SP signal S can be further divided into two parts, resulting in the SP subsets labelled by $S(b_0 = 0)$ and $S(b_0 = 1)$, each containing a total of eight out of the $M = 16$ SP symbols. In each SP subset, for example at the i^{th} level of the SP subset $S(b^0 = 0)$, the 8-symbol SP constellation segment can be further subdivided into the two 4-symbol SP subsets labelled by $S(b_0 = 0, b_1 = 0)$ and $S(b_0 = 0, b_1 = 1)$ at MLC level $(i+1)$, etc. The partitioning tree of the SP signal set is completed, when the partitioned SP-constellation subset contains only a single SP symbol at level $l-1$.

The partitioning of the 4-D SP constellation is exemplified in Figure 4.8 for the conceptually simpler stylised 1-D scenario of 16-level Amplitude Shift Keying (16ASK). As seen in Figure 4.8, the partitioning tree of the signal set is completed, when the partitioned 1-D constellation contains only a single symbol at the last level $l-1$. Please note again that in Figure 4.8 we used a simplified 1-D 16ASK constellation for the sake of conceptual simplicity, since the $M = 16$ SP constellation in two 2-D STBC symbols cannot be visualised easily.

For a 2-D STBC scheme, having $N_t = 2$ transmitter and $N_r = 1$ receiver antennas, the signal r received at the single antenna, can be represented as [110] [111]

$$r = \sum_{j=1}^{N_t} |h_j|^2 X + \Omega = \chi^2_{2N_t} X + \Omega, \tag{4.45}$$

where X is the 2-D complex-valued received signal, h_j represents the complex-valued

---

[1] The information provided by the bits of a non-binary symbol for each other may be interpreted as additional auxiliary information provided by a fictitious channel also termed as the equivalent channel in [51].

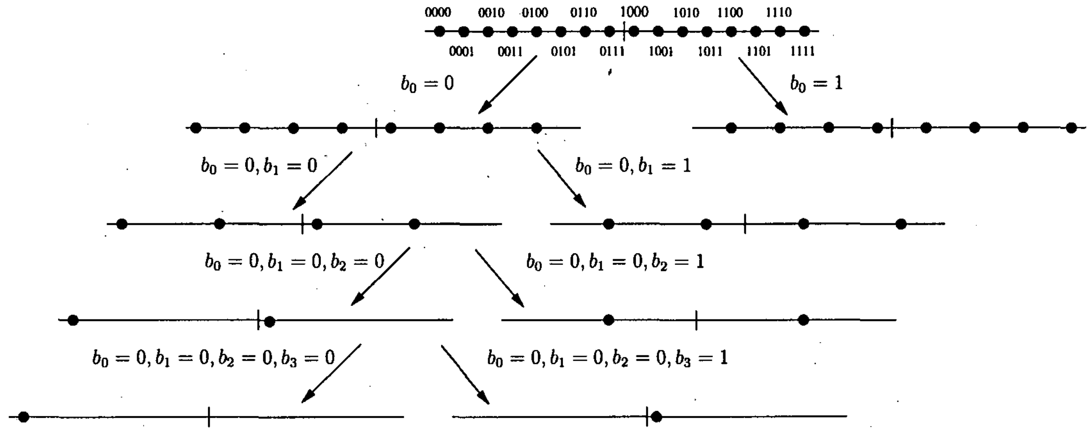

Figure 4.8: 16-ASK signal partitioning.

Rayleigh fading coefficient and $\chi^2_{2N_t}$ represents a chi-squared distributed random variable having $2N_t$ degrees of freedom. Furthermore, Ω denotes the resultant equivalent noise at the STBC receiver having zero mean and a variance of $\chi^2_{2N_t} N_0/2$ per dimension, where $N_0/2$ is the original noise variance per dimension.

The STBC-SP-MLC system of Figure 4.7 characterised in Equation (4.45) receives two complex-valued STBC symbols of the signal r and transmits the M-ary 2-D STBC signals X_m, $m \in \{0, 1, ..., M-1\}$, over the two STBC antennas in two consecutive timeslots. Given a general W-dimensional received signal r, provided that the W-dimensional M-ary signal X was transmitted, Equation (4.45) can be generalised as [110]

$$r[d] = \chi^2_{2N_t}[d] X[d] + \Omega[d], \tag{4.46}$$

where d refers to the dimension index of the signal, while $r = (r[1]...r[W])$, $X = (X[1]...X[W])$ and $\Omega = (\Omega[1]...\Omega[W])$. When $W \geq 2$ and even, we have $W/2$ number of $\chi^2_{2N_t}$ components, because $\chi^2_{2N_t}[k] = \chi^2_{2N_t}[k+1]$ for $k \in \{1, 3, 5...\}$ represents the complex-valued channel having two dimensions.

The conditional PDF of receiving a W-dimensional signal r, given the W-dimensional

M-ary transmitted signal X, is expressed as [110]

$$\begin{aligned} & p(r|X,\chi^2_{2N_t}) \\ = & \prod_{d=1}^{W} \frac{1}{\sqrt{\pi N_0 \chi^2_{2N_t}[d]}} \exp\left(\frac{-|r[d]-\chi^2_{2N_t}[d]X[d]|^2}{\chi^2_{2N_t}[d]N_0}\right) \\ = & \frac{1}{\prod_{d=1}^{W}\sqrt{\pi N_0 \chi^2_{2N_t}[d]}} \exp\left(\sum_{d=1}^{W}\frac{-|r[d]-\chi^2_{2N_t}[d]X[d]|^2}{\chi^2_{2N_t}[d]N_0}\right). \end{aligned} \tag{4.47}$$

The corresponding conditional PDF of one of the 2-D number of M-ary complex-valued received components at each of the STBC antennas is given by

$$p(r|X,\chi^2_{2N_t}) = \frac{1}{\pi N_0 \chi^2_{2N_t}} \exp\left(\frac{-|r-\chi^2_{N_t}X|^2}{\chi^2_{2N_t}N_0}\right). \tag{4.48}$$

In contrast to conventional modulation, where the maximum achievable capacity is attained when each constellation point has an equal probability of occurrence $1/M$, the probability of occurrence of all legitimate transmitted M-ary signals X_m, where m is the symbol index of $m \in \{0 \ldots M-1\}$, is in this case different. This means that at MLC partitioning level i, each legitimate 2-D STBC constellation point will be transmitted with a different relative frequency at each transmit antenna. Each of them has a probability of $p(X_m)$ for $m \in \{0,1,\ldots,M-1\}$, and the mutual information between r and X [58], can be expressed as

$$\begin{aligned} I(X;r) &= \sum_{m=0}^{M-1}\int_r p(X_m,r)\log_2\left(\frac{p(X_m,r)}{p(X_m)p(r)}\right)\mathrm{d}r \\ &= \sum_{m=0}^{M-1}\int_r p(r|X_m)p(X_m)\cdot\log_2\left(\frac{p(r|X_m)}{\sum_{n=0}^{M-1}p(r|X_n)p(X_n)}\right)\mathrm{d}r\cdot \end{aligned} \tag{4.49}$$

Expressing the mutual information with the aid of the entropy as $I(X;r) = H(X) - H(X|r)$, we arrive at [110]

$$\begin{aligned} I(X;r) = & -\sum_{m=0}^{M-1} p(X_m)\log_2(p(X_m)) - \\ & \sum_{m=0}^{M-1} p(X_m)E\left[\log_2\left(\sum_{n=0}^{M-1}\frac{p(X_n)}{p(X_m)}\exp(\Psi_{m,n})\right)|X_m\right], \end{aligned} \tag{4.50}$$

where we have $\Psi_{m,n} = \frac{-|\chi^2_{2N_t}(X_m-X_n)+\Omega|^2+|\Omega|^2}{\chi^2_{2N_t}N_0}$, and $E[A|X_m]$ is the expectation of A conditioned on X_m. The derivation of the Discrete-input Continuous-output Memoryless Channel (DCMC) capacity is further detailed in Appendix B.

The STBC-SP-MLC scheme uses a single receive and two transmit antennas, and there are two modulated STBC symbols, each gleaning the amount of mutual information quantified by Equation (4.50). At the first partitioning level, where there are two partitioning branches labelled by $S(b_1 = 0)$ and $S(b_1 = 1)$, the total mutual information between a transmitted 4-D SP symbol and the received 4-D SP symbol is the average of that of the two partitioning branches of the 2-D STBC symbols.

To obtain the mutual information for a 2-D STBC symbol at partitioning level i, given the perfect knowledge of all the previous $0...i-1$ number of partitioning levels and a total of i partitioning levels, we express Equation (4.50) as

$$I(r^i; X^i) = I(r^i; b_i...b_{l-1}|b_0...b_{i-1}), \tag{4.51}$$

where r^i and X^i denote the received and transmitted STBC symbols at partitioning level i, respectively. The total number of constellation points M in Equation (4.50) will be reduced according to the SP constellation points at the particular partitioning level i.

Finally, the information gleaned at MLC protection level i can be calculated from the chain rule of Equation (4.44) according to [51]

$$I(r; b_i|b_0...b_{i-1}) = I(r; b_i...b_{l-1}|b_0...b_{i-1}) - I(r; b_{i+1}...b_{l-1}|b_0...b_i). \tag{4.52}$$

4.5.3 Bit-to-SP-Symbol Mapping

The legitimate constellation points hosted by D_4 of the SP scheme are categorised into layers based on their norms or energy, i.e. the distance from the origin. We investigate the first two layers of the D_4 SP constellation, which are characterised in Table 4.3. For example, the SP symbol centred at (0, 0, 0, 0) has 24 closest-neighbour SP symbols around it, which are again, constituted by the various legitimate combinations of (+/-1, +/-1, 0, 0) for the Layer-1 SP scheme, seen in Table 4.10.

Note that for a 4-D SP symbol belonging to a constellation of size $M = 16$, the effective throughput η of the STBC-SP arrangement using no outer MLC encoder is η = 1 symbol/(2 time slots) × 4 bits/symbol = 2 bits/(time slot) = 2 bits/(channel use). The uncoded 2-bit/symbol QPSK or 4QAM benchmarker has the same throughput of η = 2 symbol/(2 time slots) × 2 bits/symbol = 2 bits/(channel use). Since there are 24 immediately adjacent SP neighbours at Layer-1, which have different Euclidean distances in the 4-D SP constellation [105], we select the particular 16 points, that exhibit maximum Euclidean distances.

First, the specific SP signal constellation points of D_4 having the maximum Euclidean distance amongst the adjacent or nearest neighbour points at a given energy were found using exhaustive search. The first set of bit-to-SP mapping or labelling based on this constellation space was obtained using an exhaustive computer search by maximising the summed Euclidean distance between the pair of SP symbols belonging to a specific partitioning labelled by the MLC bits, which we term as SET (as in set-partitioning). The resultant SP assignment is shown in Table 4.10. Then the BSA [97] was utilised for designing different bit-to-SP mapping schemes.

4.5.3.1 The Binary Switching Algorithm

More explicitly, the BSA [112] is employed for obtaining an optimised Cost Function (CF) in our mapping scheme. The algorithm iteratively switches the index of two symbols to reduce the initial CF after every switch. As the algorithm progresses, a monotonic decrease of the CF is produced. This permutation based switching process results in a heuristic ordering, which enables us to arrive at the final choice of mapping scheme that minimises our CF.

The BSA can be described with the aid of the flow-cart of Figure 4.9.

Symbol	a_1	a_2	a_3	a_4	Symbol	a_1	a_2	a_3	a_4
S_0	-1	-1	0	0	S_8	0	0	-1	-1
S_1	-1	1	0	0	S_9	0	0	-1	1
S_2	1	-1	0	0	S_{10}	0	0	1	-1
S_3	1	1	0	0	S_{11}	0	0	1	1
S_4	0	-1	-1	0	S_{12}	-1	0	0	-1
S_5	0	-1	1	0	S_{13}	-1	0	0	1
S_6	0	1	-1	0	S_{14}	1	0	0	-1
S_7	0	1	1	0	S_{15}	1	0	0	1

Table 4.4: The random initial bit-to-SP-symbol mapping scheme using $M = 16$ maximised ED between points. The SP symbol i is denoted as S_i while its mapping coordinate values are denoted as a_1, a_2, a_3, a_4.

1) Firstly a CF is computed and an initial random mapping is defined. Taking the CF of Equation (4.53) as our example, we choose a random initial mapping in Layer-1

of the SP constellation having the 16 best EDs as seen in Table 4.4.

2) As seen in Figure 4.9, we then calculate the total CF and the cost CS_i of each symbol i, as summarised in Table 4.5.

Symbol index	0, 1, 2, 3, 4, 5, 6, 7, 8, 9, 10, 11, 12, 13, 14, 15
Individual cost	1.25, 0.917, 0.917, 1.25, 1.25, 0.917, 0.917, 1.25, 1.25, 1.25, 1.25, 1.25, 1.25, 1.25, 1.25, 1.25
Total cost	18.6667

Table 4.5: The symbol index, individual cost and the CF for the initial random mapping.

3) After obtaining the first CF value, in the spirit of Figure 4.9 we sort the list of symbols according to a sequence of decreasing CS_i values, as shown in Table 4.6.

Symbol Index	0, 3, 4, 7, 8, 9, 10, 11, 12, 13, 14, 15, 1, 2, 5, 6
Individual cost	1.25, 1.25, 1.25, 1.25, 1.25, 1.25, 1.25, 1.25, 1.25, 1.25, 1.25, 1.25, 0.917, 0.917, 0.917, 0.917
Total cost	18.6667

Table 4.6: The symbol index, individual cost and the CF after the arrangement of decreasing sequence.

4) As seen in Figure 4.9, the index of the symbol having the highest cost is then chosen to be swapped with the next symbol index in the list. This is due to the fact that this highest-cost symbol contributes most detrimentally to the value of the total CF. This results in the indices seen in Table 4.7.

Symbol Index	3, 0, 4, 7, 8, 9, 10, 11, 12, 13, 14, 15, 1, 2, 5, 6
Individual cost	1.04167, 1.04167, 0.708333, 0.708333, 0.708333, 1.04167, 0.708333, 1.04167, 1, 1, 1.16667, 1.16667, 1.16667, 1.16667, 1, 1
Total cost	15.6667

Table 4.7: The symbol index, individual cost and the CF for the first swap.

5) According to Figure 4.9, after obtaining the new CF and the individual contributions CS_i of the new list, we continue the iterative process by swapping the first symbol index with the second symbol index j, until all the 16 symbols have been swapped in the list. The corresponding CFs are recorded. The example values seen in Table 4.8 refer to $j = 3$.

6) As observe in Figure 4.9, the mapping index, which results in the highest CF value reduction is then selected and a reordered list is generated. However, if the swap does not produce successful indices, the symbol having the second highest index is selected for swapping in order to produce the most efficient switch index. For the

Symbol Index	4, 3, 0, 7, 8, 9, 10, 11, 12, 13, 14, 15, 1, 2, 5, 6
Individual cost	1.41667, 1.04167, 0.708333, 1.41667, 1.41667, 1.04167, 0.708333, 1.41667, 1.25, 1, 1.25, 1.16667, 1.25, 1.16667, 1.25, 1
Total cost	18.5

Table 4.8: The symbol index, individual cost and the CF for the second swap.

aforementioned case, after the end of step (5), we obtain the highest CF reduction and the corresponding reordered list is summarised in Table 4.9.

Symbol Index	14, 3, 4, 7, 8, 9, 10, 11, 12, 13, 0, 15, 1, 2, 5, 6
Indiviual cost	1.41667, 1.04167, 0.708333, 1.08333, 1.08333, 0.708333, 0.708333, 1.08333, 0.916667, 0.708333, 0.708333, 1.08333, 0.958333, 1.16667, 1.08333, 0.875
Total cost	15.3333

Table 4.9: The symbol index, individual cost and the CF for the reordered list.

7) This process continues. If all symbols have been swapped with all other codewords, and no further reduction in total CF is achieved, the iteration is curtailed to obtain the mapping scheme which results in a local optimum BSA cost. We set a maximum number of random initial mappings and these random initial mappings are executed, in order to yield what is assumed to be the global optimum.

Our bit-to-SP mapping CF is the reciprocal of the squared Euclidean distance of each SP symbol with respect to other SP symbols within a specific partitioned subset, as labelled by a particular MLC bit. The CF can be formulated as [24,97,113]

$$CF = \sum_{i=0}^{l-1} \sum_{b=0}^{1} \sum_{S_k \in \Gamma_b^i} \frac{1}{|S_k - \hat{S}_k|^2}. \tag{4.53}$$

We use the simplifying assumption here that the SP demapper has perfect *a priori* information, which constitutes a good approximation at high SNRs and that the SP signal space has $M = 2^l$ constellation points. The notation Γ represents the SP-to-STBC symbol mapping function, which maps the bits $b \in \{0, 1\}$ to the SP symbols S_k. The symbol $\hat{S}_k$ has the same binary bit label as S_k, except for the i^{th} bit. The CF of Equation (4.53) is derived from the union bound of the pairwise error probability of BICM-ID, which aims at maximising the harmonic mean of the minimum squared Euclidean distance.

By minimising the CF of Equation (4.53) using the BSA, the specific partitioning

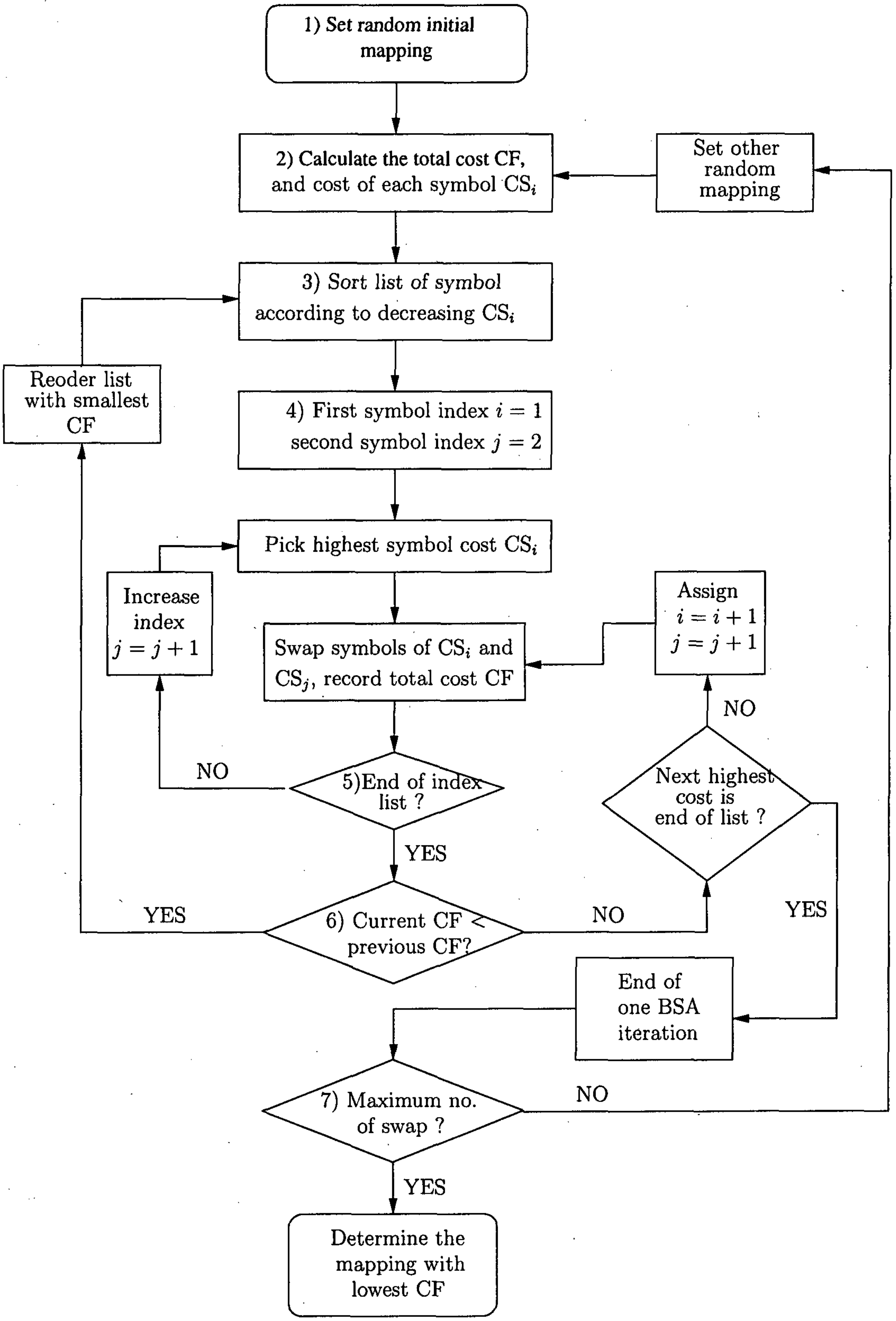

Figure 4.9: Flow-chart for BSA.

corresponding to the maximum harmonic mean of the Euclidean distance [97][2] for the SP constellation points belonging to the opposite bit values at the same SP partitioning level in the entire set of mapping schemes is chosen. We term this a Layer-1 BSA (L1-BSA) mapping and the corresponding symbol indices are given in Table 4.10.

As another design alternative, we further extend the constellation by additionally incorporating SP symbols from the Layer-2 constellation space. Observe from Table 4.3 that similarly to Layer-1, there are a total of 24 points also in Layer-2 [105]. In our second candidate scheme we select the eight highest-distance SP symbols from both Layer-1 as well as from Layer-2 to form a new SP constellation. By using the CF of Equation (4.53), we obtain a different mapping for this constellation. We refer to this as the BSA Layer-2 aided (L2-BSA) scheme, which is also characterised in Table 4.10.

The index j seen in the first column of Table 4.10 identifies the constellation points selected from both Layer-1 and Layer-2 after finding the specific points having the maximum Euclidean distance in the search space D_4. Note that the Layer-1 points span from the index $i = 0$ to 15, indicating the 16 points of Layer-1, while the Layer-2 points span from the index $i = 16$ to 23. The notation $S_i = j$ indicates that the SP symbol S_i is assigned to the constellation point of index j in Table 4.10. The index i associated with symbol S_i is assigned in increasing order from '0' to '15'. For example, referring to the L1-BSA mapping scheme of Table 4.10, the first three rows are 0, 5 and 2, which indicate the SP symbols of S_0, S_1, S_2. These symbols are associated with the indices of 0, 5 and 2, which correspond to the constellation points of (-1, -1, 0, 0), (0, 0, -1, +1) and (0, -1 +1, 0), respectively.

4.5.4 Unequal Error Protection

The STBC-SP-MLC scheme of Figure 4.7 may also be studied in comparison with an STBC-SP scheme concatenated with a single-class outer encoder. The ability to provide UEP is important for various speech and video applications, where each bit may have a different error-sensitivity. The MLC scheme is capable of providing UEP for high-quality, error-resilient speech and video transmissions.

In order to equip our STBC-SP-MLC scheme with an UEP capability [114], we invoke a *hybrid* SP constellation partitioning approach. Instead of maximising the harmonic mean Euclidean Distance (ED) of SP symbols corresponding to all bit-level

---

[2] Harmonic mean distance is the reciprocal of the arithmetic average of the reciprocal distance in the set.

Index	L-1 and L-2 Points from D_4				Symbol Index, $S_i = j, i \in \{0...15\}$				
j	a_1	a_2	a_3	a_4	i	SET	L1-BSA	L2-BSA	UEP1
0	-1	-1	0	0	0	1	0	3	6
1	0	-1	-1	0	1	0	5	12	4
2	0	-1	$+1$	0	2	8	2	5	5
3	$+1$	-1	0	0	3	9	15	0	7
4	-1	0	0	$+1$	4	2	13	15	13
5	0	0	-1	$+1$	5	12	6	9	15
6	0	0	$+1$	$+1$	6	4	4	10	2
7	$+1$	0	0	$+1$	7	5	10	6	10
8	-1	0	0	-1	8	14	12	16	8
9	0	0	-1	-1	9	15	11	17	0
10	0	0	$+1$	-1	10	7	14	18	11
11	$+1$	0	0	-1	11	6	1	19	9
12	-1	$+1$	0	0	12	13	3	20	14
13	0	$+1$	-1	0	13	3	8	21	12
14	0	$+1$	$+1$	0	14	11	9	22	1
15	$+1$	$+1$	0	0	15	10	7	23	3
16	-2	0	0	0	-	-	-	-	-
17	0	0	-2	0	-	-	-	-	-
18	2	0	0	0	-	-	-	-	-
19	0	2	0	0	-	-	-	-	-
20	0	-2	0	0	-	-	-	-	-
21	0	0	2	0	-	-	-	-	-
22	0	0	0	2	-	-	-	-	-
23	0	0	0	-2	-	-	-	-	-

Table 4.10: Bit mappings for different schemes designed for STBC-SP with $M = 16$.

symbols, this *hybrid* partitioning will tolerate lower-distance SP symbols labelled by vulnerable bits, while enhancing the protection of other selected bits by spacing their SP symbols more widely.

This is achieved by creating an unequal distance based mapping strategy. The first partitioning level of $i = 0$ now *minimises* rather than *maximises* the ED between the signal points, which creates one of the more vulnerable MLC protection classes. By minimising the power assigned to $i = 0$, we are able to expand the ED of other UEP classes by assigning higher power to them. For the rest of the STBC-SP-MLC UEP classes at $i = 1, 2, 3$, the classic Ungerböck partitioning concept is applied [16], which *maximises* the ED between the SP signal points.

The optimisation problem to be solved is to minimise the ED at the MLC level $i = 0$ and to maximise it at levels $i = 1,2,3$ by formulating the following CF :

$$CF = \sum_{i=0}^{l-1}\sum_{b=0}^{1}\Big[\sum_{S_k\in\Gamma_b^i, i=0} ||S_k - \hat{S}_k||^2 + \sum_{S_k\in\Gamma_b^i, i\neq 0} ||S_k - \hat{S}_k||^{-2}\Big], \qquad (4.54)$$

which is minimised again using the BSA [97]. As before, we assume here that the SP demapper has perfect *a priori* information, i.e., the decoder of Figure 4.7 used a sufficiently high number of iterations to have an infinitesimally low BER and that the SP signal space has $M = 2^l$ constellation points. Again, the notation Γ represents the SP-to-STBC symbol mapping function, which maps the bits $b \in \{0, 1\}$ to the SP symbols S_k. As before, the symbol $\hat{S}_k$ is the symbol in the 4-D SP-space, which is mapped according to $\Gamma^i_{\bar{b}}$, where $\bar{b}$ denotes the complement of bit b at bit index i. Having designed the bit-to-SP symbol mapping, the above-mentioned equivalent capacity based code-rate calculation for L1-BSA mapping is used for maintaining the specific coding rate at each UEP MLC level. The corresponding mapping scheme is shown in Table 4.10. We term this new mapping strategy as UEP1. We summarise all our proposed systems in Table 4.12 for convenient comparison.

4.5.5 Simulation Results

In this section, we employ LDPC codes as MLC component codes and the rest of the parameters are summarised in Table 4.11. In the simulations, various systems are summarised in Table 4.12 where different mapping schemes are invoked. The complexity of the STBC-SP-MLC encoder depends on that of the LDPC component codes, where the encoder's complexity increases as a quadratic function of the block length noted as $O(N^2)$, where N is the block length in bits. At the receiver, the complexity is also dominated by that of the LDPC decoders, since both the STBC decoder and the SP demapper imposes a negligible complexity. The overall decoding complexity associated with the detection of each LDPC coded bit in a single iteration is $4w_c$ additions and $14w_c$ multiplications, where w_c is the column weight [115] of the LDPC parity check matrix. Hence, in our STBC-SP-MLC scheme, which has a three column weight, uses five inner LDPC iterations and generates 640 LDPC encoded bits, the decoder's complexity per MLC decoder having four LDPC encoded blocks becomes $4 \times 3 \times 640 \times 4 \times 5 \times (I + 1) = 153,600(I + 1)$ number of additions and $14 \times 3 \times 640 \times 4 \times 5 \times (I + 1) = 537,600(I + 1)$ number of multiplications, where I

Sphere packing modulation	$M = 16$
Conventional modulation	QPSK
MLC component output block length	640 bits
STBC-SP-LDPC output block length	2560 bits
No. of LDPC iterations	5
LDPC column weight	3
Channel	Correlated Rayleigh Fading
Normalised Doppler frequency	0.1
Throughput STBC-SP $M = 16$ STBC-QPSK	 (without outer code) 2 bits/channel use

Table 4.11: STBC-SP-MLC system parameters.

System-1	STBC-SP-MLC, L1BSA mapping
System-2	STBC-SP-MLC, L2BSA mapping
System-3	STBC-QPSK-MLC, UP mapping
System-4	STBC-SP-LDPC(2560, 1280), SET mapping
System-5	STBC-SP-MLC, UEP1 mapping

Table 4.12: Summary of various system for STBC-SP-MLC schemes.

denotes the number of outer iterations.

Taking an example of the SET mapping scheme of STBC-SP-MLC, we use equivalent capacity based rate calculation of [51] and note that the STBC symbol $(a_1 + ja_2)$ is mapped to the 1^{st} STBC transmitter of Figure 4.7, while $(a_3 + ja_4)$ is mapped to the 2^{nd} transmitter. All the legitimate combinations of the (a_1, a_2) and (a_3, a_4) values are plotted in Figure 4.10. We have a total of nine visibly different legitimate constellation points in Figure 4.10, because some of the points are identical as suggested by the associated doubled or quadrupled probability of occurrence. For example, observe in Table 4.10 for the mapping scheme SET that the probability of the constellation point (-1,0), which corresponds to S_2 and S_6 for the first transmitter Tx1, is calculated as 2/16=0.125. Similarly, the probability of occurrence for all the specific constellation points is indicated by the number written above each point in Figure 4.10.

At the next level-1 MLC protection class, the signal representing the first STBC symbol of transmitter 1 is shown in Figures 4.11(a) and 4.11(b). Again, here we denote

Coding rate	R_0	R_1	R_2	R_3
STBC-SP-MLC L1-BSA (System-1)	0.2717 (176/640)	0.3152 (204/640)	0.6196 (398/640)	0.7826 (502/640)
STBC-SP-MLC L2-BSA (System-2)	0.3043 (195/640)	0.3913 (250/640)	0.5109 (327/640)	0.7935 (508/640)
STBC-QPSK-MLC Ungerböck part. (System-3)	0.6641 (425/640)	0.3359 (215/640)	-	-

SP gain	at BER = 10^{-5}, in E_b/N_0[dB]	
	$I = 0$	$I = 4$
System-1	4.08	3.16
System-2	3.75	3.00

Table 4.13: Coding rates and SP gains of STBC-SP-MLC and STBC-QPSK-MLC schemes. The SP gains are the modulation gains for both System-1 and System-2 as compared to that of the benchmarker STBC-QPSK-MLC (System-3) at BER 10^{-5}, invoking iteration $I = 0$ and $I = 4$, respectively.

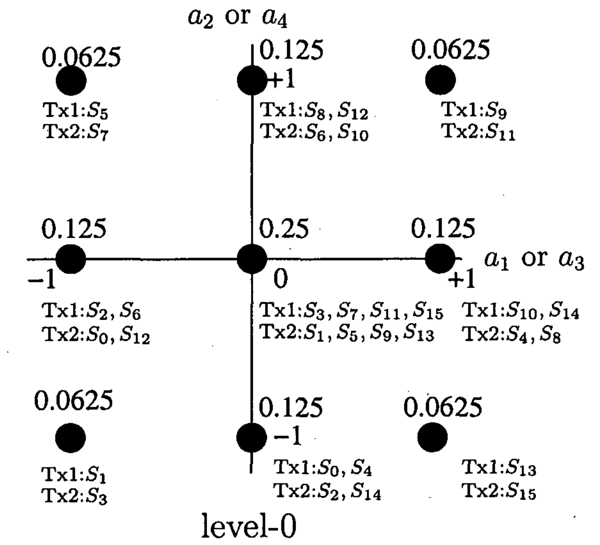

Figure 4.10: The STBC constellation points of SET mapping scheme outlined in Table 4.10 at level-0. The number above the dots indicate the probability of occurrence for the symbols, while the symbol indices at the bottom indicate the specific symbol. The first and second transmitter are represented by Tx1 and Tx2, respectively.

each 2-D STBC symbol as X. The resultant 5-point subsets $X(b_0 = 0)$ and $X(b_0 = 1)$ provide us with a partition tree of $X(0b_1...b_{l-1})$ and $X(1b_1...b_{l-1})$. Given the knowledge of bit b_0 at level-1, which identifies one of the two partitions seen in Figure 4.11, we obtain the partitioning of $X(b_1...b_{l-1}|b_0)$ at level-1 for the first transmitter. The two branches resulting from this partitioning yield the five unequal-probability constellation points shown in Figure 4.11. The partitioning process continues from level-0 to level $(l-1)$. Since in the context of MSD we assume having virtually independent channels for each protection level, the mutual information inferred at each protection level i can be calculated from Equations (4.50), (4.51) and (4.52).

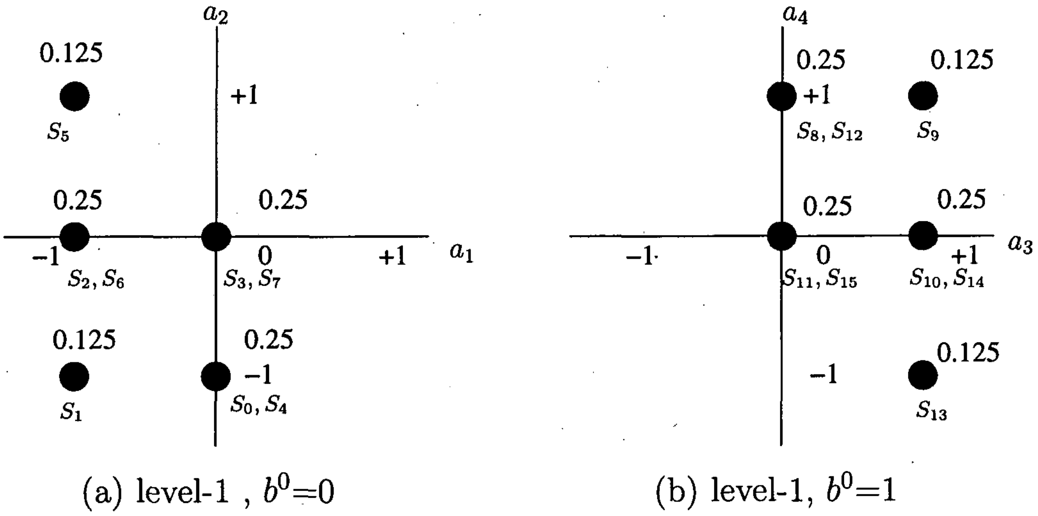

(a) level-1 , b^0=0 (b) level-1, b^0=1

Figure 4.11: The constellation points of the first STBC transmitter Tx1 at MLC level-1 based on SET mapping scheme outlined in Table 4.10. The number above the dots indicate the probability of occurrence for the symbols, while the symbol indices at the bottom indicate the specific symbol.

Figure 4.12 shows the equivalent capacity curves detailed in Section 4.5.2 for the L1-BSA mapping scheme. The vertical dashed line at the throughput of 2 bit/symbol is plotted for determining the equivalent capacity for each protection level of the MLC scheme. Since the total throughput of the SP-STBC-MLC arrangement for $M = 16$ is 2 bit/symbol or 1 bit/channel use, the throughput of the individual different-protection subchannels will sum up to be the same as the overall SP-STBC-MLC scheme's throughput. The coding rates determined from the equivalent capacity rules outlined at the end of Section 4.5.2 are (0.2717, 0.3152, 0.6196, 0.7826). The actual LDPC code rates for the rest of the mapping schemes using the same calculation method are shown in Table 4.13.

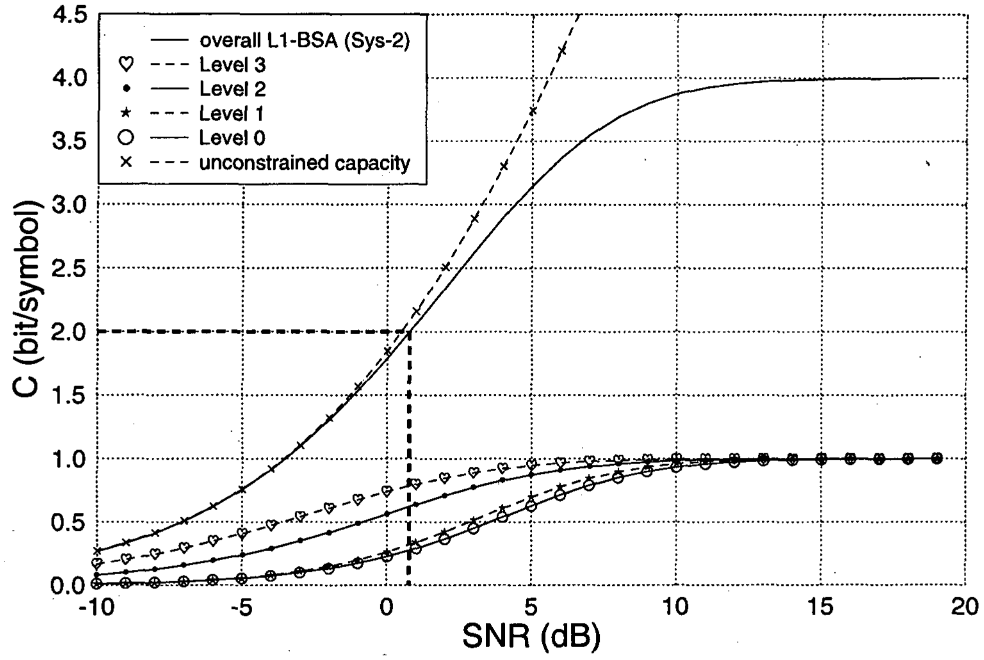

Figure 4.12: The equivalent capacity curves of the proposed SP-STBC with L1-BSA mapping scheme (System-1) communicating over Rayleigh fading channel where an STBC scheme having N_t=2 and N_r = 1 antennas was used. The proposed scheme is shown in Figure 4.7, while the L1-BSA mapping scheme is summarised in Table 4.10.

A total of 5000 frames containing 2560 MLC-encoded bits were transmitted for the sake of our BER evaluation. We construct the STBC-SP-MLC scheme with a total MLC coding rate of 1/2, giving the overall system throughput of (2 bits/channel use x 1/2) = 1 bit/channel use. Our benchmarker is based on an STBC-QPSK-MLC (System-3) structure, which is constituted by the direct serial concatenation of STBC and MLC with the identical QPSK scheme. The STBC employs two transmit antennas, a single receive antenna and the MLC maps its encoded symbols to a 2-D UP based QPSK arrangement. The overall MLC coding rate for this STBC-QPSK-MLC benchmarker is also 1/2, giving an overall system throughput of (2 bits/channel use x 1/2) = 1 bit/channel use. Both the L1-BSA (System-1) and L2-BSA (System-2) mapping schemes are characterised in Figure 4.13.

Conventional MSD-aided MLC does not perform well in a Rayleigh fading channel owing to the potential inter-layer error propagation [99], although the spatial diversity gain provided by a serially concatenated STBC scheme usefully improves its BER

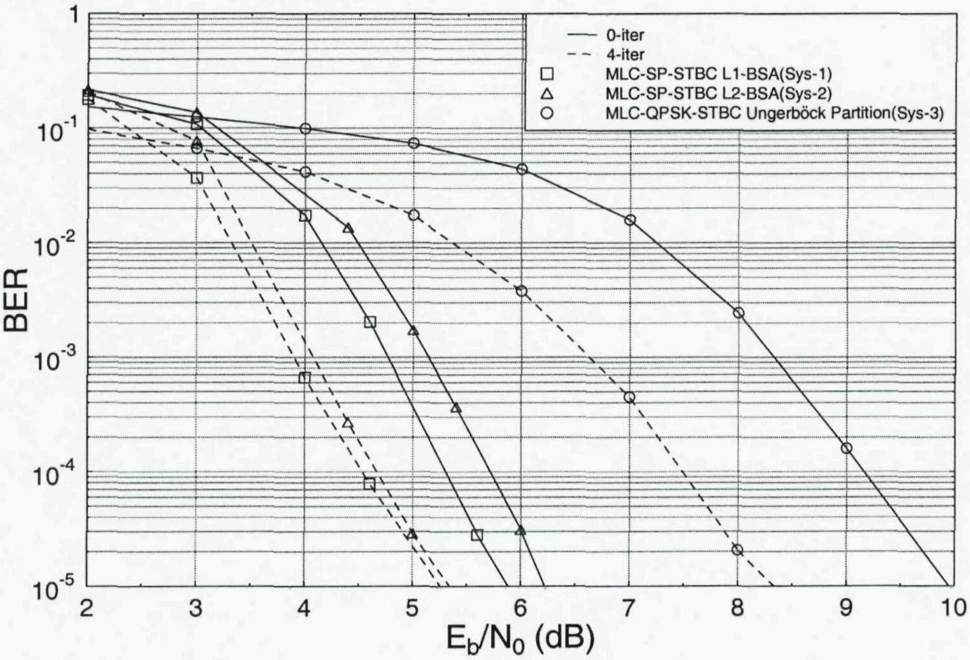

Figure 4.13: BER versus E_b/N_0 performance of the STBC-QPSK-MLC scheme (System-3) at an effective throughput of 1 bit/symbol using Ungerböck Partitioning (UP) based bit-to-symbol mapping and our proposed STBC-SP-MLC scheme of Figure 4.7 using L1-BSA (System-1) and L2-BSA mapping (System-2) strategies, when communicating over a correlated Rayleigh channel having a Doppler frequency of 0.1. All other parameters are summarised in Tables 4.11 and 4.13.

performance. The BER curve reaches 10^{-5} using four iterations at E_b/N_0 = 8.3dB. However, by invoking the proposed SP demapper, the BER dips below 10^{-5} at E_b/N_0 = 5.15dB upon using four iterations. By further expanding the SP constellation to the Layer-2 D_4 space, the BER performance also reaches 10^{-5} at around E_b/N_0 = 5.35dB.

Finally, we also constructed a single-class 1/2-rate STBC-SP-LDPC benchmark scheme having an effective throughput of 1 bit/channel use for comparison with our MLC scheme, where the MLC code is replaced by a single-class LDPC(2560,1280) scheme having a coding rate of 1/2. All LDPC component codes employed in our simulations used a total of five iterations for generating sufficiently reliable *extrinsic* LLRs. The complexity of a single 2560-coded-bit LDPC code and that of the four 640-coded-bit MLC-LDPC component codes of Table 4.13 was deemed similar in these systems. Our proposed STBC-SP-MLC (System-1) exhibits a similar BER performance to that of the single-class STBC-SP-LDPC (System-4) structure characterised in Figure 4.14, although the proposed scheme has a slightly better performance at a low number of iterations. By contrast, the single-class scheme of Figure 4.14 performs approximately 0.3dB better, when using a higher number of iterations at BER $= 10^{-5}$.

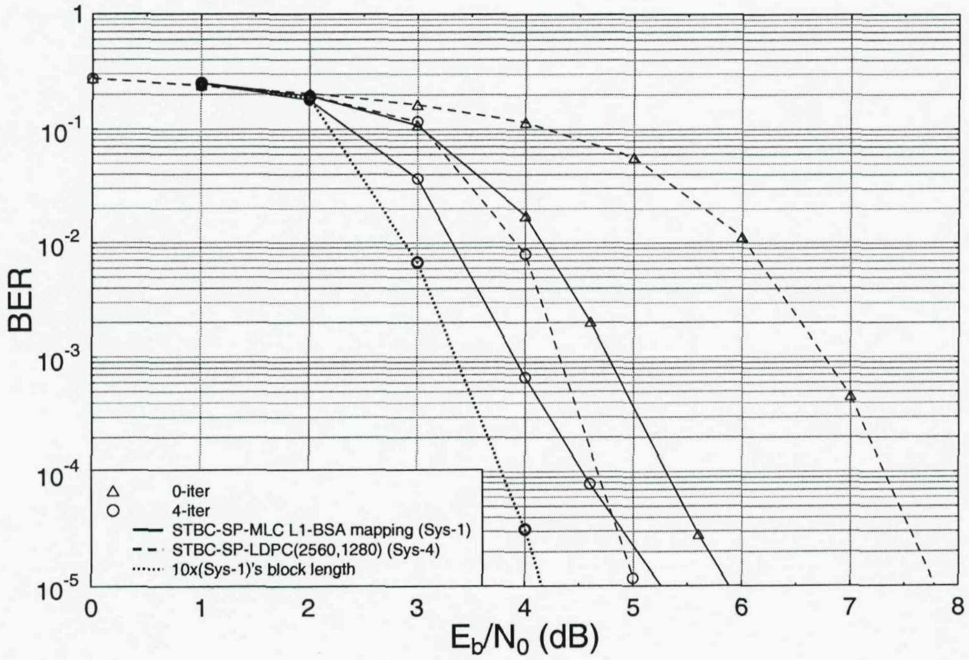

Figure 4.14: BER versus E_b/N_0 performance of the proposed STBC-SP-LDPC scheme (System-4) using a single 1/2-rate component code LDPC(2560,1280) and having an effective throughput of 1 bit/channel use in comparison to the proposed STBC-SP-MLC scheme (System-1) of Figure 4.7, when communicating over a correlated Rayleigh fading channel. All other parameters are summarised in Tables 4.11 and 4.13.

This is a consequence of the fact that each MLC component code has a four times lower codeword length compared to the single-class LDPC(2560, 1280) code. Therefore, the BER performance of the STBC-SP-MLC (System-1) scheme can be improved by increasing the block length of each LDPC component code in the MLC structure. This will reduce the associated error floor. The dotted line seen in Figure 4.14 indicates the BER performance of System-1 with each of its LDPC component code having 10 times the original block length of Table 4.13 after 4 iterations.

We next investigate the attainable performance of the UEP scheme detailed in Section 4.5.4. Figure 4.15 shows the effect of invoking the UEP1 mapping scheme (System-5), where the bits mapped to level-1 of the SP constellation are protected more strongly than the other protection levels, exhibiting an E_b/N_0 gain of around 1dB over the other classes after a single iteration and around 2dB gain compared to all the protection levels shown in System-4. This performance comparison is carried out using only one outer iteration for a typical low-latency, delay-sensitive multimedia application which requires UEP capability. Our CF optimised using the BSA may also be used for possible extension of the UEP classes to even larger M-D SP constellations in multimedia communications. By contrast, all the bits in a single-class STBC-SP-LDPC(2560, 1280) System-4 exhibit a similar BER performance.

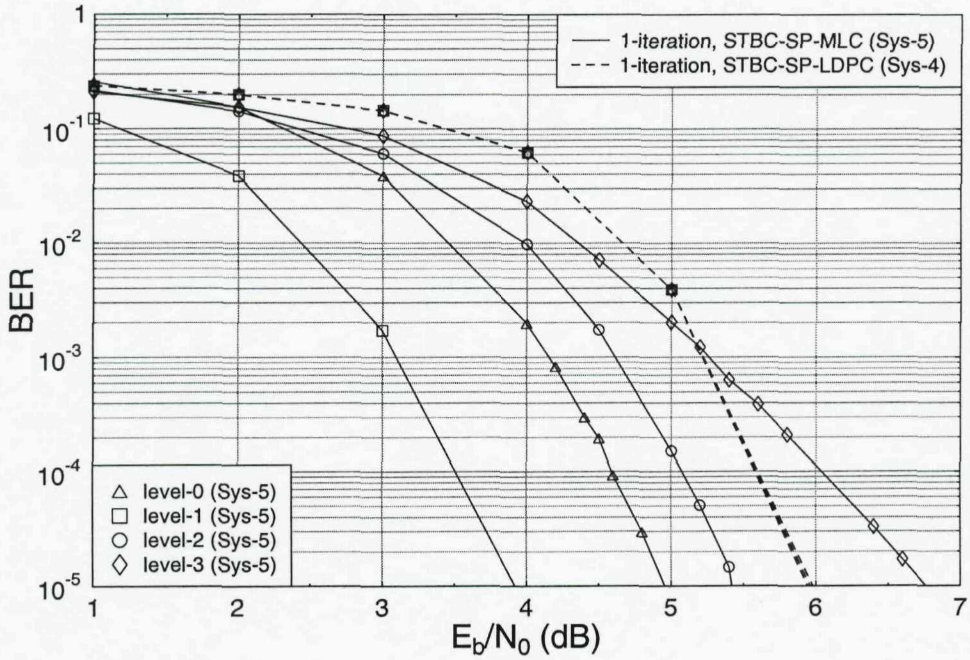

Figure 4.15: BER versus E_b/N_0 performance of the UEP1 mapping scheme (System-5) while retaining the coding rate of L1-BSA mapping, as summarised in Tables 4.10 and 4.13. The benchmarker is the single-class STBC-SP-LDPC scheme (System-4) as detailed in Tables 4.10 and 4.12.

4.6 STBC-SP-BICM

Having investigated the STBC-SP-MLC system in Section 4.5, we now consider a BICM scheme using the same type of arrangements. We propose a Bit Interleaved Space-Time block Coded Modulation scheme using Iterative Decoding (BI-STCM-ID) combined with the multi-dimensional mapping scheme of Section 4.4, which we refer to here as an STBC-SP-BICM arrangement. The BSA described in Figure 4.9 is used once again for optimising the CF of Equation (4.53) employed for deriving different mapping strategies, which are designed with the aid of EXIT charts for the sake of improving the attainable convergence behaviour of the system. The resultant system is amalgamated with a unity-rate precoder for the sake of enhancing its attainable iterative detection performance.

4.6.1 System Overview

Figure 4.16 shows the schematic of the proposed STBC-SP-BICM arrangement, where a Convolutional Code (CC) is used as the outer code. The binary source bit stream **u** is encoded by the CC and the resultant bit stream denoted by **v** is then bit-interleaved by the block π of Figure 4.16. The SP symbol **s** is fed to the STBC encoder having two transmitter antennas.

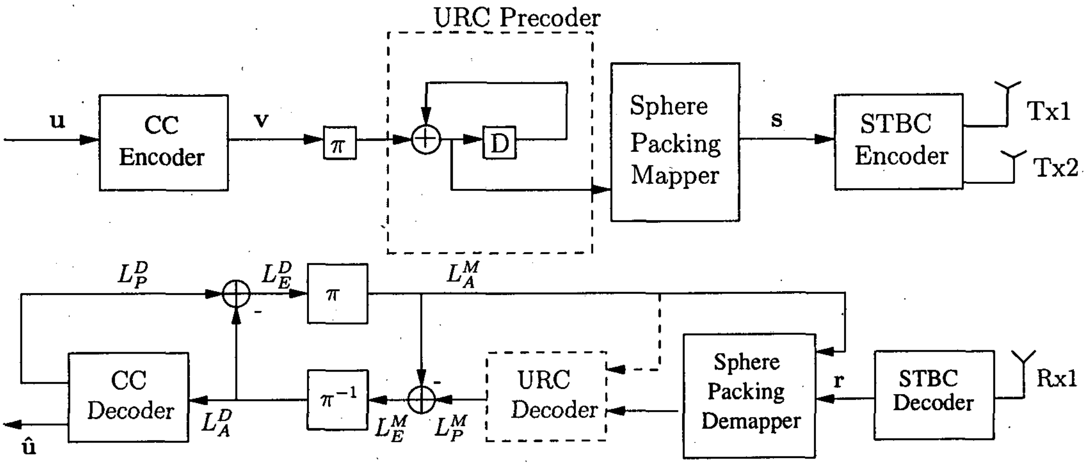

Figure 4.16: The space-time block-coded sphere packing aided bit interleaved coded modulation (STBC-SP-BICM) scheme.

At the receiver, the received SP symbol **r** is fed into the SP demapper by the STBC decoder. The *a posteriori* Log-Likelihood Ratios (LLRs) L_P^M at the output of the SP demapper seen in Figure 4.16 are subtracted from the *a priori* LLRs L_A^M in order to obtain the *extrinsic* LLRs L_E^M. This *extrinsic* information is then deinterleaved and fed - as the *a priori* LLR L_A^D - to the CC decoder of Figure 4.16. When using iterative decoding, the *a posteriori* coded LLRs L_P^D generated by the CC decoder are used for obtaining the *extrinsic* LLR L_E^D by subtracting the corresponding *a priori* LLR L_A^D of Figure 4.16. Again, the useful *extrinsic* information is fed through the bit-interleaver π and serves as the *a priori* LLR L_A^M input of the SP demapper. The SP mapper assigns the bits to different SP constellation points using various bit-to-SP-symbol mapping schemes, as outlined later in Section 4.6.2.

In order to reach the point of iterative convergence, additionally a Unity-Rate Code's (URC) encoder [79], which has been detailed in Section 3.4 is introduced as a precoder in our STBC-SP-BICM context, as shown in the box plotted in dashed line in Figure 4.16. When the URC precoder is introduced, L_P^M becomes the *a posteriori* LLR of the URC decoder instead of the SP demapper. Hence, the *extrinsic* LLR L_E^D of Figure 4.16 is fed as the *a priori* coded LLR into the URC's decoder. The decoding iterations will then be continued by exchanging *extrinsic* information between the CC decoder and the URC decoder, as shown by the dashed arrow of Figure 4.16.

4.6.2 Mapping Scheme

Again, the legitimate constellation points hosted by D_4 are organised into layers based on their norms or energy, i.e. the distance from the origin. We investigate the first 10 layers of the D_4 SP constellation points [105], as detailed in Table 4.3.

Two different STBC-SP-BICM schemes having constellation sizes of $M = 16$ and $M = 256$ are investigated, which are referred to as SP-16 and SP-256, respectively. Firstly for a 4-D SP-16 symbol, the throughput of the STBC-SP arrangement η using no outer CC encoder is $\eta = 1$ symbol/(2 time slots) × 4 bits/symbol = 2 bits/(time slots)=2 bits/(channel use). Hence uncoded QPSK is the corresponding equivalent conventional modulation having the same throughput of $\eta = 2$ symbol/(2 time slots) x 2 bits/symbol = 2 bits/(channel use). Since there are 24 immediately adjacent neighbours at layer-1 having different Euclidean distances from the (0, 0, 0, 0) symbol in the 4-D SP constellation [105], we select the particular 16 points, which exhibit maximum Euclidean distances.

In this system, we employ some of the mapping schemes which are similar to those described in Section 4.5.3, namely the SET, L1-BSA and L2-BSA mappings as characterised in Table 4.10. The CF proposed for optimising the L1-BSA and L2-BSA mapping scheme was expressed in Equation (4.53).

For a 4-D SP symbol having a total constellation size of $M = 256$ (SP-256), the throughput of the STBC-SP arrangement η operating without an outer CC encoder is $\eta = 1$ symbol/(2 time slots) × 8 bits/symbol = 4 bits/(time slot) = 4 bits/(channel use). The throughput of this STBC-SP SP-256 scheme corresponds to that of a classic 16QAM STBC scheme.

We further investigate this SP-256 scheme by selecting 256 constellation points from a single layer of the SP signal space, constituted by N constellation points where, we have $N \geq 256$. The Layer-9 SP D_4 space has a total of $N = 312 \geq 256$ constellation points [105] and hence satisfies our selection constraint. Then, upon applying the BSA for optimising the CF of Equation (4.53), we arrive at the optimised mapping, which we term as the L9-BSA scheme. As an alternative second approach, let us now select the SP constellation points from different layers of the D_4 SP space, ranging from Layer-1 to Layer-5. This scheme has a total of 312 constellation points [105] according to Table 4.3. Employing the CF of Equation (4.53) again, we generate the bit-to-SP mapping scheme having the minimum CF by applying the BSA. The second mapping scheme is termed as the BSA-Multilayer arrangement.

Both the L9-BSA and the BSA-Multilayer schemes are detailed in Tables 4.14 and 4.15. Observe from these tables that the first column represents the symbol index corresponding to the SP constellations points listed in the other eight columns. For example, let us consider the first row in Table 4.14, where the first column shows the eight SP symbol indices ranging from 0 to 7. For example, the symbol 0 is mapped to the second column SP constellation point of (0, -4, -1, 1), the SP symbol 1 is mapped to the third column's SP constellation point of (-1, 4, -1, 0) and so on. Note that this symbol '0' mapped to the SP point of (0, -4, -1 1), for example, corresponds to the coordinate values of $(a_{q,1}, a_{q,2}, a_{q,3}, a_{q,4})$ shown in Equation (4.20).

For the sake of convenience and for the ease of comparison among the different mapping schemes, we summarise the various schemes in Table 4.17 having different mappings and their corresponding parameters are given in Table 4.16. Observe in Table 4.17 that we refer to the systems using the SP-16-aided mapping schemes as System-11 to System-14, whereas to the systems using the SP-256-aided mapping schemes as System-15 and System-16.

4.6.3 Complexity Issues

The SP-16 and SP-256 constellation schemes impose a different implementational complexity. The M-D SP constellation outperforms classic 16QAM having the same overall system throughput in the context of the STBC-SP-BICM scheme. The associated complexity issues are addressed here for the sake of comparison with the aid of LLR formula of Equation (4.39), we quantify the complexity in terms of the Add, Compare and Se-

0-7	0,-4, -1, 1	-1,4, -1, 0	-1,0, 4, 1	1,-4, -1, 0	-1,-4, 0, -1	1,0, -1, -4	1,0, -1, 4	-1,-4, 0, 1
8-15	0,4, -1, 1	0,-4, -1, -1	1,0, 1, -4	1,0, 1, 4	0,1, 1, 4	1,4, -1, 0	-1,4, 0, 1	-4,1, 0, 1
16-23	0,-1, -1, 4	-1,4, 0, -1	0,1, 1, -4	0,-1, -1, -4	3,2, -2, -1	-1,1, 4, 0	2,-2, -3, -1	2,-2, -3, 1
24-31	-1,1, 0, 4	-1,1, 0, -4	2,3, -2, -1	1,-2, -3, -2	-1,0, 1, -4	-1,0, 1, 4	-3,2, 2, 1	-1,-1, 4, 0
32-39	2,-2, 3, -1	-4,1, 0, -1	1,-4, 0, -1	1,-2, -3, 2	-3,2, 2, -1	-4,-1, 0, -1	0,-1, -4, 1	-3,-1, -2, -2
40-47	2,-2, 1, 3	-3,-2, 1, -2	2,-3, 2, 1	-2,-2, -1, -3	1,1, -4, 0	-2,-3, -1, -2	-2,2, 1, 3	2,2, 1, -3
48-55	-2,-2, 1, 3	-2,2, 1, -3	-2,-2, 1, -3	2,2, 1, 3	0,4, 1, 1	0,4, -1, -1	1,-2, 3, -2	2,2, 3, -1
56-63	1,-3, -2, -2	2,-2, 1, -3	-3,2, -1, 2	2,2, 3, 1	0,-1, -4, -1	2,3, -1, -2	1,4, 0, -1	1,-3, -2, 2
64-71	4,-1, 0, -1	-1,-2, -3, 2	2,2, -3, -1	2,2, -3, 1	-1,-2, -3, -2	2,-2, 3, 1	-2,-3, 2, 1	-2,-3, -2, -1
72-79	-3,-2, -1, 2	-4,0, -1, -1	2,-2, -1, 3	2,2, -1, -3	-2,-3, -2, 1	-1,3, 2, 2	-3,2, -2, 1	2,-2, -1, -3
80-87	-2,-2, -1, 3	2,1, -3, 2	-1,-3, 2, -2	-1,2, 3, -2	-3,2, 1, -2	4,-1, 0, 1	-4,0, -1, 1	0,-4, 1, -1
88-95	2,2, -1, 3	-2,-3, 2, -1	4,1, 0, -1	-1,2, -3, 2	1,4, 1, 0	2,3, -1, 2	-2,-2, 3, -1	-2,-3, -1, 2
96-103	-3,-2, -2, -1	-1,2, -3, -2	0,-1, 4, -1	-1,2, 3, 2	2,-3, 2, -1	-4,-1, 0, 1	2,3, -2, 1	1,4, 0, 1
104-111	-2,2, -1, -3	0,-4, 1, 1	-2,2, -1, 3	-3,-2, -2, 1	0,1, 4, 1	0,4, 1, -1	-2,1, 3, 2	4,0, -1, -1
112-119	0,1, 4, -1	4,0, 1, 1	-2,3, -1, -2	-1,1, -4, 0	1,3, 2, 2	-1,-2, 3, 2	1,-4, 1, 0	-1,-2, 3, -2
120-127	-3,-2, 1, 2	2,-3, -1, 2	2,-3, -1, -2	-2,3, -1, 2	4,1, 0, 1	-2,3, 1, 2	3,2, 2, -1	-4,0, 1, 1
128-135	-2,2, 3, -1	3,2, -1, 2	-2,1, -3, 2	-2,-1, 3, 2	-2,-1, 3, -2	3,-2, 1, -2	-4,-1, 1, 0	3,-2, 1, 2
136-143	1,3, 2, -2	4,0, 1, -1	-3,-1, 2, 2	-2,2, -3, -1	-4,0, 1, -1	2,1, -3, -2	-3,2, -2, -1	-1,4, 1, 0
144-151	3,2, -2, 1	3,1, 2, 2	-3,-2, 2, -1	1,-2, 3, 2	-2,-2, -3, -1	2,1, 3, 2	0,1, -4, -1	2,3, 2, -1
152-159	3,2, -1, -2	1,0, 4, 1	1,2, -3, -2	-2,2, -3, 1	-1,3, -2, -2	1,3, -2, 2	-1,-1, -4, 0	2,-3, 1, 2
160-167	2,1, 3, -2	1,1, 4, 0	-4,1, 1, 0	-1,-4, 1, 0	-3,2, -1, -2	2,-1, -3, -2	1,2, -3, 2	3,-2, 2, -1
168-175	-2,1, 3, -2	-2,3, -2, -1	1,1, 0, 4	4,0, -1, 1	1,1, 0, -4	3,2, 2, 1	3,-1, -2, -2	-1,0, -1, 4
176-183	3,1, 2, -2	2,3, 1, -2	1,-3, 2, -2	-1,0, -1, -4	-3,2, 1, 2	3,1, -2, -2	-2,-3, 1, 2	-3,-1, -2, 2
184-191	2,-3, 1, -2	-2,-2, -3, 1	2,3, 1, 2	1,2, 3, -2	-3,-2, 2, 1	-1,-3, 2, 2	3,-2, 2, 1	0,-1, 4, 1
192-199	1,-1, 4, 0	-2,-1, -3, -2	-1,-3, -2, -2	3,-2, -1, -2	1,3, -2, -2	1,2, 3, 2	4,1, 1, 0	-2,-3, 1, -2
200-207	3,-2, -1, 2	2,-3, -2, 1	-2,3, -2, 1	4,-1, 1, 0	0,1, -1, 4	-2,3, 2, -1	-2,1, -3, -2	1,-3, 2, 2
208-215	-3,1, 2, 2	-2,-1, -3, 2	3,-1, -2, 2	-2,-2, 3, 1	0,-1, 1, -4	1,-1, 0, -4	-3,1, -2, -2	3,-2, -2, 1
216-223	1,-1, 0, 4	-4,1, -1, 0	1,0, -4, -1	4,1, -1, 0	2,-1, -3, 2	-4,-1, -1, 0	-3,1, 2, -2	3,-2, -2, -1
224-231	4,-1, -1, 0	2,3, 2, 1	-1,-3, -2, 2	-3,-1, 2, -2	-1,3, 2, -2	2,-3, -2, -1	-1,3, -2, 2	3,2, 1, 2
232-239	-1,0, -4, 1	3,1, -2, 2	-1,0, 4, -1	0,1, -1, -4	2,-1, 3, 2	-3,1, -2, 2	0,-1, 1, 4	-2,2, 3, 1
240-247	1,-4, 0, 1	-1,0, -4, -1	-3,-2, -1, -2	0,1, -4, 1	-2,3, 1, -2	-1,-1, 0, 4	-2,3, 2, 1	-1,-1, 0, -4
248-255	2,-1, 3, -2	-1,-4, -1, 0	3,2, 1, -2	3,-1, 2, 2	1,0, 4, -1	1,-1, -4, 0	3,-1, 2, -2	1,0, -4, 1

Table 4.14: Mapping scheme for L9-BSA.

0-7	-1,-1, 0, 0	-1,1, 0, 0	1,-1, 0, 0	1,1, 0, 0	-1,0, -1, 0	-1,0, 1, 0	1,0, -1, 0	1,0, 1, 0
8-15	-1,0, 0, -1	-1,0, 0, 1	1,0, 0, -1	1,0, 0, 1	0,-1, -1, 0	0,-1, 1, 0	0,1, -1, 0	0,1, 1, 0
16-23	0,-1, 0, -1	0,-1, 0, 1	0,1, 0, -1	0,1, 0, 1	0,0, -1, -1	0,0, -1, 1	0,0, 1, -1	0,0, 1, 1
24-31	2,0, 0, 0	-2,0, 0, 0	0,2, 0, 0	0,-2, 0, 0	0,0, 2, 0	0,0, -2, 0	0,0, 0, 2	0,0, 0, -2
32-39	-1,-1, -1, -1	-1,-1, -1, 1	-1,-1, 1, -1	-1,-1, 1, 1	-1,1, -1, -1	-1,1, -1, 1	-1,1, 1, -1	-1,1, 1, 1
40-47	1,-1, -1, -1	1,-1, -1, 1	1,-1, 1, -1	1,-1, 1, 1	1,1, -1, -1	1,1, -1, 1	1,1, 1, -1	1,1, 1, 1
48-55	-2,-1, -1, 0	-2,-1, 1, 0	-2,1, -1, 0	-2,1, 1, 0	2,-1, -1, 0	2,-1, 1, 0	2,1, -1, 0	2,1, 1, 0
56-63	-2,0, -1, -1	-2,0, -1, 1	-2,0, 1, -1	-2,0, 1, 1	2,0, -1, -1	2,0, -1, 1	2,0, 1, -1	2,0, 1, 1
64-71	-2,-1, 0, -1	-2,-1, 0, 1	-2,1, 0, -1	-2,1, 0, 1	2,-1, 0, -1	2,-1, 0, 1	2,1, 0, -1	2,1, 0, 1
72-79	-1,-2, -1, 0	-1,-2, 1, 0	-1,2, -1, 0	-1,2, 1, 0	1,-2, -1, 0	1,-2, 1, 0	1,2, -1, 0	1,2, 1, 0
80-87	-1,-2, 0, -1	-1,-2, 0, 1	-1,2, 0, -1	-1,2, 0, 1	1,-2, 0, -1	1,-2, 0, 1	1,2, 0, -1	1,2, 0, 1
88-95	0,-2, -1, -1	0,-2, -1, 1	0,-2, 1, -1	0,-2, 1, 1	0,2, -1, -1	0,2, -1, 1	0,2, 1, -1	0,2, 1, 1
96-103	-1,-1, -2, 0	-1,-1, 2, 0	-1,1, -2, 0	-1,1, 2, 0	1,-1, -2, 0	1,-1, 2, 0	1,1, -2, 0	1,1, 2, 0
104-111	-1,0, -2, -1	-1,0, -2, 1	-1,0, 2, -1	-1,0, 2, 1	1,0, -2, -1	1,0, -2, 1	1,0, 2, -1	1,0, 2, 1
112-119	0,-1, -2, -1	0,-1, -2, 1	0,-1, 2, -1	0,-1, 2, 1	0,1, -2, -1	0,1, -2, 1	0,1, 2, -1	0,1, 2, 1
120-127	0,-1, -1, -2	0,-1, -1, 2	0,-1, 1, -2	0,-1, 1, 2	0,1, -1, -2	0,1, -1, 2	0,1, 1, -2	0,1, 1, 2
128-135	-1,0, -1, -2	-1,0, -1, 2	-1,0, 1, -2	-1,0, 1, 2	1,0, -1, -2	1,0, -1, 2	1,0, 1, -2	1,0, 1, 2
136-143	-1,-1, 0, -2	-1,-1, 0, 2	-1,1, 0, -2	-1,1, 0, 2	1,-1, 0, -2	1,-1, 0, 2	1,1, 0, -2	1,1, 0, 2
144-151	-2,-2, 0, 0	-2,2, 0, 0	2,-2, 0, 0	2,2, 0, 0	-2,0, -2, 0	-2,0, 2, 0	2,0, -2, 0	2,0, 2, 0
152-159	-2,0, 0, -2	-2,0, 0, 2	2,0, 0, -2	2,0, 0, 2	0,-2, -2, 0	0,-2, 2, 0	0,2, -2, 0	0,2, 2, 0
160-167	0,-2, 0, -2	0,-2, 0, 2	0,2, 0, -2	0,2, 0, 2	0,0, -2, -2	0,0, -2, 2	0,0, 2, -2	0,0, 2, 2
168-175	-2,-2, -1, -1	-2,-2, -1, 1	-2,-2, 1, -1	-2,-2, 1, 1	-2,2, -1, -1	-2,2, -1, 1	-2,2, 1, -1	-2,2, 1, 1
176-183	2,-2, -1, -1	2,-2, -1, 1	2,-2, 1, -1	2,-2, 1, 1	2,2, -1, -1	2,2, -1, 1	2,2, 1, -1	2,2, 1, 1
184-191	-2,-1, -2, -1	-2,-1, -2, 1	-2,-1, 2, -1	-2,-1, 2, 1	-2,1, -2, -1	-2,1, -2, 1	-2,1, 2, -1	-2,1, 2, 1
192-199	2,-1, -2, -1	2,-1, -2, 1	2,-1, 2, -1	2,-1, 2, 1	2,1, -2, -1	2,1, -2, 1	2,1, 2, -1	2,1, 2, 1
200-207	-2,-1, -1, -2	-2,-1, -1, 2	-2,-1, 1, -2	-2,-1, 1, 2	-2,1, -1, -2	-2,1, -1, 2	-2,1, 1, -2	-2,1, 1, 2
208-215	2,-1, -1, -2	2,-1, -1, 2	2,-1, 1, -2	2,-1, 1, 2	2,1, -1, -2	2,1, -1, 2	2,1, 1, -2	2,1, 1, 2
216-223	-1,-2, -2, -1	-1,-2, -2, 1	-1,-2, 2, -1	-1,-2, 2, 1	-1,2, -2, -1	-1,2, -2, 1	-1,2, 2, -1	-1,2, 2, 1
224-231	1,-2, -2, -1	1,-2, -2, 1	1,-2, 2, -1	1,-2, 2, 1	1,2, -2, -1	1,2, -2, 1	1,2, 2, -1	1,2, 2, 1
232-239	-1,-2, -1, -2	-1,-2, -1, 2	-1,-2, 1, -2	-1,-2, 1, 2	-1,2, -1, -2	-1,2, -1, 2	-1,2, 1, -2	-1,2, 1, 2
240-247	1,-2, -1, -2	1,-2, -1, 2	1,-2, 1, -2	1,-2, 1, 2	1,2, -1, -2	1,2, -1, 2	1,2, 1, -2	1,2, 1, 2
248-255	-1,-1, -2, -2	-1,-1, -2, 2	-1,-1, 2, -2	-1,-1, 2, 2	-1,1, -2, -2	-1,1, -2, 2	-1,1, 2, -2	-1,1, 2, 2

Table 4.15: Mapping scheme for L9-Multilayer.

lect (ACS) operations, when they are carried out in the logarithmic domain, while using a lookup table to enhance the Jacobian approximation in the max-log-MAP algorithm. The term O_{ACS}^{SP-16} and O_{ACS}^{SP-256} quantify the order of ACS operations to be carried out per source bit during the log-MAP operation detection of the SP-16 and SP-256 schemes, respectively.

It may be shown that the number of ACS operations per source bit becomes $O_{ACS}^{SP-16} = 130.18$ and $O_{ACS}^{SP-256} = 2850.72$ for our novel SP mapper. Note that the classic 16QAM having the same throughput as SP-256 would exhibits a similar ACS complexity to $O_{ACS}^{SP-16} = 130.18$, when employing the max-log-MAP algorithm. Therefore the improved performance of the SP-256 scheme would impose a complexity of about 20 times higher than classic 16QAM.

4.6.4 EXIT Analysis Aided STBC-SP-BICM Design

Section 3.3 described the concept of EXIT charts, which was proposed in [77] for the semi-analytic investigation of the convergence of iterative decoders, where the exchange of mutual information between two component codes is visualised. In our STBC-SP-BICM scheme, the output of the outer CC code seen in Figure 4.16 is interleaved for providing an independent source of extrinsic information for the iterative receiver. Typical EXIT curves are generated under the assumptions of using a high interleaver length as well as assuming that the Probability Density Function (PDF) of the *a priori* LLRs is Gaussian distributed.

The mutual information of the *a priori* LLRs in the decoder is given by Equations (3.10) and (3.11), while the mutual information of the decoder's extrinsic LLRs can be expressed is Equation (3.16). The *a priori* LLR information L_A^D of the outer CC code of Figure 4.16 can be modelled by an independent zero-mean Gaussian random variable. The EXIT characteristic of the outer CC decoder is independent of the channel's E_b/N_0 value and hence can be formulated as $I_E^{CC} = T_{CC}(I_A^{CC})$, where $I_A^{CC} = I(V; L_A^D)$ is the mutual information between the outer CC's encoded bits V and the LLR value L_A^D.

As for the inner SP demapper operating without a precoder, the *a priori* LLRs L_A^M can be modelled by a Gaussian distribution and the corresponding mutual information $I_A^{SP} = I(V; L_A^M)$ is a function of V and L_A^M. By contrast, the demapper's EXIT characteristic depends on E_b/N_0 and hence can be formulated as $I_E^{SP} = T_{SP}(I_A^{SP}, E_b/N_0)$. Following the introduction of the URC precoder, the *a priori* information L_A^M is gener-

Sphere packing modulation	$M = 16$, $M = 256$
Conventional modulation	QPSK, 16QAM
STBC-SP-BICM output block length	2560 bits
Channel	Correlated Rayleigh Fading
Normalised Doppler frequency	0.1
Outer CC rate	1/2
Generator Polynomial for CC	memory-4, $(G_1, G_2) = (23_8, 25_8)$ memory-1, $(1, G_1/G_2) = (1, 2_8/1_8)$
Generator Polynomial for URC precoder	$G(D) = 1/(1 + D)$
Throughput STBC-SP $M = 16$ STBC-QPSK	(without outer code) 2 bits/channel use
Throughput STBC-SP, $M = 256$ STBC-16QAM	(without outer code) 4 bits/channel use

Table 4.16: STBC-SP-BICM system parameters.

ated at the input of the URC decoder, as shown by the arrow drawn in dashed line in Figure 4.16. The corresponding modified EXIT characteristic I_E^{SP} must be computed with the aid of L_E^M gleaned from the URC decoder's output. The precoded mapping schemes are summarised in Table 4.17 as System-17 to System-19.

4.6.5 Simulation Results

In this section, we employ a 1/2-rate outer CC and the rest of the parameters are summarised in Table 4.16. A total of 5000 frames containing 2560 CC-encoded bits were transmitted for the sake of our BER evaluations. The effective system throughput of our SP-16 system is 2 bits/channel use $\times$ $1/2 = 1$ bit/channel use, while that of our SP-256 system becomes 4 bits/channel use $\times$ $1/2 = 2$ bits/channel use.

The EXIT chart of the SP-16 scheme is seen in Figure 4.17. A classic bit-to-SP GRAY mapper exhibits a flat EXIT characteristic, showing no convergence. The rest of the SP-16 schemes do achieve a useful iteration gain. For example, the EXIT curve of the SET mapping scheme emerges from a slightly lower I_E^{SP} value than that of the GRAY arrangement, but again, exhibits an iteration gain. By contrast, in comparison to the L1-BSA and L2-BSA schemes, the SET arrangement emerges from a slightly

System Without Precoder	
System-11	SP-16, GRAY mapping
System-12	SP-16, SET mapping
System-13	SP-16, L1-BSA mapping
System-14	SP-16, L2-BSA mapping
System-15	SP-256, L9-BSA mapping
System-16	SP-256, BSA-Multilayer mapping
System With Precoder	
System-17	SP-16, GRAY mapping
System-18	SP-16, L1-BSA mapping
System-19	SP-16, L2-BSA mapping

Table 4.17: Summary of various STBC-SP-BICM schemes.

higher I_E^{SP} values, but reaches a lower convergence point of destination in Figure 4.17, indicating the lack of full convergence to the (1,1) point. The improved convergence behaviour of the L1-BSA and L2-BSA schemes indicates a slightly better iterative gain.

The attainable iterative gain, however, can be further improved by inserting the URC precoder of Figure 4.16. Note from Figure 4.18 that the EXIT characteristic of the precoded-SP mapper reaches the point of perfect convergence at (1,1). However, at $E_b/N_0 = 4$dB, the EXIT characteristic of both the precoded L1-BSA and L2-BSA schemes dips below the outer CC's EXIT curve and thus the iterations are curtailed at $E_b/N_0 = 4$dB. However, beyond $E_b/N_0 = 6$dB, the precoded-SP EXIT curves do create an open EXIT tunnel, allowing the iterative decoding trajectory to reach the point of perfect convergence. We also observe that the precoded-GRAY SP mapper exhibits the highest I_E^{SP} starting point in Figure 4.18 and allows a faster convergence by providing a wider EXIT tunnel. This demonstrates that the precoded-GRAY mapping potentially results in an improved performance gain for our STBC-SP-BICM scheme.

Our identical-throughput benchmarker is based on an STBC-QPSK-BICM structure, which is constituted by the direct serial concatenation of STBC and CC with conventional QPSK modulation. The STBC employs two transmit antennas, a single receive antenna and the outer CC maps the output symbols to a 2-D QPSK UP based modulator. The CC coding rate for this STBC-QPSK-BICM benchmarker is also 1/2, giving an effective system throughput of 2 bits/channel use × 1/2 = 1 bit/channel use.

Figure 4.19 compares the BER performance of the precoded GRAY mapping to that

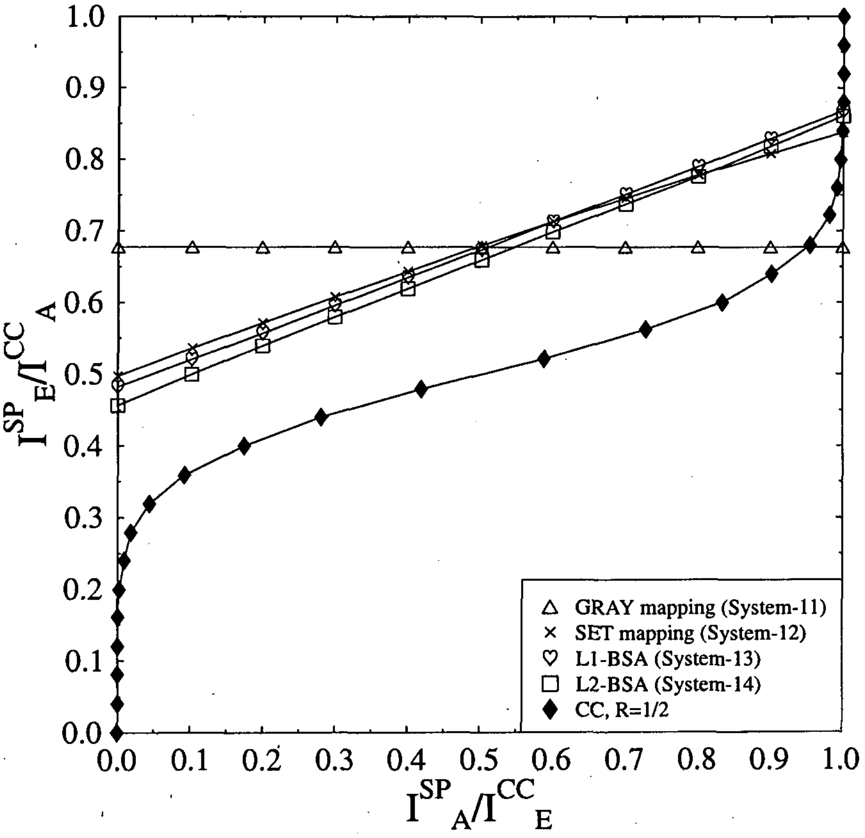

Figure 4.17: EXIT chart for the STBC-SP-BICM demapper for $M = 16$ constellation points, when invoking different SP mapping schemes at $E_b/N_0 = 4$dB in combination with an outer 1/2-rate CC.

of the SET mapping scheme for the STBC-SP-BICM system. The precoded GRAY scheme's BER curve dips further below 10^{-5} at $E_b/N_0 = 4$dB than that of the SET mapping, which exhibits an error floor. Our other benchmarker constituted by a conventional BI-STCM-ID scheme employing QPSK and Ungerböck partitioning reaches BER $= 10^{-5}$ at $E_b/N_0 = 6.5$dB after nine iterations. It is worth noting that the introduction of the URC precoder imposes only a moderate complexity increase, since it employs a simple memory-1 encoder, while achieving a significant BER improvement. However, when employing an SP mapper without the precoder, the L1-BSA mapping scheme constitutes a better choice, since it dispenses with the modest, but non-negligible extra complexity of the 2-state trellis imposed by the URC MAP decoder.

The EXIT chart of Figure 4.20 is plotted to demonstrate the attainable performance improvement of our STBC-SP-BICM scheme employing the novel SP-256 arrangement,

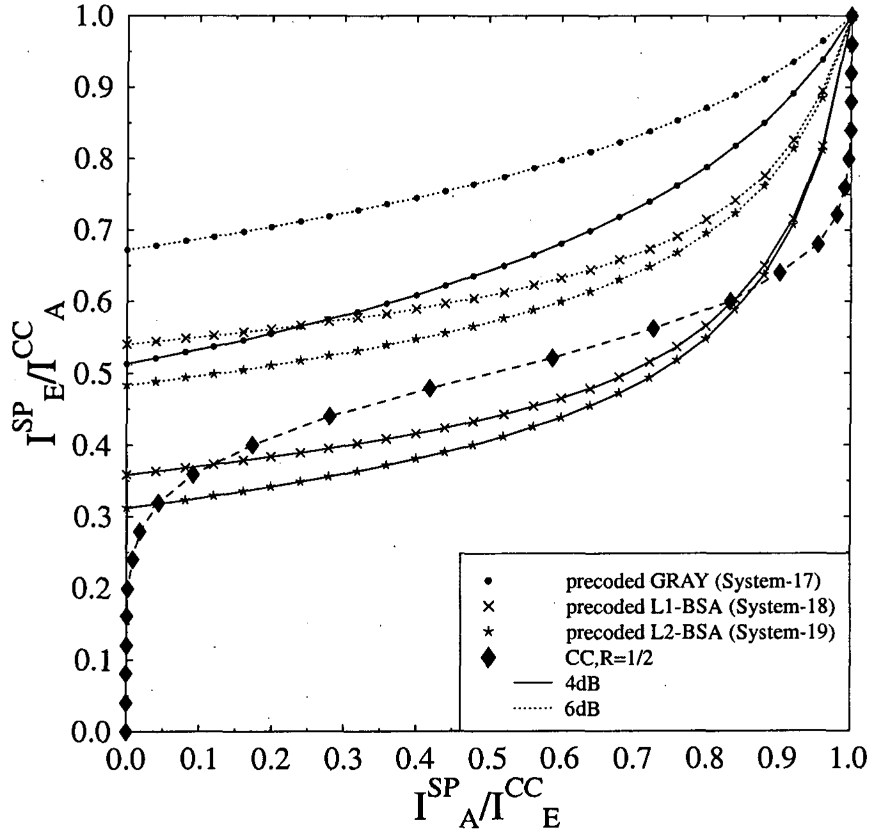

Figure 4.18: Comparison of the convergence behaviour of the precoded systems using the STBC-SP-BICM demapper employing a URC precoder as shown in Figure 4.16. The EXIT charts shown are based on the parameters outlined in Table 4.16 and 4.17, when operating at both E_b/N_0 = 4dB and 6dB, respectively.

which uses $M = 256$ SP signal constellation points, as detailed in Section 4.6.2. A comparison with the Modified Set Partitioning (MSP) scheme of [28] and with the Improved 16QAM labelling of [116] used in the context of the existing BI-STCM-ID system [29] is also beneficial. The EXIT characteristics of the L9-BSA and BSA-Multilayer mapping schemes outlined in Section 4.6.2 are illustrated in Figure 4.20. We employ a rate-1/2 nonsystematic CC for both the classic 16QAM and SP-256 schemes, which have an effective throughput of 4bits/(channel use) × 1/2 = 2 bits/(channel use).

Observe in Figure 4.20 that at E_b/N_0 = 8dB the SP-256 scheme using the L9-BSA mapper emerges from a lower I_E^{SP} value, but it reaches a higher point of convergence compared to both the MSP and to the Improved 16QAM labelling detailed in [28] [116].

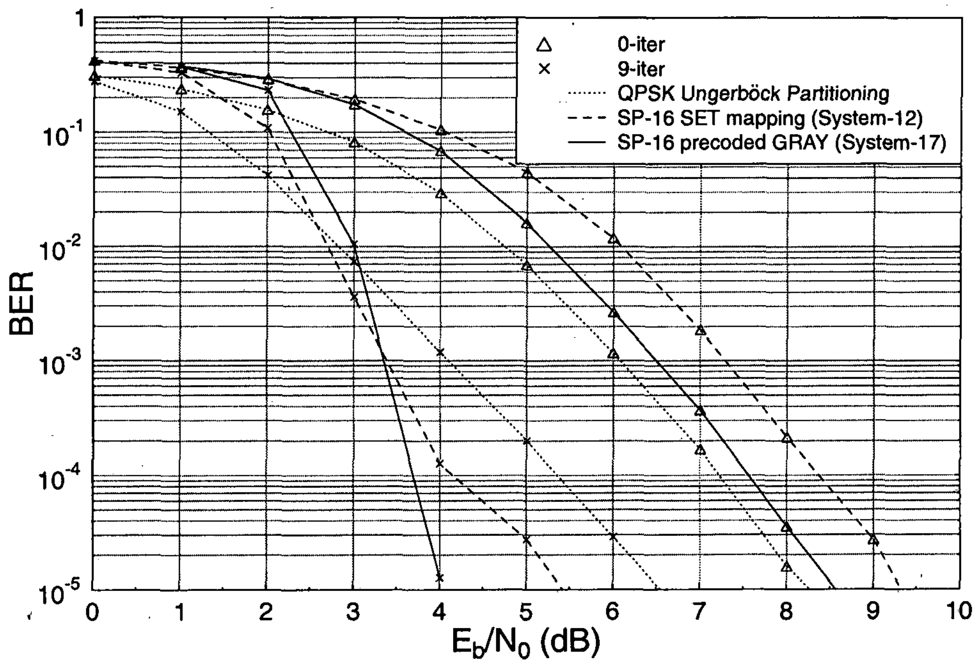

Figure 4.19: Performance comparison of the BER performance for our STBC-SP-BICM system of Figure 4.16 employing SP in conjunction with $M = 16$ invoking SET mapping and a precoded GRAY SP-demapper. A benchmarker of BI-STCM-ID employing Ungerböck's partitioning is shown with conventional QPSK modulation.

By mapping the bits to the SP constellation points across different SP layers, the BSA-Multilayer mapper becomes capable of commencing from a higher EXIT chart starting point compared to the single-layer L9-BSA mapper. This also demonstrates that our proposed BSA-Multilayer scheme becomes capable of outperforming the other mappers, provided that a sufficiently high number of iterations is affordable.

The EXIT function of the memory-1 CC is shown in Figure 4.20, which illustrates that our System-15 and System-16 are capable of achieving iterative convergence as a benefit of having an open EXIT tunnel. By contrast, the 2-D 16QAM labelling fails to maintain an open EXIT tunnel, since it exhibits a cross-over point at $I_A \approx 0.95$. Having an open EXIT tunnel is particularly beneficial, which was created with the aid of a low complexity memory-1 CC outer code having only two trellis decoding states.

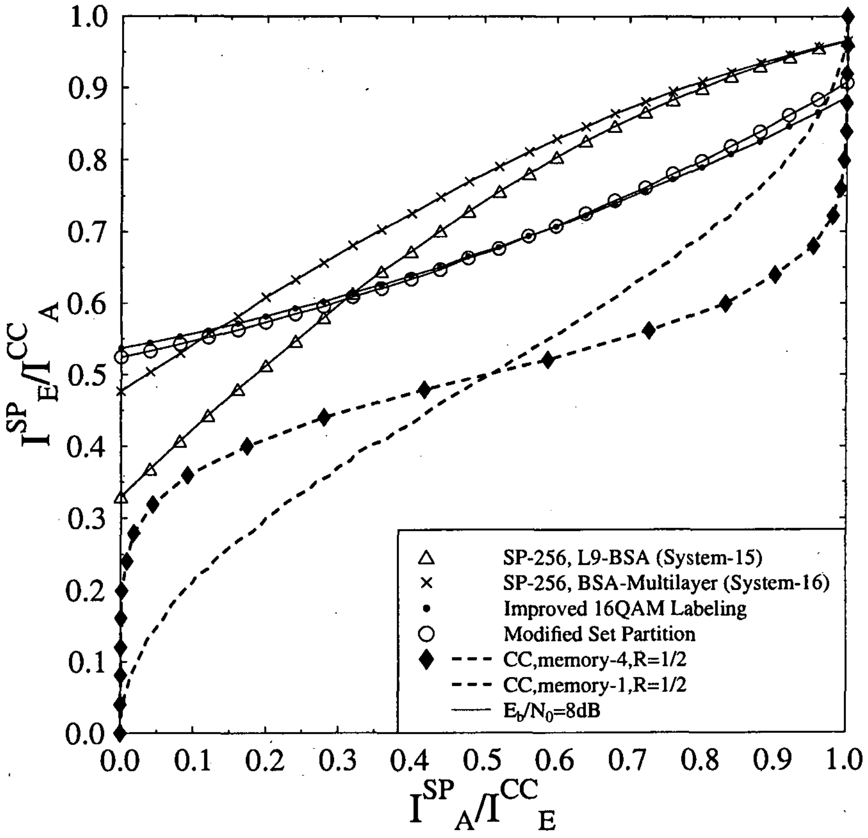

Figure 4.20: EXIT chart of an STBC-SP-BICM scheme of Figure 4.16 employing $M = 256$ SP-demapper with different mapping strategies. A comparison is made with Modified Set Partitioning mapping [28] and Improved 16QAM labelling [116], when operating at an $E_b/N_0 = 8$dB.

4.7 Chapter Conclusions

In this chapter we proposed the novel STBC-SP-MLC and STBC-SP-BICM schemes of Figures 4.7 and 4.16, invoking a twin-antenna transmitter. An introduction to STBC was presented in Section 4.2 and the G_2 design using SP modulation was described in Section 4.3. We further outlined the proposed multidimensional SP modulation scheme in Section 4.3.1, which allowed us to design the space-time signals of the two antennas and two timeslots jointly, rather than separately. The soft iterative SP demapping scheme advocated was highlighted in Section 4.4.

In Section 4.5, the proposed STBC-SP-MLC turbo transceiver was discussed that exploits both the space diversity of STBCs and the joint-SP symbol design of the two time slots. The proposed schemes benefit from a substantial diversity gain and from the employment of SP constellations using different mapping strategies. A novel equivalent capacity based code rate design was invoked for calculating the coding rate of each MLC component code, as shown in Section 4.5.2.

It is worth mentioning that by invoking this new multidimensional SP-demapper, we can achieve a coding gain of about 3dB upon using $I = 4$ iterations compared to conventional QPSK based Ungerböck partitioning. Furthermore, we designed a number of different mapping schemes, which span across different SP layers for $M = 16$, as detailed in Table 4.10 of Section 4.5.3. These mapping strategies were designed based on our proposed CF of Equation (4.53), which was minimised using the BSA of Figure 4.9. To achieve UEP, a novel UEP design was also proposed, which used a modified CF optimised by the BSA, as detailed in Section 4.5.4. The simulation results of Section 4.5.5 showed that as a benefit of our joint multidimensional SP constellation design and optimised bit-to-SP-symbol mapping, the proposed system demonstrated a coding advantage. Furthermore, the *hybrid* UEP mapping of Section 4.5.4 provided an extra gain of about 1dB at BER $= 10^{-5}$, compared to the other more vulnerable bits, as shown in Figure 4.15 .

The STBC-SP-BICM scheme of Section 4.6 was capable of exploiting both the spatial diversity of STBCs and the joint-space-time symbol design of the two time slots, as argued in Section 4.6. The proposed schemes designed for $M = 16$ benefit from a substantial diversity gain with the advent of different mapping strategies. Precoded mapping was designed for our STBC-SP-BICM scheme with the objective of exploiting the resultant recursive nature of our SP-demapper for the sake of approaching the point of perfect convergence at (1,1).

We further extended our design to an SP scheme using $M = 256$ combined with two different mappers, as characterised in Figure 4.10 and in Section 4.6.2. We compared our scheme's convergence behaviour to those of the identical-throughput MSP [28] and to the improved 16QAM labelling of [116] with the aid of EXIT chart analysis. The results provided in Section 4.6.5 showed the presence of a wider EXIT tunnel, leading to an increased iteration gain for our new scheme.

Chapter 5

MLC/BICM Schemes for Multimedia Communications and the Wireless Internet*

5.1 Introduction

In wireless communications, the achievable transmission quality and the time delay imposed are crucial in providing a Quality of Service (QoS) suitable for multimedia application. In line with the increasing tele-traffic there is an increasing demand for higher instantaneous transmission rates. Coded modulation constitutes an attractive transmission technique, since it is a bandwidth efficient scheme, which incorporates both channel coding and modulation without any bandwidth expansion. MLC facilitates a flexible coding rate adjustment, while providing UEP for diverse applications.

The MSD scheme of Figure 2.10 was advocated for decoding MLCs, since its performance approaches that of maximum-likelihood decoding, while having the benefit of reduced decoding complexity. However, due to its high time delay and owing to the potential error propagation across the multiple decoding stages, it is not readily suitable for delay-sensitive interactive audio/video applications. Alternatively, the PID technique of Figure 2.8 [51] may also be employed, where there is no information exchange amongst the protection classes.

MLC schemes may be constructed using different component codes, for example

---

*Part of this chapter is based on the collaborative research outlined in [38, 41, 45].

convolutional codes, Bose-Chaudhuri-Hocquenghem (BCH) codes or turbo codes [65]. Recently, classic LDPC codes [9] have also been commonly used as component codes [30] [117] owing to their flexible code rates and good BER performance. Belief propagation [9] may be used for iterative soft decoding at each different protection level. The employment of LDPCs as component codes has been characterised in our previous work in Chapter 4. In this chapter, we propose a novel MLC design using Generalised Low-Density Parity-Check (GLDPC) codes rather than classic LDPC codes [118] [119] as component codes, which has the benefit of an improved BER performance and an implementationally attractive parallel decoding structure.

In order to further improve the attainable performance, the design of the physical layer is amalgamated with the design of the data link layer. In both wireless and wired Internet based data communication, each data file is transmitted in terms of packets. In the data link layer, an Automatic Repeat reQuest (ARQ) [120] mechanism is used for sending a Negative-ACKnowledgement (NACK), requesting the source to retransmit lost or corrupted packets. Under hostile channel conditions, the retransmission overhead may become excessive, especially when using the extra overhead imposed by the Internet Protocol (IP). This is because after the reception of an error-infested IP header, an uncompressed header has to be transmitted. Therefore in hostile wireless channel conditions the employment of the IP header and retransmission mechanism may substantially increase the transmission overhead and hence may in fact reduce the effective throughput.

In order to prevent an excessive amount of retransmissions in conjunction with the ARQ mechanism, we investigate the employment of Luby Transform (LT) codes which are capable of dispensing with the additional retransmission of packets by inserting a certain amount of redundant packets during their original transmission. Our design objective is then to minimise the number of redundant packets required for the complete recovery of the original data file, rather than aiming for the highest possible coding rate, which is the design objective of classic FEC codes in the physical layer.

The associated design trade-off is that the number of corrupted packets can be reduced by reducing the code-rate of the FEC scheme, which however clearly requires a higher total number of packets for conveying a fixed-size data file. Our ultimate goal is hence to minimise the total amount of redundancy imposed by both FEC and LT coding, while maximising the overall integrity. Serially concatenated and iteratively detected coded modulation schemes are capable of attaining a near-capacity performance and hence in the proposed system BICM-ID is combined with a serially concatenated LT code [121] [122] [123].

LT codes were proposed by Luby [123] based on the philosophy of the so-called Fountain codes [121], which were first proposed for the sake of reliably transmitting data files over the Ethernet-based Internet. The files are assumed to be constituted by $\mathcal{K}$ information packets, each containing a specific number of bits. For the sake of reliably recovering the original data file, $\mathcal{K}' = \mathcal{K} + \mathcal{E}$ encoded data packets have to be transmitted, where $\mathcal{E}$ is the number of redundant packets that has to be as low as possible.

5.2 Multilevel Generalised Low-Density Parity-Check Codes

As mentioned in Section 5.1, MLC schemes may be constructed using different components, which we demonstrated using LDPC codes in Section 4.5, since they exhibit a flexible coding rate and an impressive BER performance. In this section we further investigate the component code design and propose a MLC scheme invoking GLDPC components, which we term as a Multilevel Generalised Low-Density Parity-Check (MLC-GLDPC) code. MLC-GLDPC codes are capable of outperforming classic LDPC component codes at a reduced decoding latency, while exhibiting an implementationally attractive parallel decoding structure.

It is widely recognised that as a benefit of their block-based nature and random generator matrix construction, long block codes are capable of 'over-bridging' the channel fades and hence no channel interleaver is required for LDPC or GLDPC component codes. For our GLDPC codes, instead of using Gallager's single-error detecting parity check code [9], we employ binary BCH and Hamming error-correcting codes [65] as the constituent codes. Simple iterative Soft-Input Soft-Output (SISO) decoders [65] are used for each constituent code of the MLC scheme. We invoke both inner iterations within the GLDPC component codes and outer iterations exchanging information between the GLDPC block codes and the demapper. Gray Mapping (GM) of the bits to modulated symbols is used for non-iterative decoding, while Ungerböck Partitioning (UP) based mapping is used for iterative decoding, because it was shown in Section 3.3.2 that it provides improved iteration gains.

Tanner [124] introduced the concept of GLDPCs with the aid of an attractive graphical representation of error control codes. Later, the Hamming-code based GLDPC was further investigated by Boutrous *et al.* [118], Lentmaier *et al.* [119] and Pothier [125]. It was also demonstrated by Pothier [125] that the GLDPC structure has the advantage of flexible code rate selection and offers an attractive design alternative in applications such as digital audio and TV broadcasting, deep space applications as well as in high-speed packet data transmission.

5.2.1 GLDPC Structure

In this section we propose a MLC invoking GLDPC component codes [118] having a Parity Check Matrix (PCM) illustrated in Figure 5.1, while the GLDPC components are constructed based on LDPC codes using the classic LDPC-specific method of generating the PCM. More explicitly, the PCM $\mathbf{H}$ was constructed by the single-error detecting parity check codes of a classic LDPC code [9], namely from the appropriately tessellated PCMs $\mathbf{H}_{\Upsilon}$ of the short constituent block codes such as BCH codes $\Upsilon(n,k)$ used as constituent codes. The PCM was constructed with the aid of W number of so-called GLDPC super-codes [1]. We opted for using $\mathsf{W}=2$, since it results in a high minimum distance [118], despite its low decoding complexity. The $\mathsf{W}=2$ super-codes are defined by two PCMs, which satisfy $\mathbf{H}^2=\pi\mathbf{H}^1$, where $\mathbf{H}^1$ denotes the block diagonal matrix of the *first* super-code, while $\mathbf{H}^2$ represents the corresponding matrix of the *second* super-code and π represents a pseudo-random column-based permutation. This code construction produces $L=N/n$ number of constituent codes, where N denotes the total coded block length.

The first block diagonal matrix $\mathbf{H}^1$ shown at the top of Figure 5.1 constitutes the direct concatenation of N/n number of constituent codes $\Upsilon(n,k)$ in the super-code $\mathfrak{C}^1$ as follows [125]

$$\mathfrak{C}^1 = \bigoplus_{i=1}^{N/n} \Upsilon, \tag{5.1}$$

where N represents the codeword length of the GLDPC(N,K) code and $\bigoplus$ denotes the concatenation process. To form the complete GLDPC PCM $\mathbf{H}$, we concatenate the

---

[1] In the context of GLDPC, a super-code contains a number of smaller sub-codes which are referred to as the constituent codes. Please refer also to footnote 2 on page 134.

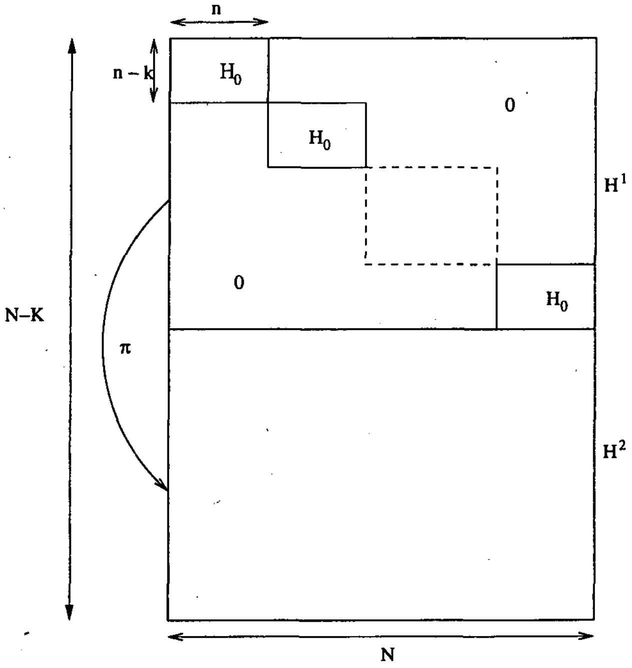

Figure 5.1: Parity check matrix (PCM) of a GLDPC code, having W = 2 super-codes.

W = 2 number of submatrices $\mathbf{H^1}$ and $\mathbf{H^2}$, which are the PCMs of the super-codes [2] $\mathfrak{C}^1$ and $\mathfrak{C}^2$, respectively.

The reception of the error-free encoded codewords $\mathcal{V}$ can be checked with the aid of the W number of PCMs of the super-codes, namely using $\mathbf{H^1H^2...H^W}$ as follows

$$\mathcal{V} \cdot (\mathbf{H^j})^T = 0, \qquad j \in \{1, 2, ..., \mathsf{W}\}. \tag{5.2}$$

Observe in Figure 5.1 that the PCM $\mathbf{H^2}$ is derived by permuting the columns of the first PCM $\mathbf{H^1}$ without interleaving the elements of the columns. Therefore, in general, the codewords of the super-codes can be expressed as

$$\mathcal{V}^j = \pi_j(\mathcal{V}^1), \tag{5.3}$$

where π_j represents the corresponding symbol-interleaver of the j^{th} super-code.

---

[2] In order to clarify the rationale of this terminology we note that since $\mathfrak{C}^1$ and $\mathfrak{C}^2$ are sub-codes of the GLDPC(N, K), it would also be appropriate to refer to them as sub-codes. However, in the literature [118,125] they were referred to as super-codes. This is because a super-code here consists of many smaller constituent codes Υ, even though W number of super-codes constitute a GLDPC code. To avoid any confusion, we also used this terminology in this thesis.

5.2.2 GLDPC Encoding

The encoding process of GLDPCs is based on first constructing the generator matrix of the GLDPC code, which is similar to that used in classic LDPCs. For a GLDPC code having $j = 2$ super-codes, the PCM $\mathbf{H}$ is constructed from the concatenation of submatrices $\mathbf{H^1}$ and $\mathbf{H^2}$, as seen in Figure 5.1. The PCM of $\mathbf{H^2}$ is formulated as $\mathbf{H^2} = \pi\mathbf{H^1}$.

Therefore the PCM $\mathbf{H}$ is constituted by a matrix of $(N-K)\times N = F\times N$ elements, where we have $F = (N-K)$. Furthermore, this $\mathbf{H}$ matrix can be subdivided into the $(N-K)\times(N-K) = (F\times F)$-element matrix $\mathbf{A}$ and the $F\times(N-F)$-element matrix $\mathbf{B}$ as follows

$$\mathbf{H}_{(F\times N)} = \left[\mathbf{A}_{(F\times F)}\middle|\mathbf{B}_{(F\times(N-F))}\right]. \tag{5.4}$$

The generator matrix $\mathbf{G}$ having $(K\times N)$ elements can be expressed as

$$\mathbf{G}_{(K\times N)} = \left[\mathbf{I}_{(K\times K)}\middle|\mathbf{B}^T.(\mathbf{A}^T)^{-1}_{(K\times F)}\right], \tag{5.5}$$

where $\mathbf{I}_{(K\times K)}$ represents the identity matrix and $(.)^T$ denotes the transpose of a matrix. Note that the matrix $\mathbf{A}^T$ must be invertible. In order to ensure that $(\mathbf{A}^T)^{-1}$ exists, the columns of the PCM $\mathbf{H}$ may have to be reordered for calculating the inverse of $\mathbf{A}^T$. For instance, the columns of $\mathbf{B}$ can be randomly swapped with the columns of $\mathbf{A}$, until the matrix $\mathbf{A}$ becomes non-singular.

The final codeword matrix $\mathcal{V}$ generated by the encoding process is given as

$$\mathcal{V}_{(1\times N)} = \mathcal{U}_{(1\times K)}.\mathbf{G}_{(K\times N)}, \tag{5.6}$$

where $\mathcal{U}$ hosts the information bits in a matrix of size $(1\times K)$.

5.2.3 GLDPC Decoding

The decoding of each constituent block code such as a BCH code can be implemented by invoking a SISO decoder for each BCH constituent code. The reduced-complexity log-MAP algorithm rather than the full-complexity MAP decoder is used for the GLDPC SISO decoder scheme due to its attractive coding performance and reduced complexity. The SISO decoder module used for GLDPC decoding is shown in Figure 5.2.

In other words, each constituent code of the *first* GLDPC super-code seen in the upper half of Figure 5.3 has an associated SISO decoder and the constituent codes are

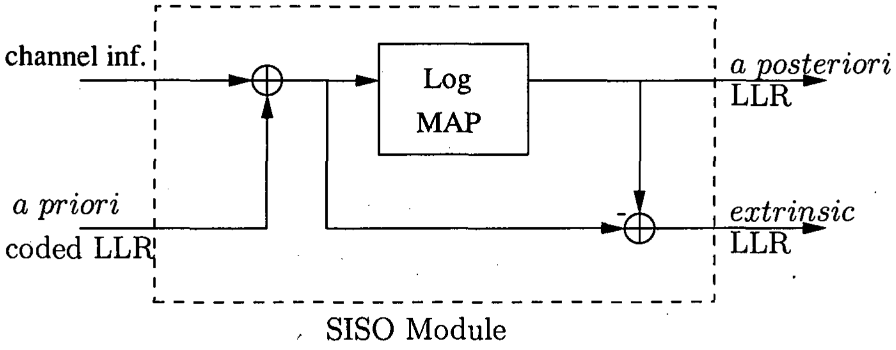

Figure 5.2: SISO module using log-MAP algorithm [125].

decoded in parallel, before the resultant *extrinsic* information is fed into the *second* interleaved GLDPC super-code portrayed at the bottom of Figure 5.3. This operation is repeated in an iterative inner GLDPC decoding loop. The substantial implementational benefit of this is that a number of cost-efficient, low-speed parallel SISO decoders may be used instead of a single high-speed decoder.

Figure 5.3 portrays the L number of SISO decoders of the L constituent codes. Since we have $\mathsf{W} = 2$ GLDPC super-codes, the channel's output information y is fed directly into the L number of parallel SISO decoders of the *first* GLDPC super-code, while after deinterleaving in the block π^{-1} into the *second* GLDPC super-code of Figure 5.3. Following the last GLDPC iteration, the *a posteriori* bit probabilities APP^2 generated at the output of the SISO decoder of Figure 5.3 will be used for generating the hard decision based GLDPC decoder output bits. The *extrinsic* outputs Ext^1 of the *first* super-code's SISO decoders are de-interleaved and used as *a priori* information Apr^2 for each of the constituent decoders of the *second* GLDPC super-code in Figure 5.3. During the next inner iteration, the *extrinsic* information Ext^2 arriving from the *second* super-code is used as the *a priori* information Apr^1 for the constituent decoders of the *first* GLDPC super-code of Figure 5.3, as in classic turbo detectors [65]. The processing block length of a constituent SISO decoder is N/n, as opposed to N in a LDPC or turbo constituent decoder.

5.2.4 GLDPC Code Rate

The code rate of GLDPCs is calculated based on the lower bound method proposed in [125] as detailed below. By investigating the PCM of GLDPCs, the number of rows in the submatrix $\mathbf{H}^{\mathsf{j}}$, where $j \in \{1, 2, ..., \mathsf{W}\}$ can be associated to $(n-k)N/n$ as shown

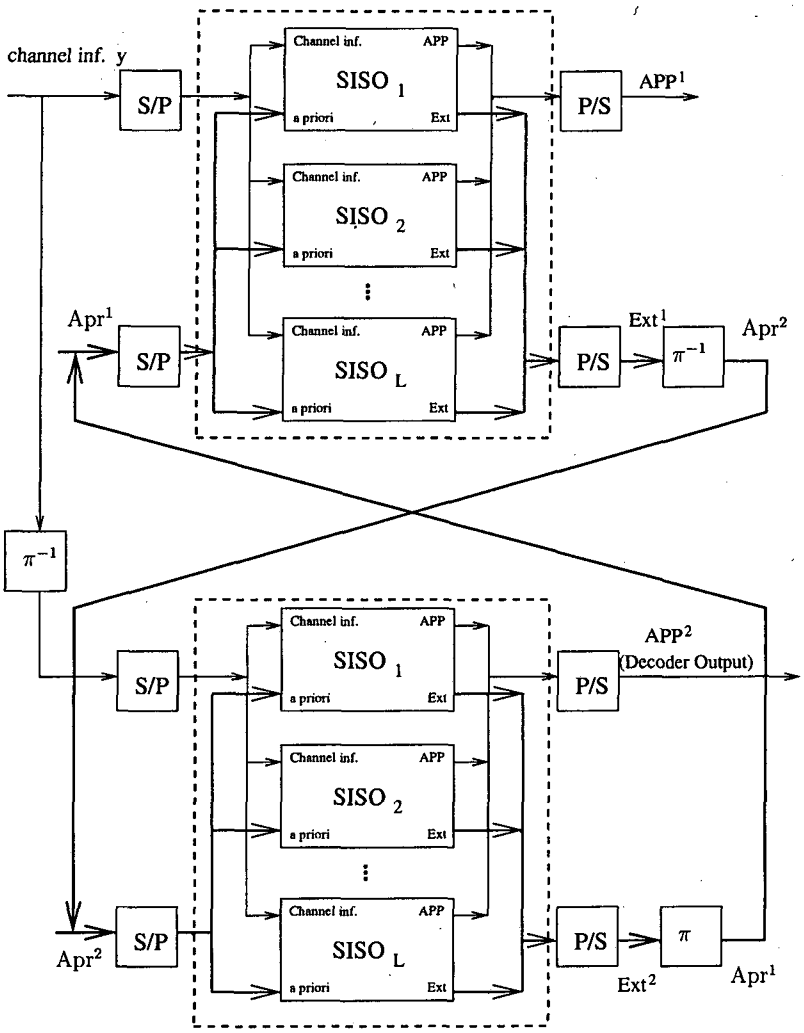

Figure 5.3: SISO constituent decoder of the GLDPC component codes.

in Figure 5.1. Hence, the total number of rows $(N-K)$ in $\mathbf{H}$ can be written as

$$N-K=\frac{\mathsf{W}(n-k)N}{n}=\mathsf{W}(1-R_{\Upsilon})N, \tag{5.7}$$

where $R_{\Upsilon}=k/n$ represents the rate of the constituent code $\Upsilon(n,k)$. Assuming that the PCM $\mathbf{H}$ has full rank when all the rows are independent of each other, the code rate R of GLDPCs can be expressed as

$$R=K/N=1-\mathsf{W}(1-R_{\Upsilon}). \tag{5.8}$$

In reality, when the rows of $\mathbf{H}$ are not guaranteed to be independent, the actual dimension of K is higher than the one used in Equation (5.8). Hence, we obtain the lower bound of the coding rate for a GLDPC as [125]

$$R = \frac{K}{N} \geq 1 - \mathsf{W}(1 - R_{\Upsilon}). \tag{5.9}$$

5.2.5 Modulation and Demodulation

The proposed Multilevel GLDPC scheme employs the PID structure depicted in Figure 2.8. For the sake of convenience, the system model is repeated in Figure 5.4.

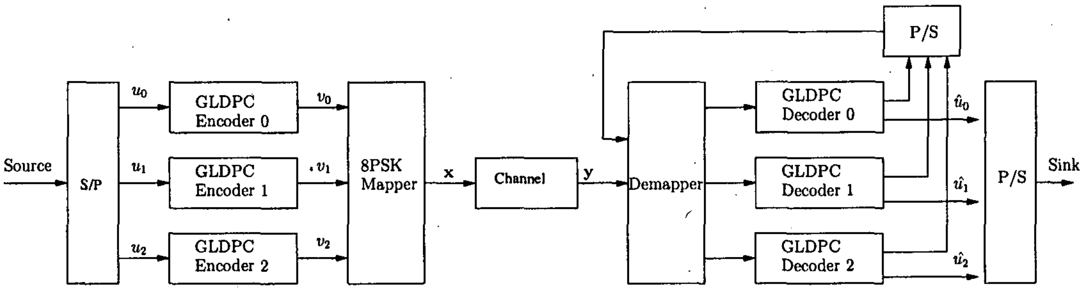

Figure 5.4: System model of the MLC/PID scheme using iteratively detected GLDPC inner codes as well as outer iterations. The iterative GLDPC decoder is seen in Figure 5.3.

The 3 bit/symbol encoded data is transmitted using 8PSK modulation. We combine the three GLDPC component codes of Figure 5.4 having different code rates, where each of the three source bits u_0, u_1 and u_2 is encoded into the associated coded bit v_0, v_1 and v_2 before the 8PSK mapper, as seen in Figure 5.4. At the output of the channel, the received bits are demodulated and decoded with the aid of their corresponding GLDPC decoders for the sake of obtaining the decoded output bits of $\hat{u}_0$, $\hat{u}_1$ and $\hat{u}_2$, as seen in Figure 5.4. The 8PSK mapper employs GM when non-iterative detection is used and UP, when iterative detection is invoked, as outlined below.

Again, Gray mapping is employed in our non-iterative scheme, where the parallel decoding of the three bits is implemented without outer iterations because this bit-to-symbol mapping provides the best achievable non-iterative detection performance. The absence of a long interleaver in Figure 5.3 has the potential of reducing the decoding delay imposed. However, for the sake of achieving a useful outer iteration gain in the decoder of Figure 5.4, we also propose an iterative scheme employing UP, as described in Section 2.2.1 and Figure 2.2. Again, the outer iterations are illustrated in Figure 5.4, while the inner iterations are portrayed in Figure 5.3. The *extrinsic* soft LLRs generated by the GLDPC decoders are converted into a stream of *a priori* bit probabilities, which are then fed back to the input of the demapper seen in Figure 5.4 as the *a priori* information to be used in the next outer iteration.

Since the *a priori* information fed to the demapper of Figure 5.4 represents non-equiprobable symbol probabilities after the first iteration, the achievable iteration gains may be expected to increase by efficiently exploiting the *a priori* probabilities, provided that an appropriate bit-to-symbol mapping scheme is used. In other words, after the first outer iteration, the channel output y seen in Figure 5.3 will be enhanced by the *a priori* information P_a provided by the previous outer iteration. The extrinsic probability expression P_e of the MLC demapper of Figure 5.4 providing new information for enhancing our confidence in y was given by [53].

Our objective is to compare the MLC employing GLDPC components with the classic LDPC component codes. We fix the coding rate in order to reduce the configurable parameters. With the aid of the equivalent capacity rule outlined in Section 2.2.2 [51], we obtain the desired code rate of each component code designed for 8PSK modulation using Gray Mapping, yielding $(R_0, R_1, R_2) = (0.510, 0.745, 0.745)$. Since the benchmarker system employs the same code rate, a fair comparison can be made. Given that the total number of uncoded input bits is k_i and the total number of channel coded output bits is n_i for the GLDPC encoder at the i^{th} MLC protection level, the coding rate of the ith GLDPC component code according to Equation (5.8) becomes [118]

$$R_i = 1 - \mathsf{W}(1 - k_i/n_i). \tag{5.10}$$

Therefore, the overall effective throughput η of the proposed system is

$$\eta = l - \mathsf{W} \sum_{i=0}^{i=l-1} (1 - k_i/n_i) \ \text{bits/symbol}, \tag{5.11}$$

where l is the total number of modulation levels and we have $i \in \{0, 1, ..., l-1\}$. The total code rate of our system is $R_t{=}\eta/\log_2 M$, where M is the total number of modem constellation points obeying $M = 2^l$. The effective throughput of the system is therefore $(0.51 + 0.745 + 0.745) = 2$ bit/symbol. The constituent codes employed in our scheme are Hamming codes due to their flexible coding rates, which approximate the above-mentioned equivalent-capacity based rates of 0.51, 0.745 and 0.745 are the $\Upsilon_0(20,15)$, $\Upsilon_1(48,42)$ and $\Upsilon_2(48,42)$ codes, respectively. The system parameters are summarised in Table 5.1. Our benchmarker scheme employing classic LDPC codes uses the equivalent PID coding rates of R_0, R_1 and R_2.

PID Coding rate	$(R_0, R_1, R_2) = (0.51, 0.745, 0.745)$
Hamming constituent codes	$[\Upsilon_0, \Upsilon_1, \Upsilon_2]=$ [(20,15), (48,42), (48,42)]
Modulation	8PSK
Non-iterative mapping scheme	Gray Mapping (GM)
Iterative mapping scheme	Ungerböck Partitioning (UP)
Number of symbols	2640

Table 5.1: System parameters table.

5.2.6 Simulation Results

The proposed MLC/PID GLDPC scheme using 8PSK modulation was investigated, when communicating over both AWGN and uncorrelated Rayleigh fading channels. We employed nine GLDPC inner iterations in the spirit of Figure 5.3. No outer iteration was used in conjunction with Gray demapping and five outer iterations employing UP mapping were carried out between the soft-decoded bits at the output of the three GLDPC decoders of Figure 5.4. Observe in Figure 5.5 that at BER $= 10^{-5}$, the proposed scheme demonstrates an E_b/N_0 improvement of around 0.5dB in AWGN channels compared to our MLC-LDPC benchmarker system, while exhibiting a convenient parallel decoding structure. When employing UP based mapping and five outer iterations over AWGN channels, both systems achieve a further 2 to 2.5 dB performance improvement and the proposed MLC-GLDPC scheme retains its performance advantage. When communicating over uncorrelated Rayleigh fading channels, as shown in Figure 5.6, our MLC-GLDPC scheme outperforms the MLC-LDPC benchmarker by about 1dB in both Gray mapping based scheme dispensing with outer iterations and in the five outer-iteration-aided UP-based scenarios at BER $= 10^{-5}$. This might appear to be a modest gain, but it is achieved with the aid of a more convenient parallel architecture.

We further investigate the effects of inner iterations in our MLC-GLDPC scheme with reference to our MLC-LDPC benchmarker in both AWGN and uncorrelated Rayleigh fading channels. The inner iterations are facilitated in the context of GLDPC component codes, since the information exchange can be carried out in the "turbo-like" architecture shown in Figure 5.3 with the aid of a number of parallel, low complexity SISO decoders, each requiring a reduced block length in comparison to LDPC or turbo component codes. The number of inner iterations required for generating the most reliable extrinsic output for the outer iterations therefore also determines the delay

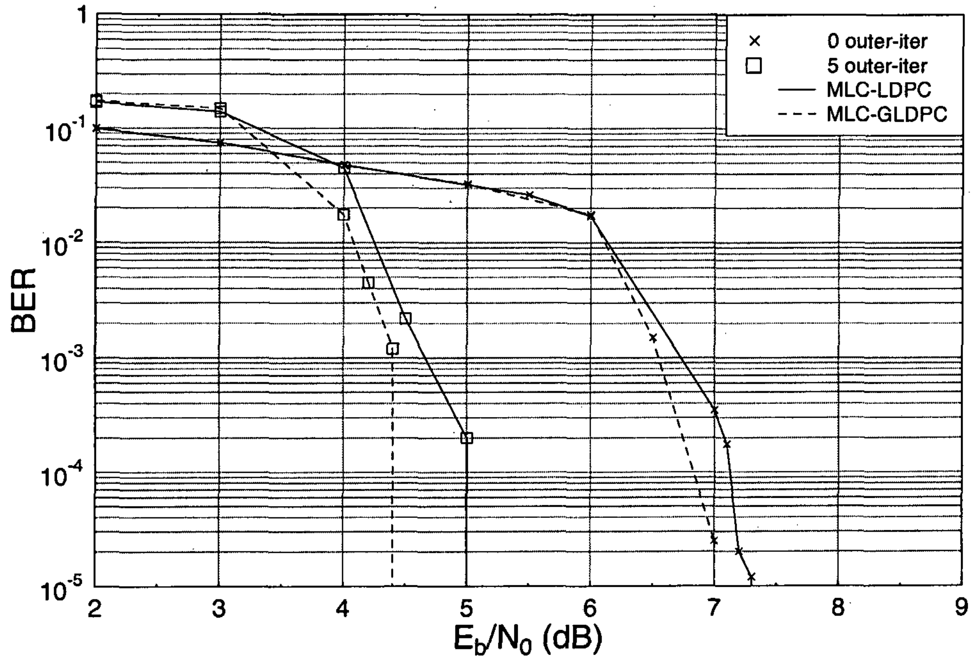

Figure 5.5: BER of both the MLC-GLDPC scheme of Figure 5.4 and MLC-LDPC over an AWGN channel invoking I_{outer}=0 or 5 outer and I_{inner}=9 inner iterations. The effective throughput was 2 bits/symbol and the constituent codes were the (20,15), (48,42) and (48,42) schemes, respectively. The parameters are summarised in Table 5.1.

imposed on the overall system.

We employ $I_{outer} = 5$ outer iterations in our MLC-GLDPC scheme, each invoking a different number of inner iterations (I_{inner}) using the UP mapping scheme. Figure 5.7 demonstrates that when transmitting over AWGN channels, our MLC-GLDPC scheme requires an E_b/N_0 value of around 4.6dB at BER = 10^{-5}, in conjunction with I_{inner} = 4 inner iterations. The MLC-LDPC benchmarker converges slowly at an E_b/N_0 close to 4.6dB, requiring up to I_{inner} = 19 inner iterations for achieving BER = 10^{-5}. In other words, the classic MLC-LDPC requires more than quadrupled number of total iterations ($I_{outer} \cdot I_{inner}$) compared to our MLC-GLDPC scheme for the sake of achieving a similar performance of BER = 10^{-5}.

Let us now extend these investigations to the uncorrelated Rayleigh fading channel, where both schemes invoke the same number of $I_{outer} = 5$ outer iterations. The MLC-GLDPC scheme achieves a coding advantage of 2dB compared to the MLC-LDPC scheme at BER = 10^{-5}, when invoking I_{inner} = 4 inner iterations, as shown in Figure 5.8. This coding advantage is reduced to about 1dB, when I_{inner} = 7 inner iterations

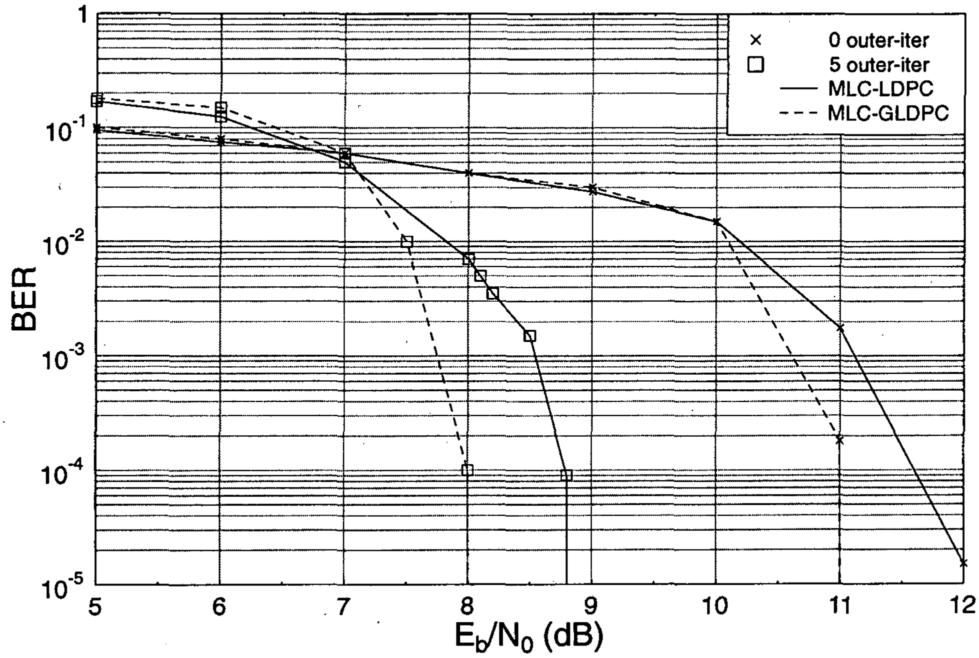

Figure 5.6: BER of both MLC-GLDPC scheme of Figure 5.4 and MLC-LDPC over an Uncorrelated (UC) Rayleigh fading Channel invoking I_{outer}=0 or 5 outer and I_{inner}=9 inner iterations. The effective throughput was 2 bits/symbol and the constituent codes were the (20,15), (48,42) and (48,42) schemes, respectively. The parameters are summarised in Table 5.1.

are employed. As observed from both Figures 5.7 and 5.8, our MLC-GLDPC scheme requires $I_{inner} = 4$ inner iterations for achieving its best possible BER performance both in AWGN and uncorrelated Rayleigh fading channels.

5.3 An Iterative Stopping Criterion for MLC-GLDPCs

Recall from Section 5.1 that the MLC-GLDPC scheme employing the PID decoding structure is capable of reducing the decoding delay imposed. In this section we propose an adaptive iterative detection aided MLC-GLDPC system, which invokes an adaptive inner and outer iteration stopping criterion, when the desired BER performance is attained.

5.3.1 GLDPC Syndrome Evaluation

As seen from the simulation results of Figures 5.5, 5.6, 5.7 and 5.8 in Section 5.2.6, we can appropriately configure the number of inner and outer iterations in order to

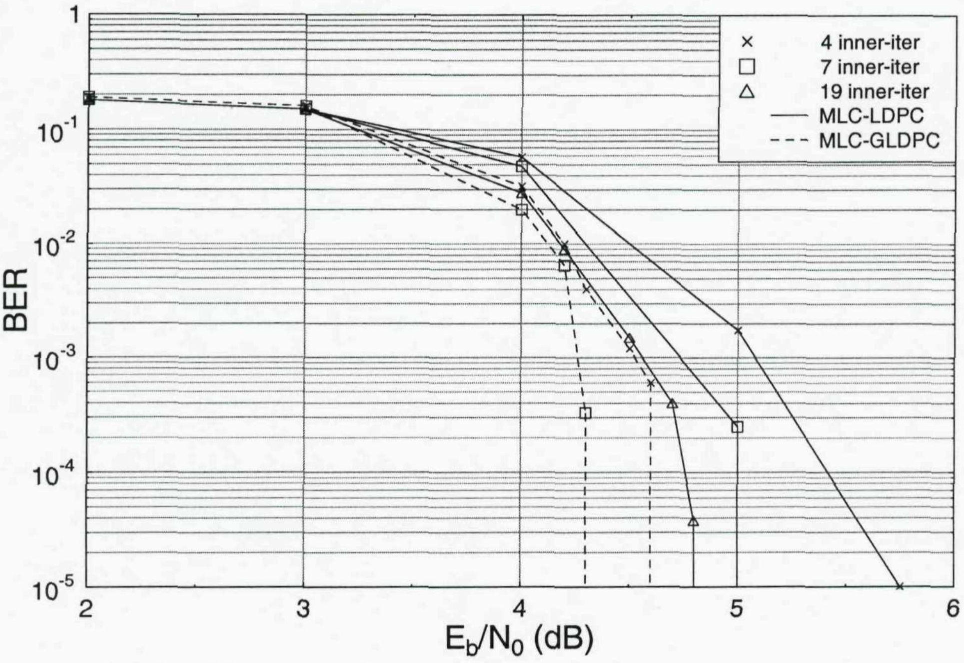

Figure 5.7: BER of both MLC-GLDPC scheme of Figure 5.4 and MLC-LDPC over an AWGN channel invoking $I_{inner} = 4$, 7 or 19 inner and $I_{outer} = 5$ outer iterations. The parameters are summarised in Table 5.1.

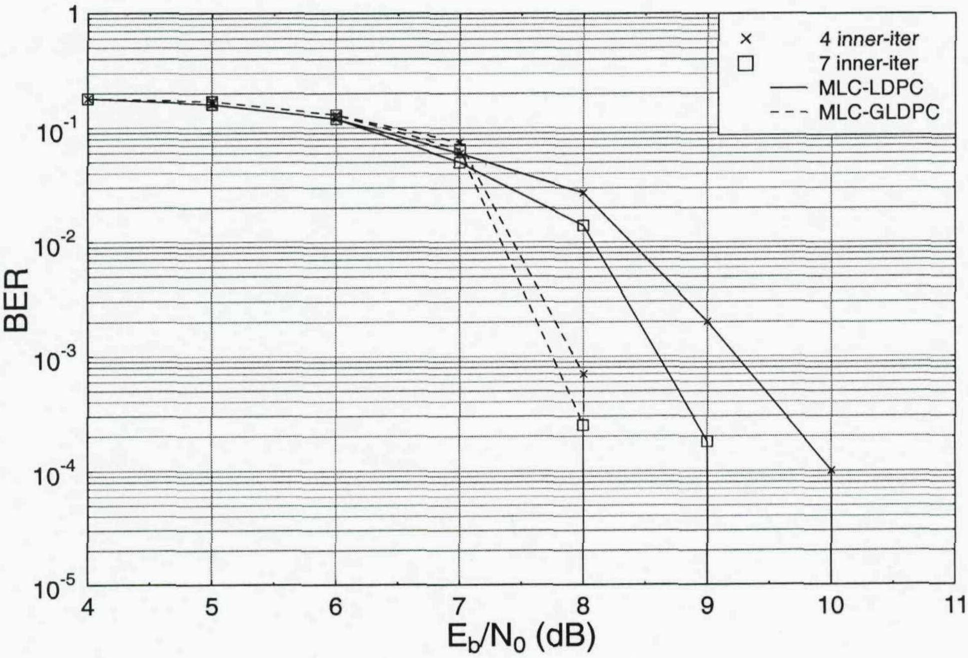

Figure 5.8: BER of both MLC-GLDPC scheme of Figure 5.4 and MLC-LDPC over uncorrelated Rayleigh fading channel invoking $I_{inner} = 4$ or 7 inner and $I_{outer} = 5$ outer iterations. The parameters are summarised in Table 5.1.

achieve a certain coding performance. Naturally, the decoder's complexity increases, as the number of iterations increases.

As described in Sections 5.2.1 and 5.2.2, the PCM of GLDPCs is constructed by concatenating L number of smaller constituent block codes $\Upsilon(n,k)$, such as BCH codes within a super-code. The PCM $\mathbf{H}$ of the GLDPC can be employed for calculating the syndrome as follows [83]

$$\mathbf{S}_{(1\times(N-K))} = \mathbf{Y}_{(1\times N)}\mathbf{H^T}_{(N\times(N-K))}, \tag{5.12}$$

where $\mathbf{S}$ denotes the syndrome and $\mathbf{Y}$ represents the received code matrix. If the syndrome $\mathbf{S}$ becomes an all-zero vector, the received codewords are legitimate.

Since a super-code of the GLDPC consists of several shorter constituent codes, the PCM of each binary constituent code denoted as $\mathbf{H}_\Upsilon$ can be shown to have a syndrome formulated as follows [83]

$$\mathbf{S}_{\mathbf{i}(1\times(n-k))} = \mathbf{Y}_{\mathbf{i}(1\times n)}\mathbf{H}_{\Upsilon}^{\mathbf{i}}{}^{\mathbf{T}}{}_{(n\times(n-k))}, \tag{5.13}$$

where the received codewords are denoted as $\mathbf{Y_i}$ and the resultant syndrome is represented by $\mathbf{S_i}$, $i \in \{1 \ldots L\}$. Figure 5.9 further illustrates this GLDPC syndrome checking process invoked to verify, whether a legitimate codeword was output by the GLDPC decoder. This diagram illustrates the first super-code's GLDPC syndrome checking process for each constituent code, as detailed in Equation (5.13).

In the context of M-ary modulation, our MLC-GLDPC scheme consists of $l = \log_2 M$ number of GLDPC component codes, each constituted by L number of short constituent codes $\Upsilon(n,k)$. Consider only the first super-code having a PCM of $\mathbf{H^1}$, and let us evaluate the syndromes formulated in Equations (5.12) and (5.13) in order to estimate the constituent codeword error rate at the output of a GLDPC component code. Naturally, a non-zero syndrome $\mathbf{S}$ found for a constituent code represents an erroneous constituent codeword at the decoder. Since there are a total of L constituent codes in a GLDPC super-code, the codeword error rate at the output of the GLDPC component code estimated after a certain number of inner iterations, is computed as follows

$$\varepsilon = \sum_{i=1}^{i=e} a_i/L, \tag{5.14}$$

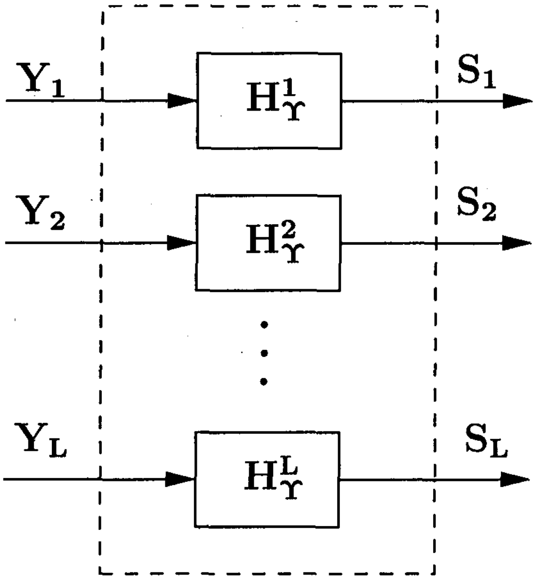

Figure 5.9: GLDPC syndrome checking.

where a_i has a value of 1, if the i^{th} constituent codeword has a non-zero syndrome and e is the number of error-infested constituent codeword. Taking the first super-code $\mathfrak{C}^1$ for example, 2640 coded bits are generated as parameterised in Table 5.1, where the number of constituent Hamming codes is $L = 2640/20 = 132$. In order to achieve a target error rate of 0.045, we set $\varepsilon = 0.045$, while the corresponding estimated value e would be 6, which results in $\varepsilon = \sum_{i=1}^{i=6} 1/132 \approx 0.045$.

Having computed the estimated codeword error ratio ε for the GLDPC component codes, we can control the number of inner iterations required, when aiming for maintaining a specific constituent error ratio ε at the output of each GLDPC code. In order to control the number of outer iterations required, we can fix the number of inner iterations, while taking into account the average codeword error ratio at the output of the MLC-GLDPC scheme as follows

$$\varepsilon_{\text{avg}} = \sum_{i=0}^{i=l-1} \varepsilon_i / l, \tag{5.15}$$

where ε_i is the error ratio of the output of the i^{th} GLDPC component code and l denotes the number of GLDPC component codes. As an example, let us invoke a three-component MLC associated with $l = 3$, while the codeword error ratio of each GLDPC component code is denoted as ε_1, ε_2 and ε_3, which was formulated in Equation (5.14). Therefore, referring to Equation (5.15), in order to achieve an overall codeword error rate of, say 0.045, our stopping criterion is satisfied when we have $\varepsilon_{\text{avg}} = 0.045$. The codeword error rate of the adaptive scheme is approximated to be the target bit error rate which might result in a slight difference of accuracy. Therefore a small constituent code with smaller number of bits in a codeword would produce a more reliable iteration stopping criterion.

In conclusion, even though the syndrome evaluation method does not provide 100% error checking reliability, this 'on the fly' codeword error rate evaluation procedure allows us to minimise the number of inner and outer iterations required by the decoder for maintaining an infinitesimally low BER.

5.3.2 Simulation Results

Our simulation results provided in this section characterise the number of inner and outer iterations required for achieving the target BER performance, as detailed in Section 5.3.1.

Figure 5.10 illustrates the BER performance of our proposed MLC-GLDPC schemes invoking a fixed number of $I_{inner} = 4$ iterations. A *maximum* of $I_{outer} = 9$ iterations were employed. The number of iterations was based on Equation (5.15), which was configured for maintaining a BER of 10^{-5}. The achievable BER performance is similar or slightly better than that seen in Figures 5.5 and 5.6, despite reducing the number of iterations from $I_{inner} = 9$ to $I_{inner} = 4$ in these figures. The effect of the number of outer iterations is shown in Figure 5.11. Note that for low E_b/N_0 values below $E_b/N_0 = 4dB$ the maximum number of $I_{outer} = 9$ iterations had to be invoked. However, as expected, the BER performance of the system starts to improve for higher E_b/N_0 values and at $E_b/N_0 = 4.5dB$ only $I_{outer} = 6$ iterations were required for transmission over AWGN channels at the achievable target BER of 10^{-5}. The number of iterations is seen to be further reduced in Figure 5.11 for higher E_b/N_0 values for transmission over both AWGN and Rayleigh channels.

Figure 5.12 shows the BER performance of the MLC-GLDPC scheme communicating over both AWGN and UC Rayleigh fading channels. Note that this time we fixed the number of outer iterations to $I_{outer} = 4$, while setting the *maximum* number of inner iterations to $I_{inner} = 9$. The corresponding number of required inner iterations can be inferred from Figure 5.13, where the target BER was 10^{-5}. Figure 5.13 details the number of inner iterations required by each individual GLDPC component code

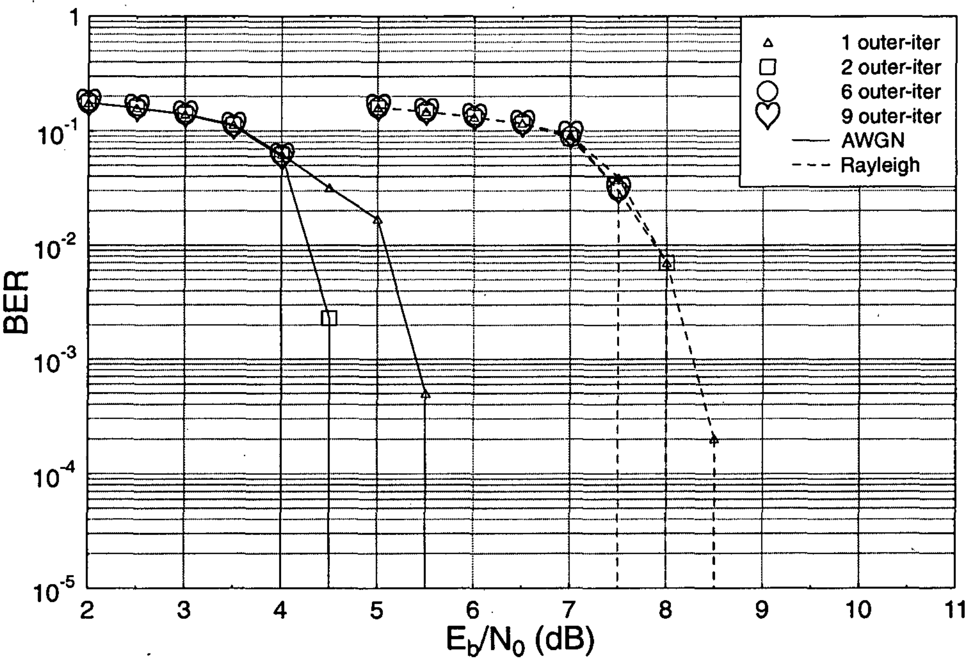

Figure 5.10: BER performance of the MLC-GLDPC scheme of Figure 5.4 for transmission over both an AWGN Channel and UnCorrelated (UC) Rayleigh fading channel invoking $I_{inner} = 4$ inner iterations. The effective throughput was 2 bits/symbol and the constituent codes were the (20,15), (48,42) and (48,42) schemes, respectively. The target BER was 10^{-5} and a *maximum* of $I_{outer} = 9$ outer iterations were used. The parameters are summarised in Table 5.1. Note that for AWGN and Rayleigh channels experiencing an E_b/N_0 less than 4dB and 7.5dB, the BER performance achieved at different number of iterations is identical and the markers in the graph overlap with one another.

at each MLC level, again, when limiting the maximum number of inner iterations to $I_{inner} = 9$. For example, when transmitting over the UC Rayleigh fading channel, the system requires a reduced number of $I_{inner} = 1$ iteration to attain a BER value of 10^{-5} for the level-0 GLDPC component code at $E_b/N_0 = 8$dB.

5.4 Coding for the Wireless Internet

As an application example, in this section a coded modulation aided wireless Internet scheme was investigated. As briefly mentioned, in Section 5.1, for the sake of addressing these wireless Internet design problems, in this section we propose a rather different solution. The Internet packets consist of a number of symbols, where each symbol contains a certain number of bits. These individual bits are transmitted in terms of non-binary modulated symbols over the wireless channel after modulation.

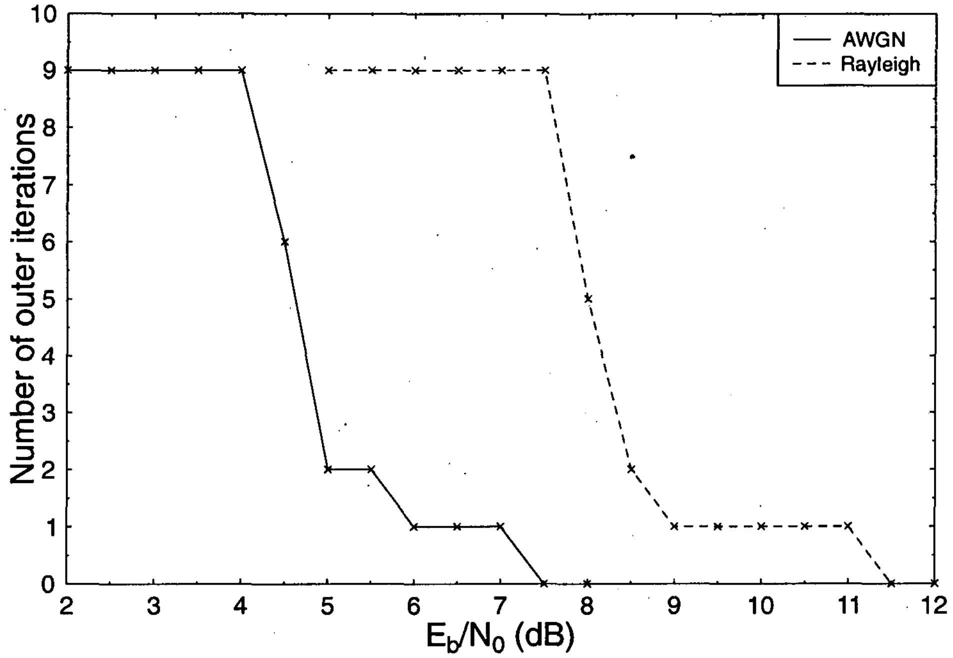

Figure 5.11: Number of outer iterations I_{outer} required for achieving the BER performance shown in Figure 5.10.

An error correcting code is employed for the sake of recovering the original symbols. However, to avoid the employment of a retransmission mechanism, which requires the provision of a feedback channel, in addition to using redundant data symbols for FEC coding, the source may transmit a limited number of redundant data packets, which helps the decoder to recover the original data file, even if the FEC code failed to remove all errors in some of the packets. This regime requires the employment of a specific code, which is capable of filling in the missing packets dropped by the statistical multiplexing function of the Internet packet router. Hence in this chapter we combine the BICM-ID scheme of Section 2.4 which is serially concatenated with LT coding. We refer to this scheme as an LT-BICM-ID arrangement.

5.4.1 Fountain Codes

Let us consider the scenario that a Mobile Station (MS) would like to fetch a data file from a server using the wireless Internet constituted by an ad hoc network of MSs. The Internet protocol using ACK-based ARQ may be expected to have an excessive transmission overhead in a hostile wireless ad hoc propagation environment

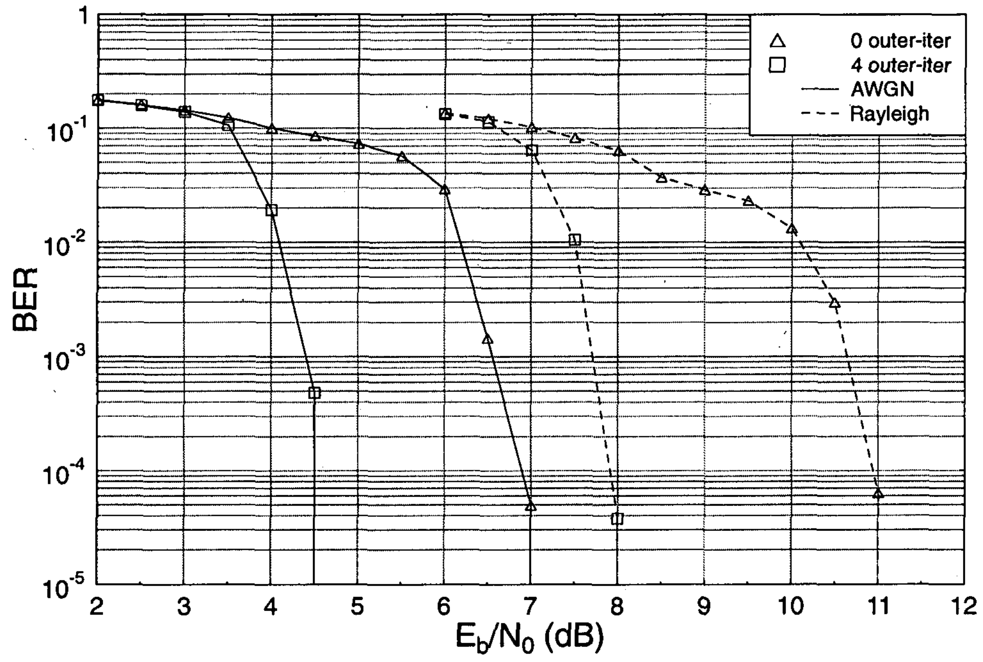

Figure 5.12: BER of MLC-GLDPC scheme of Figure 5.4 for transmission over both AWGN Channel and UC Rayleigh fading channels, when invoking $I_{outer} = 4$ outer iterations. The effective throughput was 2 bits/symbol and the constituent codes were the (20,15), (48,42) and (48,42) schemes, respectively. The target BER was 10^{-5} and the simulations were continued for a *maximum* of $I_{inner} = 9$ inner iterations. The parameters are summarised in Table 5.1.

due to the preponderance of error-infested and therefore retransmitted packets. Hence again, a more efficient design alternative is proposed here, which invokes the novel family of Fountain codes [121] [122] [123]. To elaborate a little further, Fountain codes [122] belong to the family of so-called sparse-graph codes designed for transmission over channels inflicting packet erasures, such as the wireless Internet, where files are transmitted by partitioning them into transmission packets and then forwarding them to a specific MS, for example over many independent links constituted by the routes of an ad hoc network.

In 1998, Luby and Buyers proposed the employment of sparse-graph codes [126]. They partitioned the data files into transmission packets and the number of bits per packet was defined based on the size of files [126] [127]. With the advent of these codes we are capable of transmitting as many encoded packets as necessary for recovering the source data, provided that the number of received packets is sufficiently higher than the number of original packets.

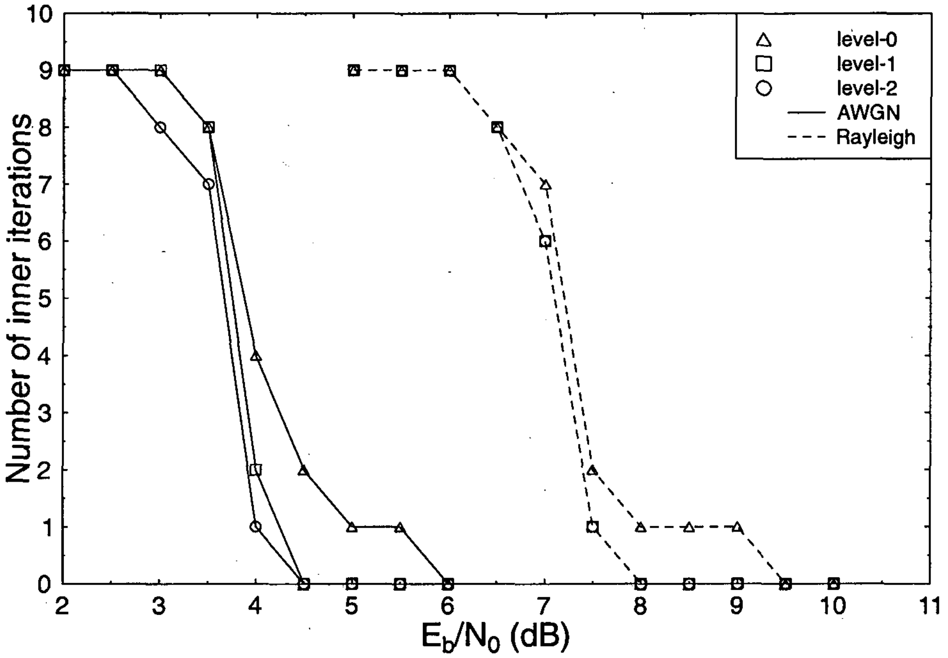

Figure 5.13: Number of inner iterations I_{inner} required to achieve the BER performance as shown in Figure 5.12.

Again, the corresponding codes are referred to as digital Fountain codes based on the analogy of a fountain [121], which is capable of producing a sufficiently large supply of water drops. Each water drop may represent a data packet of original bits. Let us assume that the number of source packets in a file is $\mathcal{K}$, where each source file has the size of $\mathcal{K}\times$ (number of bits per packet). Metaphorically speaking, the MS which would like to receive the original data file will have to fetch it drop-by-drop, i.e. packet-by-packet until the bucket is filled with the received packets. More explicitly, this bucket will collect a certain number of water drops, which is higher than the number of original packets $\mathcal{K}$. Again, when using the serially concatenated LT-BICM-ID coding scheme, a total of $\mathcal{K}\times$ (number of coded bits) are transmitted and we would like to simultaneously maximise both the concatenated scheme's coding-rate of R and the achievable integrity expressed in terms of the Packet Loss Ratio (PLR).

5.4.1.1 Random Linear Fountain Code

The generator matrix of a random linear Fountain code is constructed by a deterministic random-number generator [122]. Figure 5.14 exemplifies the generator matrix of a random linear code. The source transmits $\mathcal{K}'$ number of packets, where $\mathcal{K}'$ is higher than the number of original source packets $\mathcal{K}$. Some transmitted packets may become erased over the Internet channel which is indicated by the grey shaded columns in Figure 5.14 and a total of $\mathcal{N}$ packets are received, where $\mathcal{N}$ is higher than $\mathcal{K}$.

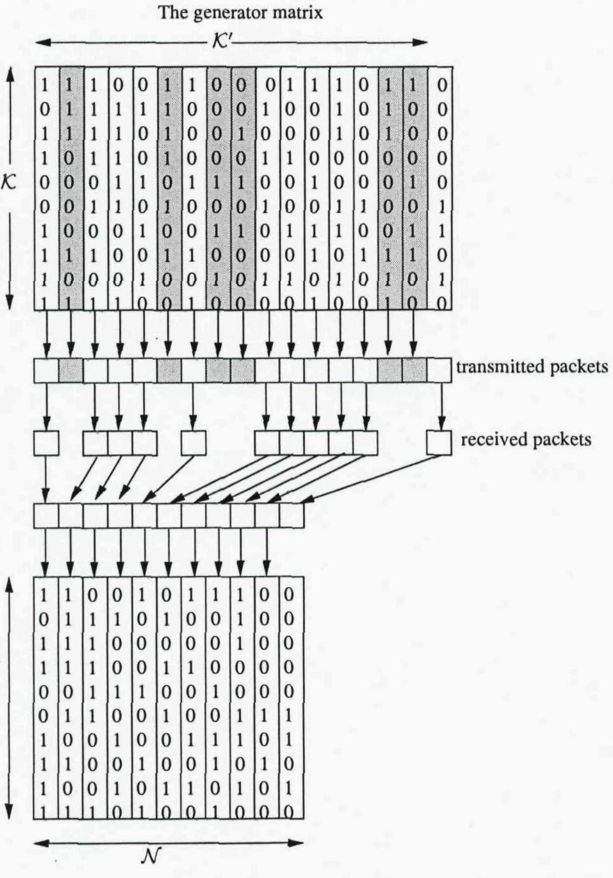

Figure 5.14: Generator matrix of a random linear code in which the grey shaded column indicates the erased packets. The receiver will receive the packets indicated by the bottom ($\mathcal{K} \times \mathcal{N}$) matrix [128].

Each column of the generator matrix $\mathbf{G}_{(\mathcal{K}\times\mathcal{K}')}$ is constituted by a random pattern at LT-encoded packet transmission instant i and is denoted as $\mathbf{G}_{ki}$. A source file constituted by $\mathcal{K}$ packets are considered, while are denoted as $\mathcal{S}_1, \mathcal{S}_2, ..., \mathcal{S}_{\mathcal{K}}$. The original LT-encoded transmitted packet $\mathcal{T}_i$ at time instant i is generated as the modulo-2 bit-wise addition of the source packets for which G_{ki} contains a binary value of 1 as follows [128]

$$\mathcal{T}_i = \sum_{k=1}^{\mathcal{K}} \mathcal{S}_k \mathbf{G}_{ki}. \tag{5.16}$$

Each source packet $\mathcal{S}_i$ consists of a string of binary symbols, depending on the size of a packet. The transmitted packet $\mathcal{T}_i$ may then be erased by the Internet channel inflicting packet erasures. In this scheme, we assume that the transmitter and receiver have a perfectly synchronised identical generator matrix, where the receiver is also aware of the erased packets' index or identifier and the associated generator matrix $\mathbf{G}_{ki}$.

The source packets can then be decoded by the Gaussian elimination process as follows [128]

$$\mathcal{S}_k = \sum_{i=1}^{\mathcal{N}} \mathcal{T}_i \mathbf{G}_{ik}^{-1}. \tag{5.17}$$

Note that legitimate decoding is only possible, if the generator matrix $\mathbf{G}$ is invertible, i.e. the inverse matrix $\mathbf{G}^{-1}$ exists.

5.4.2 LT Code

In 2002, a novel family of the Luby Transform (LT) codes [123] was proposed, which exhibited a higher source packet recovery probability and a lower complexity than the family of Fountain codes [121]. The encoding operation of LT codes is similar to that of the Fountain encoder [123], as described in Section 5.4.1.1. Based on the source packets $\mathcal{S}_1, \mathcal{S}_2, ..., \mathcal{S}_{\mathcal{K}}$, we are able to choose a degree d from the so-called *ideal soliton* distribution defined in $\rho(d)$ [121] which will be described in the next section, in order to construct a generator matrix $\mathbf{G}$.

By definition, the degree d_i of a distribution at the time instant i of generating a $\mathcal{K}$-bit transmission packet represents the number of connections or *edges* between the received packets and the original source packets, as seen in Figure 5.15, which indicates with the aid of the LT-decoding rules of [123] how the source packets can be recovered from the received packets. More explicitly, the packet duration here refers to the time interval in which $\mathcal{K}$ random bits are generated by the encoder's generator matrix. As it will be detailed in the next section, the appropriate choice of $\rho(d)$ determines the number of packets $\mathcal{K}$ in the source file to be transmitted.

To elaborate a little further, Figure 5.15 presents an example of the LT decoding process, where we observe three source packets $\mathcal{S}_i$, each packet containing n=3 information bits. These packets are represented by hollow squares, which were previously

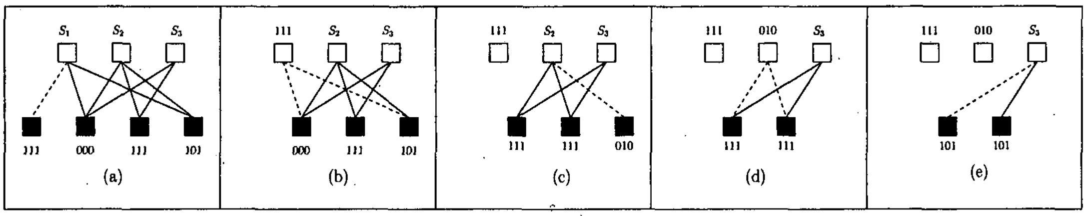

Figure 5.15: *Decoding of a LT code having $\mathcal{K} = 3$ source packets and $\mathcal{N} = 4$ transmitted packets each containing 3 bits; adopted from ©Luby [122].*

encoded into four transmitted packets represented by the filled black squares. The value of each bit within the transmitted packet is the result of the modulo-2 operation of the corresponding source packets connected to it. The decoding process is implemented as follows.

In the first cycle of the decoding process seen in Figure 5.15(a), the LT decoder determines, which of the received packets has a degree of one, indicating that this is a self-contained packet, which was not combined with any other source packet using the modulo-2 operation. Hence the decoding operation is simply constituted by outputting the corresponding source packet as indicated by the dashed line in Figure 5.15(a). At the same time, the decoder finds other transmitted packets, which are connected to this source packet of Figure 5.15(b). In order to further exploit the encoding rules of the specific LT-code used, as seen in Figure 5.15(b), the decoder erases the already exploited connections.

As the next decoding step, the received packets that have a link to the decoded degree-one packet are updated by modulo-2 adding their value to the value of each related packet, i.e. connected source packet. More explicitly, in this example the first transmitted degree-one packet found by the decoder is the packet having the value of "111" and the corresponding source packet is $\mathcal{S}_1$. Hence, in the next decoding cycle seen in Figure 5.15(b), $\mathcal{S}_1$ is decoded a value "111" and the connections drawn from this packet to the second and the fourth transmitted packets using dashed lines are erased. Correspondingly, the values of the second and fourth transmitted packets change from "000" in Figure 5.15(b) to "111" from "101" to "010", as observed in Figure 5.15(c). As seen in Figure 5.15(d) and 5.15(e), at the end of the LT decoding process all of the three source packets $\mathcal{S}_1$, $\mathcal{S}_2$ and $\mathcal{S}_3$ are recovered.

5.4.2.1 Degree Of Distribution

An appropriate choice of the degree of distribution is crucial in the design of LT codes for the sake of maintaining a low PLR. Every source packet must have at least one *edge* leading to the received packet, where an *edge* is defined as the connection in Figure 5.15, indicating the reception of a source packet, which was LT-encoded using the time-variant generator matrix defined for the corresponding packet interval. Ideally, upon the successful reception of a packet, a new self-contained degree-one received packet should appear for the sake of avoiding having redundant packets. This objective is achieved by the *ideal soliton* distribution of [122]

$$\rho(d) = \begin{cases} 1/\mathcal{K} & \text{for } d = 1, \\ \frac{1}{d(d-1)} & \text{for } d = 2, 3, ..., \mathcal{K}, \end{cases} \tag{5.18}$$

which is plotted in Figure 5.16. However, the above-mentioned ideal behaviour is only achievable with a certain probability [122]. When no degree-one packet is recovered at any stage of the consecutive LT-decoding cycles exemplified in Figure 5.15, the decoding process will be suspended and therefore the remaining packets cannot be recovered, unless a sufficiently high number of redundant packets is received. Hence the so-called *robust soliton* distribution was designed by Luby [123] for circumventing this problem by increasing the expected number of degree-one encoded packets to $\mathbb{S} \equiv c \cdot \log_e(\mathcal{K}/\delta)\sqrt{\mathcal{K}}$, where the parameter δ denotes the probability of decoding failure imposed by the lack of a degree-one packet, while c represents a constant. More explicitly, taking the above-mentioned parameters into consideration, Luby proposed the improved distribution of [123]

$$\tau(d) = \begin{cases} \frac{\mathbb{S}}{\mathcal{K}}\frac{1}{d} & \text{for } \; d = 1, 2, \ldots, \frac{\mathcal{K}}{\mathbb{S}} - 1, \\ \\ \frac{\mathbb{S}}{\mathcal{K}}\log(\frac{\mathbb{S}}{\delta}) & \text{for } d = \frac{\mathcal{K}}{\mathbb{S}}, \\ \\ 0 & \text{for } d > \frac{\mathcal{K}}{\mathbb{S}}, \end{cases} \tag{5.19}$$

which is also plotted in Figure 5.16 as a function of the degree d. Finally, for the sake of improving both the distributions of Equations (5.18) and (5.19), Luby introduced the so-called *robust soliton* distribution μ, which is constituted by the superposition of the *ideal soliton* distribution $\rho(d)$ and that of Equation (5.19) as [123]

$$\mu(d) = \frac{\rho(d) + \tau(d)}{Z}, \tag{5.20}$$

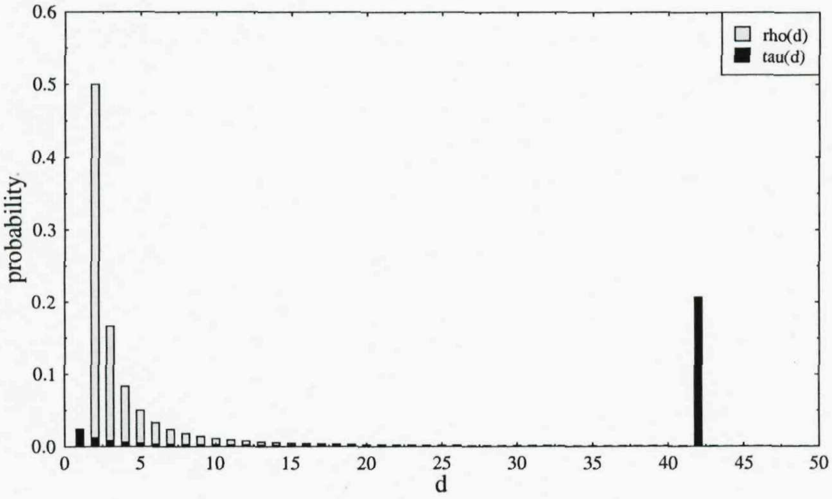

Figure 5.16: The distributions $\rho(d)$ of Equation (5.18), $\tau(d)$ of Equation (5.19) for the case of $\mathcal{K}$=10000, c=0.2, δ=0.05. [123]

where the normalisation factor of the denominator is given by $Z = \sum_d (\rho(d) + \tau(d))$, ensuring that all the probabilities sum to unity. The function $\mu(d)$ is portrayed in Figure 5.17.

In practice, an LT code is capable of recovering the transmitted file having $\mathcal{K}$ packets, if it receives about 5% more packets than the number of original source packets $\mathcal{K}$ [122], provided that the channel conditions are adequate. The values of the parameters c and δ in $\mathbb{S} \equiv c \cdot \log_e(\mathcal{K}/\delta)\sqrt{\mathcal{K}}$ determine the number of packets required for recovering all the $\mathcal{K}$ source packets.

5.4.2.2 Improved Robust Distribution

In this section, we propose an Improved Robust Distribution (IRD). Referring to Luby's *robust soliton* distribution characterised in Figure 5.17, we observe that there exist some degree distributions, which have such a low probability P_{di} that the number of packets given by the the product of P_{di} and $\mathcal{K}$ may be less than one, indicating the potential absence of packets having these degrees. It is undesirable to invoke this particular distribution in the computation of the LT encoder's generator matrix **G**. Therefore, in some cases Luby's *robust soliton* distribution defined by Equation (5.20) may lead to premature decoding abortion and a concomitant loss of packets during the

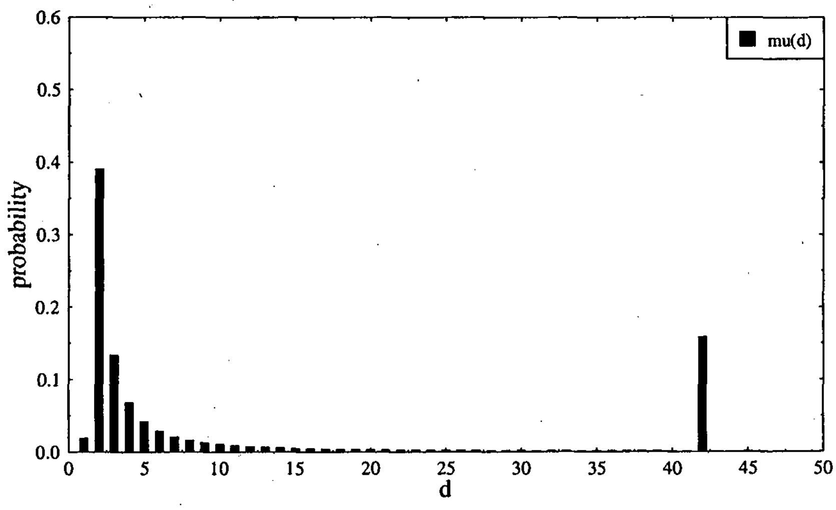

Figure 5.17: The robust distributions $\mu(d)$ of Equation (5.20) for the case of $\mathcal{K}$=10000, c=0.2, δ=0.05.

decoding process, unless the number of redundant packets is high. When the decoding process is suspended due to the absence of a degree one packet, we need more received packets for recovering all source packets.

In view of this, let us consider the case, when we have $P_{di} \cdot \mathcal{K} < 1$ in Luby's *robust soliton* distribution. Our novel proposition is to improve the distribution's behaviour by introducing an extra factor

$$\varpi = \sum \mu(d_i) \cdot \mathcal{K}, \tag{5.21}$$

for the sake of creating a more beneficial degree distribution where d_i represents the degree-i term of the distribution, satisfying the following conditions

$$\begin{cases} \left(\frac{\frac{1}{d(d-1)}+\frac{\mathbb{S}}{\mathcal{K}}\cdot\frac{1}{d}}{Z}\right)\cdot\mathcal{K} < 1 & \text{for } 2 \leq d \leq \frac{\mathcal{K}}{\mathbb{S}}-1, \\ \frac{1}{d(d-1)}\cdot\frac{\mathcal{K}}{Z} < 1 & \text{for } (\frac{\mathcal{K}}{\mathbb{S}}+1) \leq d \leq \mathcal{K}. \end{cases} \tag{5.22}$$

We determine the parameter ϖ with the aid of the set of inequalities given by Equation (5.22), so that we maximise the relative frequency of having packets of degree *one*, because this allows us to recover the source packets from a single received packet. In other words, the degree-one packets' reception probability was ignored by the original *robust soliton* distribution [122] [123] [126], which was now taken into account by our *improved robust* distribution.

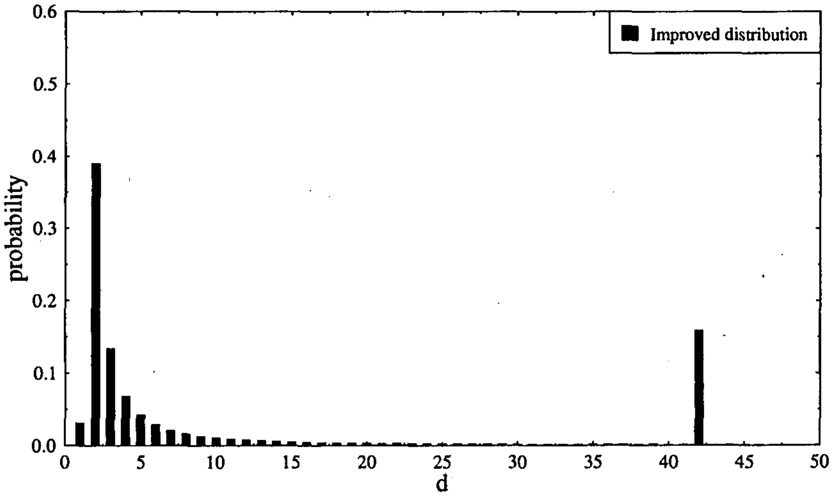

Figure 5.18: The *improved robust* distributions for the case of $\mathcal{K}$=10000, c=0.2, δ=0.05.

The measure of increasing the relative frequency of degree-one packets has however not only benefits, but also disadvantages. The main benefit is that a degree-one packet is self-contained and hence may be decoded without reference to any other received packets. By contrast, the disadvantage is that it contains less information about other received packets in comparison to higher-degree packets. Hence it may neither be used to recover other packets nor be recovered from other packets.

Figures 5.18, 5.19 and 5.20 characterise the IRD. When using Luby's *robust soliton* distribution of [122] and the LT coding scheme characterised in Figure 50.4 of [122], approximately 12 000 packets were required for recovering 10 000 packets with the probability at least $1 - \delta$ [122]. By contrast, the number of packets required was reduced to about 10 800, when using the IRD. Having characterised the proposed degree distribution [3], let us now focus our attention on the proposed system architecture.

---

[3] A more sophisticated systematic soft LT code was proposed in [129], where EXIT-chart analysis was invoked with the aid of the soft LLRs. Potentially, the degree distribution of the systematic LT can be optimised using the irregular concept detailed in Section 6.4 by invoking appropriate EXIT-chart matching algorithms.

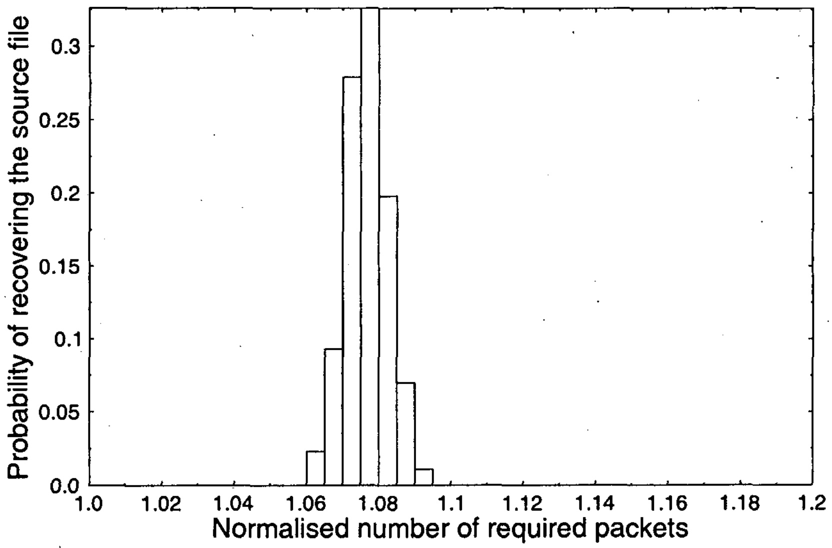

Figure 5.19: IRD based LT code specified in Figure 50.4 of [122] for c=0.1 and δ=0.5. The actual number of packets $\mathcal{N}$ required to recover the original source file of size $\mathcal{K}$=10000 packets is given by the product of $\mathcal{K}$ and the abscissa value

5.4.3 LT-BICM-ID System Overview

We propose a serially concatenated LT-BICM-ID system, as shown in Figure 5.22, where the LT coding scheme constitutes the outer code and the BICM-ID arrangement the inner code. Combining BICM with iterative decoding [23] leads to an improved performance for BICM-ID over both AWGN as well as Rayleigh channels. When using n original uncoded information bits per symbol, the number of coded BICM-ID output bits becomes $m = n + 1$. Assuming that the packets contain $\mathcal{P}$ number of symbols and that no tailing bits are used by the BICM-ID scheme, we have a total of $\mathcal{P} \cdot n$ number of bits in the LT source packets and the total rate of the LT-BICM-ID code becomes $R = \mathcal{K}n/\mathcal{K}'m$. Figure 5.21 illustrates the structure of the source packets as well as the encoded packets employed in the LT-BICM-ID scheme.

Our investigations are based on $\mathcal{P} \cdot n = 165$ bits per original source packet, which is similar to the 164-bit packet size of a transport multimedia service packet in the Time Division Duplex (TDD) mode of the Third-Generation (3G) wireless system [130]. The success or failure of a packet is decided on the basis of Cyclic Redundancy Check (CRC) detection [130]. We transmitted a total of $\mathcal{K} = 10^4$ source packets corresponding to 1 650 000 bits. The number of 'parity' packets was 3000, rendering the total number of received packets $\mathcal{N} = 13000$.

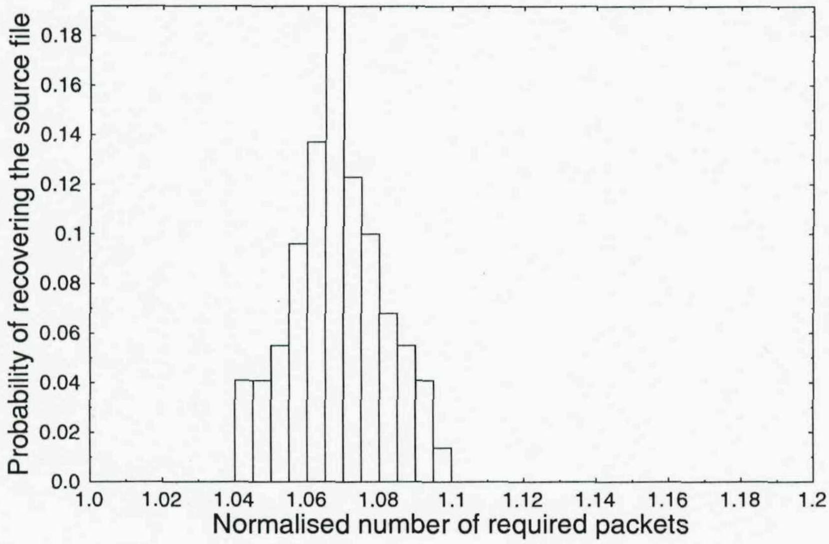

Figure 5.20: IRD based LT code specified in Figure 50.4 of [122] for c=0.03 and δ=0.5. The actual number of packets $\mathcal{N}$ required to recover the original source file of size $\mathcal{K}$=10000 packets is given by the product of $\mathcal{K}$ and the abscissa value

The BICM-ID encoder's output has $m = n+1 = 3+1 = 4$ encoded bits per symbol and therefore each packet consists of $\mathcal{P} = 165/3 = 55$ 16QAM symbols. Hence the size of the BICM-ID encoded packet transmitted over the wireless channel is constituted by $(165 \times 4/3 = 220)$ bits/packet. Each symbol is modulated using 16QAM modulation and transmitted over an AWGN channel. Additionally, random packets are assumed to be erased by the Internet modelled by the BEC . The received packet is demodulated and decoded at the receiver. The effective code rate of our system is $R = \mathcal{K} \cdot n/\mathcal{K}'m = (10000 \times 3)/(13000 \times 4) = 30000/52000 = 15/26$. The erasure channel imposes a

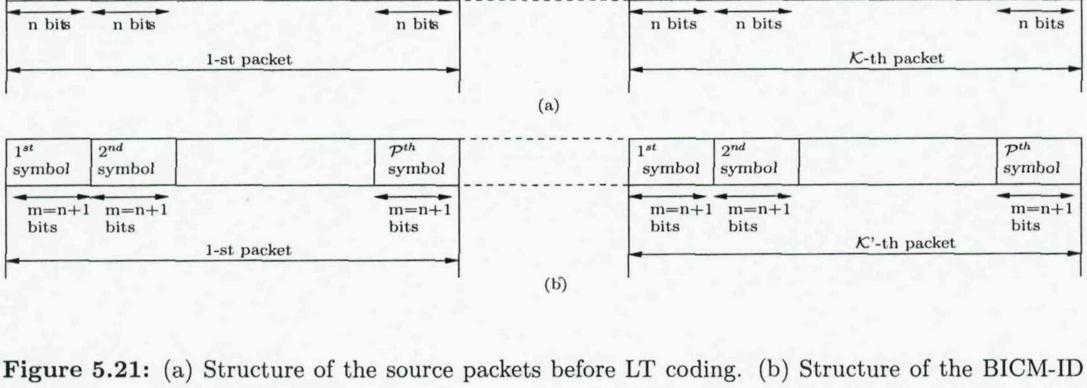

Figure 5.21: (a) Structure of the source packets before LT coding. (b) Structure of the BICM-ID encoded packets.

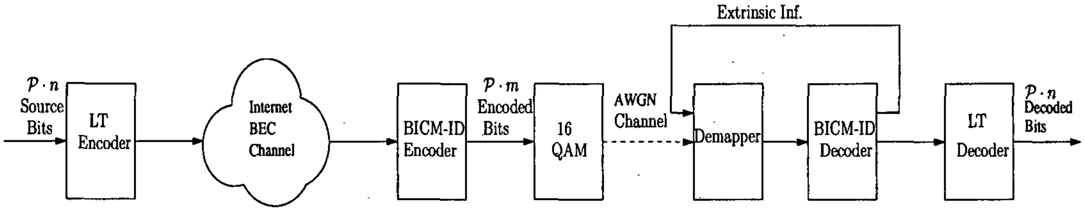

Figure 5.22: System structure of the proposed LT-BICM-ID scheme. The corresponding transmission frame structure is seen in Figure 5.21 and the associated system parameters are summarised in Table 5.2.

packet erasure probability of $P_e = 0.1$.

RS codes	C(7,3,2)
LT codes	C(10000,13000)
LT-BICM-ID codes	C(30000,52000)
BEC erasure probability	0.1
Modulation	16QAM
Number of source packets $\mathcal{K}$	10000
Number of transmitted packets $\mathcal{K}'$	13000
Number of bits per source packets $\mathcal{P}.n$	165

Table 5.2: System parameters.

At the demodulator, the received symbols are converted to soft bit values that are fed into the BICM-ID MAP decoder [65], which in turn generates the output *extrinsic* information constituting the *a priori* information to the input of the symbol-to-bit demapper seen at the input of the BICM-ID scheme in Figure 5.22. We used UP based mapping [23] for the sake of achieving an iteration gain as the benefit accruing from having a maximised Euclidean distance amongst the BICM constellation points.

The BICM-ID-decoded hard bits are then used as the input bits of the LT decoder in Figure 5.22. Since a belief propagation LT decoding algorithm is used [121], as described in Section 5.4.2, an excess number of errors found in the received packets may inflict error propagation and subsequently might degrade the reliability of the neighbouring check nodes, potentially imposing a low LT decoding performance. The output of the BICM-ID decoder ensures that the overwhelming majority of the erroneous bits has been corrected, hence reducing the probability of error propagation.

5.4.4 Simulation Results

In this section, we evaluate the BER performance of the system architecture characterised in Section 5.4.3, noting that the associated parameters are summarised in Table 5.2. These results are shown Figures 5.23 and 5.24. Reed-Solomon (RS) codes have been widely used for transmission over erasure-type channels before the introduction of Fountain codes [121], hence similar-rate RS codes were used for benchmarking.

Figure 5.23 shows the BER performance of the RS (7,3,2) code, the LT (13000, 10000) code and the proposed LT-BICM-ID (30000, 52000) code, when communicating over the BEC contaminated by AWGN, as shown in Figure 5.22. Again, the source file was constituted by $\mathcal{K} = 10000$ packets and a total of $\mathcal{K}' = 13000$ packets were transmitted. As it transpires from Figure 5.23, the stand-alone RS or LT code does not perform well, when communicating over the BEC contaminated by AWGN. The BEC employed has an erasure probability of 0.1. The LT-BICM-ID code also has a high BER for E_b/N_0 below 7.4dB, which however significantly improves above this point, as seen in Figure 5.23. This indicates that for $E_b/N_0 > 7.4$dB, the BICM-ID decoder becomes capable of correcting most of the bits in the $\mathcal{P} = 55$-symbol packets and the resultant number of corrupted bits becomes sufficiently low for the LT decoder to correct them.

Figure 5.23 also portrays the BER performance of the LT-BICM-ID scheme in conjunction with different number of inner BICM-ID iterations. The 2-iteration aided LT-BICM-ID code having a memory of eight states is only capable of achieving an error free BER performance for E_b/N_0 values in excess of 8.8dB, which is almost 1.5 dB higher than the corresponding E_b/N_0 threshold of the 10-iteration based inner code. This illustrates that as the inner code's error correcting capability improves, a higher fraction of error-free bits is passed to the LT decoder, hence enhancing the overall BER performance of the system.

Figure 5.24 further characterises a range of various LT-BICM-ID codes communicating over the BEC contaminated by AWGN and having different degree distributions [123]. For the general Poisson distribution, the degree of transmitted packets is defined by a function given in [123] as

$$\Omega_{\mathsf{B}}(x) = \frac{1}{\mu+1}\cdot\left(\mu.x + \frac{x^2}{1\cdot 2} + \frac{x^3}{2\cdot 3} + \ldots + \frac{x^{\mathsf{B}}}{(\mathsf{B}-1)\cdot\mathsf{B}} + \frac{x^{\mathsf{B}+1}}{\mathsf{B}}\right), \tag{5.23}$$

where $\mathsf{B} = [\frac{4(1+\epsilon)}{\epsilon}]$ and $\mu = (\epsilon/2) + (\epsilon/2)^2$ and ϵ is defined as a small positive real-valued

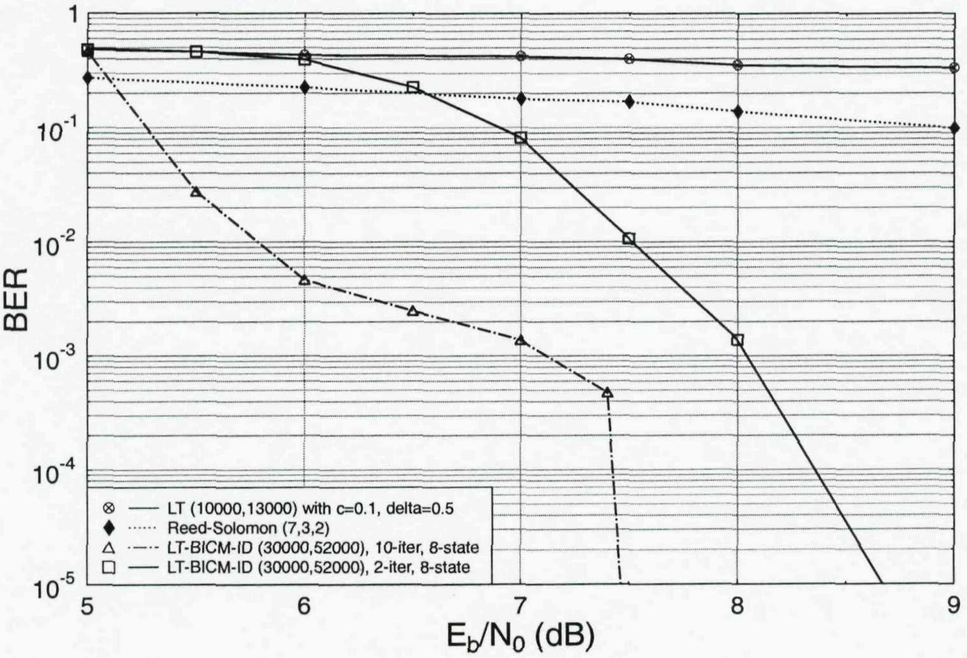

Figure 5.23: BER versus E_b/N_0 performance of the rate 15/26, 10/13 and 3/7 of LT-BICM-ID, LT and RS codes communicating over the BEC channel contaminated by AWGN, when using 16QAM. The LT-BICM-ID scheme is shown in Figure 5.22 and the corresponding parameters are summarised in Table 5.2.

number.

We further investigated the truncated Poisson 1 (Ω_1) [131], the truncated Poisson 2 (Ω_2) [131], and the *robust* degree distributions, where the Poisson degree distributions [131] were used for the sake of reducing the number of corrupted bits inflicted by the AWGN channel at low E_b/N_0. Here, we employed truncated Poisson distributions, which were defined as follows [132]

$\Omega_1(\mathrm{d}) = 0.007969d^1 + 0.5161d^2 + 0.166220d^3 + 0.072646d^4 + 0.082558d^5 + 0.056058d^8 + 0.037229d^9 + 0.0025023d^{65} + 0.003135d^{66}$,

$\Omega_2(\mathrm{d}) = 0.007544d^1 + 0.5033d^2 + 0.166458d^3 + 0.071243d^4 + 0.084913d^5 + 0.049633d^8 + 0.043365d^9 + 0.0045231d^{19} + 0.010157d^{20} + 0.010479d^{66} + 0.017365d^{67}$, where d^n represents the degree order of each of the above items.

The *improved robust* degree distribution proposed in Section 5.4.2.2 was used. Figure 5.24 demonstrates that the Poisson degree distribution Ω_1 exhibited the worst BER performance, resulting in a constant BER around 6×10^{-2} for E_b/N_0 in excess of 7 dB. The BER performance of the Ω_2 degree distributions was slightly better due to its higher mean degree of five as opposed to the average degree of 4.63 for the Ω_1 distribution. Above the E_b/N_0 of 7dB, all the Poission distributed LT-BICM-ID schemes maintain a constant BER with no further improvement in their error correction capability. This is due to the lack of connecting *edges* between the check nodes and the source nodes in the corresponding factor graph. In other words, the average degrees are insufficiently high for correcting the corrupted packets inflicted by the erasure channel.

The LT-BICM-ID scheme associated with the IRD of Section 5.4.2.2, is however, capable of correcting all the errors, when the E_b/N_0 value reaches 7.5dB in Figure 5.24, since it contains a higher number of factor graph connections between the LT-coded packets and the source packets, which assists in correcting more erroneous packets. As the decoding process continues, we may encounter a lack of degree *one* connecting edges, thus forcing the decoding process to halt prematurely. This explains the phenomenon that the BER performance does not improve upon increasing the E_b/N_0 in Figure 5.24, which is exhibited by all the Poisson distributed LT-BICM-ID schemes above the point of $E_b/N_0 = 7$dB.

We further investigate the performance of our proposed IRD compared to the original *robust* distribution of [121] in conjunction with the same value of c=0.1 and δ=0.5. We observe from Figure 5.24 that the LT-BICM-ID scheme using the original *robust* distribution of [121] performs better in the range of $E_b/N_0 < 7.5$dB. This is due to the lower number of *edges* or lower average number of degree distribution compared to our IRD scheme of Section 5.4.2.2. When the mean value of the degree distribution is lower, resulting in a reduced number of connecting *edges* in the factor graph, there would be a reduced error propagation from the source packets to the LT-coded packets, especially at a lower E_b/N_0 when the inner BICM-ID code is less capable of correcting the bits corrupted by the AWGN. This means that if a high number of received packets are corrupted, the corrupted packets are less likely to propagate their erroneous bits due to the lower number of connecting *edges* between source packets and received packets.

However, at higher E_b/N_0 values, the proposed IRD of Section 5.4.2.2 outperforms the schemes using the remaining distributions due to their higher average degree, as seen in Figure 5.18. When the inner BICM-ID code is capable of correcting most of the bit errors, the higher mean of the *robust* degree distribution scheme assists in recovering the corrupted packets, as a benefit of its increased number of connecting *edges* in the factor graph. This shows that the proposed *improved robust* distributed LT outer codes of Section 5.4.2.2 exhibit a better BER performance at higher E_b/N_0, as shown in Figure 5.24, while requiring a reduced number of extra packets for the sake of recovering the original source packets, as shown in Figures 5.19 and 5.20.

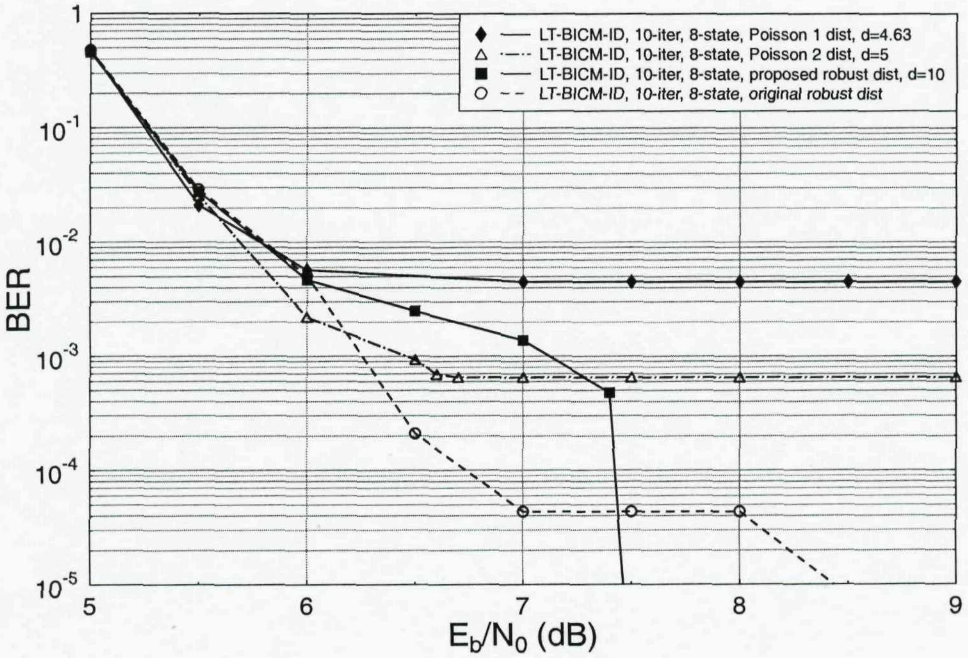

Figure 5.24: BER versus E_b/N_0 performance of various LT-BICM-ID schemes of Figure 5.22 communicating over the BEC contaminated by AWGN using various Poisson and *robust* distributions employing 16QAM. The system parameters are summarised in Table 5.2.

5.5 LT-BICM-ID Using LLR Packet Reliability Estimation

The amalgamated LT and BICM-ID design of Section 5.4.3 is further improved with the aid of a novel LLR based packet reliability estimation technique employed for the sake of detecting and disposing of erroneous packets. Subsequently, bit-by-bit LT decoding is proposed, which facilitates a further BER performance improvement at a potentially reduced number of BICM-ID iterations.

5.5.1 Introduction

The LT-BICM-ID scheme of Section 5.4.3 is investigated with the aid of an improved intrinsically amalgamated LT coding and BICM-ID design. Classic Cyclic Redundancy Checking (CRC) is used for detecting the presence of any erroneous LT-encoded packets. Furthermore, a novel LLR based packet reliability estimation scheme will also be introduced. EXIT charts are used for appropriately configuring the proposed LLR-based packet reliability estimation scheme. This solution potentially enhances the achievable error detection capability, especially at higher SNRs and hence may eliminate the redundancy introduced by the CRC overhead.

As observed in Figure 5.15, error propagation across LT packets encountered during packet decoding may cause a catastrophic failure in LT decoding. Hence, as a counter measure, in this section we introduce a bit-by-bit LT decoding technique by exploiting the LLR estimates provided by the associated BICM-ID decoder. We reduce the probability of occurrence of erroneous packets, which would otherwise have to be discarded. We will demonstrate in Section 5.5.4 that when corrupted bits are in the same symbol index location of different source packets, we can readily discard these packets and still may be able to recover all original source packets with the aid of bit-by-bit LT decoding, as long as the number of received LT-encoded packets remains sufficiently high for the error-free file recovery.

5.5.2 System Overview

The schematic of this new joint LT-BICM-ID arrangement is shown in Figure 5.25. Consider the single-transmit and single-receive antenna aided system seen in Figure 5.25, when the source data file to be transmitted consists of $\mathcal{K}$ number of packets. The LT decoder will require the transmission of $\mathcal{K}' = \mathcal{K} + \mathcal{E}$ number of LT encoded packets requiring $\mathcal{E}$ redundant packets for the success of the decoding process. After transmission over the BEC imposing an erasure probability of P_e, $(P_e \cdot \mathcal{K}')$ number of the original LT encoded packets will be obliterated.

At the physical layer, we deal with frame-by-fame transmission. Each transmission frame consists of a number of packets. A transmission packet is in turn broken into $\mathcal{P}$ number of symbols. Each BICM-ID source symbol is comprised of n source bits and the BICM-ID encoded symbols have $m = n + 1$ encoded bits. The encoded bits

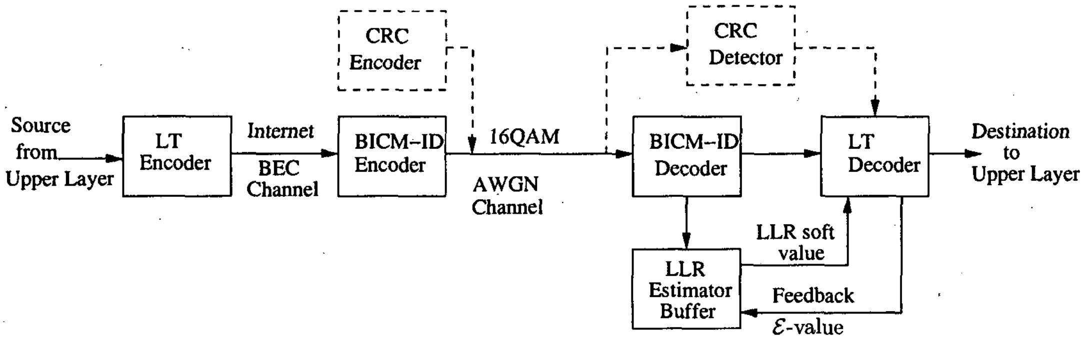

Figure 5.25: *System structure of the joint LT-BICM-ID design.*

are mapped to M-ary constellation before transmission over an AWGN channel. The transmission packet structure is identical to those described in Figure 5.21.

At the receiver seen in Figure 5.25, the BICM-ID decoder receives *a priori* information from the demodulator and outputs *extrinsic* information, which is to be fed back to the demodulator for iterative decoding. The sufficiently reliable output bits are then passed to the LT decoder after a number of BICM-ID iterations. We assume here that the perfectly synchronised LT encoder and LT decoder are capable of identifying the indices of the lost bits and packets. The CRC encoder inserts CRC bits into the LT encoded packets while the CRC detector extracts the CRC bits and verifies the detectable errors within each packet.

5.5.3 Estimation Scheme

The LT decoder using the belief propagation algorithm [133] is inherently sensitive to error propagation. An erroneous packet which contains corrupted bits may propagate the errors from the source nodes of the LT encoder's generator matrix to the check nodes, when modulo-2 operations are performed during the belief propagation decoding [41].

By ensuring that a minimum of $\mathcal{E}$ redundant packet is available, we can improve the achievable decoding performance by reducing the associated error propagation. This can be achieved by discarding erroneous packets, as and when corrupted bits are detected in a packet. Subsequently we employ classic CRC detection scheme, for example the CRC-12 code, which is widely used in telecommunication systems for error detection in conjunction with the generator polynomial $x^{12}+x^{11}+x^3+x^2+x+1$

[134]. This error detection approach improves the attainable system performance, but introduces an overhead. Observe in Figure 5.25 that the CRC encoder injects the CRC bits into the BICM-ID encoded 16QAM stream, before transmitting them over the AWGNs contaminated BEC. In this section, we map four bits to the 16QAM constellation points. The received CRC bits are extracted and are used for detecting the presence of any erroneous bits.

As an alternative, the joint design of LLR-based LT-packet reliability estimation using BICM-ID has the ability to further improve the system's performance. This potentially allow us to eliminate the CRC overhead bits, while maintaining reliable detection, especially at a high SNRs. As seen in Figure 5.25, the soft LLR output of the BICM-ID decoder is stored in the LLR estimator's buffer. The BICM-ID decoder will set a threshold value for the LLRs, in order to determine which LT packet may contain erroneous bits. Based on their LLR values, each of the corresponding bit is flagged with a '0' or '1' to indicate a reliable or unreliable bit, which allows the LT decoder to mitigate the associated error propagation effects during the decoding process. A feedback signal is provided by the LT decoder to control the LLR estimator's threshold for the sake of achieving the highest possible detection accuracy.

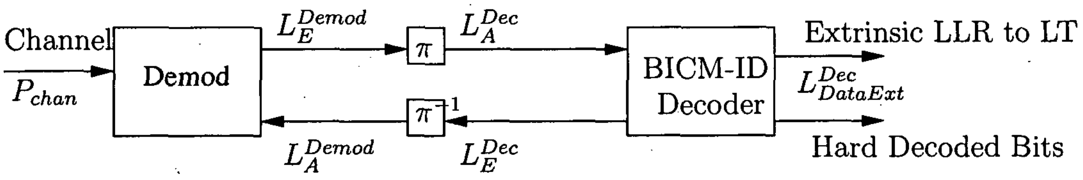

Figure 5.26: BICM-ID system structure.

Figure 5.26 shows the basic BICM-ID scheme, where π and π^{-1} denote the interleaver and deinterleaver. The channel's output information is passed to the demodulator, which receives the *a priori* LLRs L_A^{Demod} from the BICM-ID decoder and provides the *extrinsic* LLRs L_E^{Demod} for the decoder. The channel decoder of Figure 5.26 receives the *a priori* LLRs L_A^{Dec} from the demodulator and outputs the *extrinsic* LLRs L_E^{Dec} in order to perform iterative decoding by exchanging the *extrinsic* information between the BICM-ID decoder and demodulator. The reliability of the demodulator's decisions depends on the channel's SNR and on the *a priori* information L_A^{Demod}, yielding $L_E^{Demod} = f(L_A^{Demod}|SNR_{chan})$.

By contrast, the reliability of the channel decoder's decisions depends solely on the *a priori* LLRs received from the demodulator, since it only has a single input and hence it is not directly dependent on the SNR [135]. Hence the *extrinsic* mutual information obeys $I_E^{Dec} = f(I_A^{Dec})$ and $I_{DataExt}^{Dec}=g(I_A^{Dec})$. Referring to the technique proposed in [135], it is possible to plot both the EXIT chart and the corresponding BER values in Figure 5.28, assuming that the variance σ^2 of the Gaussian distributed decoder output is known [135]. The system parameters used in this section are detailed in Table 5.3.

BICM-ID code rate	R=3/4
Modulation	16QAM
Number of source packets	10000
Number of transmitted packets	13000
Number of bits per source packet	165
BEC erasure probability	P_e=0.1
LT degree of distribution	Improved Robust Dist. (IRD)

Table 5.3: System parameters.

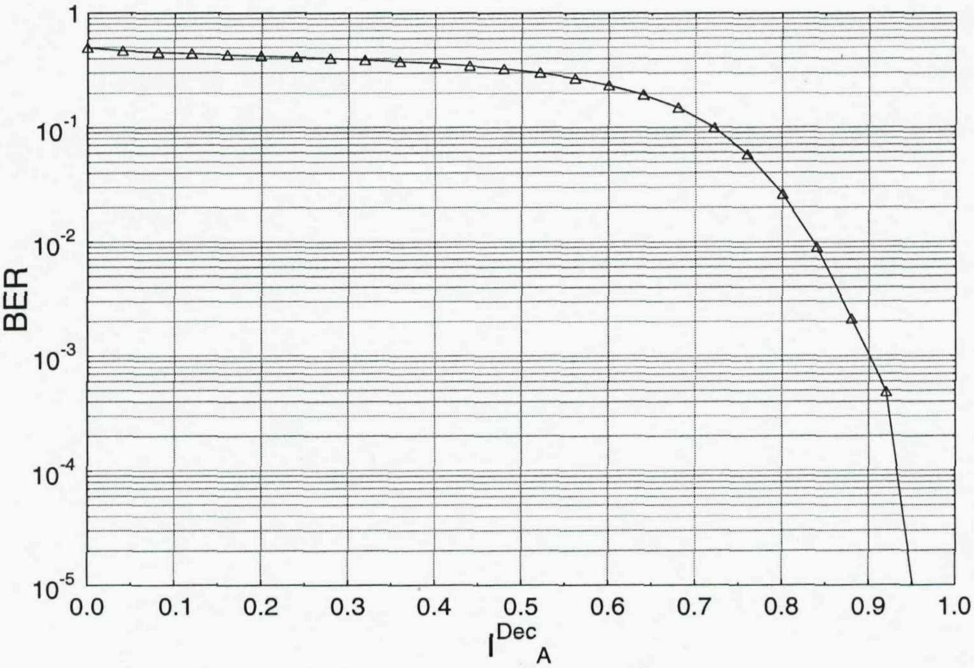

Figure 5.27: BER versus I_A^{Dec}.

Here, we employ an even more straightforward method of directly estimating the BER of the decoded bits with the aid of the EXIT chart. For the sake of using EXIT chart based bit-reliability estimates, we generate a random source bit stream and record the LLRs $L_{DataExt}^{Dec}$ at the output of the BICM-ID decoder, where a hard

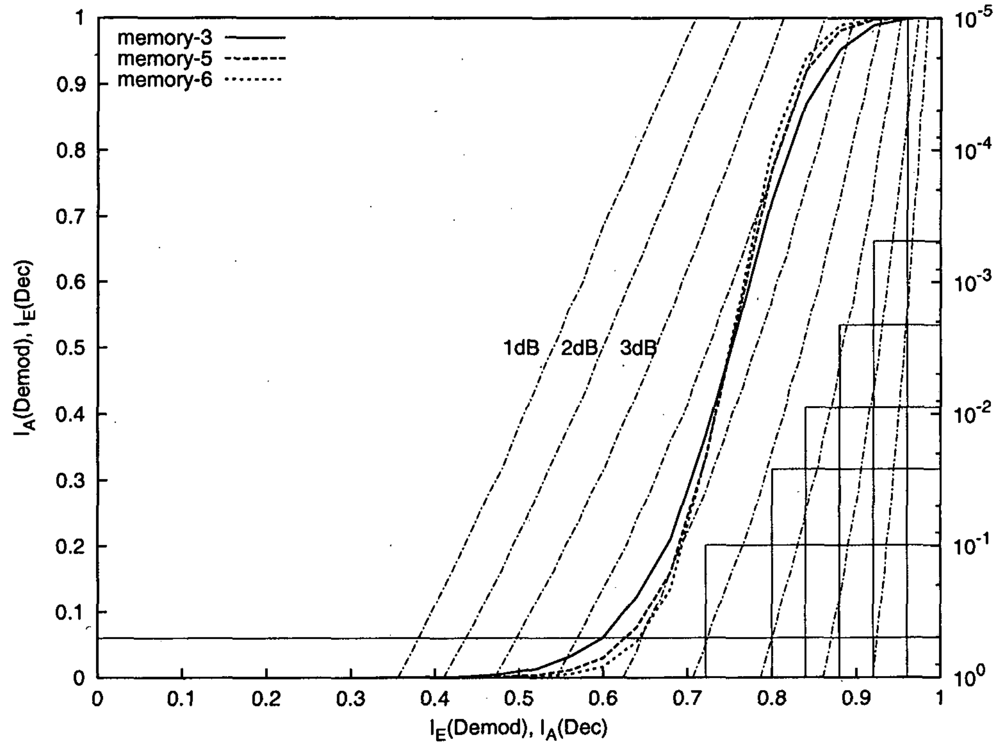

Figure 5.28: EXIT chart for BICM-ID scheme of Figure 5.26, while the system parameters are summarised in Table 5.3.

decision is made, in order to facilitate the BER performance evaluation of the system. The resultant BER versus I_A^{Dec} relationship was recorded from our simulations, as shown in Figure 5.27. From the BER versus I_A^{Dec} relationship of Figure 5.27, we arrive at Figure 5.28.

More explicitly, Figure 5.28 details the EXIT characteristics of both the demodulator and of the BICM-ID decoder. The nine dotted lines represents the EXIT characteristics of the demodulator recorded for E_b/N_0 values ranging from 1dB to 9dB using Ungerböck's Partitioning (UP). The *extrinsic* information characteristics recorded for BICM-ID having a coding rate of $R = 3/4$ and employing the memory lengths of $\varphi = 3, 4, 5$ are shown by the I_A^{Dec} versus I_E^{Dec} curves of Figure 5.28. The BER of the decoder having $m = 3$ is plotted in the same figure with the aid of the solid horizontal and vertical lines (similar to a histogram graph). More explicitly, since for transmission over an AWGN channel there is an unambiguous one-to-one relationship between I_A^{Dec} and the BER, the output characteristic of the BICM-ID decoder is independent of the channel SNR and the corresponding BER curve is based on the function of

$P_b = f'[I_A^{Dec}]$ as detailed in [135], which can be directly inferred from Figure 5.27. For further illustration, at I_A^{Dec}=0.800083 for example, we have BER = 0.026177, as shown in Figure 5.28.

The threshold value used for activating the feedback link from the LT decoder to the LLR estimator buffer of Figure 5.25 determines the minimum number of redundant packets required for successful LT decoding. In our forthcoming discourse we attempt to characterise the intricate interplay between the LT code's generator matrix employing different degree of distributions and the specific portion of redundant packets providing vital information for the LLR estimation buffer in order to adjust its LLR threshold value. The IRD described in Section 5.4.2.2 having parameters of c=0.1 and δ=0.5 [41] was used, which required 10 percent redundant packets for successful decoding in the specific scenario of [41].

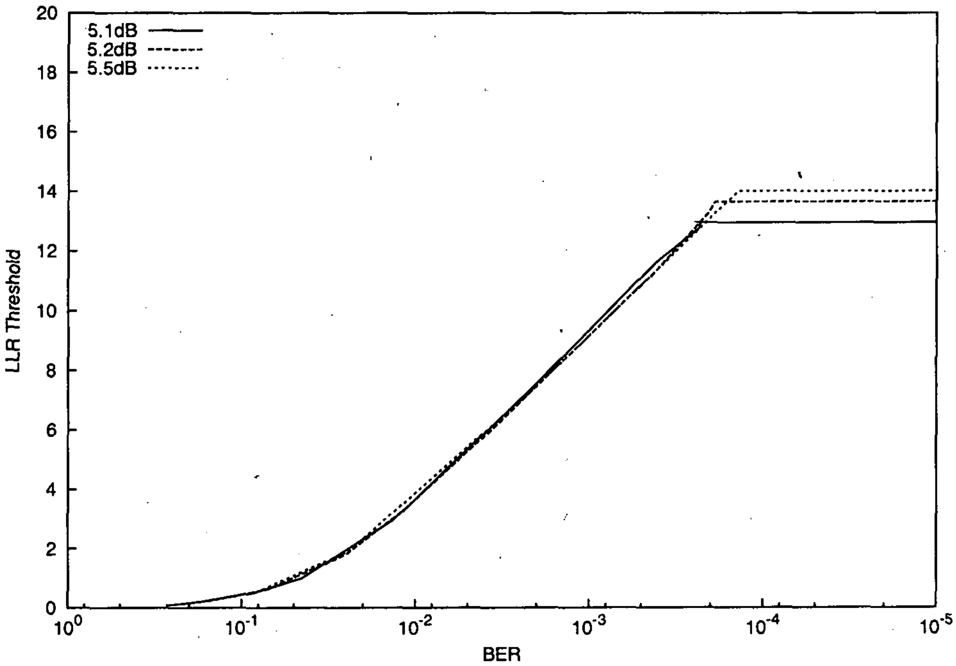

Figure 5.29: LLR threshold value necessitated for requiring $\mathcal{E}$=10% redundant packets for the system of Figure 5.26 and Table 5.3. The required values were averaged over 165 bits/packet with a total of 10000 LT source packets.

Based on the system parameters listed in Table 5.3, we conducted a series of simulations in order to determine the LLR threshold required for achieving certain BERs at the target E_b/N_0 value. Figure 5.29 shows the LLR threshold value determined by simulation for maintaining a normalised $\mathcal{E}$-value of 0.1 at E_b/N_0 = 5.1dB, 5.2dB and 5.5dB, respectively. The horizontal section of the curves in Figure 5.29 represents the specific LLR threshold values, when the 10% target value of $\mathcal{E}$ has been reached. The LLR-based packet reliability becomes sufficiently confident, when the BER of the BICM-ID decoder becomes as low as 2×10^{-4}.

In Figure 5.30 the LLR values are plotted for 200 bits against the bit-index for a random sample. The entire sample has a total of $165 \times 13000 \times (1 - 0.1) = 1,930,500$ bits based on Table 5.3. The circles denote the correctly decoded bits, while the crosses denote the erroneously decoded bits. Note that most of the bits that are located outside the threshold region represented by the horizontal lines are indeed likely to be error-free, since at the BER of 2×10^{-4} on average a 20 000 bit segment would have a single error. By contrast, all the corrupted bits tend to be inside the threshold region, even though some LLR values within the same region may also yield correct bits.

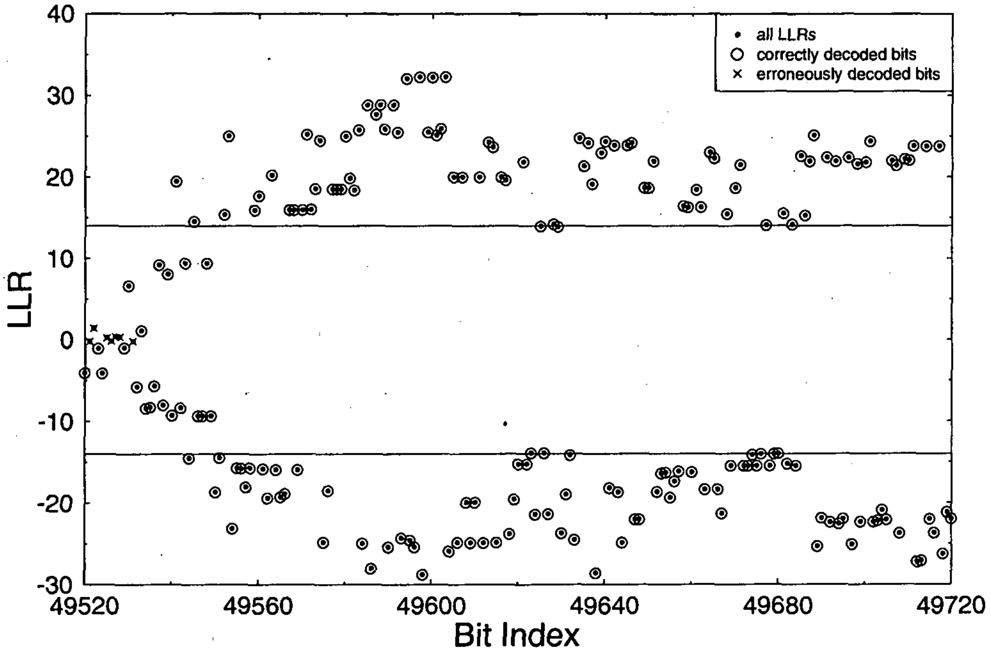

Figure 5.30: A set of 200 LLR values recorded for the system of Figure 5.26 detailed in Table 5.3, given the threshold value of Figure 5.29 at $E_b/N_0 = 5.5dB$.

Since we require a BER between 10^{-3} to 10^{-4} in order to arrive at a confident LLR based packet-reliability decision, we observe in Figure 5.28 that the BER of 3×10^{-4} satisfies this requirement at $I_A \approx 0.92$. This may also be associated with $E_b/N_0 > 5.0$dB for four or more iterations.

5.5.4 Bit-by-bit LT Decoding

It is widely recognised that LT packet decoding is sensitive to error propagation across the LT packets owing to their modulo-2 based interdependence. Since LT codes were originally designed for the BEC channel, they have to be combined with FEC codes for removing the transmission errors imposed by the wireless channel. For example, the BER of the packets contaminated by the wireless channel may be mitigated by the BICM-ID decoder. An unsuccessfully decoded BICM-ID symbol is likely to cause error propagation to other LT packets due to their modulor-2 relationship. If the BEC's packet erasure probability P_e is high and the number of redundant LT packets is insufficient, the LT packet decoding operation will be curtailed without successfully decoding the original source packets. This problem can be mitigated using a novel bit-by-bit LT decoding scheme, where the intrinsically inherited LLR-based reliability estimation, can be used to allow or disallow the detection of bits.

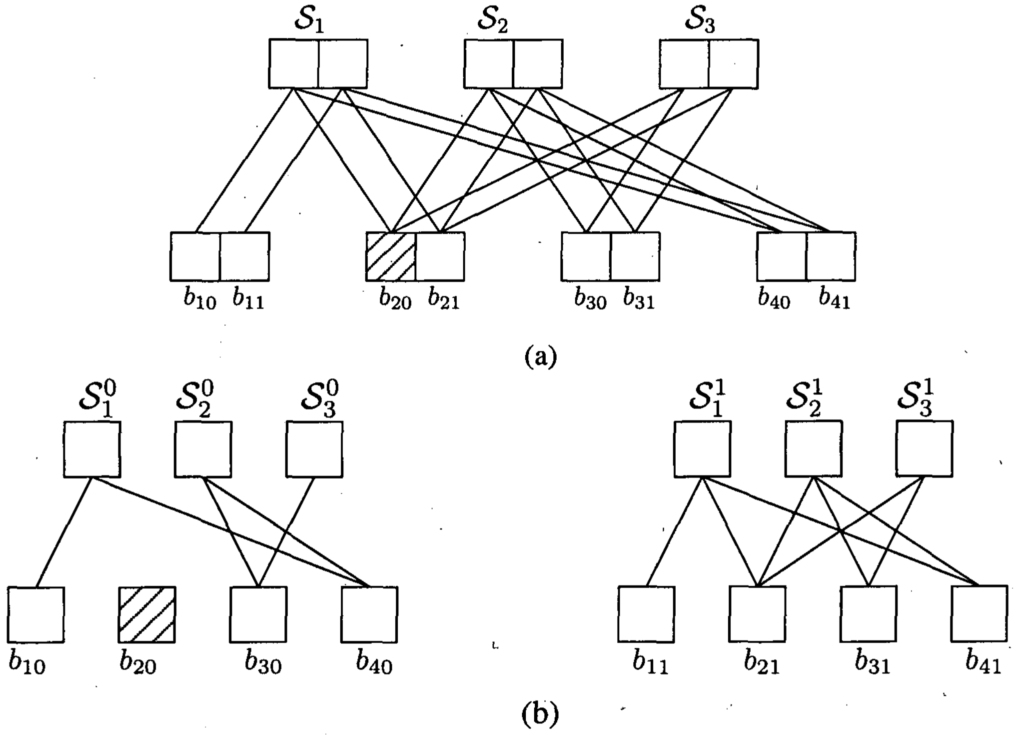

(a)

(b)

Figure 5.31: Packet-based LT decoding and bit-by-bit LT decoding. The shaded bits represent the corrupted bits indicated by LLR-based estimation.

First we consider this bit-by-bit LT decoding method in a little more detail. Figure

5.15 introduced the original LT packet decoding technique using a simple example, where each packet $\mathcal{S}$ consisted of three bits. By contrast, for the bit-by-bit LT decoder, we modify the decoding structure introduced in Section 5.15 to that seen in Figure 5.31. In this example, each LT packet consists of two bits for the sake of simplicity, although the choice of packet-length is arbitrary. The 2-bit LT source packets of Figure 5.31 are $\mathcal{S}_1, \mathcal{S}_2, \mathcal{S}_3$ and the transmitted LT encoded packets are constituted by the bits b_{ij}, where i is the packet index and j is the bit index in the transmitted packet, as shown in Figure 5.31(a). The LT-encoding process is identical to the bit-based modulo-2 addition of the specific packets selected by an appropriate random number generator, as seen in Figure 5.15.

Decoding takes place by considering all the individual bits at a given bit index of all transmitted packets. Figure 5.31(b) shows the bit-by-bit decoding at each individual bit index of the received LT packets. Note that the shaded box indicates a corrupted bit spotted by the LLR-based reliability estimator and the resultant truncated LT packets are denoted as $\mathcal{T}_2^0$. For example, the erased coded bit b_{20} has no connection to the message source nodes during the decoding process. Therefore, the error propagation caused by corrupted bits would be discarded in $\mathcal{T}_2^0$ decoding to improve the performance of packet recovery. By contrast, the connections of the received bit b_{21} are not affected, while the decoding of $\mathcal{T}_2^1$ would be carried out without discarding any of those connections. This would enhance the decoding efficiency without having to discard both b_{20} as well as b_{21} if the original LT packet decoding is invoked.

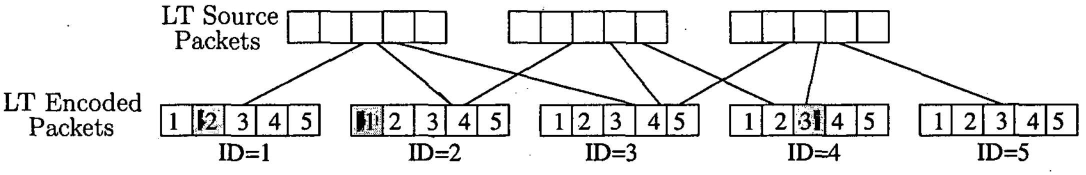

(a) Packet–based LT Decoding

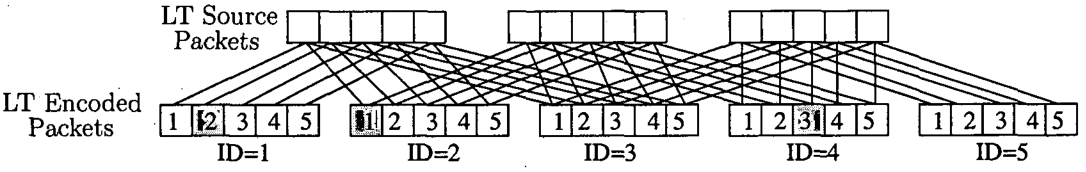

(b) Bit–by–bit LT Decoding

Figure 5.32: Packet-based LT decoding and bit-by-bit LT decoding.

To elaborate a little further, Figure 5.32 contrasts (a) our packet-based LT-decoding and (b) bit-by-bit LT-decoding strategies. The low-reliability or corrupted bits of the packets are shown as filled grey-shaded rectangles in the figure. Observe that when using packet-by-packet decoding, a corrupted bit in a packet will contaminate the whole decoded packet at the end of the decoding cycle. Furthermore, having typically different corrupted bits in different LT encoded packets, will reduce our chance of discarding erroneous packets before the commencement of LT-decoding, because when too many packets are discarded by the LLR-based packet reliability estimator, the minimum requirement of retaining at least $\mathcal{E}$ redundant packets might not be met.

When using bit-by-bit decoding, the potentially corrupted bits can be identified with the aid of the LLR-based reliability estimation technique of Figure 5.30 and this enables us to use the rest of the reliable LT-encoded bits to the decoder's benefit and hence to continue the LT decoding process. As seen in Figure 5.32 (b), the LT packets of ID = 1, 2 and 4 have low-reliability bits that are shaded, which would be discarded, when using bit-by-bit LT decoding. However, in contrast to the packet decoding based regime of Figure 5.32 which discarded the corrupted packets, bit-by-bit LT decoding only discards those bits which are deemed to be corrupted, as declared by the LLR-based reliability estimation.

5.5.5 Simulation Results

In this section we embark on quantifying the performance of the scheme seen in Figure 5.25. The system parameters employed in our simulations are shown in Table 5.3.

The BER performance of the BICM-ID scheme using different number of decoding iterations combined with LT coding is shown in Figure 5.23 and repeated in Figure 5.33 for convenience, which is contrasted to that of our benchmark scheme operating without any soft LLR information exchange between the BICM-ID and the LT decoder. An infinitesimally low BER is achieved for E_b/N_0 values in excess of 7.4dB. By invoking two iterations, the BICM-ID scheme becomes capable of correcting most of the AWGN-contaminated bits and any further iterations would have little effect on the achievable BER.

When assuming perfectly reliable CRC estimation in the schematic of Figure 5.25, the combined scheme of Figure 5.25 achieves a BER improvement upon using four iterations, as seen in Figure 5.34. This was predicted by the EXIT chart of Figure

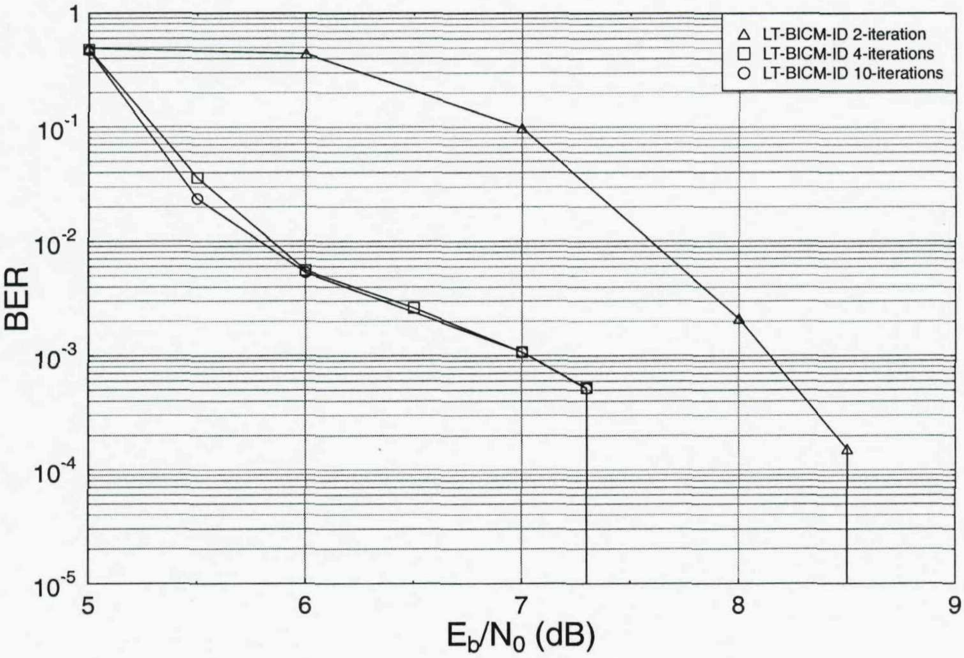

Figure 5.33: BER versus E_b/N_0 performance, when communicating over a BEC channel having $P_e = 0.1$ and contaminated by AWGN, when using the *improved robust* degree distribution of Section 5.4.2.2. The system schematic is shown in Figure 5.22, while the system parameters are summarised in Table 5.2.

5.28, when the system refrains from including the CRC bits. According to Figures 5.27 and 5.28 we may expect convergence to an infinitesimally low BER for $E_b/N_0 > 5$dB, provided that we use more than four iterations. Observe in Figure 5.34 that even though the system exhibits performance improvements as a benefit of discarding the erroneous LT packets, this scheme introduces an overhead owing to the insertion of the redundant CRC bits.

Compared to the scheme characterised in Figure 5.33, we observe in Figure 5.34 that the BER becomes infinitesimally low for both packet-based and bit-by-bit LT decoding for $E_b/N_0 > 6.7$dB. This is a coding improvement of around 0.5dB compared to our previous benchmarker characterised in Figure 5.33. Observe also that bit-by-bit LT decoding improves the system's BER performance for a low number of iterations, but achieves a similar performance to packet-based LT decoding upon using four or more iterations.

When forwarding soft information from the LLR buffer to the LT decoder of Figure 5.25, Figure 5.35 shows the significant performance improvements achieved by the

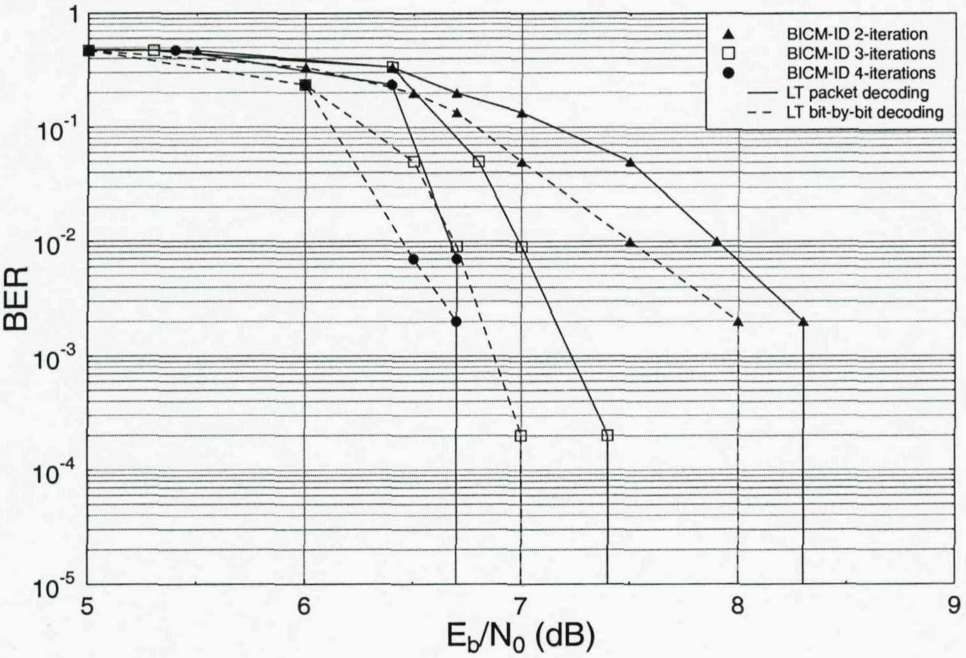

Figure 5.34: BER versus E_b/N_0 performance, when communicating over a BEC channel having $P_e = 0.1$ contaminated by AWGN using perfect CRC estimation as well as the parameters of Table 5.3. The system schematic is shown in Figure 5.25.

system. Figure 5.35 illustrates the results recorded for both the packet-based as well as for the bit-by-bit LT decoding methods. Note that the LLR estimation aided scheme achieves BER $= 10^{-5}$ for E_b/N_0 values between 5.7dB and 6dB. This corresponds to a coding gain of around 1.5dB compared to the benchmarker benefiting from no soft information, as observed in Figure 5.33. Furthermore, bit-by-bit LT decoding shows a coding advantage of 0.5dB over the classic packet-based LT decoding at two iterations and a further modest 0.2dB, when activating four BICM-ID iterations.

5.6 Chapter Conclusions

In Section 5.2 we introduced GLDPC component codes used in the context of our MLC structure. Section 5.2 outlined the proposed MLC-GLDPC schemes invoking MLC component codes, employing GLDPCs, having $\mathsf{W} = 2$ super-codes and using Hamming code as constituent codes. The simulation results shown in Figures 5.5, 5.6, 5.7 and 5.8 of Section 5.2.6 exhibited coding performance improvements over the classic MLC invoking LDPC component codes.

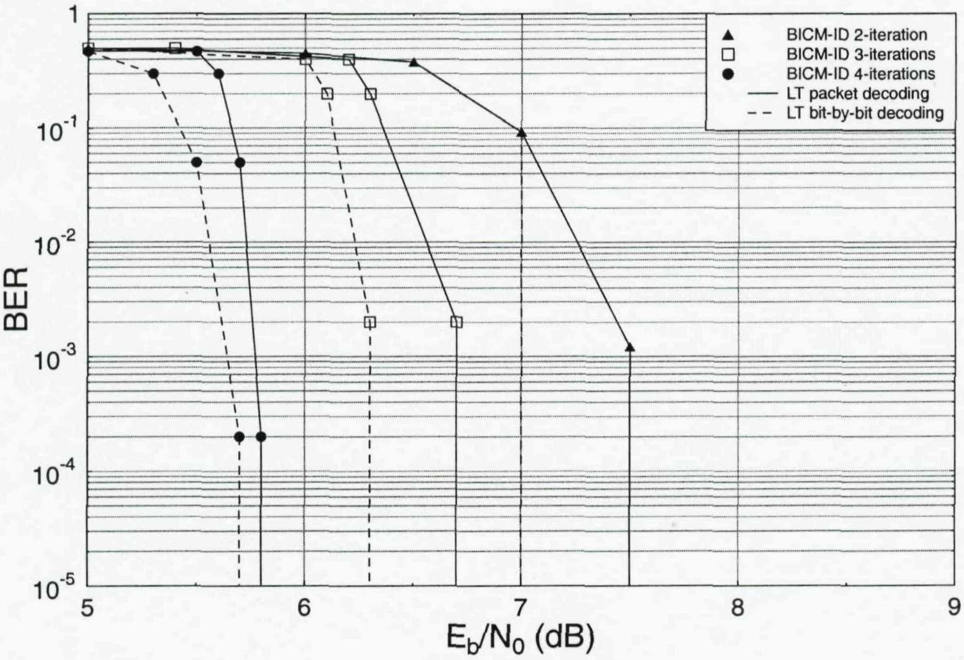

Figure 5.35: BER versus E_b/N_0 performance, when communicating over a BEC channel having $P_e = 0.1$ and contaminated by AWGN using LLR based reliability estimation and the parameters of Table 5.3. The system schematic is shown in Figure 5.25.

Our simulation results suggested that the attainable E_b/N_0 improvements compared to a classic LDPC component code based MLC benchmarker ranged between 0.5dB and 2dB. This was achieved using the same number of iterations and an implementationally beneficial parallel architecture. We argued in the context of Figure 5.4 that multilevel coding combined with parallel independent decoding is attractive in the context of supporting low-latency real-time applications. The concept of Section 5.2.1 was further extended to an adaptive scheme quantifying the decoding reliability by introducing the syndrome test described in Section 5.3. The architecture of the scheme was outlined in Section 5.3.1, which curtailed the decoding iterations, once the target BER was attained. Figures 5.11 and 5.13 illustrated both the number of outer and inner iterations required for achieving a BER performance of 10^{-5}.

A wireless Internet scenario was introduced in Section 5.4. We studied the ability of LT codes to eliminate the retransmission of packets required by a typical ARQ scheme, as discussed in Sections 5.4.1 and 5.4.2. The LT-encoder's packet degree distribution is a crucial factor in determining the achievable performance, as argued in Section 5.4.2.1. In Section 5.4.2.2, we proposed a novel packet degree distribution, for enhancing the

LT decoder's performance.

In Section 5.5 a sophisticated serial concatenated LT-BICM-ID scheme was designed, which is capable of improving the attainable BER performance of packetised data transmission, when communicating over the AWGN-contaminated BEC. The concept of using a BICM-ID scheme to improve the attainable BER of the LT codes invoked for correcting the packet errors was the main benefit of the proposed scheme, as mentioned in Section 5.4.3. With the advent of using the proposed IRD of Section 5.4.2.2 and a strong BICM-ID inner code, in Section 5.4.4 we demonstrated that our scheme is capable of achieving a better BER performance than that of the classic RS (7,3,2) and LT (10 000, 13 000) benchmarkers, when communicating over the AWGN contaminated BEC. This scheme is particularly attractive in a wireless Internet scenario. We elaborated on the joint optimisation of the inner and outer code-rates for the sake of maximising both the effective throughput and the attainable integrity of the system.

Following the investigation of our proposed LT-BICM-ID scheme, we outlined a novel LLR-based packet reliability estimation scheme in Section 5.5, which forwarded the soft LLR information from the BICM-ID decoder to the LT decoding process. The BICM-ID scheme exploiting the EXIT characteristics of Figure 5.28 provided reliable LLR threshold after a certain number of iterations for assisting the LT decoder's operation, as illustrated in Figure 5.30. Finally, bit-by-bit LT decoding was introduced in Section 5.5.4 for the sake of achieving further improved decoding results. The simulation-based performance results of the soft LLR estimation aided bit-by-bit LT decoding scheme were provided in Section 5.5.5.

Chapter 6

Near-Capacity Irregular BICM-ID Scheme*

6.1 Introduction

In the previous chapters we have investigated various MLC and BICM-ID designs for the sake of improving their BER performance. In this chapter we further improve the BICM-ID scheme for the sake of achieving an infinitesimally low BER close to the theoretical capacity limit. In view of this, we introduce the irregular code-design concept contrived for BICM-ID schemes in order to create a more flexible system, which is capable of achieving a near-capacity performance. Alternatively, with the aid of these irregular components, we strike a more attractive trade off between near-capacity performance and a moderate system complexity.

BICM-ID [23] was described in Section 2.4, which consists of three main blocks - a convolutional encoder, bit-interleavers and a bit-to-symbol mapper. Iterative detection was achieved by exchanging soft extrinsic information between the symbol-to-bit demapper and the decoder. The BER versus E_b/N_0 curve of this BICM-ID scheme exhibits a turbo-like cliff and the achievable convergence performance can be characterised with the aid of EXIT charts [77].

Different bit-to-symbol mapping schemes have been investigated in order to improve the convergence behaviour of BICM-ID [136, 137] by shaping the demapper's EXIT characteristic for the sake of creating an open EXIT tunnel and hence to achieve

---

*Part of this chapter is based on the collaborative research outlined in [49, 50].

an infinitesimally low BER. Furthermore, an adaptive BICM arrangement using various iterative decoding schemes was proposed in [138], which employed different signal constellations and bit-to-symbol mapping within one codeword. This flexible signalling scheme required the knowledge of the average signal quality at the transmitter, for invoking advanced Adaptive Modulation and Coding (AMC) [139] in order to improve the overall BICM-ID scheme's achievable performance.

A Unity-Rate Code (URC) can be used as a precoder for reaching the (1,1) EXIT chart convergence point [93] and hence to achieve an infinitesimally low BER. A precoded mapper scheme was also proposed for a three-stage - encoder, precoder and modulator - design constituted by either a bit-based or a symbol-based precoder [140]. Furthermore, a flexible irregular demapper combined with modulation doping was proposed in [141] for the sake of producing an open EXIT tunnel.

The Irregular Convolutional Coding (IrCC) [142, 143] concept was proposed for improving the convergence behaviour of serially concatenated codes, which can be employed as the encoder component of an Ir-BICM-ID. Furthermore, in order to introduce a more diverse set of EXIT characteristics for creating an IrCC, we invoke low-complexity Convolutional Codes (CC) constituted from a hybrid combination of memoryless repetition codes.

The novel contribution of this chapter is that we propose an irregular BICM-ID arrangement for the sake of creating an adaptive BICM-ID scheme, which can either exhibit near-capacity performance or lower-complexity implementation. Our approach is based on invoking EXIT chart analysis for minimising the area of the open EXIT tunnel in order to achieve a near-capacity performance. Alternatively, the width of the EXIT tunnel can be increased for the sake of reducing the system's complexity.

6.2 Irregular Bit-Interleaved Coded Modulation Schemes

The classic BICM-ID scheme of Section 2.4 exchanges extrinsic information between the CC decoder and the demapper, as shown again in Figure 6.1 for convenience. The precoder concept was proposed in [79] which was then used to create a recursive demapper at the decoder, as previously described in Section 3.4. By combining the precoder and the demapper, we will demonstrate that the demapper will facilitate convergence to the (1,1) EXIT trajectory point. The system's schematic is shown in

Figure 6.2.

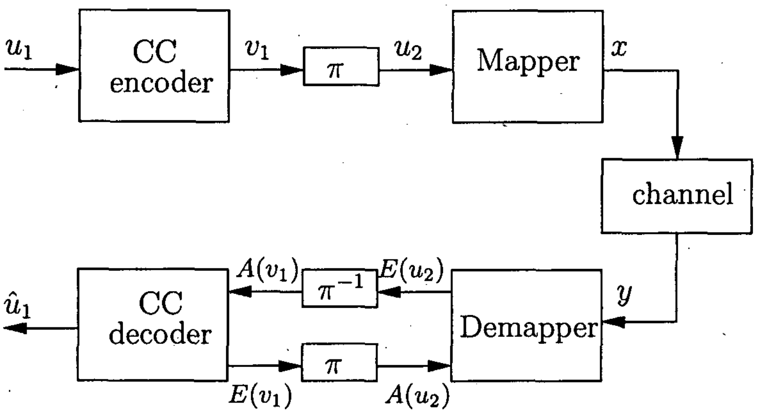

Figure 6.1: The general structure of the classic BICM-ID scheme. The binary source bit stream u_1 is encoded by the CC encoder and the encoded bits v_1 are interleaved by the bit interleaver π, yielding the permuted bits u_2. The inner iterations exchange extrinsic information between the demapper and the CC decoder, where the notation $A(.)$ represents the *a priori* information quantified in terms of LLRs, while $E(.)$ denotes the *extrinsic* information also expressed in terms of LLRs.

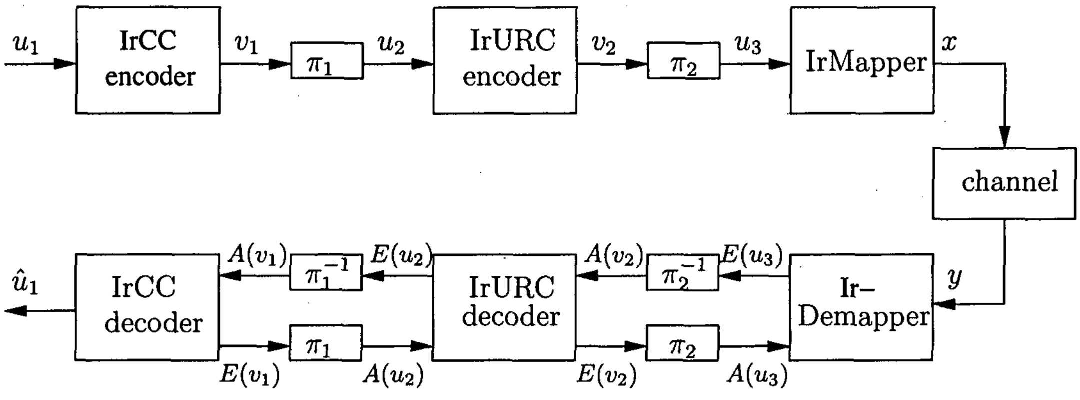

Figure 6.2: The general structure of the Ir-BICM-ID scheme.

6.2.1 System Overview

Each component of the irregular scheme proposed consists of different subcodes. To provide more detailed illustration, the schematic of the proposed Ir-BICM-ID scheme is shown in Figure 6.3, which is constituted by the three main component blocks, namely the IrCC, the bit interleaver and the mapper. In our Ir-BICM-ID design, the IrCC is constituted by F number of low-complexity Convolutional Codes (*CC*). The

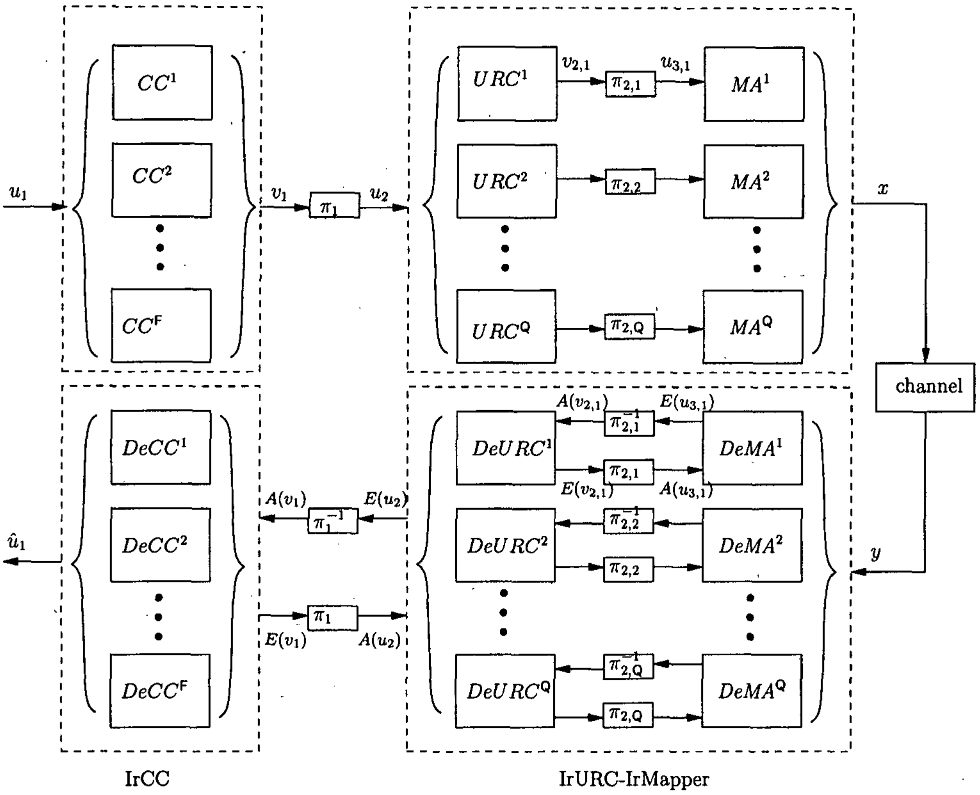

Figure 6.3: The Ir-BICM-ID structure using irregular components, detailing the individual subcodes. The braces indicate both multiplexing and demultiplexing operations.

inner component module of Figure 6.3 contains Q number of URCs and Q number of MAppers (*MA*).

The binary source bit stream u_1 is encoded by the IrCC encoder and the encoded bits v_1 are interleaved by the bit interleaver π_1, yielding the permuted bits u_2. The bit stream u_2 is then fed into the IrURC encoder and each of the URC^i codes yields the encoded bits $v_{2,i}$ according to the appropriately assigned weighting coefficients, where i denotes the component index. The resultant bits $v_{2,i}$ are interleaved by the corresponding bit interleaver $\pi_{2,i}$ and the permuted bits $u_{3,i}$ are then mapped to the input of the associated mapper MA^i, as shown in Figure 6.3. This adaptive mapping scheme is referred to as the Irregular Mapper (IrMapper). The modulated symbols x are transmitted via a Rayleigh fading channel and the received symbols y are demodulated.

At the receiver, an iterative decoder is invoked, exchanging extrinsic information between the inner and outer components. The inner iterations exchange extrinsic information between the irregular demapper and the IrURC decoder, where the notation

$A(.)$ represents the *a priori* information quantified in terms of LLRs, while $E(.)$ denotes the *extrinsic* information also expressed in terms of LLRs. Observe in Figure 6.3 that each component of the URC decoder and demapper is termed as $DeURC^i$ and $DeMA^i$, respectively and only the first component is labeled for clarity. The inner component is represented by the IrURC-IrMapper block.

By contrast, the outer iterations are invoked between the IrURC decoder and the IrCC decoder of Figure 6.3. Here, each of the IrCC component decoder is termed as $DeCC^i$. Since both the IrURC and IrCC schemes are trellis-based, their decoders employ the MAP algorithm.

The original three-stage arrangement of the IrCC, IrURC and IrMapper schemes would require a 3-D EXIT chart analysis, which is hard to interpret visually. However, our investigations not included here suggest that the inner $DeURC^i$ and $DeMA^i$ blocks require only a few iterations in our 3-stage system to reach the (1,1) point of perfect convergence. We can therefore view these two blocks as a combined decoder using several inner iterations and this allows us to simplify the 3-D EXIT analysis to 2-D EXIT functions, while using the most beneficial activation order of the iterative decoder components.

1. The inner iterative decoder continues iterations, until no more mutual information improvement is achieved.
2. This is then followed by an outer iterative decoding.
3. With the aid of the resultant *a priori* information, the inner iterative decoder is invoked again.
4. This process continues, until the affordable number of iterations is reached.

The resultant inner decoder block of the Ir-BICM-ID scheme is portrayed in Figure 6.4. The deinterleaver within the inner code is denoted as $\pi_{2,i}^{-1}$, where i is the index of the subcode. The corresponding interleaver length of subcode i is constrained to be shorter than the outer interleaver length of π_1, although it would be more beneficial to have a longer interleaver for the sake of achieving a better inner iteration gain.

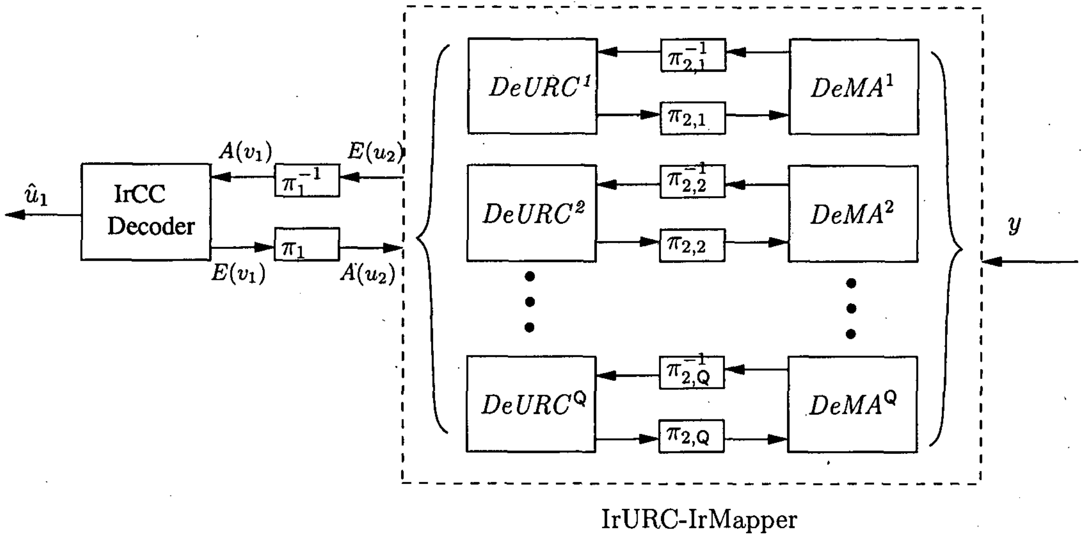

Figure 6.4: The Ir-BICM-ID inner block. The braces indicate both multiplex and demultiplex operations.

6.3 EXIT Chart Analysis

In this section EXIT chart analysis is performed in order to characterise the scheme's achievable iterative decoding convergence. The basics of EXIT chart analysis were outlined in Section 3.3. Again, the Ir-BICM-ID scheme of Figure 6.3 is a three-stage arrangement, which requires 3-D EXIT analysis, as presented in [91]. However, since the Irregular Demapper (IrDemapper) of Figure 6.4 constitutes a low-complexity component, the low-complexity inner iterations are continued until the mutual information $E(v_{2,i})$ becomes near-constant, because no more extrinsic information may be gleaned by any of these two components, without the third component's intervention. Hence, we can simplify the three-stage EXIT chart representation to a 2-D EXIT curve, as detailed below.

Let $I_{A(b)}$ represent the mutual information between the *a priori* information $A(b)$ and the bit b, while $I_{E(b)}$ denotes the mutual information between the *extrinsic* information $E(b)$ and the bit b. Observe from Figure 6.3 that the EXIT function of the IrDemapper can be represented as a function of $I_{E(u_3)}$ and the channel's E_b/N_0 value as follows

$$I_{E(u_3)} = \frac{1}{Q}\sum_{i=1}^{Q} f_{u_3}[I_{A(u_{3,i})}, E_b/N_0]. \tag{6.1}$$

Observe in Figure 6.3 that in a typical three-stage concatenated design, the IrURC decoder has two mutual information outputs, namely $I_{E(u_2)}$ and $I_{E(v_2)}$, where $I_{E(v_2)}$ is the total mutual information of $I_{E(v_{2,i})}$, $\forall i$. Both of these mutual information components depend on two *a priori* mutual information inputs, namely on $I_{A(u_2)}$ and $I_{A(v_2)}$. The two functions can be defined as

$$\begin{aligned} I_{E(u_2)} &= f_{u_2}[I_{A(u_2)}, I_{A(v_2)}], && (6.2) \\ I_{E(v_2)} &= f_{v_2}[I_{A(u_2)}, I_{A(v_2)}]. && (6.3) \end{aligned}$$

Again, in this Ir-BICM-ID scheme, we continue invoking inner iterations, until we succeed in generating sufficiently reliable mutual information $I_{E(u_2)}$, before activating the outer iterations. Hence we may combine the inner component blocks according to Figure 6.4, where the dotted box indicates the inner IrURC-IrMapper component. The EXIT function of this inner component can be defined by

$$I_{E(u_2)} = f_{u_2}[I_{A(u_2)}, E_b/N_0]. \tag{6.4}$$

For the IrCC decoder, the EXIT function becomes

$$I_{E(v_1)} = f_{v_1}[I_{A(v_1)}]. \tag{6.5}$$

6.3.1 Area Property

The so-called area-property of EXIT charts [144] can be exploited for creating a near-capacity Ir-BICM-ID scheme based on EXIT curve matching. The area property of EXIT charts [144] states that the area under the EXIT curve of an inner decoder component is approximately equal to the attainable channel capacity, provided that the channel's input symbols are equiprobable. As for the outer component, the area under its EXIT function is equivalent to $(1 - R_o)$, where R_o is the outer component's coding rate.

According to [144], the area property of EXIT charts may be exploited by considering Figure 6.5. Explicitly, the area under the EXIT curve [144] of the inner code quantifies the capacity of the communication channel (the upper *a priori* channel 1 in Figure 6.5), when the communication channel's input is constituted by equiprobable M-ary symbols, while the *a priori* channel (the lower *a priori* channel 2 in Figure 6.5) is represented by a Binary Erasure Channel (BEC). This area property was shown to be valid for arbitrary inner codes and communication channels, provided that the *a priori* channel 2 of Figure 6.5 is the BEC [144, 145]. Furthermore, there is experimental evidence that the area property of EXIT charts is also valid for the *a priori* Channel 1 of Figure 6.5, when it is constituted by AWGN [91] and Rayleigh fading channels [146].

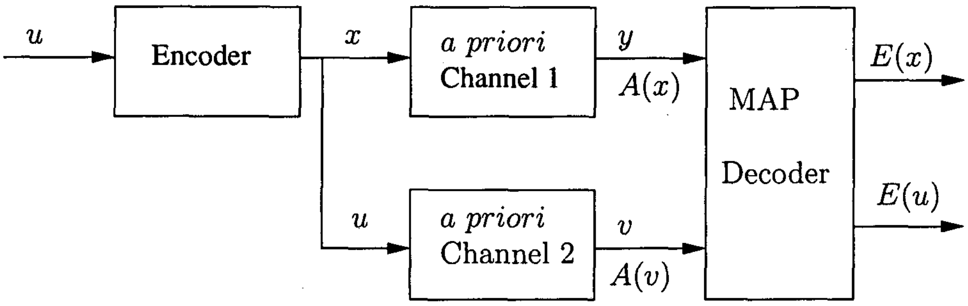

Figure 6.5: The encoding and decoding processes of an intermediate encoder. The input bits u emanate from an outer encoder, whose output symbols x are fed to an inner encoder. The *apriori* channels are used to model the outer and inner decoders. The notations $A(.)$ and $E(.)$ represent the *a priori* and *extrinsic* information, respectively.

Let A_{v_1} and $\bar{A}_{v_1}$ be the areas under the EXIT function of $f_{v_1}(i)$ and $f_{v_1}^{-1}(i)$, where $i \in [0, 1]$, which can be defined as

$$A_{v_1} = \int_0^1 f_{v_1}(i)di, \quad \bar{A}_{v_1} = \int_0^1 f_{v_1}^{-1}(i)di = 1 - A_{v_1}. \tag{6.6}$$

Therefore the area $\bar{A}_{v_1}$ under the inverse of the EXIT function is approximately equivalent to the coding rate, $\bar{A}_{v_1} \approx R_o$. Since the IrURC has a coding rate of unity, the area A_{v_2} under the combined inner component block's EXIT curve in Figure 6.3, can be defined as follows

$$A_{v_2} \approx C_{channel}, \tag{6.7}$$

where $C_{channel}$ is the achievable channel capacity in the presence of equi-probable symbols. If the inner code rate is not equal to one or the precoder does not have a unity code rate, there would be a capacity loss, which the outer code is unable to recover. Our aim is to create a near-capacity design associated with a narrow EXIT tunnel between the inner and outer EXIT function, reaching the convergence point (1,1), which typically yields an infinitesimally low BER.

6.4 Irregular Components

The irregular components consist of several subcodes, each of which exhibits a different EXIT function, at a different coding rate. The irregular components employed by the Ir-BICM-ID scheme are the IrCC, IrURC and the IrMapper of Figure 6.3, where the IrCC is invoked as the irregular outer component, while the IrURC and IrMapper are combined as the irregular inner component.

6.4.1 Irregular Outer Codes

In this chapter, we introduce a hybrid combination of irregular repetition codes and convolutional codes, which constitute the Ir-BICM-ID encoder. The original outer IrCC component was proposed by Tüchler and Hagenauer [143], which consists of different-rate components created from a mother code by puncturing. To be more specific, the IrCC was designed from a 1/2-rate memory-4 mother code defined by the Generator Polynomials (GPs) $(1, G_2/G_1)$, where puncturing was employed to generate a set of codes having gradually increasing coding rates. The feedback polynomial is defined by $G_1 = 1 + D + D^4 = (31)_8$ and the feedforward polynomial is represented by $G_2 = 1 + D^2 + D^3 + D^4 = (27)_8$.

For lower code rates, two additional generator polynomials, namely $G_3 = 1 + D + D^2 + D^4 = (35)_8$ and $G_4 = 1 + D + D^3 + D^4 = (33)_8$ are employed. The total number of subcodes in the memory-4 IrCC arrangement is $\mathsf{F} = 17$, having code rates spanning the range of [0.1,0.9], with a step size of 0.05.

The EXIT functions of these IrCC subcodes are shown in Figure 6.6, indicated by the dotted lines. Observe in Figure 6.6 that the original memory-4 IrCC exhibits a near-horizontal portion in the EXIT chart, which is typical of strong CCs having a memory of four and associated with 16 trellis states. In order to match the shape of the inner codes' EXIT curves more accurately, the shape of the outer codes' EXIT functions can be adjusted in a way, which allows us to match a more diverse-shaped set of inner-code EXIT functions. Hence we introduce a more diverse range of EXIT functions, particularly along the diagonal region of the EXIT chart. This can be achieved by invoking weaker codes having a lower memory.

Accordingly, memory-1 CCs are also in corporated in the IrCC scheme, which have a simple two-state trellis diagram. The generator polynomial of this memory-1 0.5-rate

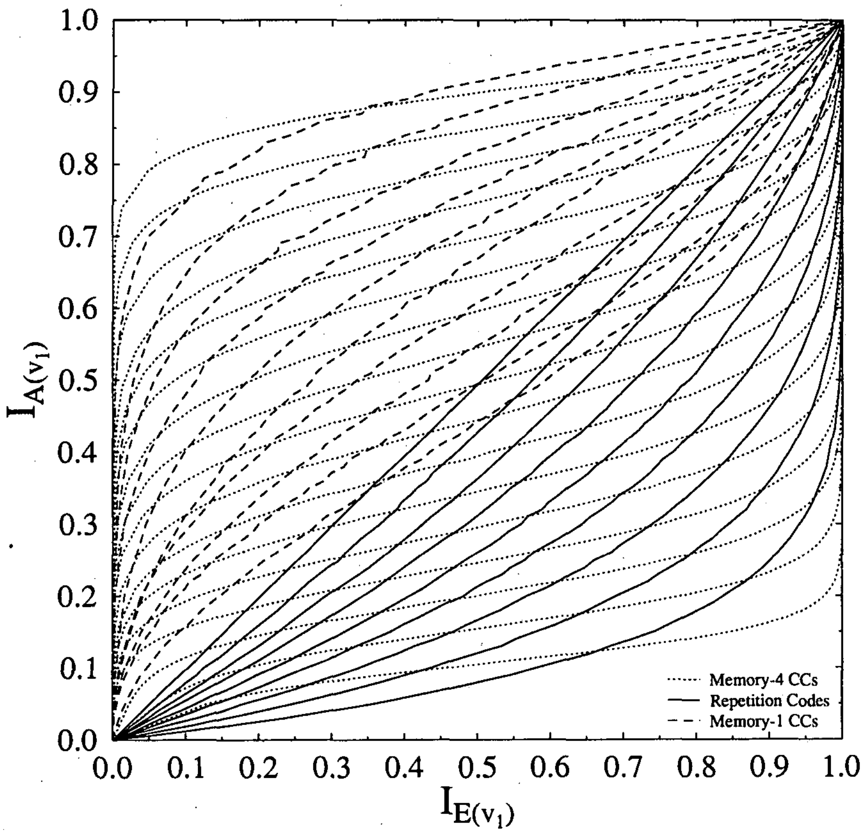

Figure 6.6: EXIT functions of the F = 36 subcodes of the IrCC scheme of Figure 6.3 as specified in Table 6.2.

mother code is defined by GPs $(1, G_2/G_1)$, where we have $G_1 = D$ and $G_2 = 1$. For lower code rates, an extra output GP, namely G_3 is used, where $G_3 = G_2$. For higher code rate, the puncturing pattern of the memory-4 IrCC is employed [143]. This way we generate 10 additional EXIT functions, as shown by the dashed lines in Figure 6.6, spanning the range of [0.45,0.9], with a step size of 0.05. The 10 memory-1 CC are specified by the tuples $\{r, (w_1, w_2, w_3), l, (p_1, p_2, p_3, p_4)\}$, where r represents the code rate, w_i specifies how often the GP G_i occurs, l is the puncturing period and the puncturing pattern is defined by p_i, which is the octal representation associated with G_i [142, 143]. These additional 10 memory-1 CC is detailed in Table 6.1.

A repetition code is a simple memoryless code, which consists of only two codewords, namely the all-zero word and the all-one word. Since it has no memory, the EXIT functions of such repetition codes are diagonally-shaped. In Figure 6.6, we have nine different-rate repetition codes as indicated by the solid lines and spanning the code-rate range of [0.1,0.5] with the step size of 0.05.

r	w_1, w_2, w_3	l	p_1, p_2, p_3, p_4
0.45	1,1,1	9	777,777,021
0.5	1,1	1	1,1
0.55	1,1	11	3777,2737
0.6	1,1	3	7,3
0.65	1,1	13	17777,05253
0.7	1,1	7	177, 025
0.75	1,1	3	7,1
0.8	1,1	4	17,1
0.85	1,1	17	377, 777, 010, 101
0.9	1,1	9	777,1

Table 6.1: The additional 10 memory-1 CC specified by the tuples $\{r, (w_1, w_2, w_3), l, (p_1, p_2, p_3, p_4)\}$.

Each of these $\mathsf{F} = 36$ subcodes encodes a specific fraction of the bit stream u_1 of Figure 6.3 according to a specific weighting coefficient α_i, where $i = 1, 2, ..., 36$. More specifically, let us assume that there are L number of encoded bits v_1 in Figure 6.3, where each subcode i encodes a fraction of $\alpha_i r_i L$ and generates $\alpha_i L$ encoded bits using a coding rate of r_i. Let us assume that there are F number of subcodes and that the following conditions must be satisfied:

$$\sum_{i=1}^{\mathsf{F}} \alpha_i = 1, \tag{6.8}$$

where $R_o = \sum_{i=1}^{\mathsf{F}} \alpha_i r_i$ with $\alpha_i \in [0,1]$, $\forall i$ and R_o is the average outer code rate. The EXIT functions of all $\mathsf{F} = 36$ IrCC subcodes are shown in Figure 6.6. The subcodes of the outer component code are summarised in Table 6.2.

6.4.2 Irregular Inner Codes

In order to generate a narrow but nonetheless open EXIT chart tunnel, which leads to the convergence point of $(I_A, I_E) = (1, 1)$, we have to design inner EXIT functions which match the shape of those in Figure 6.6 and exhibit a wide variety of EXIT characteristic shapes. Again, in this chapter, we propose an inner decoder block, which consists of an IrURC and IrMapper combination.

First, we investigate the effect of having different precoder memories, when communicating over an uncorrelated Rayleigh fading channel using 8PSK modulation employing GM. The serial concatenated precoder and mapper represents the inner component

Code Index i	Type	Coding Rate	Code Index i	Type	Coding Rate
1	CC mem-4	0.10	19	Rep. Code	0.15
2	CC mem-4	0.15	20	Rep. Code	0.20
3	CC mem-4	0.20	21	Rep. Code	0.25
4	CC mem-4	0.25	22	Rep. Code	0.30
5	CC mem-4	0.30	23	Rep. Code	0.35
6	CC mem-4	0.35	24	Rep. Code	0.40
7	CC mem-4	0.40	25	Rep. Code	0.45
8	CC mem-4	0.45	26	Rep. Code	0.50
9	CC mem-4	0.50	27	CC mem-1	0.45
10	CC mem-4	0.55	28	CC mem-1	0.50
11	CC mem-4	0.60	29	CC mem-1	0.55
12	CC mem-4	0.65	30	CC mem-1	0.60
13	CC mem-4	0.70	31	CC mem-1	0.65
14	CC mem-4	0.75	32	CC mem-1	0.70
15	CC mem-4	0.80	33	CC mem-1	0.75
16	CC mem-4	0.85	34	CC mem-1	0.80
17	CC mem-4	0.90	35	CC mem-1	0.85
18	Rep. Code	0.10	36	CC mem-1	0.90

Table 6.2: The outer CC with different number of memories (mem.) and repetition (rep.) subcodes used in the hybrid IrCC component of Figure 6.6, where each subcode index i corresponds to the α_i weighting coefficient in Equation (6.8).

block shown in Figure 6.4, although, without inner iterations. We conducted a full search for all URCs, invoking a memory of up to three. The 10 most distinct EXIT functions are plotted in Figure 6.8. The GPs of the URC are defined in the form of (G_1, G_2), where G_1 and G_2 represent the feedforward and feedback polynomials in octal format. The corresponding shift-register component schematics are shown in Figure 6.7.

URC index i	G_1	G_2	URC index i	G_1	G_2
URC_1	2_8	3_8	URC_6	10_8	13_8
URC_2	4_8	7_8	URC_7	15_8	14_8
URC_3	16_8	17_8	URC_8	10_8	17_8
URC_4	7_8	5_8	URC_9	13_8	17_8
URC_5	6_8	7_8	URC_{10}	7_8	6_8

Table 6.3: The outer URC subcodes used in the hybrid IrCC component, where each subcode index i corresponds to the α_i weighting coefficient in Equation (6.8).

Note from Figure 6.8 that the bit-to-8PSK symbol mapper employing GM does not benefit from the iterations, since its EXIT function is a horizontal line, as shown

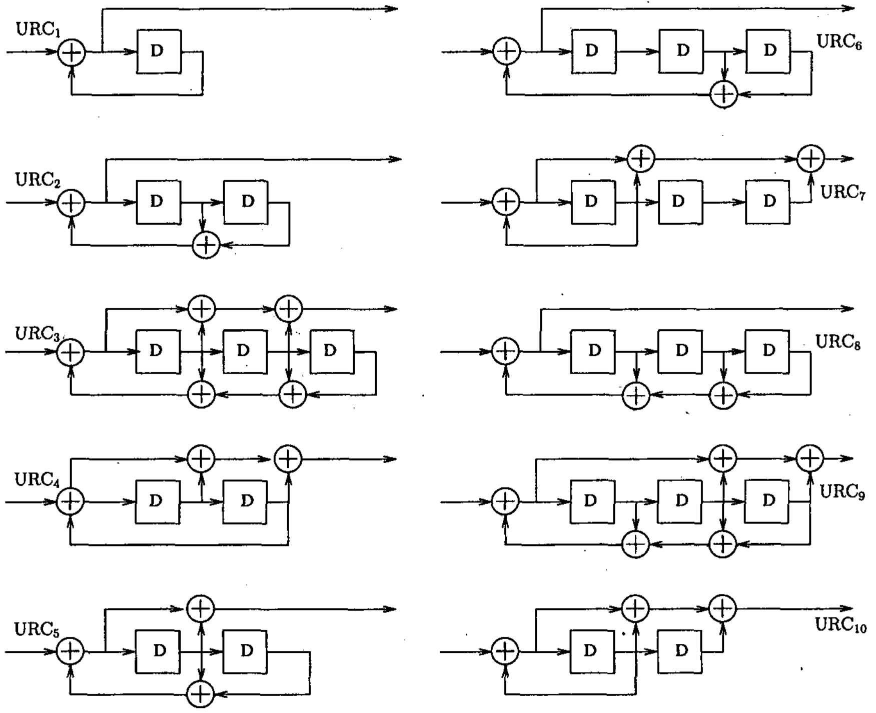

Figure 6.7: Shift-register encoder schematics for Q = 10 URC components.

in Figure 3.15. In contrast, the modulator invoking other mappers would require iterations within the inner component, since the corresponding EXIT function is not a horizontal line. Therefore, a near-capacity scheme requires inner iterations between the URC decoder and the demapper of Figure 6.4.

Let us now create a range of IrURC schemes consisting of three URCs, each having a different memory length. After evaluating the EXIT chart of all possible combinations of up to three different-memory URCs, we selected the three most dissimilar URC EXIT functions. More specifically, we used the GPs (G_1, G_2) of $(2,3)_8$, $(4,7)_8$ and $(16,17)_8$, or $(1, 1+D)$, $(1, 1+D+D^2)$ and $(1+D+D^2, 1+D+D^2+D^3)$, which are termed as URC$_1$ URC$_2$ URC$_3$, respectively, as part of the subcodes specified in Table 6.3.

Finally, the IrMapper of Figure 6.3 consists of irregular mapping schemes, each invoking a different bit-to-symbol mapping strategy. Here, we consider an 8PSK constellation and employ four different mapping schemes, which exhibit dissimilar EXIT functions, namely Gray Mapping (GM), Ungerböck's Partitioning (UP) [16], Block Partitioning (BP) and Mixed Partitioning (MP) [51], as defined and specified earlier

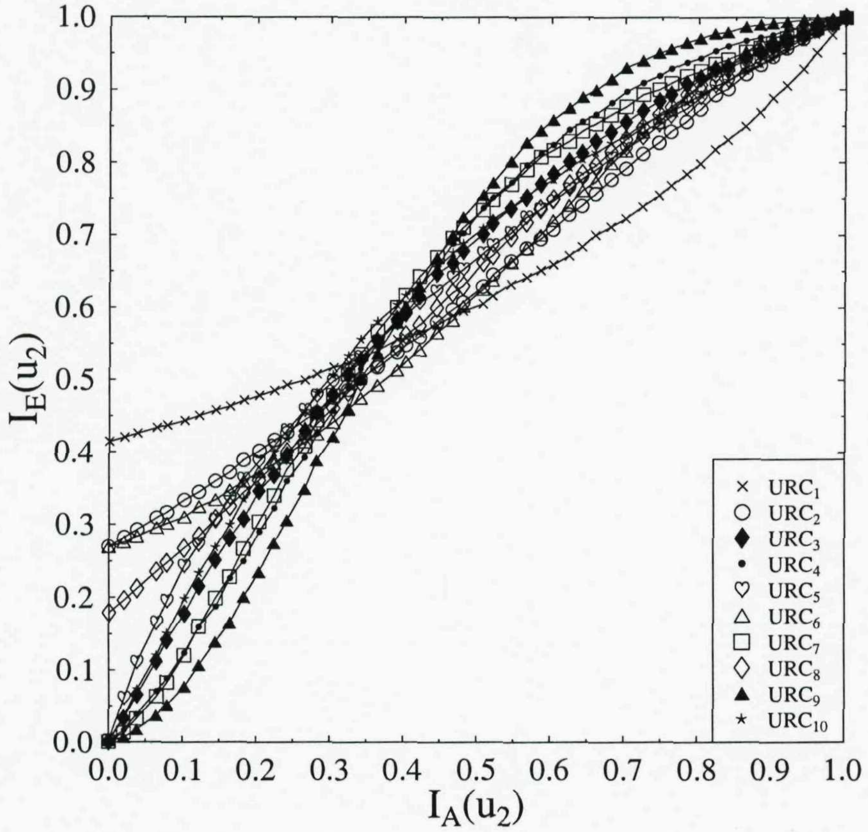

Figure 6.8: EXIT functions of the Q = 10 inner URC sub-components of Figure 6.7, specified in Table 6.3, when communicating over uncorrelated Rayleigh fading channels at $E_b/N_0 =$ 5.3dB. The precoders of Table 6.3 having memories of 1, 2 and 3 were employed in conjunction with an 8PSK GM using no inner iteration.

in Table 3.1. The corresponding bit-to-symbol mapping schemes are repeated in Table 6.4 for convenience.

With the IrURC and IrMapper schemes defined, we proceed by creating Q = 12 different EXIT functions for the inner decoder components, each invoking a different combination of the IrURC and IrMapper schemes of Table 6.4. For example, the URC_1 scheme employing the GM arrangement was defined in Table 6.4 as UM_1.

The EXIT functions of the Q = 12 combined inner IrURC-IrMapper components are plotted in Figure 6.9 for $E_b/N_0 = 5.3$dB. Note that these EXIT functions exhibit a wider range of shapes compared to the non-iterative, Gray-mapped IrURC shown in Figure 6.8. The weighting coefficients are defined as β, satisfying the following

Mapping Type	Mapping Indices to Corresponding Signal Points ($\cos 2\pi i/M$, $\sin 2\pi i/M$) for $i \in$ 0 1 2 3 4 5 6 7
GM	0 1 3 2 6 7 5 4
UP	0 1 2 3 4 5 6 7
BP	7 3 6 2 4 0 5 1
MP	0 2 1 7 4 6 5 3

Inner Component	URC Type/Mapping Type
UM_1	URC_1/GM
UM_2	URC_2/GM
UM_3	URC_3/GM
UM_4	URC_1/UP
UM_5	URC_2/UP
UM_6	URC_3/UP
UM_7	URC_1/BP
UM_8	URC_2/BP
UM_9	URC_3/BP
UM_{10}	URC_1/MP
UM_{11}	URC_2/MP
UM_{12}	URC_3/MP

Table 6.4: Various mapping schemes and URC Mapper (UM) combinations, each exhibiting a different inner EXIT function. The bit-to-symbol mapping strategies were Gray Mapping (GM), Ungerböck's Partitioning (UP), Block Partitioning (BP) and Mixed Partitioning (MP) [51], where M is the number of constellation points.

conditions:

$$\sum_{i=1}^{Q} \beta_i = 1 \quad \text{and } \beta_i \in [0,1], \quad \forall i. \tag{6.9}$$

6.4.3 EXIT Chart Matching

We adopt the EXIT chart matching algorithm of [143] to jointly match the EXIT functions of both the irregular inner and outer components, as detailed in Section 6.4.2. The EXIT functions to be considered are described in Equations (6.4) and (6.5). More explicitly, we intend to minimise the EXIT-tunnel area represented by the square of the error function of

$$e(i) = [f_{v_2}(i, E_b/N_0) - f_{v_1}^{-1}(i)]. \tag{6.10}$$

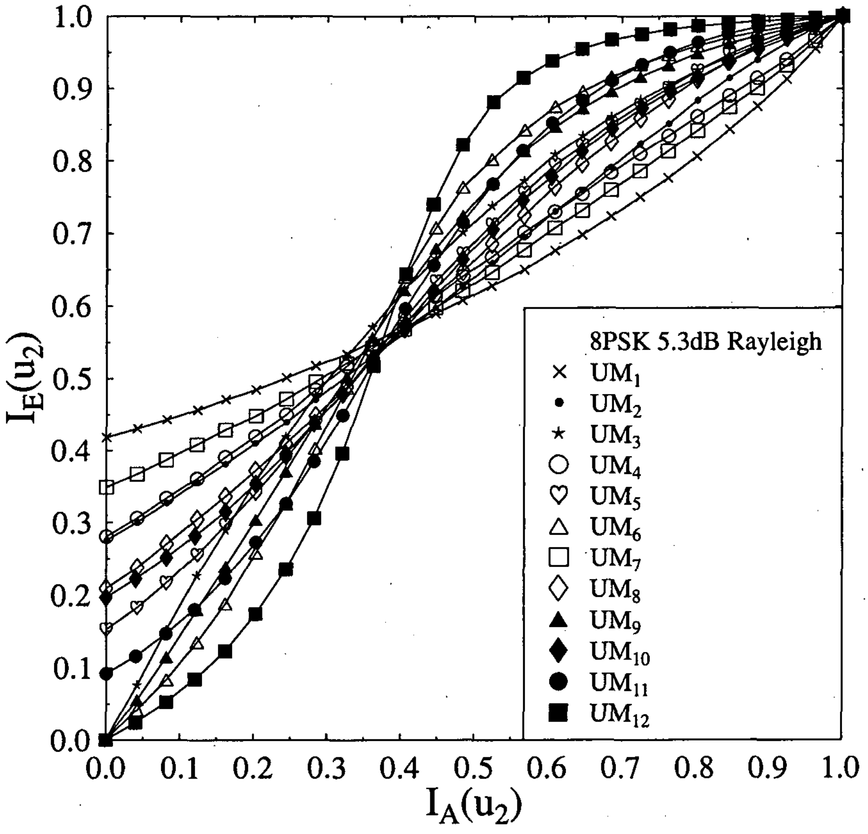

Figure 6.9: EXIT functions of the Q = 12 inner sub-components of Figure 6.4 and Table 6.4, when communicating over uncorrelated Rayleigh fading channel at $E_b/N_0 = 5.3$dB.

Furthermore, the error function should be larger than zero and may be expressed as [143]:

$$\begin{aligned}\mathcal{J}(\alpha_1, ..., \alpha_\mathsf{F}) &= \int_0^1 e(i)^2 di, \quad e(i) > 0, \forall i \in [0,1], \quad \text{OR} \\ \mathcal{J}(\beta_1, ..., \beta_\mathsf{Q}) &= \int_0^1 e(i)^2 di, \quad e(i) > 0, \forall i \in [0,1], \end{aligned} \tag{6.11}$$

where Q or F is the number of irregular sub-codes used either by the inner or by the outer components, depending on where the matching process is executed. We term the constraint of Equation (6.11) as condition C:1. Another constraint we impose here is that of ensuring that Equations (6.8) and (6.9) are fulfilled and we term these as condition C:2 and C:3, respectively. The term function $\mathcal{J}(.)$ of Equation (6.11) satisfies these conditions, depending on where the matching process is executed. When the matching algorithm is executed with respect to the outer codes, the term α_i of Equation (6.8) would be used and when it is executed with respect to the inner codes, the term β_i of Equation (6.9) would be considered.

The joint EXIT chart matching algorithm of [143] is applied alternatively to the inner and outer components in order to find the optimal value of $\alpha_{\mathbf{opt}}$ and $\beta_{\mathbf{opt}}$ which is summarised as follows

Step 1: Create the F outer components of the IrCC and the Q inner URC Mapper components (UM), as shown in Figures 6.6 and 6.8.

Step 2: Select one out of Q UMs, as the inner component to be used.

Step 3: Select an initial outer coding rate R_0, to be employed in the EXIT-chart matching algorithm of [143]. This R_0 is the initial R_{IR} to be placed in the matrix **d** as detailed in [143].

Step 4: Employ the EXIT chart matching algorithm [143] to obtain $\alpha_{\mathbf{opt}}$, subject to the constraints of C:1 and C:2, given by Equations (6.11) and (6.8).

Step 5: Repeat **Step 3** and **Step 4** iteratively, until a sufficiently high initial rate R_0 is obtained.

Step 6: Record the resultant outer EXIT curve.

Step 7: Invoke the EXIT chart matching algorithm for finding the best weights of the Q number of UMs to match the IrCC's outer EXIT curve of **Step 6**, in order to obtain $\beta_{\mathbf{opt}}$. This process is subject to the constraints of C:1 and C:3, given by Equations (6.11) and (6.9).

Step 8: Record the resultant inner EXIT curve and repeat the EXIT chart matching process of **Step 4**, **Step 6** and **Step 7**, each time with a small increment of R_0, until no more increment is possible.

Step 9: Activate the EXIT matching algorithm to find the best-matching outer code EXIT chart function for the target inner code EXIT function, this time using one out of Q UMs, which was not used in **Step 2**. Repeat **Step 4**, **Step 6**, **Step 7** and **Step 8**, until all the Q number of UMs were tested.

Step 10: Terminate the algorithm, choose the best values of $\alpha_{\mathbf{opt}}$ and $\beta_{\mathbf{opt}}$, yielding the highest possible outer coding rate.

Eventually, at the end of the EXIT chart matching process, the EXIT function $f_{v_1}[I_{A(v_1)}]$ of Equation (6.5) corresponds to the best IrCC, which might be constructed from $\mathsf{F} = 36$ subcodes, where each subcode EXIT function is defined as $f^i_{v_1}[I_{A(v_1)}]$. This also implies that the EXIT function $f_{v_1}[I_{A(v_1)}]$ is the weighted superposition of $\mathsf{F} = 36$ EXIT functions, satisfying the following conditions

$$f_{v_1}[I_{A(v_1)}] = \sum_{i=1}^{\mathsf{F}} \alpha_i f^i_{v_1}[I_{A(v_1)}]. \tag{6.12}$$

In a similar fashion, the EXIT function of $f_{u_2}[I_{A(u_2)}, E_b/N_0]$ in Equation (6.4) corresponds to that specific irregular inner component, which might be constructed from $\mathsf{Q} = 12$ subcomponents. The weighted superposition of the EXIT function $f^i_{u_2}[I_{A(u_2)}, E_b/N_0]$ of each sub-component results in

$$f_{u_2}[I_{A(u_2)}, E_b/N_0] = \sum_{i=1}^{\mathsf{Q}} \beta_i f^i_{u_2}[I_{A(u_2)}, E_b/N_0]. \tag{6.13}$$

6.5 Simulation Results

In this section we embark on characterising the proposed Ir-BICM-ID scheme in terms of its EXIT chart based convergence behaviour for transmission over the uncorrelated Rayleigh fading channel. Let us employ the EXIT chart matching algorithm described in Section 6.4.3, invoking the hybrid combination the IrCC, IrURC as well as IrMapper schemes. The adjustable shapes of the EXIT functions enable us to reduce the open EXIT tunnel area and hence to create a near-capacity Ir-BICM-ID scheme. As a further benefit, we are able to shift the inner EXIT function closer to the $(I_A, I_E) = (1, 1)$ point for the sake of achieving an infinitesimally low BER.

Since the inner IrURC component has a unity rate by definition, the effective throughput of the Ir-BICM-ID scheme may be expressed as $\eta = R \cdot \log_2 M$ bits per channel use, where M is the number of constellation points and R denotes the coding rate of the outer IrCC. The relationship of the SNR (E_s/N_0) and E_b/N_0 can be represented as $E_s/N_0 = E_b/N_0 \cdot \eta$, where N_0 is the noise power spectral density and E_s as well as E_b denotes the transmit energy per channel symbol use and per bit of source information, respectively.

Later in this section, we will analyse the complexity of the near-capacity IrCC scheme, which can be quantified in terms of the number of trellis states of the IrCC and IrURC components. The complexity of the IrMapper is low and hence it is ignored in the complexity calculation. In order to reduce the complexity, we are also able to adjust the weighting coefficient α_i for the various subcodes CC^i, creating a flexible Ir-BICM-ID scheme.

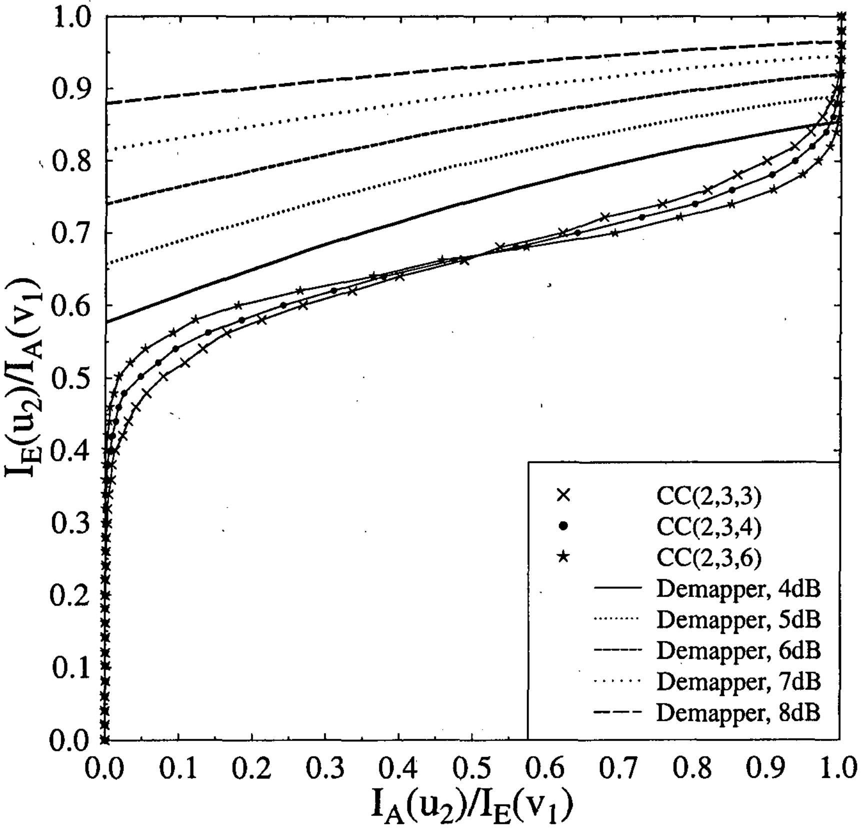

Figure 6.10: EXIT functions of the classic BICM-ID inner and outer components of Figure 6.1, when transmitting over an uncorrelated Rayleigh fading channel using 8PSK UP modulation.

The conventional BICM-ID scheme dispenses with the URC, hence the inner component consists of a simple demapper. Therefore in Figure 6.3, the dashed box surrounding the inner component representing the BICM-ID scheme is constituted solely by the demapper. The outer code, is constituted by a convolutional code. Figure 6.10 illustrates the EXIT functions of both the inner and outer components, where the outer code rate was 2/3, associated with a memory of $\varphi = 3, 4$ and 6.

Observe from Figure 6.10 that the inner demapper does not reach the point of convergence at (1,1). Furthermore, there is a mismatch between the corresponding EXIT curve shapes, indicating an E_b/N_0 'loss' with respect to the capacity. A further

E_b/N_0 improvement is achieved upon introducing the IrCC outer code, which reduces the area of the open EXIT tunnel, as shown in Figure 6.11, but still exhibits a 'larger-than-necessary' EXIT tunnel. Figure 6.11 shows that the shape of the outer IrCC EXIT function is better matched to that of the inner codes, as indicated by the dotted line shifting upwards, when the channel's E_b/N_0 value increases.

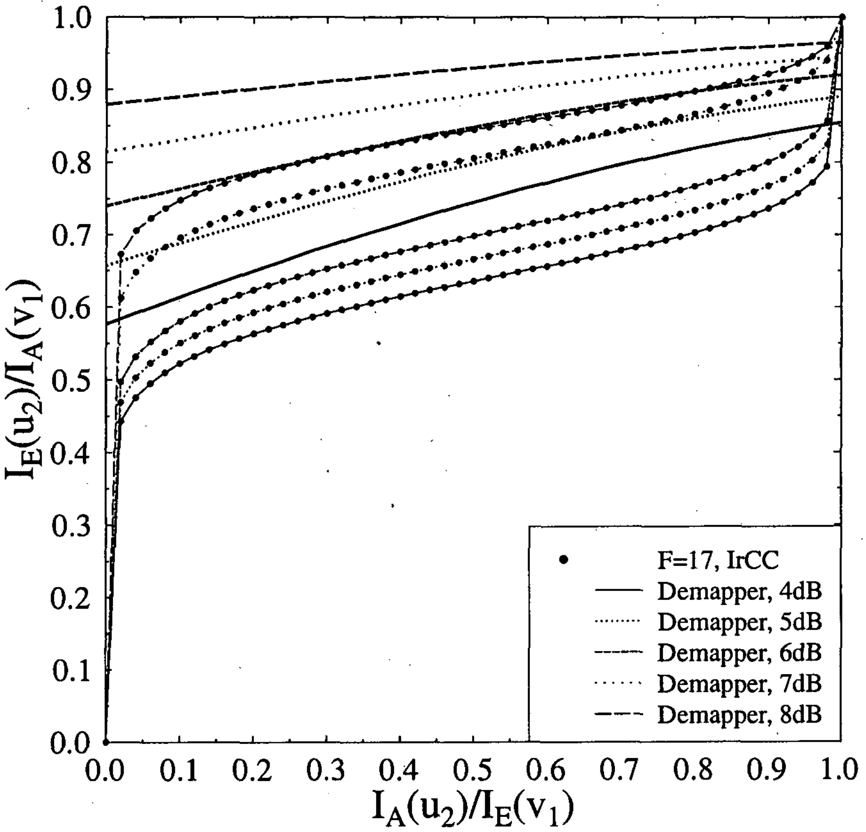

Figure 6.11: EXIT functions of the BICM-ID inner and outer components, using a F = 17 IrCC of memory-4 as the outer component, when communicating over an uncorrelated Rayleigh fading channel invoking 8PSK UP modulation. The general structure of the schematic is shown in Figure 6.1 by replacing the CC encoder with the F = 17 IrCC of memory-4, as detailed in Table 6.2.

Let us finally employ the EXIT chart matching algorithm described in Section 6.4.3, invoking the IrCC, IrURC as well as IrMapper schemes. The shape of the EXIT functions enables us to reduce the open EXIT tunnel area and hence to create a near-capacity Ir-BICM-ID scheme. As a further benefit, we are able to shift the inner EXIT function closer to the (1,1) point for the sake of achieving an infinitesimally low BER.

We observe from Figure 6.12 that the open EXIT tunnel of the resultant scheme

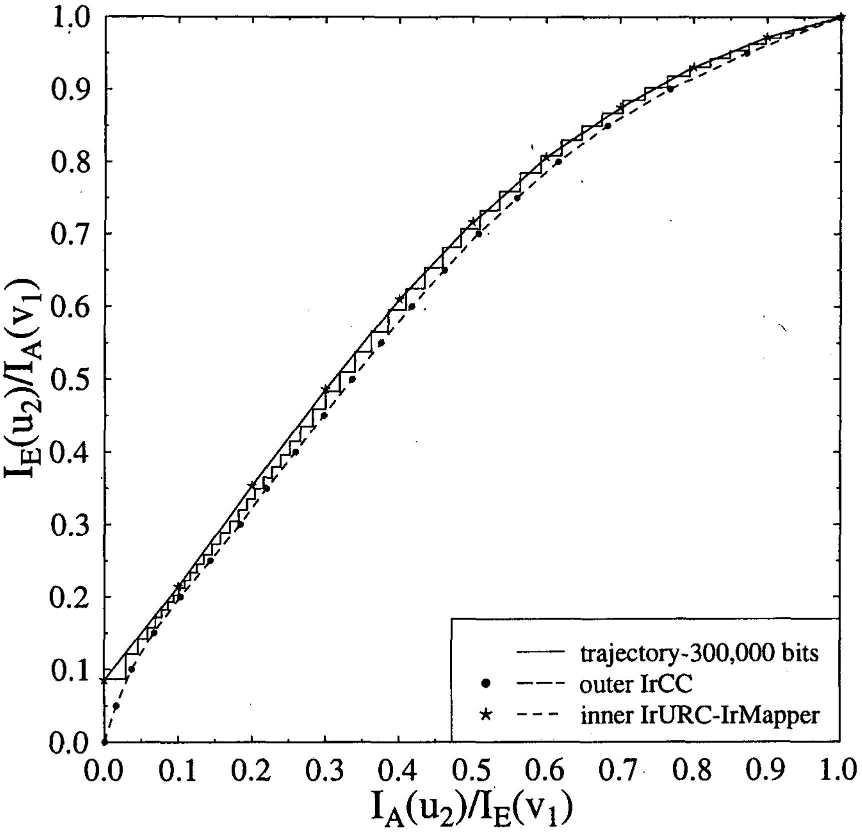

Figure 6.12: EXIT functions and the trajectory of the Ir-BICM-ID schemes of Figure 6.3 designed for transmission over an uncorrelated Rayleigh fading channel at $E_b/N_0 = 5.3$dB. The overall code rate is 0.635, the effective throughput is 1.905 bit/symbol and the modulation scheme is 8PSK. The weighting coefficients α_{opt} and β_{opt} are given in Equations (6.14) and (6.15), while the individual subcodes are detailed in Tables 6.2 and 6.4.

is narrow and reaches the point of convergence at $(I_A, I_E) = (1, 1)$. However, since the number of iterations required increases, the decoding complexity is also increased. Figure 6.12 also illustrates that the trajectory matches the inner and outer EXIT functions and evolves within the narrow tunnel, reaching the $(I_A, I_E) = (1, 1)$ point of convergence for an interleaver length of 300,000.

Note that the proposed Ir-BICM-ID scheme has advantages over the bit-interleaved irregular modulation scheme of [138], when we further explore the effects of various mapping schemes combined with URCs having different memory lengths. This gives us the flexibility of adjusting the EXIT curve shape in order to achieve a low BER, without having to change the number of modulated constellation points, which would require complex state-of-the-art AMC [139]. Furthermore, we employ the joint EXIT chart matching algorithm of Section 6.4.3 to produce flexible inner and outer component codes. The complexity imposed by the iterations between the IrURC and IrMapper schemes is low compared to that of the outer IrCC. Our hybrid IrCC scheme employs low-memory CCs and two-state memoryless repetition codes, which allows us to reduce the trellis complexity of the scheme.

The EXIT function of Figure 6.12 was recorded for the EXIT chart matching algorithm of Section 6.4.3 for an overall coding rate of 0.635. The resultant weighting coefficients of $\alpha_{\mathbf{opt}}$ and $\beta_{\mathbf{opt}}$ are

$$\begin{aligned}
\alpha_{\mathbf{opt}} &= [\alpha_1, ..., \alpha_{36}] \\
&= [0, 0, 0.0311597, 0, 0, 0, 0, 0, 0, 0, 0, 0.0293419, 0.0228237, 0, 0.0309682, \\
&\quad 0, 0, 0, 0, 0, 0, 0, 0.0837582, 0, 0, 0, 0.404757, 0, 0, 0, 0, 0, 0, 0, 0, 0.397229] \\
&= [\alpha_3^{0.0311597}, \alpha_{12}^{0.0293419}, \alpha_{13}^{0.0228237}, \alpha_{15}^{0.0309682}, \alpha_{23}^{0.0837582} \\
&\quad \alpha_{27}^{0.404757}, \alpha_{36}^{0.404757}], \qquad (6.14) \\
\beta_{\mathbf{opt}} &= [\beta_1, ..., \beta_{12}] \\
&= [0, 0, 0.340268, 0, 0.550512, 0, 0, 0, 0.109219, 0, 0, 0] \\
&= [\beta_3^{0.340268}, \beta_5^{0.550512}, \beta_9^{0.109219}], \qquad (6.15)
\end{aligned}$$

where α_i^j and β_i^j refer to the weighting coefficient of α_i and β_i having a value of j. Those components having 0 weighting coefficient are ignored in the expression for clarity.

The theoretical Discrete-input Continuous-output Memoryless Channel's (DCMC) capacity [110] was described in Section 4.5.2 which is plotted in comparison to the maximum achievable capacity of the proposed Ir-BICM-ID scheme in Figure 6.13. Note that the achieveable capacity of the Ir-BICM-ID scheme is close to the DCMC's capacity. For example, at SNR = 6dB the discrepancy between the theoretical capacity and the proposed coded modulation scheme's is less than 0.1dB in Figure 6.13. This confirms the benefits of the proposed EXIT chart matching approach.

The dashed line combined with the dot marker of Figure 6.13 shows the achievable throughput of the Ir-BICM-ID scheme, when employing Tüchler's $\mathsf{F} = 17$ memory-4 IrCC [143]. Since the EXIT functions of the 17 subcodes consist of memory-4 CCs, the EXIT curves exhibit a rather gently shaping, near-horizontal shapes in their middle

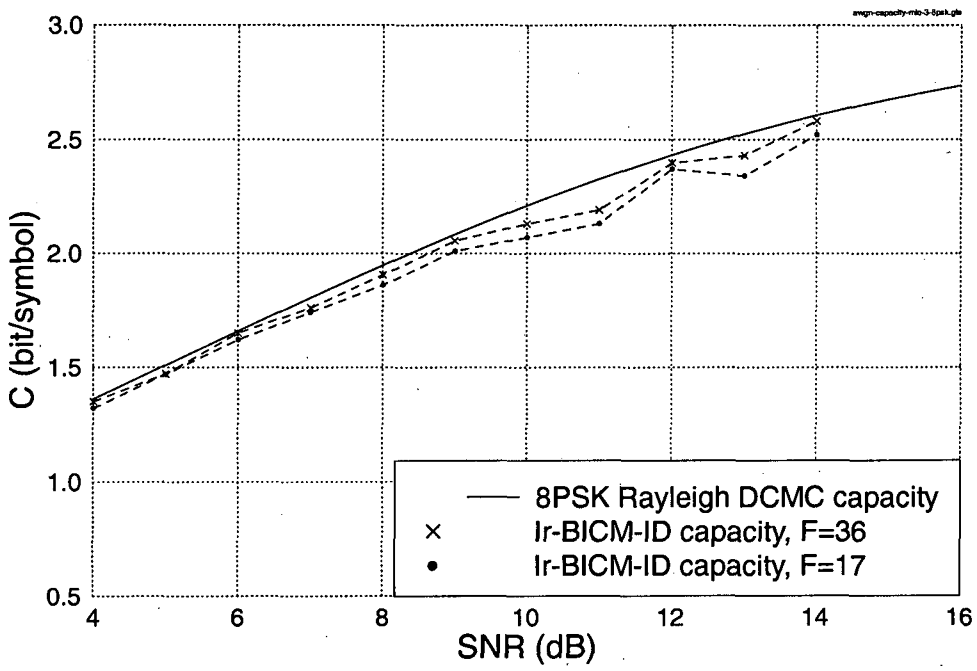

Figure 6.13: The maximum effective throughput of the propose Ir-BICM-ID scheme of Figure 6.3 in comparison to the theoretical DCMC capacity plot [147] using 8PSK-modulated transmission over the uncorrelated Rayleigh fading channel.

section as can been seen in Figure 6.6. Therefore the matching process exhibits a higher discrepancy from the DCMC's capacity. When introducing the whole range of F = 36 subcodes for the new hybrid IrCCs, we attain a closer match to the channel capacity, as shown by the cross-markers of Figure 6.13.

Figure 6.14 shows the BER performance of the Ir-BICM-ID scheme for different interleaver lengths. The DCMC's capacity limit is $E_b/N_0 = 4.89$dB at a throughput of 1.905 bit/symbol using 8PSK. By interleaving over 300,000 bits, the Ir-BICM-ID design becomes capable of achieving an infinitesimally low BER as close as 0.32dB from the theoretical capacity limit, as shown in Figure 6.14. When we decrease the interleaver length by a factor of 10 to 30,000 bits, the performance degrades, but still remains within about 0.75dB of the capacity. We include the classic 1/2- and 2/3-rate BICM-ID benchmarker scheme [23] having a 300,000-bit interleaver length as well as the BICM-ID scheme employing the F = 17 IrCC [143] outer code of rate-0.62. All the benchmarkers exhibit BER $> 10^{-5}$ even at $E_b/N_0 = 8$dB, which is relatively far from the capacity limit of $E_b/N_0 = 4.89$dB.

The complexity of the scheme is illustrated in Figure 6.15, quantified in terms of

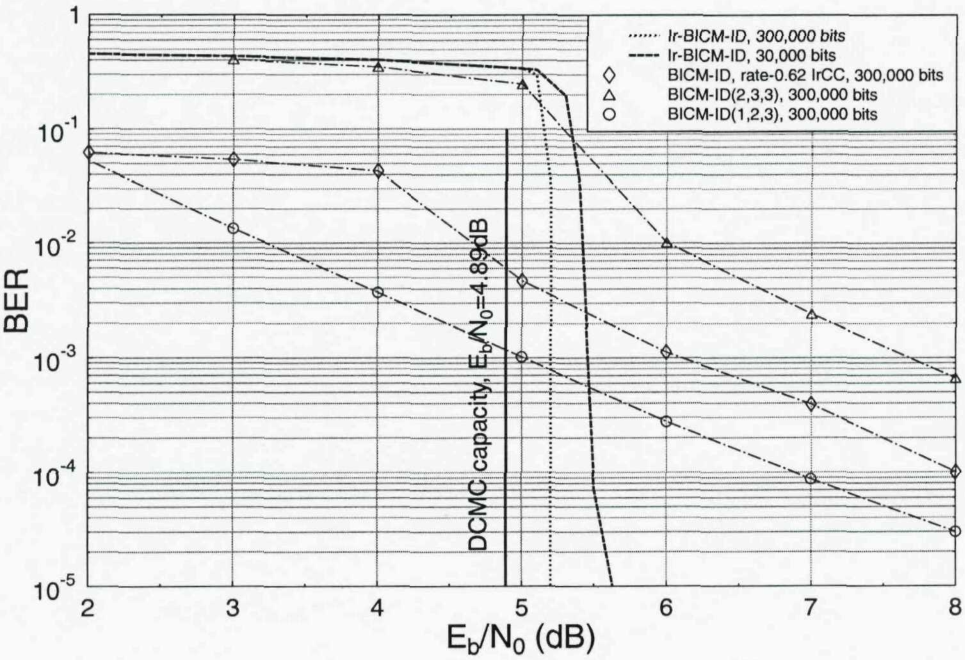

Figure 6.14: The BER performance of rate-0.635 Ir-BICM-ID schemes of Figure 6.3 at an effective throughput of 1.905 bit/symbol, using two different interleaver lengths and that of the classic 8PSK UP BICM-ID of Figure 6.1, employing a coding rate of $R = 1/2$ and $2/3$, respectively. A BER benchmarker of BICM-ID scheme invoking rate-0.62 outer IrCC proposed in [143] employing UP mapper is also attained. All subcodes of the irregular codes invoking IrCC and UM are detailed in Tables 6.2 and 6.4.

the number of trellis states for both the IrCC and IrURC schemes. As shown in Figure 6.15, the system requires a higher complexity for performing closer to capacity, namely at $E_b/N_0 = 5.3$dB. Note that we involve a total of about 6×10^8 trellis states of the IrURC and IrCC decoder for decoding 300,000 bits. By increasing the E_b/N_0 values, we are able to reduce the complexity of the system, as the EXIT tunnel becomes wider. Figure 6.16 illustrates the benefits of increasing E_b/N_0 from 4dB to 10dB. At $E_b/N_0 = 6.5$dB, the number of trellis states involved decreases exponentially to around 1.8×10^8.

Another way of reducing the complexity is to decrease the IrCC scheme's coding rate, in which case we would also sacrifice the near-capacity performance. The EXIT functions recorded for coding rates of $R = 0.5$ and $R = 0.4$ are shown in Figure 6.17, where the number of outer iterations was $I = 10$ and 7, respectively. The weighting coefficients α_{opt} for the IrCC having coding rates of $R = 0.5$ and $R = 0.4$ are detailed in Table 6.5.

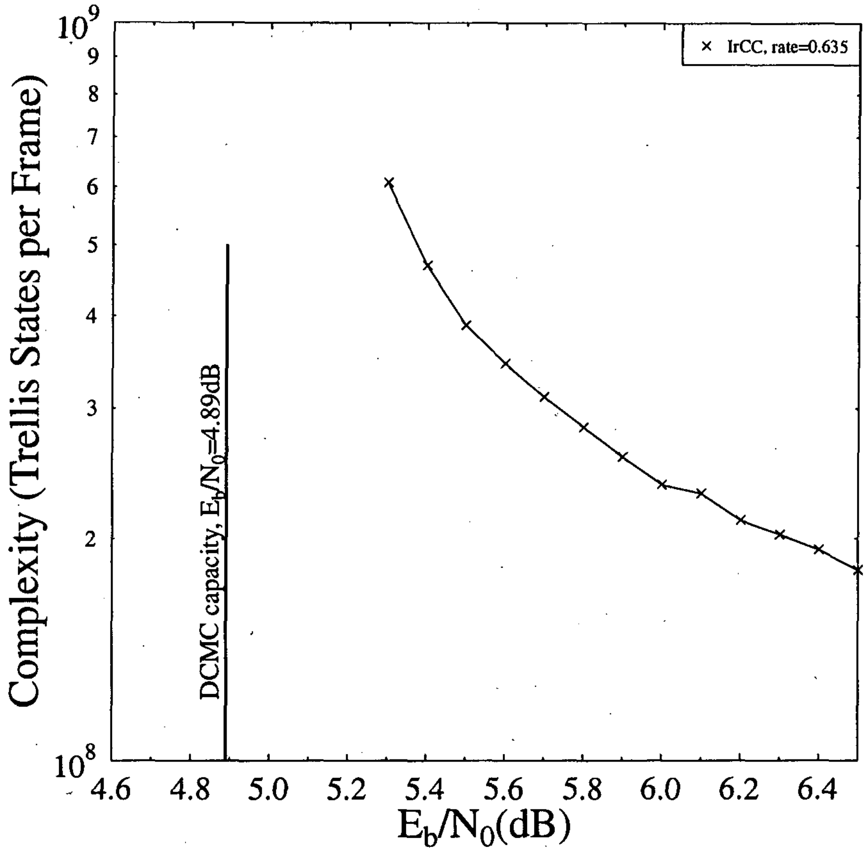

Figure 6.15: The complexity of the Ir-BICM-ID scheme of Figure 6.3 measured with respect to the number of trellis states employing the same weighting coefficients as in Figure 6.14 to achieve a BER of 10^{-5}. This scheme communicated over an uncorrelated Rayleigh fading channel using interleaver over a total of 300,000 bits/frame.

IrCC Coding Rate	Weighting Coefficient $\alpha_{\mathbf{opt}} = [\alpha_1, ..., \alpha_{36}]$
0.5	[0, 0, 0, 0, 0, 0, 0, 0, 0, 0, 0, 0.168897, 0.0151061, 0, 0, 0.158275, 0.124163, 0, 0, 0, 0.533687, 0, 0, 0, 0, 0, 0, 0, 0, 0, 0, 0, 0, 0, 0, 0] $[\alpha_{12}^{0.168897}, \alpha_{13}^{0.0151061}, \alpha_{16}^{0.158275}, \alpha_{17}^{0.124163}, \alpha_{21}^{0.533687}]$
0.4	[0, 0, 0, 0, 0, 0, 0, 0, 0, 0, 0, 0.157339, 0, 0, 0.139792, 0.0657432, 0, 0.195015, 0, 0, 0.442172, 0, 0, 0, 0, 0, 0, 0, 0, 0, 0, 0, 0, 0, 0, 0] $[\alpha_{12}^{0.157339}, \alpha_{15}^{0.139792}, \alpha_{16}^{0.0657432}, \alpha_{18}^{0.195015}, \alpha_{21}^{0.442172}]$

Table 6.5: Weighting coefficients $\alpha_{\mathbf{opt}}$ for IrCC having coding rates of $R = 0.5$ and $R = 0.4$.

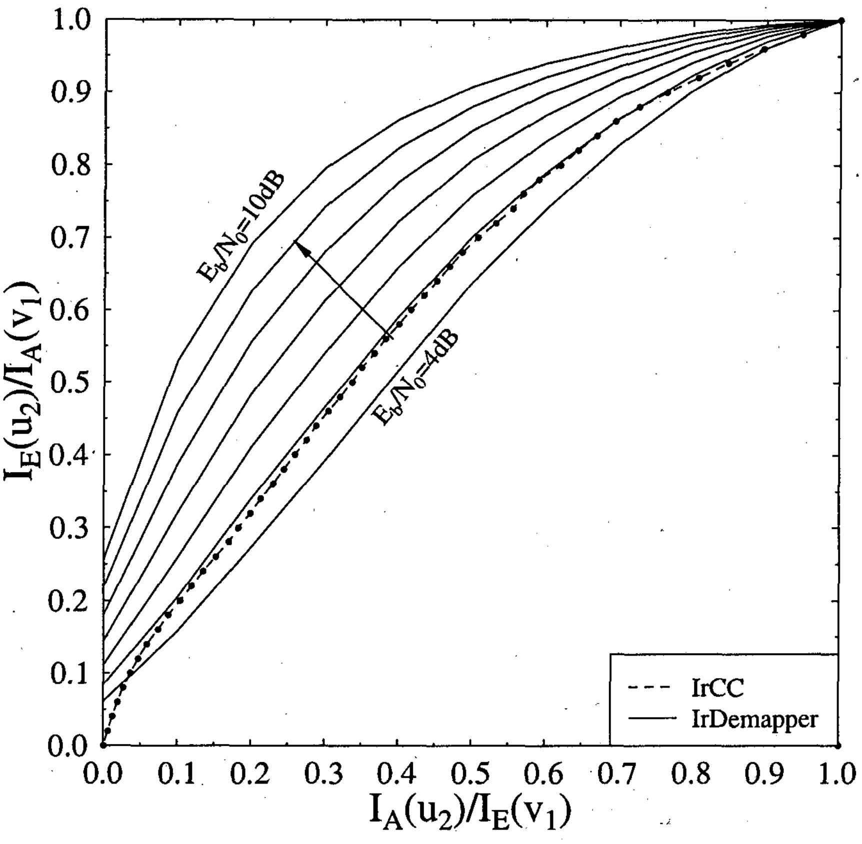

Figure 6.16: The EXIT functions of Ir-BICM-ID scheme of Figure 6.3 for the inner component having a coding rate of $R = 0.635$, when communicating over an uncorrelated Rayleigh fading channel at various E_b/N_0 values. The weighting coefficients α_{opt} and β_{opt} are detailed in Equations (6.14) and (6.15), respectively.

6.6 Chapter Conclusions

In this chapter, we proposed an Ir-BICM-ID scheme, invoking irregular encoders, precoders and modulators. Each component consists of irregular structures of various subcodes. Section 6.2 details the structure of the Ir-BICM-ID scheme specifying the activation order of both the outer and inner components. This three-stage concatenated system can be regarded as a two-stage system, when treating the IrURC and IrMapper as the combined inner block. The EXIT chart of Figure 6.9 in Section 6.3 illustrates the corresponding 2-D EXIT functions.

The irregular IrCC components are further improved by introducing more EXIT functions with the aid of designing new memory-1 CCs and repetition codes, as de-

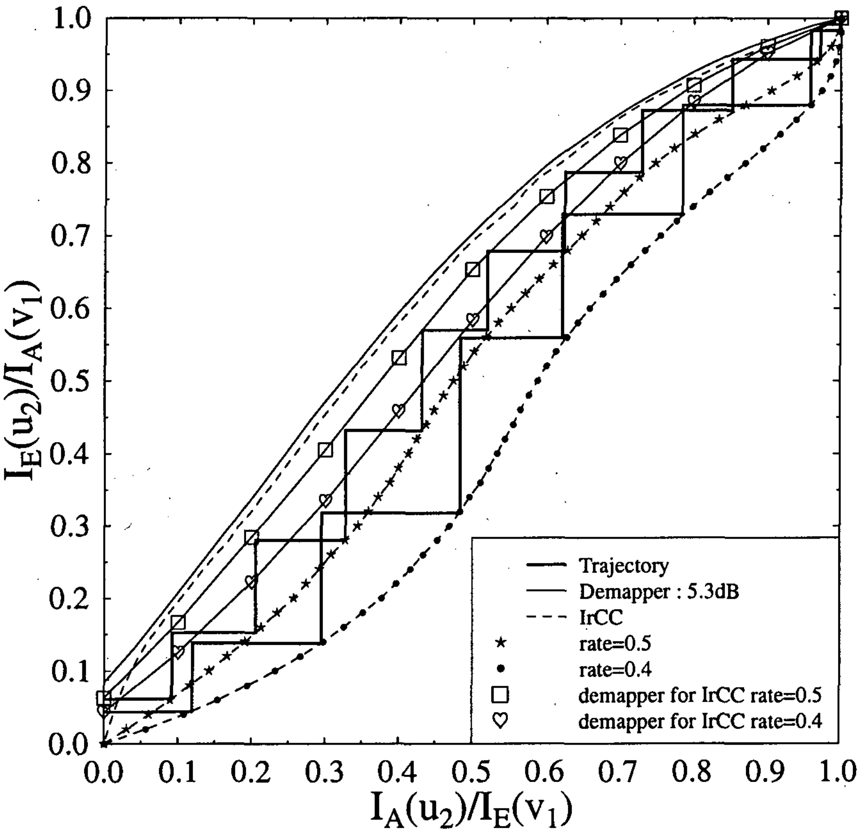

Figure 6.17: The EXIT functions for IrCCs of coding rates $R = 0.5$ and $R = 0.4$, when communicating over an uncorrelated Rayleigh fading channel. The weighting coefficients α_{opt} and β_{opt} are detailed in Table 6.5 and Equation (6.15), respectively.

scribed in Section 6.4 of Table 6.2. The outer component of the hybrid IrCC consists of F = 36 subcodes, while the inner component consists of Q = 12 subcodes, which are given in Tables 6.2 and 6.4, respectively. As detailed in Section 6.4.2, the proposed inner code consist of a combination of memory-1 up to memory-3 IrURCs, each invoking various mapping strategies, as outlined in Table 6.4.

The EXIT matching algorithm of [143] was modified to match both the inner and outer irregular components, as described in Section 6.4.3. The result of this matching procedure is the weighted superposition of both the inner and outer EXIT functions, having the weighting coefficients of α_{opt} and β_{opt}. This results in a narrow EXIT tunnel, as shown in Figure 6.12.

Section 6.5 illustrated the attainable performance of the proposed Ir-BICM-ID scheme. Figure 6.13 quantifies the discrepancy of this new scheme with respect to the theoretical capacity. At low SNR, for example at SNR = 6dB, the capacity of the system can be as close as 0.1dB from the capacity. The BER curve of the system exhibits an infinitesimally low value at about 0.32dB from the DCMC's capacity limit, when using an interleaver length of 300,000 bits, as shown in Figure 6.14.

Due to its close-to-capacity performance, the Ir-BICM-ID may require a high number of iterations. Figure 6.15 shows the complexity of the scheme quantified in terms of the total number of decoding trellis states of the IrCC and IrURC schemes. We can observe that the closer this system operates to the capacity, the higher the implementational complexity imposed. The complexity decreases exponentially, as the distance from capacity increases. However, the complexity imposed may be reduced by increasing the operational E_b/N_0 values, as shown in Figure 6.16. Furthermore, by adjusting α_{opt} in order to reduce the coding rate, we can increase the width of the EXIT tunnel, as seen in Figure 6.17.

Chapter 7

Conclusions and Future Work

The summary of the thesis is provided in Section 7.1, while a range of future research ideas is suggested in Section 7.2.

7.1 Summary and Conclusions

7.1.1 Chapter 1

In Chapter 1, we presented a historical perspective of various coded modulation schemes, including MLC, BICM, BICM-ID, TCM and TTCM. An overview of the related research contributions was provided in Section 1.1. The main contributions on coded modulation schemes were summarised in Table 1.1. Chapter 1 also presented the general organisation of this thesis, as outlined in Section 1.2.1. Finally, the novel contributions based on the related publications were discussed in Section 1.2.2.

7.1.2 Chapter 2

In Chapter 2, we provided an overview of the theoretical background on multilevel coding, which constitutes a powerful bandwidth efficient coded modulation scheme employing several component codes and invoking appropriate bit-to-symbol mapping. In Section 2.2, we considered the traditional design of MLCs, based on an $M = 2^l$-PSK signal constellation employing l number of component codes, as seen in Figure 2.1. In Section 2.2.1, we discussed various labelling or bit-to-symbol mapping strategies proposed in the literature. The equivalent channel model based on the chain rule of mutual information was presented in Section 2.2.2.

The iterative decoding of MLCs based on the PID structure was illustrated in Figure 2.8, where the signal labels were independently grouped without any *a priori* knowledge during the first decoding step within the PID scheme. The decoding of MLCs employing the MSD structure was shown in Figure 2.10, where the component codes were decoded stage-by-stage. The soft information bit provided by any of the previous stages was passed to the next stage during the decoding process. In order to determine the optimum coding rate for each component code of the MLC scheme in Section 2.2.5, we discussed two different rate-design rules suggested in the literature. First, the capacity rule [51] based on equivalent channel was presented in Section 2.2.5.1. Secondly, the balanced distance [51] rule considering the Euclidean distance between different signal pair sequences was outlined in Section 2.2.5.2. The MLC UEP design, which is capable of protecting the more significant bits more strongly, was introduced in Section 2.2.6.

A single level coded modulation scheme, namely the BICM, which can be considered as a subset of MLCs was detailed in Section 2.3. Here, we discussed the encoder and decoder structure of BICM, as shown in Figures 2.15 and 2.18. BICM consists of three general blocks, namely the encoder, the interleaver and the mapper as well as their corresponding decoder, deinterleaver and demapper counterparts. The iteratively detected version of BICM, namely BICM-ID, was further discussed in Section 2.4. Given the iterative decoding structure of Figure 2.20, we studied the *extrinsic* probability provided by the SISO module, which may be used to generate a soft-information feedback for the demodulator in order to achieve further iterative gains. Various bit-to-symbol mapping schemes can be designed for BICM-ID, which were detailed in Section 2.4.1, where different criteria based on the intra-set Euclidean distance and on the bit-wise mutual information were presented.

7.1.3 Chapter 3

In Chapter 3, we considered an EXIT-chart based design of our iterative BICM-ID and MLC schemes. We first conducted a comparative study of various coded modulation schemes in terms of their delay imposed by the interleaver block lengths, iterative protection aided performance as well as their complexity versus the number of their decoding trellis-states. The system model of these schemes was presented in Section

3.2.1, while the system parameters including the generator polynomials and puncturing matrix were shown in Section 3.2.2. Figure 3.1 portrayed the system structure of the coded modulation scheme considered in this comparative study.

We plotted the BER performance curves based on our simulation results in Section 3.2.3 for various parameters. Figures 3.5 and 3.6 showed the BER performance of various coded modulation schemes having different trellis-complexity and different interleaver block lengths. Table 7.1 summarises the attainable coding gain of these coded modulation schemes with respect to different trellis-state complexities and interleaver lengths. The UEP capability of our MLC schemes was characterised in Figure 3.7 for each of the different MLC protection levels.

Again, EXIT chart analysis was introduced in Section 3.3. First we considered the mutual information exchanged between the two constituent decoders of the iterative decoding scheme. We discussed the principles of EXIT chart construction based on a serially concatenated system, as highlighted in Figure 3.8. In Sections 3.3.1.1 and 3.3.1.2, we detailed these two iterative decoding blocks, exemplified by the serially concatenated inner and outer codes constituted by the demapper and the SISO decoder.

The EXIT chart analysis of BICM-ID was provided in Section 3.3.2. We highlighted the EXIT curves of both the inner and outer codes in Figure 3.11, portraying a range of inner EXIT functions for E_b/N_0 values ranging from 0dB to 10dB. Observe that having the inner code's EXIT function above that of the outer EXIT function would create an open EXIT tunnel, which can ensure iterative decoding convergence to an infinitesimally low BER. Hence, an open EXIT tunnel recorded for the BICM-ID scheme was exemplified in Figure 3.12. By altering the rate and the constraint length of the outer convolutional code, we can observe the change of shape for the outer code's EXIT functions, as shown in Figure 3.14. The employment of an appropriate mapping scheme is crucial for ensuring iterative decoding convergence to an infinitesimally low BER, since the EXIT function of the inner demapper would exhibit different shapes for different bit-to-symbol mappers, as seen in Figure 3.15. Figure 7.1 shows the initial and final values of I_E for the inner demapper employing the block-, mixed-, Gray- and Ungerböck-partitioning based mapping schemes of Table 3.1. Observe in Figure 7.1 that among all the mapping schemes, Gray mapping facilitates no iterative I_E improvements, while the EXIT curve of mixed partitioning ranges from the lowest I_E value in Figure 7.1, but attains the highest I_E increments.

	E_b/N_0 [dB]		Coding Gain [dB]	
	BER = 10^{-3}	BER = 10^{-5}	BER = 10^{-3}	BER = 10^{-5}
Uncoded QPSK	6.65	9.60	0	0
Overall trellis-complexity, $\nu = 32$ states/coded bit, Interleaver length = 1800 symbols				
MLC, 32 states	5.56	7.19	1.09	2.41
BICM, 32 states	5.63	7.97	1.02	1.63
TCM, 32 states	4.66	6.44	1.99	3.16
TTCM, 2×16 states	7.16	9.81	-0.51	-0.21
BICM-ID, 32 states	8.80	11.5	-2.15	-1.9
Overall trellis-complexity, $\nu = 128$ states/coded bit Interleaver length = 1800 symbols				
MLC, 32 states, 4*I*	3.88	5.5	2.77	4.1
BICM, 128 states	5.31	7.1	1.34	2.5
TCM, 128 states	4.41	6.31	2.24	3.29
TTCM, 2×16 states, 4*I*	3.63	3.84	3.02	5.76
BICM-ID, 32 states, 4*I*	4.25	5.13	2.40	4.47
Overall trellis-complexity, $\nu = 128$ states/coded bit Interleaver length = 180 symbols				
MLC, 32 states, 4*I*	4.94	6.63	1.71	2.97
BICM, 128 states	5.94	9.38	0.71	0.22
TCM, 128 states	4.81	7.66	1.84	1.94
TTCM, 2×16 states, 4*I*	4.56	5.44	2.09	4.16
BICM-ID, 32 states, 4*I*	5.5	7.0	1.15	2.6

Table 7.1: Coding gains of various coded modulation schemes, namely the MLC, BICM, TCM, TTCM and BICM-ID arrangement of Section 3.2.1 in conjunction with 8PSK modulation against an identical effective-throughput 2 bit/symbol (BPS) uncoded QPSK scheme at BER of 10^{-3} and 10^{-5}. The system parameters were outlined in Table 3.5, when imposing a different overall complexity associated with both 32 and 128 trellis-states/coded bit. The interleaver block lengths were 1800 and 180 symbols respectively, transmitting over an AWGN channel. The term I denotes the number of iterations. These values were extracted from Figures 3.5 and 3.6.

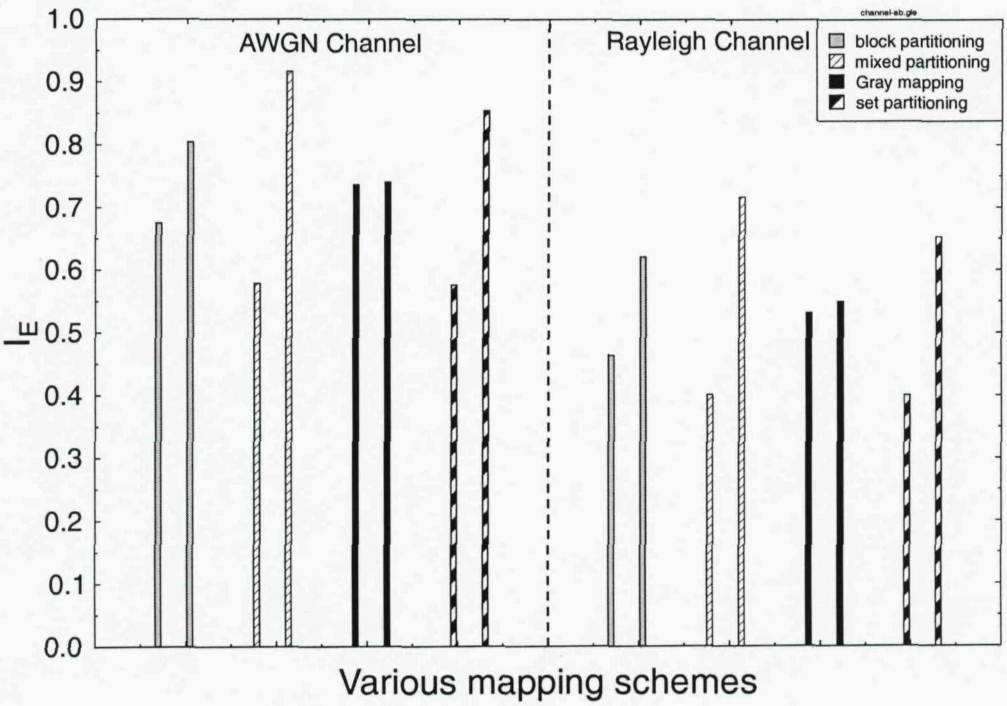

Figure 7.1: The start and end values of I_E for the various bit-to-symbol mapping schemes of Table 3.1 at $E_b/N_0 = 4$dB, where the left and right bars associated with the same mapping scheme represent the value of the demapper's EXIT function at $I_A = 0$ and 1, respectively. Part of these values were extracted from Figure 3.15.

In Section 3.3.3, we proposed a 3-D EXIT chart analysis concept for analysing a three-stage MLC scheme using MSD. The MLC MSD EXIT chart construction concept was introduced in Figure 3.17. In order to further improve the iterative detection performance of the MLC MSD scheme, we designed a precoder-aided MLC arrangement based on EXIT chart analysis, as outlined in Section 3.4. Specifically, the EXIT chart based convergence analysis of this new scheme was discussed in Section 3.4.2, where the 3-D EXIT charts were illustrated along with the corresponding bit-by-bit simulation based decoding trajectory in Figures 3.18, 3.19, 3.20 and 3.25.

The associated BER performance was discussed in Section 3.4.3. The results were presented for both the MSD and PID decoding structure, when communicating over an uncorrelated Rayleigh fading channel. Table 7.2 characterises the proposed MLC system, where the achievable precoder gain indicates the E_b/N_0 advantage attained by inserting a URC into the corresponding schemes, as seen in the schematic of Figures

	E_b/N_0 [dB]		Precoder gain [dB]	
	BER = 10^{-3}	BER = 10^{-5}	BER = 10^{-3}	BER = 10^{-5}
AWGN channel				
MLC MSD scheme, $6I$	3.69	5.62	0	0
MLC PID scheme, $6I$	5.42	7.62	0	0
Precoded MLC MSD scheme, $6I$	4.92	5.15	-1.23	0.47
Precoded MLC PID scheme, $6I$	5.23	5.38	0.19	2.24
Uncorrelated Rayleigh channel				
MLC MSD scheme, $6I$	12.61	*	0	0
MLC PID scheme, $6I$	9.09	14.5	0	0
Precoded MLC MSD scheme, $6I$	9.26	12	3.35	∞
Precoded MLC PID scheme, $6I$	8.83	9.17	0.26	5.33

Table 7.2: E_b/N_0 values and the corresponding precoder gains of the MLC MSD as well as PID schemes of Section 3.4 in conjunction with 8PSK modulation at an effective throughput of 2 bit/symbol (BPS) at BER of 10^{-3} and 10^{-5}. The system parameters are outlined in Table 3.5. The interleaver block length is 1800 symbols, while the schemes communicated over both AWGN and uncorrelated Rayleigh channels. The term I denotes the number of iterations and * indicates that an error floor persists for the scheme dispensing with the precoder. These values were extracted from Figures 3.26, 3.27, 3.28 and 3.29.

3.21 and 3.22. Various coded modulation schemes having a decoding complexity associated with 128-trellis states were compared, when communicating over an uncorrelated Rayleigh channel, as shown in Figure 3.30. The precoded MLC scheme exhibited a significant precoder gain of more than 5dB for both MSD and PID.

7.1.4 Chapter 4

In Chapter 4, we constructed a MLC and BICM design based on a sphere packing aided space time block code. The general concept of STBCs was presented in Section 4.2 in order to provide transmit diversity for the scheme, as exemplified in Figure 4.1. We discussed the SP design based on this STBC scheme in Section 4.3, where we designed the space-time signal by jointly mapping the two transmit antennas' signals to the SP constellation points of the lattice D_4. In Section 4.4, the iterative demapping of the SP modulation scheme was outlined based on the soft-input and soft-output values.

The resultant STBC-SP-MLC system was introduced in Section 4.5, which employed a four-component-code MLC scheme, as shown in Figure 4.7. In order to determine the most beneficial coding rate for each of the component codes, we designed it using the equivalent capacity based design rules of [51], as discussed in Section 4.5.2.

	E_b/N_0 [dB]		SP gain [dB]	
	BER = 10^{-3}	BER = 10^{-5}	BER = 10^{-3}	BER = 10^{-5}
STBC-SP-MLC L1-BSA, $4I$ (System-1)	3.88	5.24	2.71	3.05
STBC-SP-MLC L2-BSA, $4I$ (System-2)	4.09	5.35	2.5	2.94
STBC-QPSK-MLC UP, $4I$ (System-3)	6.59	8.29	0	0
STBC-SP-LDPC UP, $4I$ (System-4)	4.29	5.0	2.3	3.29
STBC-SP-MLC L1-BSA, $4I$ (10xSystem-1's block length)	3.35	4.18	3.24	4.11

Table 7.3: E_b/N_0 values and the corresponding SP gains of the various STBC-SP-MLC schemes of Table 4.12 at an effective throughput of 1 bit/(channel use) recorded at BER of 10^{-3} and 10^{-5}. The system parameters are outlined in Table 4.11. The interleaver block length is 2560 bits, while the schemes communicated over a Rayleigh fading channel. The variable I denotes the number of iterations. These values were extracted from Figures 4.13 and 4.14.

This equivalent capacity based design was also detailed in Section 2.2.2, but the concept was extended in Section 4.5 to the 4-D SP scheme.

A bit-to-SP mapping scheme was introduced in Section 4.5.3, which was specifically designed for SP modulation. The BSA of Section 4.5.3 was employed for optimising the cost function for the different mapping schemes, which was presented in the flow chart of Figure 4.9, outlining the algorithm in a step-by-step manner. The resultant unequal protection design based on the BSA was discussed in Section 4.5.4, using the so-called *hybrid* partitioning scheme.

The corresponding simulation results were discussed in Section 4.5.5, where the BER performance recorded for the different systems were characterised. Based on the proposed STBC-SP-MLC, we summarise the SP gain compared to the classic 2-D scheme dispensing with SP in Table 7.3, which highlights the E_b/N_0 advantage gleaned from the employment of SP modulation in the system.

BICM-ID invoking an STBC has been considered for example in [29,33,102,116,148]. We further proposed a STBC-SP-BICM scheme in Section 4.6, which utilises this multi-dimensional SP modulation incorporated into the STBC design. Figure 4.16 illustrates the model of the proposed STBC-SP-BICM scheme. A precoder was also used in Figure 4.16 in order to achieve an improved iterative decoding convergence. We concluded that the choice of using a GRAY mapper provided a beneficially high I_E^{SP} value at $I_A^{SP} = 0$, as highlighted in Figure 7.2, where an open EXIT tunnel was obtained at $E_b/N_0 = 3$dB.

Different mapping schemes based on 256 SP points were investigated with the aid of the CF optimised using the BSA in Section 4.6.2. The attainable performance was analysed with the aid of EXIT charts in Figure 4.20, which demonstrated that the decoding convergence was indeed achievable, even for a low-complexity memory-1 outer decoder. Table 7.4 highlights the respective E_b/N_0 gain for both the non-precoded and precoded SP schemes.

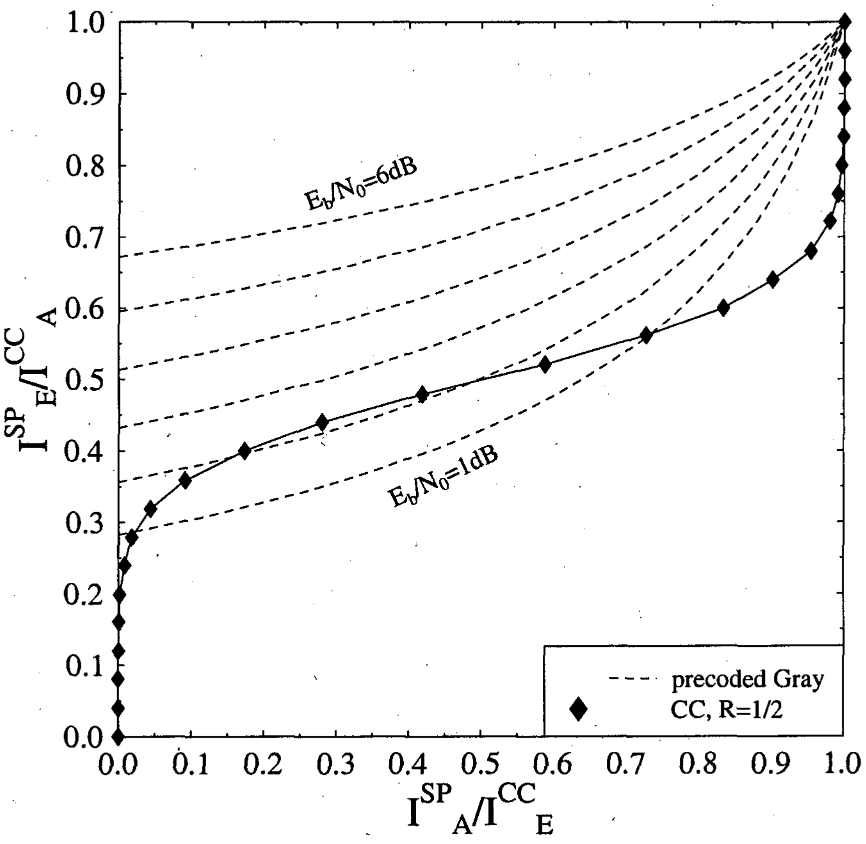

Figure 7.2: EXIT chart for the STBC-SP-BICM demapper of Figure 4.16 for $M = 16$ constellation points, when invoking precoded Gray SP mapping schemes for E_b/N_0 values ranging from 1dB to 6dB in combination with an outer 1/2-rate CC. The system parameters were summarised in Table 4.16.

7.1.5 Chapter 5

In Chapter 5, we discussed multimedia communications employing a MLC scheme as well as a wireless Internet scenario, invoking a BICM-ID design. The multimedia trans-

	E_b/N_0 [dB]		Gain [dB]	
	BER = 10^{-3}	BER = 10^{-5}	BER = 10^{-3}	BER = 10^{-5}
STBC-QPSK-BICM UP, $9I$ (Benchmarker)	4.11	6.59	0	0
STBC-SP-BICM SET SP-16, $9I$ (System-12)	3.37	5.44	0.74	1.15
STBC-SP-BICM precoded GRAY, $9I$ (System-17)	3.33	4.0	0.78	2.59

Table 7.4: E_b/N_0 values and the corresponding SP gains of the various STBC-SP-BICM schemes of Section 4.6 at an effective throughput of 1 bit/(channel use) as well as at BER of 10^{-3} and 10^{-5}. The system parameters are outlined in Table 4.16. The interleaver block length is 2560 bits, while the schemes communicated over a Rayleigh fading channel. The variable I denotes the number of iterations. These values were extracted from Figure 4.19.

mission was based on a low-latency application aiming for a minimum-delay decoding. The structure of the MLC scheme using GLDPC component codes was presented in Section 5.2. The parity check matrix of GLDPC encoder was shown in Figure 5.1, while the decoding procedure of the GLDPC scheme was highlighted in Figure 5.3. The system architecture of this new MLC-GLDPC scheme, invoking GLDPCs as the MLC component codes, and employing both inner as well as outer iterations, was outlined in Section 5.2.5.

Section 5.2.6 characterised the performance of the MLC-GLDPC scheme, while Table 7.5 summarised the gain obtained by the MLC-GLDPC arrangement compared to the MLC benchmarker scheme employing classic LDPC components. Furthermore, based on the syndrome of each constituent code in the GLDPC scheme, in Section 5.3 we designed an adaptive iterative MLC-GLDPC scheme. This provided a useful inner- and outer-iteration stopping criterion when the desired BER performance was attained and hence resulted in a reduced complexity. The system's performance was characterised in Section 5.3.2.

A wireless Internet scheme was proposed in Section 5.4, based on the joint design of BICM-ID and LT coding. We presented a general overview of Fountain codes in Section 5.4.1. Based on the concept of Fountain codes, LT coding was proposed in [123] and its design principles were summarised in Section 5.4.2. The degree distribution of the LT-encoded packets was outlined in Section 5.4.2.1, while our proposed degree distribution was detailed in Section 5.4.2.2.

	E_b/N_0 [dB]		Gain [dB]	
	BER = 10^{-3}	BER = 10^{-5}	BER = 10^{-3}	BER = 10^{-5}
AWGN channel				
$I_{outer} = 5$, $I_{inner} = 4$				
MLC-LDPC	5.07	5.75	0	0
MLC-GLDPC	4.52	4.59	0.55	1.16
$I_{outer} = 5$, $I_{inner} = 9$				
MLC-LDPC	4.66	5.00	0	0
MLC-GLDPC	4.39	4.39	0.27	0.61
Uncorrelated Rayleigh channel				
$I_{outer} = 5$, $I_{inner} = 4$				
MLC-LDPC	9.24	10.00	0	0
MLC-GLDPC	7.92	8.00	1.32	2.00
$I_{outer} = 5$, $I_{inner} = 9$				
MLC-LDPC	8.55	8.79	0	0
MLC-GLDPC	7.74	8.00	0.81	0.79

Table 7.5: E_b/N_0 values and the corresponding gains of the MLC-GLDPC scheme of Section 5.2 in conjunction with 8PSK modulation at an effective throughput 2 bit/symbol (BPS) as well as at BER of 10^{-3} and 10^{-5}. The gain here refers to the coding advantage of MLC-GLDPC compared to the classic MLC-LDPC benchmarker scheme. The system parameters were outlined in Table 5.1. The schemes communicated over both AWGN and uncorrelated Rayleigh channels. These values were extracted from Figures 5.5, 5.6, 5.7 and 5.8.

In Section 5.4.3, we proposed a serially concatenated LT-BICM-ID system, which was characterised in the context of the wireless Internet propagation scenario of the AWGN-contaminated BEC. Our simulation results were presented in Section 5.4.4, characterising the BER performance for different number of BICM-ID iterations, as well as comparing the benefits of the proposed new degree distribution to those of other degree distributions.

To further improve the attainable system performance, a new LT-BICM-ID design using LLR-based packet reliability estimation was investigated in Section 5.5, where the system's schematic was shown in Figure 5.25. EXIT charts were used as a tool to predict the desired LLR threshold for LLR-based packet reliability estimation, as portrayed in Section 5.5.3. The improved scheme using the novel concept of bit-by-bit rather than packet-by-packet LT decoding was also discussed in Section 5.5.4. The performance of this scheme was highlighted in Section 5.5.5. Table 7.6 summarises the coding advantage of the LT-BICM-ID schemes considered in conjunction with different

	E_b/N_0 [dB]		Gain [dB]	
	BER $= 10^{-3}$	BER $= 10^{-5}$	BER $= 10^{-3}$	BER $= 10^{-5}$
Original Robust distribution, LT-BICM-ID, $10I$	6.25	8.43	0	0
IRD, LT-BICM-ID, $2I$	8.04	8.67	-1.79	-0.24
IRD, LT-BICM-ID, $10I$	7.12	7.46	-0.87	0.97
IRD, LLR-estimation, LT-BICM-ID, $4I$	5.78	5.81	0.47	2.62
IRD, LLR-estimation, LT bit-by-bit decoding, LT-BICM-ID, $4I$	5.64	5.70	0.61	2.73

Table 7.6: E_b/N_0 values and the corresponding gains of the LT-BICM-ID schemes of Sections 5.4.3 and 5.5.2 in conjunction with 8PSK modulation at an effective throughput of 2 bit/symbol (BPS) as well as at BER of 10^{-3} and 10^{-5}. The gain here refers to the coding advantage compared to the LT-BICM-ID benchmarker employing the *robust* degree distribution of Section 5.4.2.1. The schemes communicated over BEC contaminated by AWGN. These values were extracted from Sections 5.4.4 and 5.5.5 of Figures 5.23, 5.24 and 5.35, respectively.

LT degree-distributions, different number of BICM-ID iterations, when using bit-by-bit LT decoding as well as the LLR-based packet-reliability estimation scheme.

7.1.6 Chapter 6

In Chapter 6, we investigated a near-capacity irregular BICM-ID design approach with the aid of EXIT chart analysis. The proposed Ir-BICM-ID scheme was highlighted in Section 6.2, where three different irregular components were designed, namely an IrCC, an IrURC and an IrMapper. Figure 6.3 showed the general Ir-BICM-ID structure, detailing each individual subcomponents and the corresponding interleavers. In Section 6.3, we discussed the employment of EXIT charts for creating a narrow but marginally open EXIT tunnel associated with a near-capacity performance.

The irregular components employing several different subcodes were presented in Section 6.4. We designed an IrCC invoking both memory-1 and memory-4 as well as repetition codes, as summarised in Table 6.2. For the inner components, an iterative scheme exchanging extrinsic information between the IrURC and the IrMapper was considered, each invoking various bit-to-symbol mapping strategies as well as different-memory URC subcodes, as highlighted in Table 6.4. This approach created a diverse range of EXIT functions for both the inner and outer components, providing a higher degree of freedom in designing an 'open-but-narrow' EXIT tunnel. The EXIT chart matching algorithm described in Section 6.4.3 was invoked for the sake of finding optimal weighting coefficient values of α_{opt} and β_{opt} which determined the specific function of the input bit stream to be encoded by particular component of the irregular scheme. The whole process of designing Ir-BICM-ID scheme is summarised in Figure 7.3.

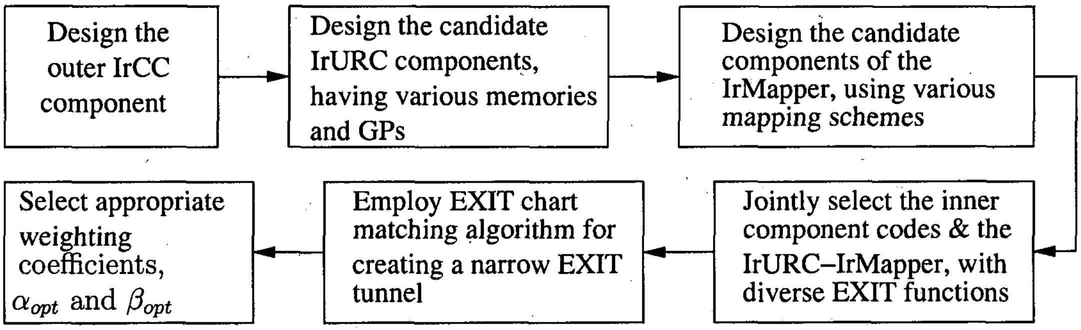

Figure 7.3: The Ir-BICM-ID design process.

Simulation were performed to characterise the Ir-BICM-ID schemes in Section 6.5. By simply employing different-memory CCs, as shown in Figure 6.10, we may not have the capability of adjusting the area of the EXIT tunnel in a sufficiently flexible manner. The situation improved, when we employed a $\mathsf{F} = 17$-component IrCC as portrayed in Figure 6.11, but the performance of the resultant scheme was still some distance away from the theoretical capacity limit. Figure 6.12 showed a narrow EXIT tunnel, hence the corresponding scheme exhibited a near-capacity performance, when employing the proposed Ir-BICM-ID using different irregular components.

The maximum throughput of the Ir-BICM-ID scheme of Section 6.2 compared to the theoretical DCMC capacity limit was detailed in Figure 6.13, where the proposed scheme exhibited a near-capacity performance. The BER performance was characterised in Figure 6.14 for an interleaver length of 300,000 bits, demonstrating that the BER curve was merely 0.32 dB away from the theoretical capacity limit. The associated complexity trade-offs were characterised in Figure 6.15, where the complexity increased rapidly, as the system approached the capacity bound. Therefore, in order to implement a physically feasible yet economic system, we also provided solutions by creating a 'wider-than-necessary' EXIT tunnel. Naturally, the resultant solutions required an increased of E_b/N_0 value at the same IrCC coding rate. Alternatively, we could employ a lower IrCC coding rate at the same E_b/N_0 value, as portrayed in Figures 6.16 and 6.17, despite the fact that a lower coding rate is typically associated with an increased complexity.

Table 7.7 summarises the attainable performance of the Ir-BICM-ID schemes of Section 6.2 at a certain complexity and interleaver length. The IrCC component having a rate of 0.635 was employed as our benchmarker for comparison of the distance from the theoretical capacity limit. The table demonstrates that by employing a lower IrCC coding rate of $R = 0.4$ or $R = 0.5$, we can reduce the complexity at the price of increasing the 'gap' with respect to the capacity. Again, in general, a low coding rate incurs a higher trellis complexity compared to a higher coding rate due to the larger amount of parity bits generated. However, in the near-capacity scheme, the number of iterations required for achieving an infinitesimally low BER outweights the complexity penalty imposed by the extra number of parity bits introduced at a lower coding rate. Observe that having a sufficiently high interleaver length is also important for the sake of achieving a near-capacity performance.

7.2 Future Work

In this section, we present a range of future research ideas. Figure 7.4 shows the trade-offs between different factors to be considered in designing a channel coding and modulation scheme. Our future work will consider the design trade-offs illustrated in Figure 7.4,.while aiming for improving the schemes portrayed in this thesis.

In Chapter 3, we demonstrated that a 3-D EXIT chart may be used for estimating the convergence behaviour of a three-component MLC MSD scheme. Our future work may generalise this approach to an N-component MLC MSD scheme, invoking EXIT charts for convergence study, when communicating over both AWGN as well as Rayleigh fading channels. A technique may be investigated for projecting 3-D EXIT chart analysis to its corresponding 2-D EXIT curves for convenient visualisation. The precoded MLC MSD and MLC PID schemes of Section 3.4 may be further extended to include more effective precoder designs based on different-memory unity-rate precoders

Scheme	Capacity bound E_b/N_0 [dB]	Distance from capacity E_b/N_0 [dB]	Interleaver length [bits]	Complexity [number of trellis states per frame]
IrCC rate-0.635	4.89	0.75	30,000	5.06×10^7
IrCC rate-0.635	4.89	1.11	30,000	2.28×10^7
IrCC rate-0.5	4.89*	0.75	30,000	1.87×10^7
IrCC rate-0.4	4.89*	0.75	30,000	1.49×10^7
IrCC rate-0.635	4.89	0.32	300,000	6.08×10^8
IrCC rate-0.635	4.89	1.11	300,000	2.37×10^8
IrCC rate-0.5	4.89*	0.32	300,000	1.80×10^8
IrCC rate-0.4	4.89*	0.32	300,000	1.45×10^8
IrCC rate-0.5	2.68	1.22	30,000	4.80×10^7
IrCC rate-0.5	2.68	1.22	300,000	9.14×10^8
IrCC rate-0.4	2.09	1.01	30,000	4.46×10^7
IrCC rate-0.4	2.09	0.81	300,000	9.98×10^8

Table 7.7: E_b/N_0 values of the DCMC's capacity bound evaluated from Equation (4.50) of Section 4.5.2 and the corresponding distance from capacity for the Ir-BICM-ID scheme of Figure 6.3 in conjunction with 8PSK modulation at BER of 10^{-5}. The interleaver length is given in bits and the complexity is quantified in terms of the number of trellis states associated with a transmission frame, where the frame constitutes the total number of bits in an interleaved block. In scenario marked by *, the channel capacity bound of the IrCC rate-0.635 is used for comparison with respect to the associated interleaver delay and complexity cost.

as well as different-rate block-coded precoders. Based on EXIT chart analysis, we expect that we should be able to improve the scheme by finding an optimum combination of generator polynomials for the outer convolutional codes.

The transmit diversity achieved and the benefits of SP modulation were combined in Chapter 4. It would be interesting to generalise the STBC-SP-MLC and STBC-SP-BICM schemes to multiple transmit antennas. It would be worthwhile further investigating the performance versus complexity benefits of high-dimensional STBCs. The D_4 lattice was used for the twin-antenna STBC scheme. As a further extension, we would consider SP modulation having higher dimensions and larger constellations. This may potentially increase the degree of freedom in designing an improved bit-to-SP-symbol mapping scheme.

The best known SP lattice which has the highest minimum Euclidean distance in the $2(k+1)$-dimensional real-valued Euclidean space $\mathbb{R}^{2(k+1)}$ was outlined in [105]. In Table 7.8 we summarised a range of higher-dimensionsal SP modulation scheme having

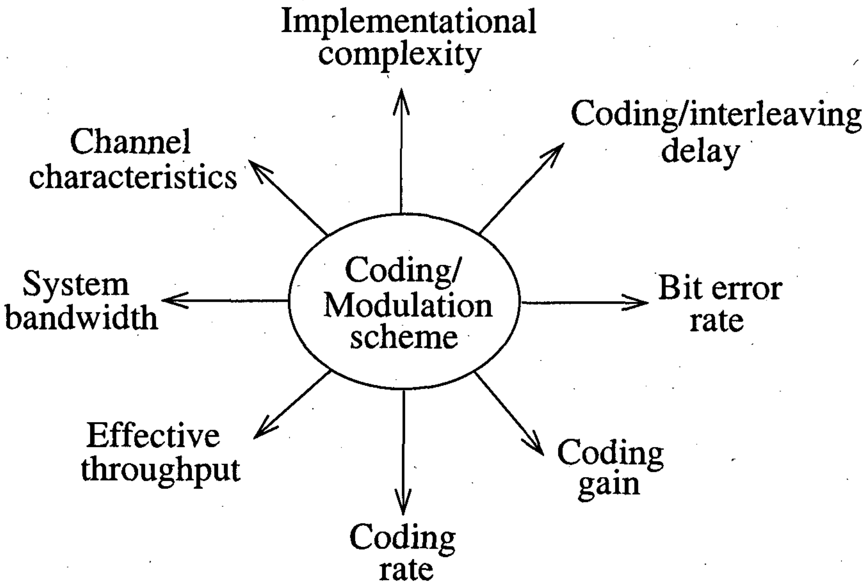

Figure 7.4: Trade off among various factors in the design of channel coded modulation schemes, © Hanzo *et al.* [65].

D values up to 24, which could potentially be explored for a generalised N-transmit-antenna scheme. Furthermore, an optimised bit-to-SP-symbol mapping scheme could be obtained based on the BSA of Section 4.5.3 as well as Reactive Tabu Search (RTS) [37]. It is anticipated that an improved BER performance may be achieved at an increased implementational complexity, as highlighted in terms of the design trade-offs seen in Figure 7.4.

In Chapter 5, an LT-BICM-ID scheme was proposed for wireless Internet scenarios, where the LT decoder was used for avoiding retransmission of corrupted packets by transmitting a certain proportion of redundant packets under time-invariant channel conditions. Both HARQ and LT can be designed to operate efficiently, but when the channel conditions become time-variant, the required amount of LT-coding redundancy cannot be determined in advance. However, this scheme could be further improved by creating an adaptive HARQ LT system, in which a type-II HARQ [55] scheme would be used in conjunction with LT coding. The resultant scheme may switch to conventional HARQ based retransmissions, when further parity packets have to be transmitted. In an error-infested channel, particularly at low SNRs, the LT coding might be invoked for avoiding excessive retransmissions. The adaptive scheme may potentially increase

k	Dimension $2(k+1)$	Lattice	Number of constellation points in first layer
1	4	D_4	24
2	6	E_6	72
3	8	E_8	240
4	10	P_{10c}	372
5	12	K_{12}	756
6	14	Λ_{14}	1422
7	16	Λ_{16}	4320
8	18	Λ_{18}	7398
9	20	Λ_{20}	17400
10	22	Λ_{22}	49896
11	24	Λ_{24}	196560

Table 7.8: Sphere packing lattices with the best known minimum Euclidean distance adopted from [105].

the system's effective throughput. The aforementioned adaptive concept may also be applied in a HARQ LT MLC scheme, in order to improve the HARQ MLC arrangement proposed in [134]. The LT coding aims for improving the overall system throughput by avoiding packet retransmission as well as dispensing with ARQ feedback links. Furthermore, the additional parity bits and already received but error-infested packets would be combined with the aid of various combining method [149,150] for the sake of improving the attainable BER performance.

The design of near-capacity schemes capable of operating at an infinitesimally low BER, while striking an attractive trade-off in terms of complexity, interleaver delay and other design factors is outlined in Figure 7.4 in a stylised form and was exemplified in Chapter 6 in the context of our Ir-BICM-ID scheme. Our future work may include the design of a low-delay schemes for interactive multimedia communications. Arriving at an adaptive iterative stopping criterion and a more precise activation order for the different component codes might also be a promising research field.

In this thesis, we assumed the availability of perfect Channel State Information (CSI) for all the schemes. However, in realistic communication systems the CSI has to be estimated. The employment of various channel estimation schemes in all the systems considered would constitute an interesting challenge, in order to carry out a comparison with the perfect CSI-aided schemes. Furthermore, with the aid of EXIT-charts we could design three-stage serially concatenated schemes consisting of the channel estimator and two-stage concatenated codes using the best activation order of the different component blocks.

The design of coding schemes for differentially encoded schemes [151] dispensing with channel estimation is also of high importance, similarly to rotationally invariant schemes, which are capable of seamless operation also in the presence of false-locking carrier-recovery events. Iterative CSI, synchronisation equalisation and decoding remains a burgeoning research field, particularly in the context of network-coding aided cooperative communications.

Appendix A

EXIT Chart Calculation

The LLRs used for EXIT chart analysis can be modeled by an independent Gaussian random variable n_a in conjunction with the information bits $x \in \{+1, -1\}$. The *a priori* LLR L_A can be represented as

$$L_A = \varrho_a \cdot x + n_a, \tag{A.1}$$

where $\varrho_a = \sigma_a^2/2$ and σ_a^2 is the variance of the noise, while the corresponding mean is zero.

The signal received via an AWGN channel is given as

$$z = x + n. \tag{A.2}$$

The corresponding conditional PDF is given by

$$p(z|X = x) \quad = \quad \frac{\mathrm{e}^{((z-x)^2/2\sigma_n^2)}}{\sqrt{2\pi}\sigma_n}. \tag{A.3}$$

The binary transmitted bits are denoted by the random variable X having realisations of $x = \{-1, +1\}$. The corresponding LLRs of Z are denoted as

$$\begin{aligned} Z &= \ln \frac{p(z|x = +1)}{p(z|x = -1)} \\ &= \ln \frac{\mathrm{e}^{-(z-1)^2/2\sigma_n^2}}{\mathrm{e}^{-(z+1)^2/2\sigma_n^2}} \\ &= \frac{-(z-1)^2 + (z+1)^2}{2\sigma_n^2} \\ &= \frac{2}{\sigma_n^2} Z \\ &= \frac{2}{\sigma_n^2}(x + n). \end{aligned} \tag{A.4}$$

Note that the variable n is Gaussian distributed with a mean of zero and variance of $\sigma_n^2 = N_0/2$. Therefore we have

$$\begin{aligned} Z &= \frac{2}{\sigma_n^2}(x+n) \\ &= \mu_Z x + n_Z, \end{aligned} \tag{A.5}$$

where $\mu_Z = \frac{2}{\sigma_n^2}$ and $n_Z = \frac{2}{\sigma_n^2} \cdot n$.

Hence, the variable n_Z would have a mean of zero and standard deviation of $\sigma_Z = \frac{2}{\sigma_n^2} \cdot \sigma_n$. The standard deviation can be expressed as

$$\sigma_Z = \frac{2}{\sigma_n^2} \cdot \sigma_n = \frac{2}{\sigma_n}. \tag{A.6}$$

The variance of Equation (A.6) is denoted as

$$\sigma_Z^2 = \frac{4}{\sigma_n^2}. \tag{A.7}$$

Given the term $\mu_Z = \frac{2}{\sigma_n^2}$, we arrive at

$$\mu_Z = \frac{2}{4/\sigma_Z^2} = \frac{\sigma_Z^2}{2}. \tag{A.8}$$

This relationship is useful for modeling the *a priori* LLR L_A, as given in Equation (A.1).

The mutual information representing the *a priori* knowledge can be quantified between the transmitted bits X and the LLR L_A as follows

$$\begin{aligned} I_A &= \sum_{x=-1,x=+1} \int_{-\infty}^{\infty} p(Y|X=x)p(X=x) \cdot \log_2 \frac{p(Y|X)}{p(Y)} dY \\ &= \sum_{x=-1,x=+1} \int_{-\infty}^{\infty} p(Y|X=x) \cdot \frac{1}{2} \cdot \\ &\quad \log_2 \frac{p(Y|X)}{p(Y|X=+1)p(X=+1) + p(Y|X=-1)p(X=-1)} dY \\ &= \frac{1}{2} \sum_{x=-1,x=+1} \int_{-\infty}^{\infty} p(Y|X=x) \cdot \log_2 \frac{p(Y|X)}{1/2 \cdot p(Y|X=+1) + 1/2 \cdot p(Y|X=-1)} dY \\ &= \frac{1}{2} \sum_{x=-1,x=+1} \int_{-\infty}^{\infty} p(Y|X=x) \cdot \log_2 \frac{2p(Y|X)}{p(Y|X=+1) + p(Y|X=-1)} dY. \end{aligned} \tag{A.9}$$

Appendix B

DCMC Capacity Calculation

The capacity of the Discrete-input Continuous-output Memoryless Channel (DCMC) can be calculated using the mutual information between two random variables. Let X and Y be random variables having a joint probability of $p(X, Y)$. For an M-ary signal constellation, the mutual information can be expressed as

$$\begin{aligned} I(X;Y) &= \sum_{m=0}^{M-1} \int_Y p(X_m, Y) \cdot \log_2 \frac{p(X_m, Y)}{p(X_m)p(Y)} dY \\ &= \sum_{m=0}^{M-1} \int_Y p(Y|X_m)p(X_m) \cdot \log_2 \frac{p(Y|X_m)}{\sum_{n=0}^{M-1} p(Y|X_n)p(X_n)} dY. \end{aligned} \tag{B.1}$$

The mutual information can also be expressed with the aid of the entropy as follows

$$I(X;Y) = H(X) - H(X|Y). \tag{B.2}$$

Rearranging Equation (B.1), we arrive at

$$\begin{aligned} I(X;Y) &= \sum_{m=0}^{M-1} \int_Y p(Y|X_m)p(X_m) \cdot \log_2 \frac{p(Y|X_m) \cdot p(X_m)}{(\sum_{n=0}^{M-1} p(Y|X_n)p(X_n)) \cdot p(X_m)} dY \\ &= \sum_{m=0}^{M-1} \int_Y p(Y|X_m)p(X_m) \cdot \log_2 \frac{1}{p(X_m)} dY + \\ &\quad \sum_{m=0}^{M-1} \int_Y p(Y|X_m)p(X_m) \cdot \log_2 \frac{p(Y|X_m) \cdot p(X_m)}{\sum_{n=0}^{M-1} p(Y|X_n)p(X_n)} dY \\ &= H(X) - H(X|Y). \end{aligned} \tag{B.3}$$

Therefore the entropy is expressed as follows

$$\begin{aligned} H(X) &= -\sum_{m=0}^{M-1}\int_Y p(Y|X_m)p(X_m)\cdot \log_2 p(X_m)dY \\ &= -\sum_{m=0}^{M-1} p(X_m)\cdot \log_2 p(X_m), \end{aligned} \tag{B.4}$$

and the conditional entropy is formulated as follows

$$\begin{aligned} H(X|Y) &= -\sum_{m=0}^{M-1}\int_Y p(Y|X_m)p(X_m)\cdot \log_2\left(\frac{p(Y|X_m)p(X_m)}{\sum_{n=0}^{M-1} p(Y|X_n)p(X_n)}\right) dY \\ &= \sum_{m=0}^{M-1}\int_Y p(Y|X_m)p(X_m)\cdot \log_2\left(\frac{\sum_{n=0}^{M-1} p(Y|X_n)p(X_n)}{p(Y|X_m)p(X_m)}\right) dY \\ &= \sum_{m=0}^{M-1}\int_Y p(Y|X_m)p(X_m)\cdot \log_2\left(\frac{\sum_{n=0}^{M-1} p(X_n)\cdot p(Y|X_n)}{p(X_m)\cdot p(Y|X_m)}\right) dY \\ &= \sum_{m=0}^{M-1}\int_Y p(Y|X_m)p(X_m)\cdot \log_2\left(\sum_{n=0}^{M-1}\frac{p(X_n)}{p(X_m)}\cdot\frac{p(Y|X_n)}{p(Y|X_m)}\right) dY \\ &= \sum_{m=0}^{M-1}\int_Y p(Y|X_m)p(X_m)\cdot \log_2\left(\sum_{n=0}^{M-1}\frac{p(X_n)}{p(X_m)}\exp(\Psi_{m,n})\right) dY \\ &= \sum_{m=0}^{M-1} p(X_m)\mathrm{E}\left[\log_2\left(\sum_{n=0}^{M-1}\frac{p(X_n)}{p(X_m)}\exp(\Psi_{m,n})\right)|X_m\right] dY, \end{aligned} \tag{B.5}$$

where $\exp(\Psi_{m,n}) = \frac{p(Y|X_n)}{p(Y|X_m)}$ and $\Psi_{m,n} = \frac{-|\chi^2_{2N_t}(X_m - X_n)+\Omega|^2+|\Omega|^2}{\chi^2_{2N_t}N_0}$.

Let $Y = \chi^2_{2N_t}X_m + \Omega$, where we have

$$\begin{aligned}
\exp(\Psi_{m,n}) &= \exp\left(\frac{-|\chi^2_{2N_t}(X_m - X_n) + \Omega|^2 + |\Omega|^2}{\chi^2_{2N_t}N_0}\right) \\
&= \exp\left(\frac{-|\chi^2_{N_t}X_m - \chi^2_{N_t}X_n + Y - \chi^2_{N_t}X_m|^2 + |Y - \chi^2_{N_t}X_m|^2}{\chi^2_{2N_t}N_0}\right) \\
&= \exp\left(\frac{-|Y - \chi^2_{N_t}X_n|^2 + |Y - \chi^2_{N_t}X_m|^2}{\chi^2_{2N_t}N_0}\right) \\
&= \exp\left(\frac{-|Y - \chi^2_{N_t}X_n|^2 - (-|Y - \chi^2_{N_t}X_m|^2)}{\chi^2_{2N_t}N_0}\right) \\
&= \frac{\exp\left(\frac{-|Y-\chi^2_{N_t}X_n|^2}{\chi^2_{N_t}N_0}\right)}{\exp\left(\frac{-|Y-\chi^2_{N_t}X_m|^2}{\chi^2_{N_t}N_0}\right)} \\
&= \frac{p(Y|X_n)}{p(Y|X_m)}.
\end{aligned} \tag{B.6}$$

Finally, the DCMC capacity can be formulated as follows

$$\begin{aligned}
I(X;Y) &= -\sum_{m=0}^{M-1} p(X_m)\cdot \log_2 p(X_m) - \\
&\quad \sum_{m=0}^{M-1} p(X_m)\mathrm{E}\left[\log_2\left(\sum_{n=0}^{M-1}\frac{p(X_n)}{p(X_m)}\exp(\Psi_{m,n})\right) \Big| X_m\right] dY.
\end{aligned} \tag{B.7}$$

List of Symbols

General notation

- The superscript * is used to indicate complex conjugation. Therefore, a^* represents the complex conjugate of the variable a.
- The superscript ^{T} is used to indicate matrix transpose operation. Therefore, $\mathbf{a}^T$ represents the transpose of the matrix $\mathbf{a}$.
- The superscript $^{\mathcal{H}}$ is used to indicate complex conjugate transpose operation. Therefore, $\mathbf{a}^{\mathcal{H}}$ represents the complex conjugate transpose of the matrix $\mathbf{a}$.
- The notation $\hat{x}$ represents the estimate of x.

Special symbols

$a_{q,i}$: The i-th coordinate of the q^{th} SP symbol $\mathbf{s}^q$.

b_i: The binary bit at position i.

C: Channel capacity.

C^i: Equivalent channel capacity at MLC protection level i.

c_t^i: The complex symbol transmitted by transmit antenna i at time slot t.

$\mathbf{C}$: The space-time signal matrix.

$\mathbb{C}^i$: The constituent encoder of MLC at protection level i.

$\mathbb{D}^i$: The constituent decoder of MLC at protection level i.

D: Shift register stage.

E_b: Bit energy.

E_s: Symbol energy.

E_{total}: The total energy of a constellation set.

$E[k]$: The expected value of k.

F: Number of subcodes in a family of IrCC.

f_D: The normalised Doppler frequency.

$\mathbf{G}$: Generator matrix.

$\mathbf{H}$: Parity check matrix.

$\mathcal{H}^i(D)$: The coefficient of the generator polynomials for bit i in the TCM code.

h_i: The channel impulse response.

$I(x;y)$: Mutual information between x and y.

I_A: The mutual information associated with the *a priori* information.

I_E: The mutual information associated with the *extrinsic* information.

$\mathbf{I}_n$: The identity matrix of size $(n \times n)$.

$J(.)$: The mutual information as a function of σ.

$\mathcal{J}(.)$: The error function of EXIT-chart matching algorithm.

$\mathcal{K}$: Number of original source packets.

$\mathcal{K}'$: Number of LT-encoded packets.

L_A^j: The *a priori* LLR values of the component code j.

L_E^j: The *extrinsic* LLR values of the component code j.

L_P^j: The *a posteriori* LLR values of the component code j.

l: The number of bits/levels in a modulated symbol.

M: The size of the legitimate modulation constellation.

$\mathcal{N}$: Number of received LT-encoded packets after the erasure channel.

N_t: Number of transmit antennas.

N_r: Number of receive antennas.

n_A: The zero-mean Gaussian random variable used for modelling the *a priori* information input.

n_f: A normalisation factor.

$\mathcal{P}$: Number of symbols in a LT packet.

Q: Number of subcodes in a family of IrURC-IrMapper.

R: Coding rate.

$\mathbf{r}$: The received sphere packing symbol.

$\mathbb{R}^n$: The n-dimensional real-valued Euclidean space.

S: The legitimate SP constellation symbol.

$\mathcal{S}$: LT source packet.

$\mathbf{S}_{i\times j}$: Syndrome of a matrix $i \times j$.

$\mathbf{s}^q$: The q^{th} sphere packing legitimate symbol.

$\mathcal{T}_i$: The original LT-encoded transmitted packet at time instant i.

u: Uncoded information bit.

$\mathcal{V}^i$: Codeword of i super-code of a GLDPC encoder.

v: Coded bit.

W: Number of GLDPC super-codes.

$\mathbf{w}$: A four-dimensional Gaussian random variable.

$\mathbb{Z}$: The legitimate constellation set.

Z_0^k: The subset of the legitimate constellation set $\mathbb{Z}$ that contains all symbols having $b_k = 0$.

Z_1^k: The subset of the legitimate constellation set $\mathbb{Z}$ that contains all symbols having $b_k = 1$.

π: Interleaver.

π^{-1}: Deinterleaver.

σ_n^2: The complex noise's variance.

ν: Complexity of coded modulation schemes in terms of number of trellis states.

φ: Memory of a code.

ψ: Sphere packing mapper.

Γ: STBC mapper.

κ: Coded modulation signal mapper.

$\bigoplus$: Concatenation process of several constituent codes.

Υ^i: The i^{th} constituent code employed in the super-code of a GLDPC scheme.

$\mathcal{E}$: Number of redundant packets required for successful LT decoding.

μ: Robust soliton distribution for LT coding.

ρ: Ideal soliton distribution for LT coding.

η: Effective throughput of a system.

α: The weighting coefficient of subcodes in a IrCC.

$\overline{\alpha}$: The forward variable of a MAP decoder.

β: The weighting coefficient of subcodes in the inner component IrURC-IrMapper.

$\overline{\beta}$: The backward variable of a MAP decoder.

$\overline{\gamma}$: The branch transition metric of a MAP decoder.

χ_b^i: The subset that contains all the phasors for which the position i of the phasor has the binary value, where $b \in \{0, 1\}$.

ϖ: An extra factor introduced for Improved Robust distribution.

Glossary

16ASK	16-level Amplitude Shift Keying
16QAM	16-level Quadrature Amplitude Modulation
8ASK	8-level Amplitude Shift Keying
8PSK	8-level Phase Shift Keying
ACS	Add, Compare and Select arithmetic operation
AMC	Adaptive Modulation and Coding
APP	A Posteriori Probability
ARQ	Automatic Repeat reQuest
AWGN	Additive White Gaussian Noise
BCH	Bose-Chaudhuri-Hocquenghem code
BDR	Balanced Distance Rule
BEC	Binary Erasure Channel
BER	Bit Error Ratio, the number of the bits received incorrectly
BI-STCM-ID	Bit-Interleaved Space-Time Coded Modulation using Iterative Decoding
BICM	Bit-Interleaved Coded Modulation
BICM-ID	Bit-Interleaved Coded Modulation with Iterative Decoding

BP	Block Partitioning
BPSK	Binary Phase Shift Keying
BSA	Binary Switching Algorithm
BSA-Multilayer	Multiple layers of BSA aided SP mapping scheme
CC	Convolutional Code
CDMA	Code-Division Multiple-Access
CF	Cost Function
CRC	Cyclic Redundancy Check
CSI	Channel State Information
DCMC	Discrete-input Continuous-output Memoryless Channel
ED	Euclidean Distance
EXIT	EXtrinsic Information Transfer
FEC	Forward Error Correction
FED	Free Euclidean Distance
GLDPC	Generalised Low-Density Parity Check
GM	Gray Mapping
GPs	Generator Polynomials
HARQ-II	Hybrid Automatic Repeat reQuest type-II
IP	Internet Protocol
Ir-BICM-ID	Irregular Bit-Interleaved Coded Modulation with Iterative Decoding
IrCC	Irregular Convolutional Code
IRD	Improved Robust Distribution
IrDemapper	Irregular Demapper

IrMapper	Irregular Mapper
IrURC	Irregular Unity Rate Code
L1-BSA	Layer-1 BSA aided SP mapping scheme
L2-BSA	Layer-2 BSA aided SP mapping scheme
L9-BSA	Layer-9 BSA aided SP mapping scheme
LDPC	Low Density Parity Check
LLR	Log-Likelihood Ratio
LT	Luby Transform code
LT-BICM-ID	Serially concatenated Luby Transform coding and Bit-Interleaved Coded Modulation with Iterative Decoding scheme
M-D	M-Dimensional
MAP	Maximum A Posteriori
ML	Maximum Likelihood
MLC	MultiLevel Coding
MLC-GLDPC	Multilevel Generalised Low Density Parity Check coding scheme
MLD	Maximum Likelihood Decoding
MP	Mixed Partitioning
MS	Mobile Station
MSD	MultiStage Decoding
MSED	Minimum Squared Euclidean Distance
MSP	Modified Set Partitioning
NACK	Negative-Acknowledgement
PCM	Parity Check Matrix
PD	Product Distance

PDF	Probability Density Function
PID	Parallel Independent Decoding
PSD	Power Spectral Density
PSK	Phase Shift Keying
QoS	Quality of Service
RCPC	Rate-Compatible Puncture Convolutional codes
RS	Reed-Solomon code
RTS	Reactive Tabu Search
SET	SET Partitioning aided SP mapping scheme
SISO	Soft-Input Soft-Output
SNR	Signal to Noise Ratio, noise energy compared to the signal energy
SP	Sphere Packing
SP-16	Sphere Packing with $M = 16$ constellation points
SP-256	Sphere Packing with $M = 256$ constellation points
STBC	Space-Time Block Coding
STBC-QPSK-MLC	Space-Time Block Code Quadrature Phase Shift Keying Multi-Level Coded modulation scheme
STBC-SP-BICM	Space-Time Block Coded Sphere Packed Bit-Interleaved Coded Modulation scheme
STBC-SP-LDPC	Single-class Space-Time Block Coded Sphere Packed Low Density Parity Check codes
STBC-SP-MLC	Space-Time Block Code Sphere Packed MultiLevel Coded modulation scheme
TC	Turbo Codes

TCM	Trellis Coded Modulation
TDD	Time Division Duplex
TTCM	Turbo Trellis Coded Modulation
UEP	Unequal Error Protection
UM	URC Mapper
UP	Ungerböck's set Partitioning
URC	Unity Rate Code
VA	Viterbi Algorithm

Bibliography

[1] C. E. Shannon, "A Mathematical Theory of Communication," *The Bell system Technical Journal*, vol. 27, pp. 379–656, July 1948.

[2] R. Hamming, "Error detecting and error correcting codes," *Bell System Technical Journal*, vol. 29, pp. 147–160, 1950.

[3] P. Elias, "Coding for noisy channels," *IRE Conv. Rec. pt.4*, pp. 37–47, 1955.

[4] A. J. Viterbi, "Error bounds for convolutional codes and asymtotically optimum decoding algorithm," *IEEE Transactions on Information Theory*, vol. IT-13, pp. 260–269, April 1967.

[5] L. R. Bahl, J. Cocke, F. Jelinek and J. Raviv, "Optimal Decoding of Linear Codes for Minimizing Symbol Error Rate," *IEEE Transactions on Information Theory*, vol. 20, pp. 284–287, March 1974.

[6] A. Hocquenghem, "Codes correcteurs d'erreurs," *Chiffres (Paris)*, vol. 2, pp. 147–156, September 1959.

[7] R. C. Bose and D. K. Ray-Chaudhuri, "On a class of error-correcting binary group codes," *Information and Control*, vol. 3, pp. 68–79, March 1960.

[8] I. Reed and G. Solomon, "Polynomial codes over certain finite fields," *J. Soc. Ind. Appl. Math.*, vol. 8, pp. 300–304, June 1960.

[9] R. Gallager, *Low Density Parity Check Codes*. USA: MIT Press, 1963.

[10] C. Berrou, A. Glavieux and P. Thitimajshima, "Near Shannon Limit Error-Correcting Coding and Decoding : Turbo Codes," in *Proceedings, IEEE International Conference on Communications*, pp. 1064–1070, 1993.

[11] S. Benedetto and G. Montorsi, "Design of Parallel Concatenated Convolutional Codes," *IEEE Transactions on Communications*, vol. 44, pp. 591–600, May 1996.

[12] S. Benedetto and G. Montorsi, "Iterative Decoding of Serially Concatenated Convolutional Codes," *IEE Electronics Letters*, vol. 32, pp. 1186–1188, June 1996.

[13] S. Benedetto and G. Montorsi, "Serial Concatenation of Block and Convolutional Codes," *IEE Electronics Letters*, vol. 32, pp. 887–888, May 1996.

[14] H. Imai and S. Hirawaki, "A New Multilevel Coding Method Using Error Correcting Codes," *IEEE Transactions on Information Theory*, pp. 371–377, May 1977.

[15] A.R. Calderbank, "Multilevel Codes and Multistage Decoding," *IEEE Transactions on Communications*, vol. 37, pp. 222–229, March 1989.

[16] G. Ungerböck, "Channel Coding with Multilevel/Phase Signals," *IEEE Transactions on Information Theory*, vol. 28, pp. 55–67, January 1982.

[17] E. Zehavi, "8-PSK trellis codes for a Rayleigh fading channel," *IEEE Transactions on Communications*, vol. 40, pp. 873–883, May 1992.

[18] L.-F. Wei, "Trellis-coded modulation with multidimensional constellations," *IEEE Transactions on Information Theory*, vol. 33, pp. 483–501, July 1987.

[19] G. J. Pottie and D. P. Taylor, "Multilevel Codes Based on Partitioning," *IEEE Transactions on Information Theory*, vol. 35, pp. 87–98, January 1989.

[20] N. Seshadri and C-E. W. Sundberg, "Multilevel Trellis Coded Modulations for the Rayleigh Fading Channel," *IEEE Transactions on Communications*, vol. 41, pp. 1300–1310, September 1993.

[21] Y. Kofman, E. Zahavi and S. Shamai, "Performance Analysis of a Multilevel Coded Modulation System," *IEEE Transactions on Communications*, vol. 42, pp. 299–312, February 1994.

[22] J. Huber and U. Wachsmann, "Capacities of Equivalent Channels in Multilevel Coding Schemes," *IEE Electonics Letter*, vol. 30, pp. 557–558, March 1994.

[23] X. Li and J. A. Ritcey, "Bit-interleaved coded modulation with iterative decoding," *IEEE Communications Letters*, vol. 1, pp. 169–171, November 1997.

[24] G. Caire, G. Taricco and E. Biglieri, "Bit-Interleaved Coded Modulation," *IEEE Transactions on Information Theory*, vol. IT-44, pp. 927–946, May 1998.

[25] P. Robertson and T. Wörz, "Bandwidth-Efficient Turbo Trellis-Coded Modulation Using Punctured Component Codes," *IEEE Journal on Selected Areas in Communications*, vol. 16, pp. 206–218, February 1998.

[26] R. H. Morelos-Zaragoza, M. P. C. Fossorier, S. Lin and H. Imai, "Multilevel Coded Modulation for Unequal Error Protection and Multistage Decoding-Part I: Symmetric Constellations," *IEEE Transactions on Communications*, vol. 48, pp. 204–213, February 2000.

[27] M. Isaka, M. P. C. Fossorier, R. H. Morelos-Zaragoza, S. Lin and H. Imai, "Multilevel Coded Modulation for Unequal Error Protection and Multistage Decoding-Part II: Asymmetric Constellations," *IEEE Transactions on Communications*, vol. 48, pp. 774–786, May 2000.

[28] A. Chindapol and J. A. Ritcey, "Design, Analysis and Performance Evaluation for BICM-ID with Square QAM Constellations in Rayleigh Fading Channels," *IEEE Journal on Selected Areas in Communications*, vol. 19, pp. 944–957, May 2001.

[29] Y. Huang and J. A. Ritcey, "Tight BER Bounds for Iteratively Decoded Bit-Interleaved Space-Time Coded Modulation," *IEEE Communication Letters*, vol. 8, pp. 153–155, March 2004.

[30] J. Hou and M. H. Lee, "Multilevel LDPC Codes Design for Semi-BICM," *IEEE Communications Letters*, pp. 674–676, Nov. 2004.

[31] L. H-J. Lampe, R. Schober and R. F. H. Fischer, "Multilevel Coding for Multiple-Antenna Transmission," *IEEE Transactions on Wireless Communications*, vol. 3, pp. 203–208, January 2004.

[32] P. A. Martin, D. M. Rankin and D. P. Taylor, "Multi-Dimensional Space-Time Multilevel Codes," *IEEE Transactions on Wireless Communications*, vol. 5, pp. 3287–3295, November 2006.

[33] A. S. Mohammed, W. Hidayat and M. Bossert, "Multidimensional 16-QAM Constellation Labeling of BI-STCM-ID With the Alamouti Scheme," *IEEE Wireless Communications and Networking Conference (WCNC)*, vol. 3, pp. 1217–1220, April 2006.

[34] A. S. Mohammed, Y. Gong and M. Bossert, "On Multidimensional BICM-ID with 8-PSK Constellation Labeling," *IEEE 18th International Symposium on Personal, Indoor and Mobile Radio Communications (PIMRC)*, pp. 1–5, September 2007.

[35] T. Matsumoto, S. Ibi, S. Sampei and R. Thomä, "Adaptive Transmission With Single-Carrier Multilevel BICM," *Proceedings of the IEEE*, vol. 95, pp. 2354–2367, December 2007.

[36] F. Simoens, H. Wymeersch and M. Moeneclaey, "Linear Precoders for Bit-Interleaved Coded Modulation on AWGN Channels: Analysis and Design Criteria," *IEEE Transactions on Information Theory*, vol. 54, pp. 87–99, January 2008.

[37] R. Battiti and G. Tecchiolli, "Reactive Search : Toward Self-Tuning Heuristics," *Operations Research Society of Americ (ORSA) Journal on Computing*, vol. 6, pp. 126–140, November 1994.

[38] R. Y. S. Tee, F. C. Kuo and L. Hanzo, "Multilevel Generalised Low-Density Parity-Check Codes," *IEE Electronics Letters*, vol. 42, pp. 167 – 168, 2 February 2006.

[39] R. Y. S. Tee, S. X. Ng and L. Hanzo, "Three-Dimensional EXIT Chart Analys'is of Iteraltive Detecltion Aided Coded Modulaltion Schemes," in *IEEE Vehicular Technology Conference-Spring (VTC)*, vol. 5, (Melbourne, Austrialia), pp. 2494 – 2498, May 2006.

[40] R. Y. S. Tee, F. C. Kuo and L. Hanzo, "Generalized Low-Density Parity-Check Coding Aided Multilevel Codes," in *IEEE Vehicular Technology Conference-Spring (VTC)*, vol. 5, (Melbourne, Australia), pp. 2398 – 2402, May 2006.

[41] R. Y. S. Tee, T. D. Nguyen, L. L. Yang and L. Hanzo, "Serially Concatenated Luby Transform Coding and Bit-Interleaved Coded Modulation Using Iteratlive Decoding for the Wireless Internet," in *IEEE Vehicular Technology Conference-Spring (VTC)*, vol. 1, (Melbourne, Australia), pp. 22 – 26, May 2006.

[42] R. Y. S. Tee, S. X. Ng and L. Hanzo, "Precoder-aided iterative detection assisted multilevel coding and three-dimensional EXIT-chart analysis," in *IEEE Wireless Communications and Networking Conference (WCNC)*, vol. 3, (Las Vegas, USA), pp. 1322 – 1326, 3-6 April 2006.

[43] R. Y. S. Tee, O. Alamri and L. Hanzo, "Joint Design of Twin-Antenna Assisted Space-Time Multilevel Sphere Packing Aided Coded Modulation," in *IEEE Vehicular Technology Conference-Fall (VTC)*, (Montreal, Canada), pp. 1–5, September 2006.

[44] R. Y. S. Tee, O. Alamri, S. X. Ng and L. Hanzo, "Equivalent-Capacity-Based Design of Space-Time Block-Coded Sphere-Packing-Aided Multilevel Code," in *IEEE Conference on Communications (ICC)*, (Glasgow, UK), pp. 4173 – 4178, 24-28 June 2007.

[45] R. Y. S. Tee, T. D. Nguyen, S. X. Ng, L-L. Yang and L. Hanzo, "Luby Transform Coding Aided Bit-Interleaved Coded Modulation for the Wireless Internet," in *IEEE Vehicular Technology Conference-Fall (VTC)*, (Baltimore, USA), pp. 2025 – 2029, October 2007.

[46] M. El-Hajjar, R. Y. S. Tee, H. Bin, L-L. Yang and L. Hanzo, "Downlink Steered Space-Time Spreading Assisted Generalised Multicarrier DS-CDMA Using Sphere-Packing-Aided Multilevel Coding," in *IEEE Vehicular Technology Conference-Fall (VTC)*, (Baltimore, USA), pp. 472 – 476, October 2007.

[47] R. Y. S. Tee, O. Alamri, S. X. Ng and L. Hanzo, "Bit-Interleaved Sphere-Packing Aided Space-Time Coded Modulation," *IEEE Transactions on Vehicular Technology*, accepted for publication.

[48] R. Y. S. Tee, O. Alamri, S. X. Ng and L. Hanzo, "Equivalent Capacity Based Joint Multilevel Coding And Space Time Transmit-Diversity Design," *IEEE Transactions on Vehicular Technology*, accepted for publication.

[49] R. Y. S. Tee, R. Maunder, J. Wang and L. Hanzo, "Near-Capacity Irregular Bit-Interleaved Coded Modulation," in *IEEE Vehicular Technology Conference-Spring (VTC)*, (Singapore), May 2008.

[50] R. Y. S. Tee, R. G. Maunder and L. Hanzo, "EXIT-Chart Aided Near-Capacity Irregular Bit-Interleaved Coded Modulation Design," *IEEE Transactions on Wireless Communications*, accepted for publication.

[51] U. Wachsmann, R. F. H. Fischer and J. B. Huber, "Multilevel Codes: Theoretical Concepts and Practical Design Rules," *IEEE Transactions on Information Theory*, vol. 45, pp. 1361–1391, July 1999.

[52] M. Isaka and H. Imai, "On the Iterative Decoding of Multilevel Codes," *IEEE Journal on Selected Areas in Comms*, vol. 19, pp. 935–943, May 2001.

[53] X. Li and J. A. Ritcey, "Bit-interleaved coded modulation with iterative decoding using soft feedback," *IEE Electronics Letters*, vol. 34, pp. 942–943, May 1998.

[54] X. Li, J. A. Ritcey, "Trellis-Coded Modulation with Bit Interleaving and Iterative Decoding," *IEEE Journal on Selected Areas in Communications*, vol. 17, pp. 715–724, April 1999.

[55] S. Lin and D. J. Costello Jr, *Error Control Coding: Second Edition.* USA: Prentice Hall, 2003.

[56] D-F. Yuan, Z-W. Li and F. Zhang, "Two-Level Unequal Error Protection Scheme in Image Transmission System Using Multilevel Codes in Rayleigh Fading Channel," in *IEEE Military Communications Conference (MILCOM)*, vol. 2, pp. 1445 - 1449, October 2001.

[57] M. Isaka, H. Imai, R. H. Morelos-Zaragoza, M. P. C. Fossorier and S. Lin, "Multilevel Codes and Multistage Decoding for Unequal Error Protection," *IEEE Conference for Personal Wireless Communication*, pp. 249–254, February 1999.

[58] R. Gallager, *Information Theory and Reliable Communication.* New York: Willey, 1968.

[59] C. Berrou, A. Glavieux and P. Thitimajshima, "Near Shannon Limit Error-Correcting Coding and Decoding: Turbo Codes," *Proceedings of the International Conference on Communications*, pp. 1064–1070s, May 1993.

[60] D. F. Yuan, P. Zhang, Q. Wang and W. E. Stark, "A Novel Multilevel Codes With 16QAM," *IEEE Wireless Communications and Networking Conference*, pp. 260–263, 2002.

[61] L. Papke and K. Fazel, "Combined Multilevel Turbo-code with MR-modulation," in *IEEE International Conference on Communication*, vol. 2, pp. 668–672, June 1995.

[62] L. Papke and K. Fazel, "Combined Multilevel Turbo-code with 8PSK Modulation," in *IEEE Global Communications Conference (GLOBECOM)*, vol. 1, pp. 649–653, November 1995.

[63] T. Woerz and J. Hagenauer, "Iterative Decoding for Multilevel Codes Using Reliability Information," in *IEEE Global Communications Conference (GLOBECOM)*, vol. 3, pp. 1779–1784, December 1992.

[64] R. Bose and D. R.-Chaudhuri, "On a Class of Error Correcting Binary Group Codes," *Information and Control*, vol. 3, pp. 68–79, 1960.

[65] L. Hanzo, T. H. Liew and B. L. Yeap, *Turbo Coding, Turbo Equalisation and Space Time Coding for Transmission over Wireless channels*. New York, USA: John Wiley IEEE Press, 2002.

[66] T. M. Cover and J. A. Thomas, *Elements of Information Theory*. Canada: John Wiley and Sons Inc., 1991.

[67] U. Wachsmann and J. Huber, "Power and Bandwidth Efficient Digital Communication Using Turbo Codes in Multilevel Codes," *European Transactions on Telecommunications (ETT)*, vol. 6, pp. 557–567, September 1995.

[68] R. Pellizzoni, A. Sandri, A. Spalvieri and E. Biglieri, "Analysis and Implementation of An Adjustable-Rate Multilevel Coded Modulation System," *IEE Proceedings of Communication*, vol. 144, pp. 1–5, February 1997.

[69] J. Hagenauer, "Rate-Compatible Punctured Convolutional Codes and thier Applications," *IEEE Transactions on Communication*, vol. 36, pp. 389–400, April 1988.

[70] S. Lin and P. S. Yu, "A Hybrid ARQ Scheme with Parity Retransmission for Error Control of Satellite Channels," *IEEE Transactions on Communications*, vol. COM-31, pp. 1701–1719, July 1982.

[71] J.-F. Cheng, "Coding Performance of Hybrid ARQ Schemes," *IEEE Transactions on Communications*, vol. 54, pp. 574–574, March 2006.

[72] Q. Huang, S. Chan, L. Ping and K.-T. Ko, "Performance of Hybrid ARQ Using Trellis-Coded Modulation Over Rayleigh Fading Channel," *IEEE Transactions on Vehicular Technology*, vol. 56, pp. 2784–2790, September 2007.

[73] J. Wang, N. S. Othman, J. Kliewer, L. L. Yang and L. Hanzo, "Turbo-Detected Unequal Error Protection Irregular Convolutional Codes Designed For The Wideband Advanced Multirate Speech Codec," *IEEE Transactions on Vehicular Technology*, vol. 2, pp. 927 – 931, September 2005.

[74] S. Benedetto, D. Divsalar, G. Montorsi and F. Pollara, "A Soft-Input Soft-Output APP Module for Iterative Decoding of concatenated codes," *IEEE Communications Letter*, vol. 1, pp. 22–24, January 1997.

[75] N. H. Tran and H. H. Nguyen, "Signal Mappings of 8-Ary Constellations for Bit Interleaved Coded Modulation With Iterative Decoding," *IEEE Transactions on Broadcasting*, vol. 52, pp. 92–99, March 2006.

[76] S. T. Brink, J. Speidel and R-H. Yan, "Iterative Demapping and Decoding for Multilevel Modulation," in *IEEE Global Communications Conference (GLOBECOM)*, vol. 1, pp. 579 – 584, November 1998.

[77] S. T. Brink, "Convergence Behavior of Iteratively Decoded Parallel Concatenated Codes," *IEEE Transactions on Communications*, pp. 1727–1737, October 2001.

[78] F. Schreckenbach and G. Bauch, "EXIT charts for iteratively decoded multilevel modulation," *12th European Signal Processing Conference (EUSIPCO)*, 2004.

[79] D. Divsalar, S. Dolinar and F. Pollara, "Serial Concatenated Trellis Coded Modulation with Rate-1 Inner Code," *IEEE Global Telecommunications Conference*, pp. 777–782, Nov. 2000.

[80] A. Burr, "Turbo-Codes: The Ultimate Error Control Codes?," *IEE Electronics and Communication Engineering Journal*, vol. 13, pp. 155–165, August 2001.

[81] Y. Yasuda, K. Kashiki and Y. Hirata, "High-Rate Punctured Convolutional Codes for Soft Decision Viterbi Decoding," *IEEE Transactions on Communications*, pp. 315–319, March 1984.

[82] S. Lin and D. J. Costello, Jr, *Error Control Coding: Fundamentals and Applications.* Inc. Englewood Cliffs, New Jersey 07632: Prentice-Hall, 1983.

[83] J. G. Proakis, *Digital Communications.* Mc-Graw Hill International Editions, 3rd ed., 1995.

[84] Y. Bian, A. Popplewell and J. J. O'Reilly, "New Very High Rate Punctured Convolutional Codes," *IEE Electronics Letters*, vol. 30, pp. 1119–1120, July 1994.

[85] G. Ungerböck, "Trellis-coded modulation with redundant signal sets. Part 1 and 2," *IEEE Communications Magazine*, vol. 25, pp. 5–21, February 1987.

[86] L. Hanzo, C. Somerville, and J. Woodard, *Voice and Audio Compression for Wireless Communications.* New York, USA: John Wiley IEEE Press, 2007.

[87] L. Hanzo, P.J. Cherriman and J. Street, *Video Compression and Communications: From Basics to H.261, H.263, H.264, MPEG4 for DVB and HSDPA-Style Adaptive Turbo-Transceivers.* Chichester, England: John Wiley and Sons Ltd, 2007.

[88] S. T. Brink, "Convergence of Iterative Decoding," *IEE Electonics Letter*, vol. 35, pp. 806–808, May 1999.

[89] F. Brännström, L. K. Rasmussen and A. J. Grant, "Convergence Analysis and Optimal Scheduling for Multiple Concatenated Codes," *IEEE Transactions on Information Theory*, vol. 51, pp. 3354–3364, September 2005.

[90] J. Hagenauer, "The EXIT Chart - Introduction To Extrinsic Information Transfer In Iterative Processing," *European Signal Processing Conference*, pp. 1541–1548, September 2004.

[91] M. Tüchler, "Convergence prediction for iterative decoding of threefold concatenated systems," *IEEE Global Telecommunications Conference*, pp. 1358–1362, Nov. 2002.

[92] F. Brännström, L. K. Rasmussen and A. Grant, "Optimal Scheduling for Iterative Decoding," *IEEE International Symposium on Information Theory*, p. 350, 2003.

[93] K. R. Narayanan, "Effect of Precoding on the Convergence of Turbo Equalization for Partial Response Channels," *IEEE Journal on Selected Areas in Communications*, pp. 686–698, Apr. 2001.

[94] I. Lee, "The Effect of a Precoder on Serially Concatenated Coding Systems With an ISI Channel," *IEEE Transaction On Communications*, pp. 1168–1175, 2001.

[95] A. G. Lillie, A. R. Nix and J. P. McGeehan, "Performance and Design of a Reduced Complexity Iterative Equalizer for Precoded ISI Channels," *Vehicular Technology Conference (VTC)*, pp. 299–303, 2003.

[96] N. H. Tran and H. H. Nguyen, "Signal Mappings of 8-ary Constellations for BICM-ID Systems Over a Rayleigh Fading Channel," *IEEE Communications Letters*, pp. 4083–4086, October 2005.

[97] F. Shreckenbach, N. Görtz, J. Hagenauer and G. Bauch, "Optimization of Symbol Mappings for Bit-Interleaved Coded Modulation With Iterative Decoding," *IEEE Communication Letters*, pp. 593–595, December 2003.

[98] F. Simoens, H. Wymeersch and M. Moeneclaey, "Multi-dimensional Mapping for Bit-Interleaved Coded Modulation," *IEEE Vehicular Technology Conference-Spring (VTC)*, pp. 733–737, May 2005.

[99] D-F. Yuan, F. Zhang, A-F. So, Z-W. Li, "Concatenation of Space-Time Block Codes and Multilevel Coding over Rayleigh Fading Channels," in *IEEE Vehicular Technology Conference*, (Atlantic City, USA), pp. 192–196, October Fall 2001.

[100] S. M. Alamouti, "A Simple Transmitter Diversity Scheme for Wireless Communications," *IEEE Journal on Selected Areas in Communications*, vol. 16, pp. 1451–1458, October 1998.

[101] V. Tarokh, H. Jafarkhani and A.R. Calderbank, "Space-Time Block Codes from Orthogonal Designs," *IEEE Transactions on Information Theory*, vol. 45, pp. 1456–1467, July 1999.

[102] W. Su, Z. Safar, and K. J. R. Liu, "Space-Time Signal Design for Time-correlated Rayleigh Fading Channels," in *IEEE International Conference on Communications*, (Anchorage, Alaska), pp. 3175–3179, May 2003.

[103] O. Alamri, B. L. Yeap, L. Hanzo, "Turbo Detection of Channel-Coded Space-Time Signals Using Sphere Packing Modulation," in *IEEE Vehicular Technology Conference*, (Los Angeles, USA), pp. 2498–2502, September Fall 2004.

[104] O. Alamri, B. L. Yeap and L. Hanzo, "A Turbo Detection and Sphere-Packing-Modulation Aided Space-Time Coding Scheme," *IEEE Transactions on Vehicular Technology*, vol. 56, pp. 575–582, March 2007.

[105] J. H. Conway and N. J. Sloane, "Sphere Packings, Lattices and Groups," *Spinger-Verlag*, 1999.

[106] O. Alamri, B. L. Yeap, L. Hanzo, "Turbo Detection of Channel-Coded Space-Time Signals Using Sphere Packing Modulation," in *IEEE Vehicular Technology Conference*, (Los Angeles, USA), pp. 2498–2502, September Fall 2004.

[107] O. R. Alamri, *Turbo Detection of Sphere Packing Modulation Aided Space-Time Coding Schemes.* PhD Thesis, University of Southampton, 2007.

[108] V. Tarokh, N. Seshadri and A. R. Calderbank, "Space-time Codes for High Rate Wireless Communication: Performance analysis and code construction," *IEEE Transactions on Information Theory*, vol. 44, pp. 744–765, March 1998.

[109] G. H. Golub and C. F. Van-Loan, *Matrix Computations.* Baltimore, MD: Johns Hopkins, 1996.

[110] S. X. Ng and L. Hanzo, "On the MIMO Channel Capacity of Multi-Dimensional Signal Sets," *IEEE Transactions on Vehicular Technology*, vol. 55, pp. 528–536, March 2006.

[111] L. He and H. Ge, "A New Full-Rate Full-Diversity Orthogonal Space-Time Block Coding Scheme," *IEEE Communications Letters*, vol. 7, pp. 590–592, December 2003.

[112] K. Zeger and A. Gersho, "Pseudo-Gray Coding," *IEEE Transaction On Communications*, vol. 38, pp. 2147–2158, December 1990.

[113] X. Li, A. Chindapol and J. A. Ritcey, "Bit-Interleaved Coded Modulation with Iterative Decoding and 8PSK Signaling," *IEEE Transactions on Communication*, pp. 1250–1257, August 2002.

[114] M. Isaka, R. H. M-Zaragoza, M. P. C. Fossorier, S. Lin and H. Imai, "Multilevel Coded 16-QAM Modulation with Multistage Decoding and Unequal Error Protection," in *Global Communication Conference*, vol. 6, (Sydney, Austrialia), pp. 3548–3553, November 1998.

[115] F. Guo, "Low Density Parity Check Coding," *Ph.D thesis, University of Southampton, UK*, 2005.

[116] Y. Huang and J. A. Ritcey, "Improved 16-QAM Constellation Labeling for BI-STCM-ID With the Alamouti Scheme," *IEEE Communications Letters*, vol. 9, pp. 157–159, February 2005.

[117] J. Hou. P. H. Siegel, L. B. Milstein and H. D. Pfister, "Multilevel Coding with Low-Density Parity-Check Component Codes," *IEEE Global Telecommunications Conference*, pp. 1016–1020, Nov. 2001.

[118] J. Boutros, O. Pothier and G. Zḿor, "Generalized Low Density (Tanner) Codes," *Proceedings of the International Conference of Communication*, pp. 441–445, 1999.

[119] M. Lentmaier and K. S. Zigangirov, "On Generalized Low-Density Parity-Check Codes Based on Hamming Component Codes," *IEEE Communications Letters*, pp. 248–250, Aug. 1999.

[120] Bernard Sklar, *Digital communications: Fundamentals and Applications.* Inc. Englewood Cliffs, New Jersey 07632: Prentice-Hall, 1988.

[121] D. J. C. MacKay, *Fountain Codes.* http://www.inference.phy.cam.ac.uk/-mackay/CodesTheory.html: Cavendish Laboratory, University of Cambridge, 2004.

[122] D. J. C. MacKay, *Information Theory, Interference and Learning Algorithms.* http://www.inference.phy.cam.ac.uk/mackay/itila/: Cambridge University Press, 2003.

[123] M. Luby, "LT codes," in *Proceedings of the 43rd Annual IEEE Symposium on Foundations of Computer Science*, pp. 271–282, November 2002.

[124] R. M. Tanner, "A Recursive Approach To Low Complexity Codes," *IEEE Transaction On Information Theory*, pp. 533–547, September 1981.

[125] O. Pothier, *Compound Codes Based On Graphs and Their Iterative Decoding.* PhD Thesis, Ecole Nationale Suprieure des Telecommunications, 2000.

[126] J. Buyers, M. Luby, M. Mitzenmacher and A. Rege, "A digital Fountain approach to reliable distribution of bulk data," *In Proceedings of ACM SIGCOMM'98*, September 1998.

[127] M. G. Luby, M. Shokrollahi, M. Watson and T. Stockhammer, "Raptor Forward Error Correction Scheme," *Reliable Multicast Transport Internet-Draft*, June 2005. URL available at :*http://www.rfc-archive.org/getrfc.php?rfc=5053.*

[128] D. J. C. MacKay, "Fountain Codes," *IEEE Proceedings in Communications*, no. 6, pp. 1062–1068, 2005.

[129] T. D. Nguyen, L. L. Yang and L. Hanzo, "Systematic Luby Transform Codes and Their Soft Decoding," *IEEE Workshop on Signal Processing Systems (SiPS)*, pp. 67–72, October 2007.

[130] L. Hanzo, L-L. Yang, E-L. Kuan and K. Yen, *Single- and Multi-Carrier DS-CDMA.* New York, USA: John Wiley IEEE Press, 2003.

[131] A. Shokrollahi, "Raptor Codes," *International Symposium on Information Theory*, p. 36, June 2004.

[132] A. Shokrollahi, *Raptor Codes.* http://algo.epfl.ch: Technical Report, June 2003.

[133] J. Buyers, M. Luby and M. Mitzenmacher, "A Digital Fountain Approach to Asynchronous Reliable Multicast," *IEEE Journal on Selected Areas in Communications*, vol. 20, pp. 1528–1540, October 2002.

[134] Q. Luo and P. Sweeney, "Hybrid-ARQ Protocols Based on Multilevel Coded Modulation," *IEE Electronics Letters*, vol. 39, pp. 1063 – 1065, July 2003.

[135] T. Clevorn, S. Godtmann and P. Vary, "BER Prediction Using EXIT Charts For BICM With Iterative Decoding," *IEEE Communications Letters*, vol. 10, pp. 49–51, January 2006.

[136] N. H. Tran and H. H. Nguyen, "Signal Mappings of 8-Ary Constellations for BICM-ID Systems over a Rayleigh Fading Channel," *IEICE Transcations Letter on Communication*, pp. 4083–4086, October 2005.

[137] F. Simoens, H. Wymeersch and M. Moeneclaey, "Multi-dimensional Mapping for Bit-Interleaved Coded Modulation," *Vehicular Technology Conference, Spring*, vol. 2, pp. 733–737, June 2005.

[138] F. Schreckenbach and G. Bauch, "Bit-Interleaved Coded Irregular Modulation," *European Transactions on Telecommunications*, vol. 7, pp. 269–282, April 2006.

[139] L. Hanzo, C. H. Wong, and M. S. Yee, *Adaptive Wireless Transceivers: TurboCoded, TurboEqualized and SpaceTime Coded TDMA, CDMA, and OFDM Systems.* Chichester, UK: John Wiley IEEE Press, August 2002.

[140] F. Simoens, H. Wymeersch and M. Moeneclaey, "Design and Analysis of Linear Precoders for Bit-Interleaved Coded Modulation with Iterative Decoding," in *International Symposium on Turbo Codes and Related Topics*, (Munich, Germany), April 2006.

[141] L. Szczecinski, H. Chafnaji and C. Hermosilla, "Modulation Doping for Iterative Demapping of Bit-Interleaved Coded Modulation," *IEEE Communications Letters*, vol. 9, pp. 1031–1033, 2005.

[142] M. Tüchler, "Design of Serially Concatenated Systems Depending on The Block Length," *IEEE Transactions on Communications*, vol. 52, pp. 209–218, February 2004.

[143] M. Tüchler and J. Hagenauer, "EXIT Charts of Irregular Codes," *IEEE Conference on Information Sciences and Systems*, pp. 748–753, March 2002.

[144] A. Ashikhmin, G. Kramer and S. T. Brink, "Extrinsic Information Transfer Functions: Model and Erasure Channel Properties," *IEEE Transactions on Information Theory*, vol. 50, pp. 2657–2673, November 2004.

[145] A. Ashikhmin, G. Kramer and S. T. Brink, "Code Rate and the Area under Extrinsic Information Transfer Curves," *IEEE International Symposium on Information Theory*, p. 115, June 2002.

[146] R. G. Maunder and L. Hanzo, "Near-capacity irregular variable length coding and irregular unity rate coding," accepted by *IEEE Transactions on Wireless Communications*, available at *:http://eprints.ecs.soton.ac.uk/14471/.*

[147] L. Hanzo, S. X. Ng, T. Keller and W. Webb, *Quadrature Amplitude Modulation.* Chichester, UK : John Wiley and Sons, 2004.

[148] L. Zhao, L. Lampe and J. Huber, "Study of Bit-Interleaved Coded Space-Time Modulation with Different Labeling," *IEEE Information Theory Workshop*, pp. 199–202, March 2003.

[149] D. Chase, "A Combined Coding and Modulation Approach for Communication over Dispersive Channels," *IEEE Transactions on Communications*, pp. 159 – 173, March 1973.

[150] B. A. Harvey and S. B. Wicker, "Packet combining systems based on the Viterbi decoder," *IEEE Transactions on Communications*, vol. 42, pp. 1544 – 1557, March 1994.

[151] L. Y. Song and A. G. Burr, "A Simple Differential Modulation Scheme for Quasi-Orthogonal Space-Time Block Codes with Partial Transmit Diversity," *EURASIP Journal on Wireless Communications and Networking*, vol. 2007, pp. 13–19, January 2007.

Index

Author Index